Micromechanics of cavitation in confined soft polymer layers

Flora-Maud Le Menn

To cite this version:

Flora-Maud Le Menn. Micromechanics of cavitation in confined soft polymer layers. Material chemistry. Université Paris sciences et lettres, 2022. English. NNT : 2022UPSLS044 . tel-04026010

HAL Id: tel-04026010
https://pastel.hal.science/tel-04026010

Submitted on 13 Mar 2023

PSL UNIVERSITÉ PARIS

THÈSE DE DOCTORAT
DE L'UNIVERSITÉ PSL

Préparée à ESPCI Paris - SIMM

Micromécanique de la cavitation dans des films d'élastomères confinés

Micromechanics of cavitation in confined soft polymer layers

Soutenue par
Flora-Maud LE MENN
Le 16 décembre 2022

École doctorale n°397
Physique et Chimie des Matériaux

Spécialité
Physique et Chimie des Matériaux

Composition du jury :

Renaud NICOLAY Professeur, ESPCI Paris	*Président*
Catherine GAUTHIER Professeur, INSA Lyon	*Rapporteure*
Julien JUMEL Professeur, ENSTA Bretagne	*Rapporteur*
Chelsea DAVIS Assistant professor, Purdue University	*Examinatrice*
Etienne BARTHEL Directeur de recherche, ESPCI Paris	*Co-directeur de thèse*
Costantino CRETON Directeur de recherche, ESPCI Paris	*Directeur de thèse*

ESPCI PARIS | PSL

Micromechanics of cavitation in confined soft polymer layers

Flora-Maud LE MENN

Costantino CRETON
Etienne BARTHEL

December 16, 2022

Remerciements

This PhD work was possible thanks to the industrial partnership with DSM and then Covestro and their interest in the protection of optic fibres. I want to thank especially Guido Hensen for the fruitful discussions on the chemistry and for taking part in my jury as guest. Thanks to the members of my jury: Julien Jumel, Catherine Gauthier, Chelsea Davis and Renaud Nickolaÿ for the interesting discussions and comments on my work.

J'aimerais également remercier mes deux encadrants. Merci pour la confiance et la liberté que vous m'avez accordée. Merci pour vos conseils, votre soutien, surtout pendant la rédaction quand tout s'est accéléré: l'histoire qui en est sortie en valait le coup. Costantino, merci pour les discussions, pas toujours très régulières, mais dont j'ai beaucoup appris. Etienne, merci pour toutes les discussions du soir où je te présentais mes déboires et tu y répondais avec humour. Ton optimisme envers mes manips et mes résultats était indéfectible, tes citations souvent mémorables (*"La force, c'est la force !"*). Merci pour ta présence pendant les derniers moments de rédaction et les discussions quasi philosophiques sur "la bulle ou la fracture ?"

Merci à toutes les personnes qui m'ont aidée au cours de ces trois années. D'abord mes deux stagiaires, Ana Goulée et Ludovic Dulac, pour avoir travaillé avec moi sur des variations de formulation, avec leurs lots de surprises ! Merci beaucoup à Christophe Chendon du LSABM pour les mesures de TOF et Jean-Marie Chassot de l'Institut Langevin pour l'essai de mesures en OCT. Au sein du SIMM, merci à Bruno Bresson pour les mesures en AFM, Jean-Baptiste d'Espinose pour la RMN du solide et Mohamed Hanafi pour l'aide sur la DSC. Merci à Krupal Patel pour la formation sur Abaqus, Alex Cartier et Atul Sharma pour les mécanophores. Merci à Hélène Montes pour sa bonne humeur communicative et pour m'avoir permis de faire des tutorats à l'ESPCI. Merci à Fabienne Decuq pour toutes les situations administratives démêlées tout en gardant le sourire ! Enfin, un immense merci à Ludovic Olanier et Jean-Claude Mancer pour la fabrication des systèmes de polymérisation et de cavitation. Merci pour votre bonne humeur à toute épreuve et pour tous les bons moments passés à l'atelier !

Cette thèse n'aurait pas été la même sans l'ambiance du SIMM. Merci à tous pour les discussions, les karaokés, les week-ends labo, ... Merci à mes co-bureaux pour les anecdotes et la décoration fantastique, merci à la dream team de l'escape game pour les records battus. Merci à tous les "1A en thèse", ça a été un plaisir de progresser ensemble en partageant les percées mais aussi les grands moments de flottement. Merci Madame Barbier pour ta bonne humeur, Anusree for the discovery of Indian cuisine and ballet evenings. Enfin, merci Julie pour l'aventure en Californie, les discussions sur l'organisation du labo, le management de l'INSTRON et surtout les grands moments de rires.

Merci à tous mes amis. Merci pour le partage d'expériences et les digressions scientifiques entre thésards, merci aux autres d'avoir supporté patiemment ces discussions ! Merci à Romane de me suivre depuis si longtemps, merci à la Garderie pour tous ces beaux moments.

Merci à ma famille pour votre soutien et de m'avoir donné la volonté de toujours donner le meilleur. Finalement, j'espère vous avoir convaincu que oui, j'ai trouvé quelque chose.

Enfin, pour toi qui voudrais faire de la silanisation ou de la cavitation, n'oublie pas :

"En essayant continuellement on finit par réussir. Donc : plus ça rate, plus on a de chance que ça marche."
Jacques Rouxel - Les Shadoks

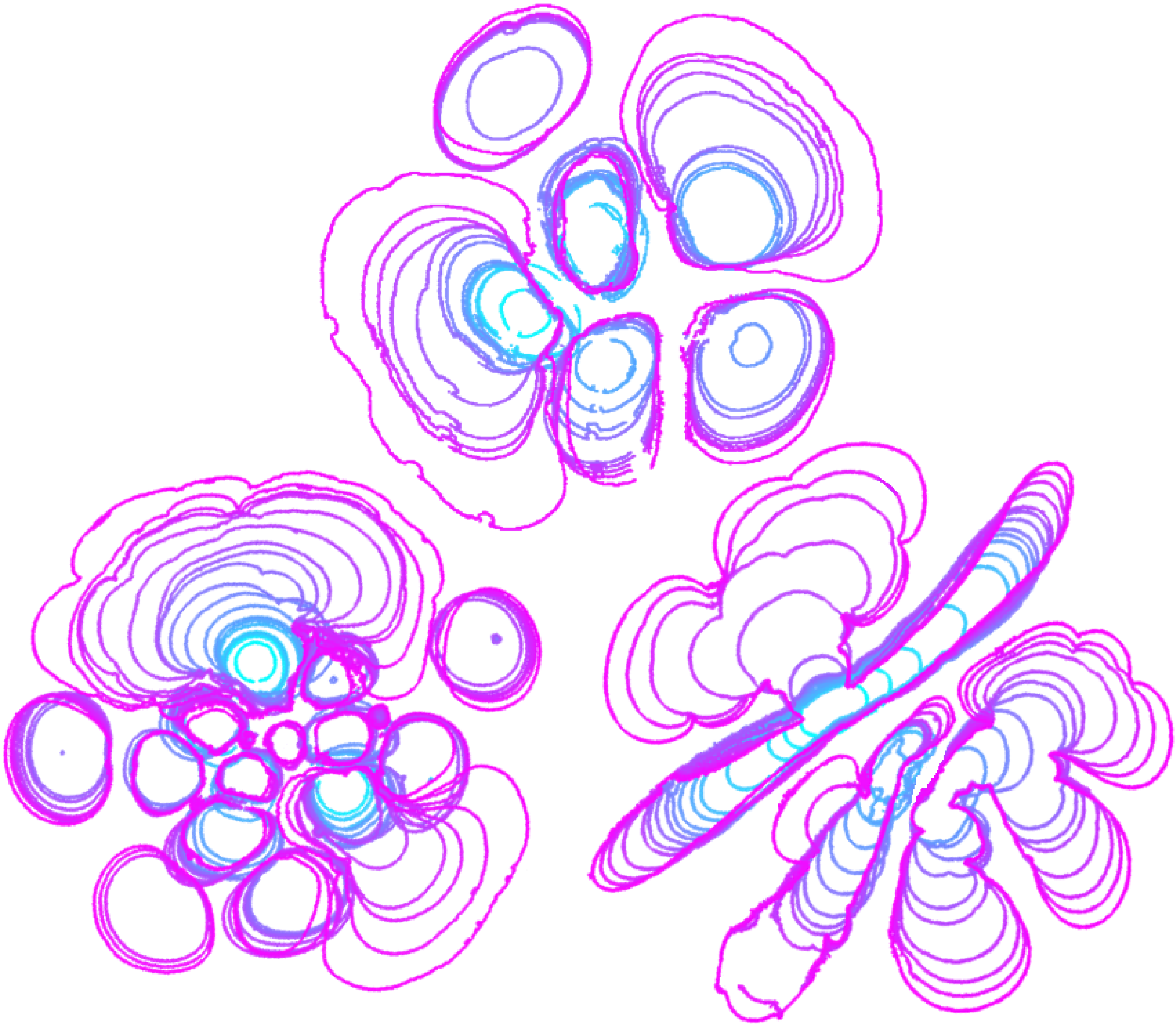

Résumé général en français

Introduction

Aujourd'hui, plus de 1,2.10^6 km de fibres optiques sous-marines relient les continents entre eux. Grâce à la réfection totale de la lumière dans les fibres de verre, le transfert de données peut se faire sur de grandes distances. Pour protéger la fibre de verre, elle est recouverte de couches de polymères : une couche molle en premier lieu, qui se déforme pour éviter les flexions du verre puis une couche plus dure, comme représenté sur l'encart de la Figure 1. Les fibres optiques sont fabriquées à des vitesses allant jusqu'à 180 km/h, poussant la polymérisation des résines à se faire extrêmement rapidement par illumination UV à haute intensité. Cette production rapide soumet la première couche de coating à une pression hydrostatique constante, menant à l'ouverture de cavités en son sein. Ce problème industriel a motivé DSM, puis Covestro, à financer cette étude.

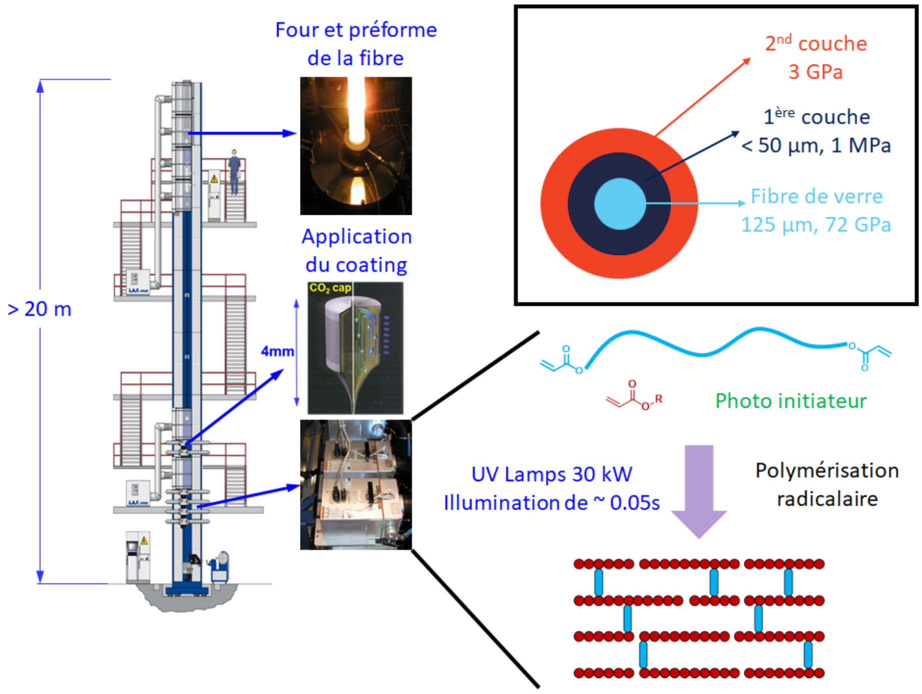

FIGURE 1: Production de fibres optiques - Fourni par Covestro. Le verre est fondu au sommet de la tour et tombe sous la forme d'une fibre unique. Cette fibre de verre est recouverte d'une ou plusieurs couches de résines qui sont ensuite polymérisées en un flash. Les résines polymères sont majoritairement composées d'oligomères et de monomères acrylates. Encart : Épaisseurs respectives et modules d'Young des coatings.

La nucléation et la croissance de cavités dans les matériaux mous est un problème largement étudié. Au cours des années, les modèles théoriques analysant la croissance de cavités dans les matériaux polymères ont évolués d'une description purement élastique et réversible [1] vers une description de propagation de fracture [2]. Certains modèles proposent même des évolutions instables des cavités ([3], [4]). De nombreuses techniques expérimentales permettent de tester la cavitation par saturation des matériaux (huile [5], pression de gaz [6]), par traction hydrostatique entre cylindres ([7], [8]), en géométrie plan/plan [1] ou sphère/plan [9], ou enfin en créant un défaut majeur par injection d'eau ou d'air au travers d'une aiguille plantée dans le matériau [10]. Cependant, le phénomène de nucléation de bulles et l'effet du confinement du matériau sur la dynamique de la cavitation sont encore mal compris. Le but de notre étude sera de tester des formulations proches des réseaux industriels et réticulés par un processus flash, produisant des défauts et hétérogénéités dans les réseaux polymères. Le second challenge sera de confiner des couches d'une épaisseur de l'ordre d'une centaine de micromètres, afin d'approcher les épaisseurs utilisées sur les fibres commerciales, et de les tester sous traction hydrostatique.

Chimie

La formulation de base des réseaux a été proposée par DSM (puis Covestro), se basant sur un ratio massique 70/30 d'oligomère polypropylène glycol de 8000 g/mol bi-fonctionnalisé avec un acrylate (OL HEA) ou un méthacrylate (OL HEMA) et de monomères EHA et PEA, comme décrits en Figure 2. Des réseaux bimodaux ont également été formulés à partir du mix de référence OL HEA 15% EHA 15% PEA en substituant 1% (resp. 5%) massique de l'oligomère par le IPDI(HEA)$_2$. Ces nouvelles formulations sont nommées 1%bi (resp. 5%bi). Un taux massique de 1% de photoinitiateur est utilisé pour assurer une bonne conversion lors de la polymérisation flash. Des films de résines sont produits par étalement des mix sur une plaque de verre avec un docteur blade et illumination par une lampe Phoseon Firejet FJ801 395 nm. Après optimisation du protocole et vérification de la conversion totale des acrylates par mesures en IR sur des échantillons d'épaisseur allant jusqu'à 800 μm, un protocole d'illumination à 70% de puissance de la lampe et 1s d'illumination en atmosphère inerte est choisi pour tous les réseaux. Cela correspond à une énergie totale de polymérisation de 1 J/cm^2. Les réseaux formés sont dans leur domaine caoutchoutique à température ambiante, leur température de transition vitreuse est aux environs de -60°C.

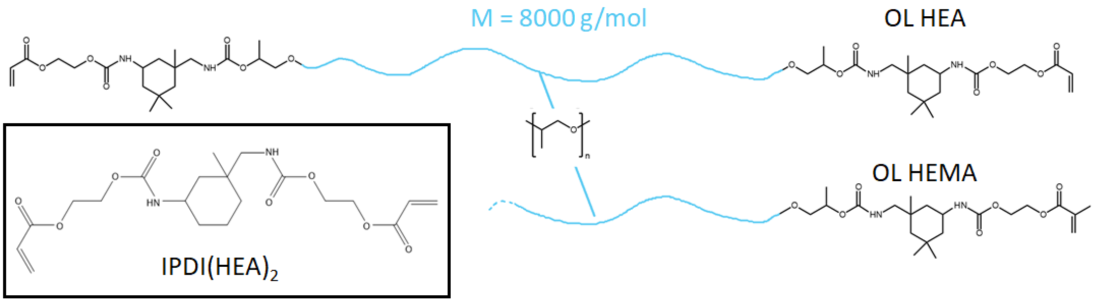

(A) Oligomer PPG8000 fonctionnalisé acrylate (OL HEA) et methacrylate (OL HEMA)

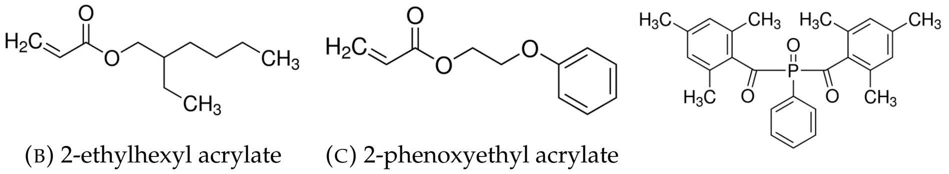

(B) 2-ethylhexyl acrylate (EHA)

(C) 2-phenoxyethyl acrylate (PEA)

(D) BAPO

FIGURE 2: Oligomère et monomères acrylates pour former les réseaux. (A) Encart : Court diacrylate utilisé pour engendrer de la bimodalité dans le réseau. (D) BAPO : photoinitiateur

Propriétés mécaniques

Les propriétés mécaniques les plus intéressantes dans le cadre de notre étude sont testées suivant les trois techniques décrites en Figure 3 :

- Le module d'Young E est déterminé par fit de l'élasticité linéaire (petites déformations) sur un test en traction uniaxiale. Ce test permet également d'observer l'adoucissement aux moyennes déformations.
- Le raidissement J_m est mesuré par gonflement biaxial hydraulique de l'échantillon. Le domaine des grandes déformations est atteint car le gonflement biaxial permet de se libérer de l'effet des défauts de bords qui provoquent la rupture précoce observée en traction uniaxiale. Les courbes contrainte/déformation sont ensuite fittées par le modèle de Gent qui permet une description du raidissement.
- L'énergie de fracture G_c est mesurée par traction uniaxiale sur un dumbbell entaillé au préalable.

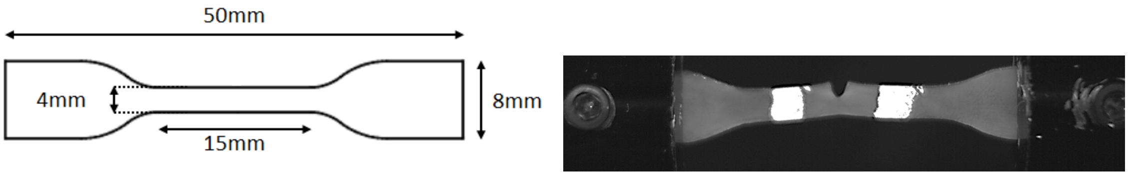

(A) Schéma des dumbbells

(B) Echantillon de fracture sous traction

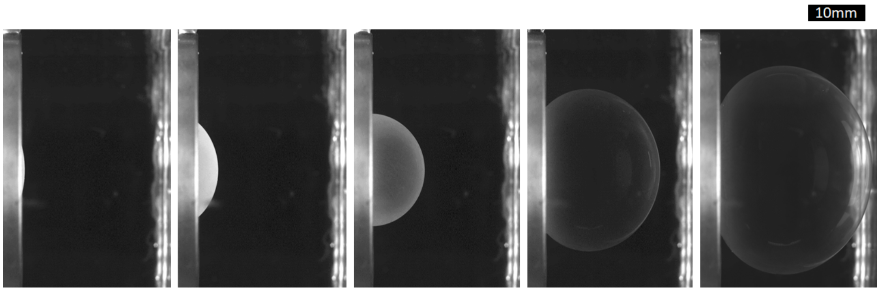

(C) Gonflement des membranes

FIGURE 3: Schéma des échantillons pour l'uniaxial et le gonflement biaxial. (A) L'échantillon est clampé sur les parties larges, la déformation et la contrainte sont homogènes dans la partie centrale. (B) L'énergie de fracture est mesurée par traction uniaxiale sur un dumbbell entaillé au préalable. (C) Un film de polymère est testé en plusieurs cycles de gonflement par volume contrôlé jusqu'à rupture.

Les propriétés mécaniques sont résumées dans le Tableau 1, l'écart-type sur les valeurs n'est pas négligeable et provient de la variabilité entre les batchs et les événements de polymérisation. Néanmoins, la différence entre les formulations est suffisamment importante pour pouvoir les différencier. G_c dépend fortement de la vitesse de test ce qui suggère un phénomène de dissipation accru autour de la tête de fracture ([11], [12]). Sans surprise, les réseaux avec un grand E présentent également une grande énergie de fracture et un grand raidissement (= petit J_m). Il ne sera donc pas évident de déterminer l'effet d'une propriété matériau indépendamment des autres. Les deux seuls réseaux qui dévient légèrement de cette tendance sont les réseaux bimodaux qui présentent un plus fort raidissement que les formulations usuelles mais une énergie de fracture proche de celle du réseau OL HEA 30% PEA.

Formulation		E (MPa)	Model de Gent		G_c (J/m^2)	
		uniaxial	E_G (MPa)	J_m	0.0067 %/s	3.33 %/s
OL HEA	15% 15%	1.156 ± 0.025	0.989	54.88	40.07 ± 5.74	145.32 ± 27.52
	1%bi	1.210 ± 0.160	X	X	49.96	220.48 ± 57.54
	5%bi	1.488 ± 0.119	*1.450*	*20.24*	55.92	432.70 ± 171.80
	30% EHA	0.958 ± 0.007	0.810	69.30	49.98 ± 28.09	119.62 ± 33.37
	30% PEA	1.564 ± 0.065	1.241	34.12	63.76 ± 9.56	254.26 ± 114.56
OL HEMA	15% 15%	0.967 ± 0.060	0.840	38.01	47.63 ± 2.63	139.48 ± 24.85
	30% EHA	0.853 ± 0.023	0.842	76.00	32.55 ± 0.17	126.13 ± 63.91
	30% PEA	1.301 ± 0.049	1.287	46.26	33.40 ± 3.39	213.40 ± 25.50

TABLE 1: Bilan des propriétés mécaniques des différentes formulations. Le fit de Gent est réalisé sur les données biaxiales, sauf pour les formulations bimodales.

Tester des élastomères sous pression hydrostatique

Présentation du set-up

En vue des fines épaisseurs considérées dans cette étude, la meilleure technique expérimentale pour tester ces réseaux est la traction hydrostatique. Dans le but de provoquer une bulle de cavitation dans le centre de l'échantillon, un confinement en géométrie sphère/plan qui permet une concentration de la pression hydrostatique à l'apex de la bille semblait le plus pertinent. Une fois polymérisée, la couche de polymère confinée entre les surfaces de verre est mise sous traction hydrostatique à vitesse constante. En plus de mesurer la force appliquée sur l'échantillon et le déplacement associé, les événements de cavitation sont observés au travers de la lame de verre en temps réel. Grâce à une analyse en éléments finis sur Abaqus, la force mesurée au moment de l'ouverture de la première cavitation peut être reliée à la pression hydrostatique locale, ce qui permet de caractériser la résistance à la cavitation des matériaux. Pour tous les échantillons et toutes les formulations, la pression de cavitation de la première bulle était supérieure à la limite théorique de 5E/6 proposée par Gent et Lindley [1].

(A) Schéma de l'échantillon

(B) Système de polymérisation

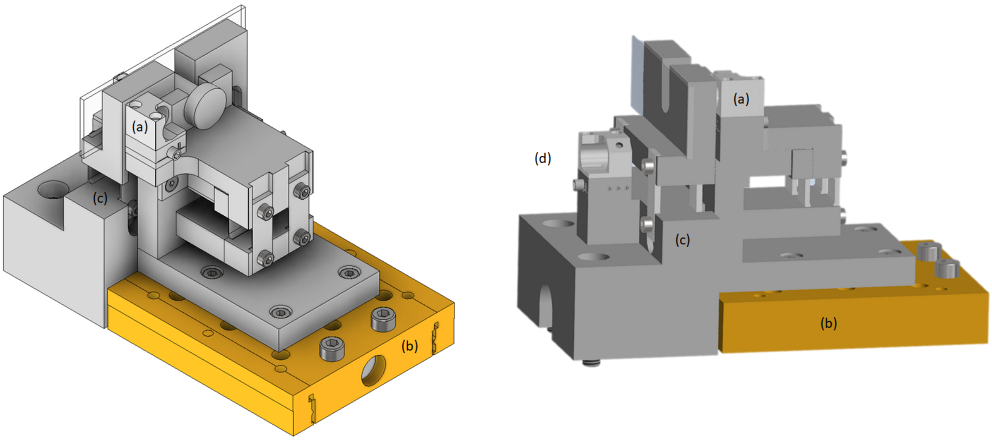

(C) Système de traction hydrostatique

FIGURE 4: Echantillons de cavitation et set-up de traction. Design : Ludovic Olanier et Jean-Claude Mancer - atelier de l'ESPCI. (A) Echantillon de polymère confiné entre la plaque de verre et la bille de verre. Encart : zoom sur la zone confinée. (B) Système de polymérisation qui permet de contrôler l'épaisseur par ajout de cales. (C) Set-up de traction hydrostatique. (a) Capteur capacitif (1 mm) - mesure du déplacement (b) Platine de déplacement contrôlée par un moteur pas-à-pas (gamme de déplacement de 25 mm) (c) Double cantilever pour la mesure de la force, raideur de $S = 4,166.10^6$ N/m (d) Capteur capacitif (50 μm) - mesure de force

Effet de l'épaisseur

Tout d'abord, l'effet de l'épaisseur de la zone confinée a été testé sur la formulation de référence OL HEA 15% EHA 15% PEA. Alors que l'impact du confinement sur la pression de cavitation de la 1ère bulle n'est pas évident, le comportement de cavitation entre les couches épaisses (500 μm) et fines (100 μm) est drastiquement différent. De manière reproductible, les couches épaisses présentent un événement de cavitation marqué par une brusque chute de la force. Cette fracture se déstabilise rapidement en plusieurs fronts qui finissent par se rejoindre et créer une large fracture circulaire. La couche fine, elle, présente une multitude de bulles de cavitation, qui sont chacune associées à une petite chute de la force. La plupart de ces fractures se stabilisent sous forme de "pancake", seules quelques-unes se déstabilisent dans une multitude de fronts de fracture, en forme "raspberry" (nom inspiré de Morelle et al. [13]), pour finalement former la large fracture circulaire. L'évolution des bulles est analysé par l'aire projetée dans le plan d'observation, comme montré en Figure 5 (C).

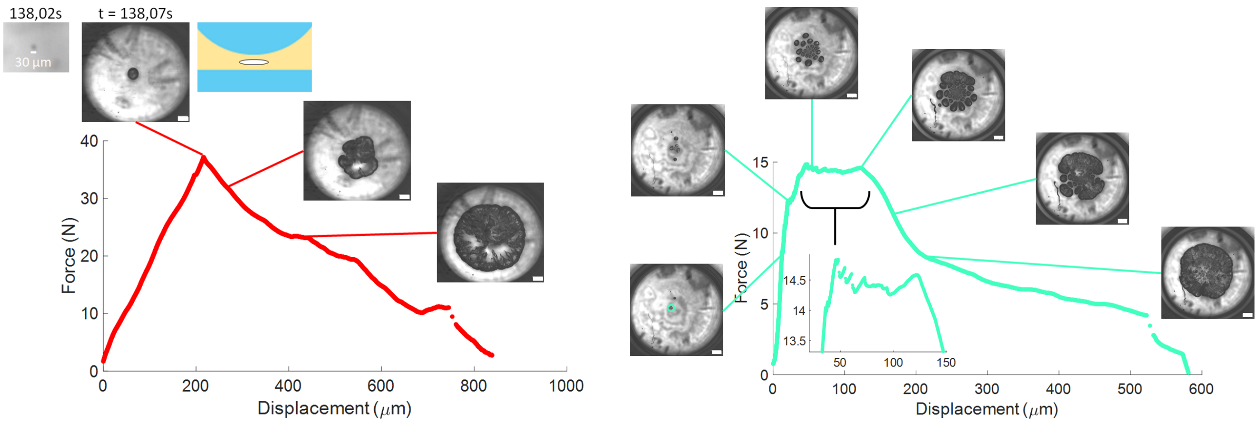

(A) Test d'un échantillon d'épaisseur de 500 μm

(B) Test d'un échantillon d'épaisseur de 100 μm

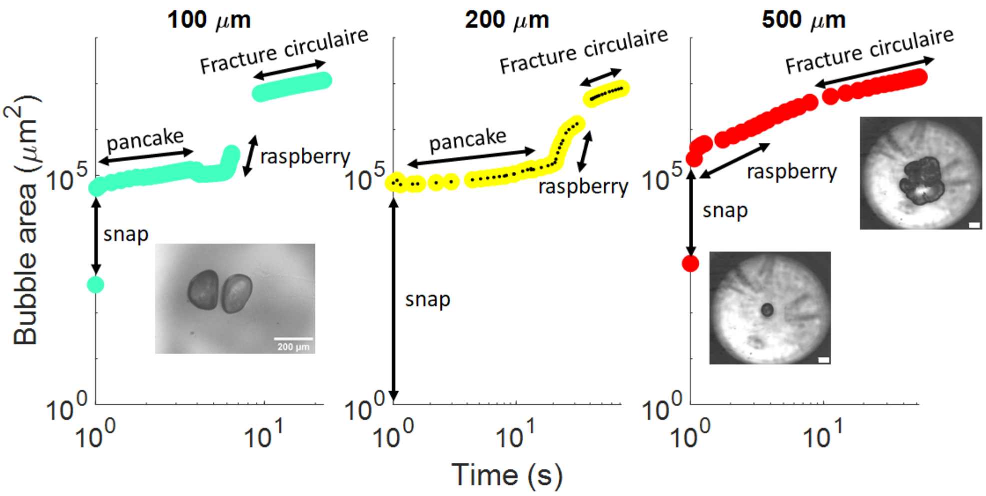

(C) Effet de l'épaisseur sur le comportement des bulles critiques

FIGURE 5: Comportement représentatif de la cavitation dans des échantillons d'épaisseur différente sous traction à 5 μm/s. (A) Test de cavitation sur une couche épaisse : une bulle s'ouvre et transite directement en fracture globale de l'échantillon. Échelle : 500 μm. Encart : Schéma de la fracture ouverte dans la couche confinée. L'image de la bulle vue par la lame de verre est circulaire mais la vision dans un plan perpendiculaire à la couche est une ellipse. (B) Test d'une fine couche confinée : une multitude de bulles s'ouvrent et restent sous forme de fractures ouvertes stables. Plusieurs autres bulles s'ouvrent et certaines transitent vers la fracture critique. Échelle : 500 μm. (C) Évolution temporelle de l'aire projetée de la bulle d'une cavité critique. Echelle graphe de gauche : 200 μm, Echelle graphe de droite : 500 μm. Les bulles de cavitation s'ouvrent toutes par fracture instable, nommée snap, fixé à t = 1s. Les couches fines stabilisent cette fracture en mode pancake puis la bulle se déstabilise par différents fronts de fracture (raspberry). Enfin, l'échantillon est fracturé par un front global circulaire.

Effet d'une variation des propriétés mécaniques

Enfin, les différentes formulations ont toutes été testées sur des échantillons de 100 μm et l'effet des propriétés mécaniques peut être résumé en Figure 6. Encore une fois, la variabilité des pressions de cavitation ne peut pas nous permettre de discerner un effet net de l'élasticité ou de l'énergie de fracture. Cependant, l'évolution des cavités semble dépendre fortement du raidissement du matériau. Alors que les réseaux présentant une faible énergie de fracture et un faible raidissement présentent une stabilité accrue des bulles sous forme de pancake, un grand raidissement semble déstabiliser rapidement le front de la fracture pancake pour transiter vers la forme raspberry. Cette observation doit cependant être nuancée par le fait qu'un nombre limité de test a pu être effectué sur chacune des formulations.

Conclusion

Lors de cette étude, nous avons synthétisé des films fins de résines dont la formulation et le processus de polymérisation sont comparables aux coatings industriels de protection de fibres optiques. Après la caractérisation de leurs propriétés mécaniques (module d'Young, raidissement, énergie de fracture), leur résistance à la cavitation a été explorée au moyen d'un set-up original. Suite à l'optimisation du protocole de fabrication des échantillons et du design du set-up, nous avons montré qu'il était possible de confiner et de tester sous pression hydrostatique ces fines couches de résines acrylates polymérisées en un flash. Au travers de l'analyse FEM, nous avons également pu relier la force macroscopique mesurée lors du test à la pression hydrostatique locale pour le premier événement de cavitation, ce que nous avons assimilé à la résistance à la cavitation. La mesure de cette pression d'apparition de première bulle est assez variable suivant les échantillons et le nombre d'échantillons testé est trop faible pour pouvoir discerner une tendance marquée de l'effet des propriétés matériaux sur leur résistance à la cavitation.

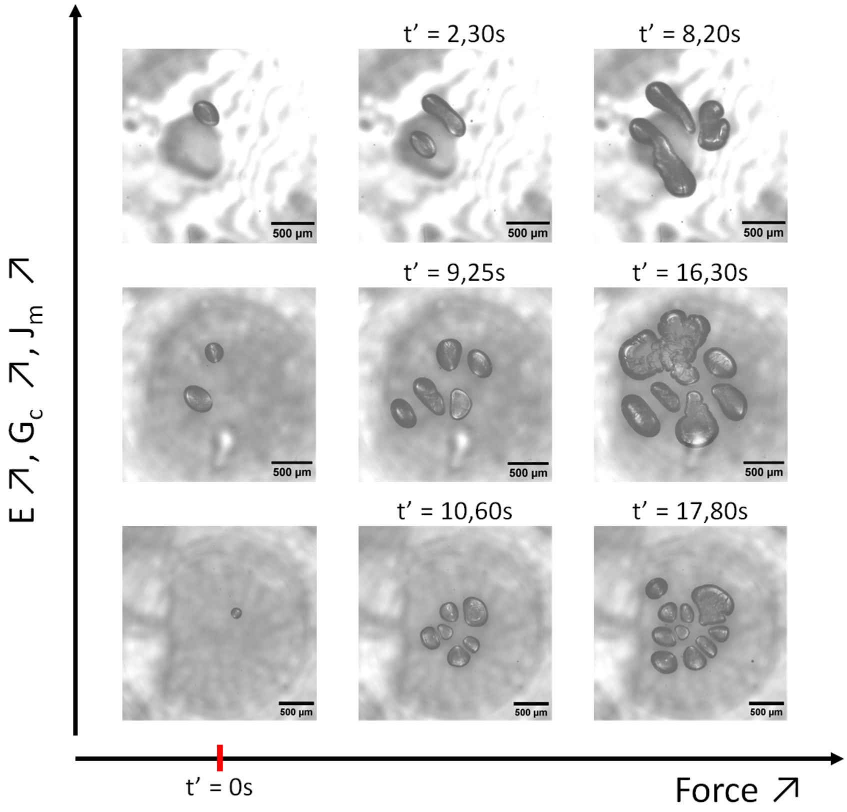

FIGURE 6: Effet du raidissement sur la morphologie des bulles - expériences caractéristiques. Le timing de la première image est fixé à t' = 0s afin de comparer les effets de la formulation sur la dynamique de croissance des bulles et leur transition vers la fracture. De haut en bas, par décroissance de raidissement : OL HEA 15% EHA 15% PEA 5%bi, OL HEA 15% EHA 15% PEA 1%bi et OL HEA 30% EHA, épaisseur de 100 μm et vitesse de test de 5 μm/s. Les cavités apparaissant dans le matériau le plus raidissant (1ère ligne) semblent se déformer en plus gros lobes et transiter vers la fracture plus rapidement que dans la formulation la moins raidissante.

Cependant, des effets très intéressants et reproductibles ont été observés sur l'évolution des bulles de cavitation, d'une part en fonction de l'épaisseur de la zone confinée, d'autre part en fonction de la formulation. L'étude de l'épaisseur de l'échantillon a permis de mettre en lumière un comportement particulier : les bulles de cavitation sont des fractures gonflées qui s'ouvrent dans des plans aléatoires de la couche et dont la croissance n'est pas stable. Dans les couches confinées, probablement dû à la diminution de l'énergie élastique disponible, les fractures se stoppent et paraissent stabilisées alors que dans les grandes épaisseurs, elles transitent directement vers une propagation en plusieurs fronts. Enfin, notre étude sur l'effet de la formulation apporte une nouvelle lumière sur la stabilité de ces fractures qui semble fortement dépendre du raidissement du matériau. L'analyse de la morphologie des bulles en fonction du confinement et des propriétés mécaniques semble prometteuse car bien que des comportements similaires sont souvent observés ([5], [13], [14], [15]), l'explication d'un tel comportement de fracture n'est pas triviale. Une manière d'approfondir l'étude des morphologies pourrait passer par l'analyse de l'endommagement provoqué par la croissance des cavités, notamment grâce à l'aide de mécanophores, marqueurs post-mortem des chaînes polymères brisées.

Contents

List of Abbreviations

OL HEA	Oligomer PPG8000-(IPDI-HEA)$_2$ = acrylate functionalised oligomer
OL HEMA	Oligomer PPG8000-(IPDI-HEMA)$_2$ = methacrylate functionalised oligomer
EHA	2-Ethylhexyl acrylate
EHMA	2-Ethylhexyl methacrylate
PEA	2-Phenoxyethyl acrylate
PEMA	2-Phenoxyethyl methacrylate
BAPO	Phosphine Oxide, Phenylbis(2,4,6-trimethylbenzoyl)
BDA	1,4-Butanediol diacrylate

Chapter 1

Introduction

There is big trouble that arises below the ocean. And it is called cavitation. Strictly speaking, cavitation is "the forming of gas bubbles in liquids, caused by changes in pressure" (definition from the Cambridge dictionary). It appears when a liquid is brought to high temperatures or low pressures. In both cases, it leads to local steaming, and therefore the creation of gaseous cavities. However, these cavities are not stable and collapse, which creates localized high pressures and temperatures [16], leading to a shock wave propagation when the collapse is complete. This shock wave is responsible for material damage and sound emission. But where does this cavitation happen?

It's the shrimps? The mantis shrimp punches so hard and quick its victims that it creates a deadly cavitation bubble, while the pistol shrimp causes cavitation by the fast closing of its claw.

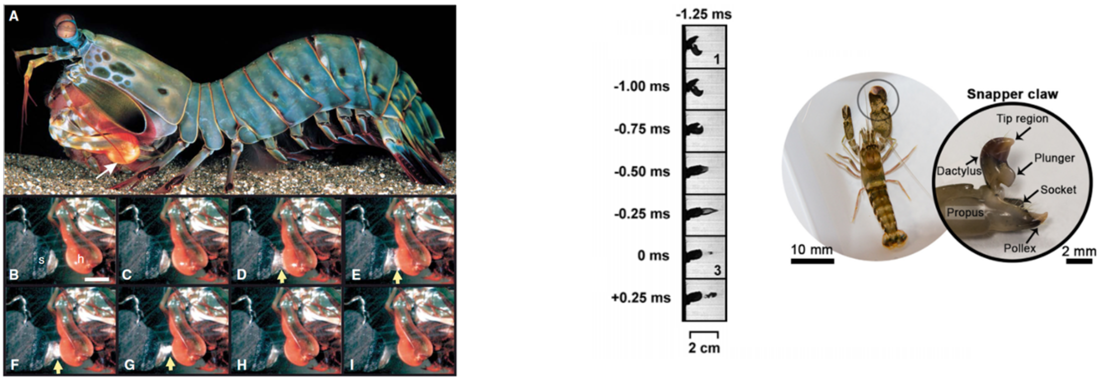

(A) Mantis shrimp attack on a snail

(B) Pistol shrimp

FIGURE 1.1: Cavitation in water - shrimps packing heat. (A) The cavitation bubble is marked by the yellow arrow. It results from the punch of the shrimp's appendix (marked h) on the snail (s) [17]. The images are taken at 0.2 ms intervals, scale bar: 1 cm. (B) Left: High speed imaging of the cavitation resulting from the closing of the pistol shrimp claw [18]. Right: Macro-photograph depicting the location of the snapper claw and its various segments [19].

It's the submarines? Cavitation arises around propellers as they locally create depressions in the water. This causes significant material damage during their collapse. It can also be a security problem, as it creates a distinctive sound of the submarine that can lead to their detection and localisation.

No, it's the underwater optic cables! Nowadays, 95% to 98% of the data that transit via internet goes through optic cables. There are more than $1,2.10^6$ km of cables running across the oceans to connect the data centres worldwide. This makes the optic fibre topic both economic, sociological and political. However, in our field, it is mostly a material challenge, as cavitation threatens your internet speed.

1.1 Industrial context

As the first transatlantic optic fibre cable was connected in 1988, the field of research, both academic and industrial, on the fibre protection optimisation is quite wide. The fact that the glass fibre needs protection should be a surprise to no-one. Indeed, beside the obvious breaking risk, any microbending of the glass fibre leads to a signal decrease which can be up to 100 dB/km [20]. Considering that the longest optic cable is 10 000 km, this kind of loss in unacceptable, as it would mean to use much more signal amplifiers along the way. The solution found to prevent this microbending is the use of polymer resins as coatings. The optimum seems to consist of a soft first coating that will deform, preventing the bending, and a second coating acting as a harder shell. The requirements for those coating are summarized in Table 1.1.

Primary Coating	
	Low modulus over the range of operation (< 10 MPa)
	Good adhesion to the glass
	High index of refraction (> 1.46)
	Long term durability
	Low hydrogen generation
Secondary coating	
	High modulus to resist external lateral forces (> 1 GPa)
	Low coefficient of friction
	Excellent resistance to environmental factors
	Low water absorption
	Low hydrogen generation
Processability	
	Rapid cure speed (5 m/s)
	Optimum viscosity (< 10 Pa.s)

TABLE 1.1: General requirements of UV-curable resin for optical fibre - taken from [21]

The processability is a key point, as the production of optic fibre needs to be quick in order to be less costly. As described on Figure 1.2, the glass fibre is molten at the top of a high tower and is directly coated by the polymer resins. Depending on the installation, the first and the second coating can be applied at the same time and polymerised together, or one after the other. Once protected, the optic fibre is rolled. A key parameter is the coating and polymerisation speed: draw speeds at 3000 m/min (180 km/h) are common! Due to the rapidity of the polymerisation, the coatings can not relax their internal stresses due to polymerisation induced volume shrinkage. This causes the first coating, sandwiched between two harder surfaces, to be held under hydrostatic stress, which eventually leads to the opening of cavities.

This cavitation behaviour is described on Figure 1.3. Indeed, it is highly unlikely that cavities appear in solids under hydrostatic pressure through sublimation. As soon as the cavities open, the protection capacity of the first coating decreases, leading to signal loss. This becomes an industrial problem, as it qualifies certain coating formulations as unsuitable for the optic fibre application. This was the motivation for DSM to finance this work. They then sold their coating application to Covestro, who pursued the interest in our study. The academic interest lies especially in the fact that the layers considered here are very thin and confined which makes their study not trivial.

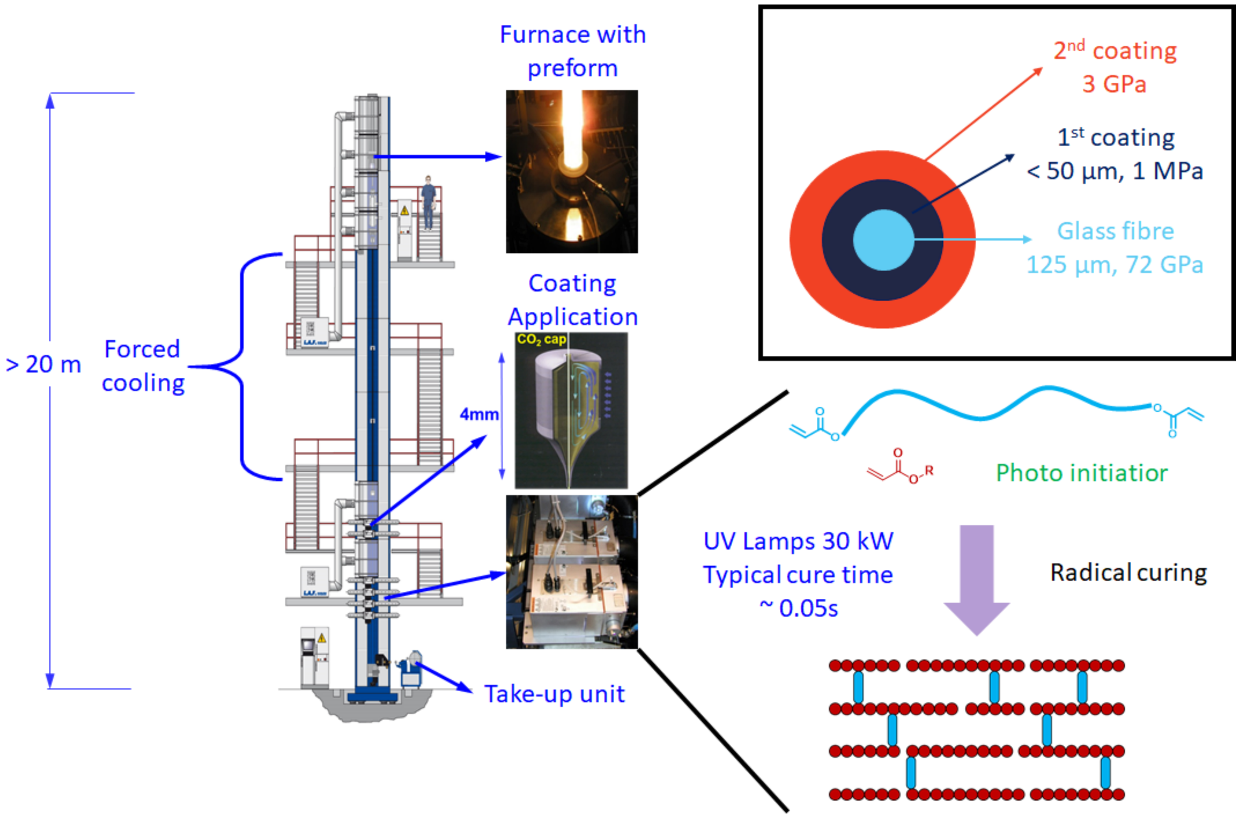

FIGURE 1.2: Tower for optic fibre production - Courtesy of Covestro. The glass is molten at the top of the tower and falls in the shape of a single fibre that is coated by one or several layers of resin. This resin is then polymerised in a flash. Insert: schematic and respective thicknesses and Young modulus of the coatings on the glass fibre.

1.2 Ideas from the literature and expected challenges

Now, the study of the cavitation resistance of soft confined polymer layers is not a new topic. A more detailed review of the state of the art on cavitation will be done in Chapter 4. In a nutshell, the evolution of the theories on the growth of cavities in soft networks showed that the key material parameters seem to be the elasticity (Young's modulus E) and their fracture resistance (energy release rate Γ). Furthermore, many experimental studies showed a significant size effect, meaning that small samples seem to withstand higher pressures before cavitation. This suggests an effect of the defect size distribution.

Based on this knowledge and on the many examples of ways to test the cavitation resistance in soft materials, our experimental challenge will consist of characterizing polymer films with formulations close to the industrial ones, polymerised and crosslinked in a flash free radical polymerisation. Adding to that, the confinement of a thin layer of such a network to test it under hydrostatic traction will require the design of a specific set-up of microcharacterisation. First, we wish to observe the cavitation process in the thin layers and investigate their fracture mechanism. Our goal would be to understand the respective role of the elasticity, the fracture properties and the strain hardening of the networks on the growth of cavities. Finally, we hope to shed some light on the nucleation process of those cavities.

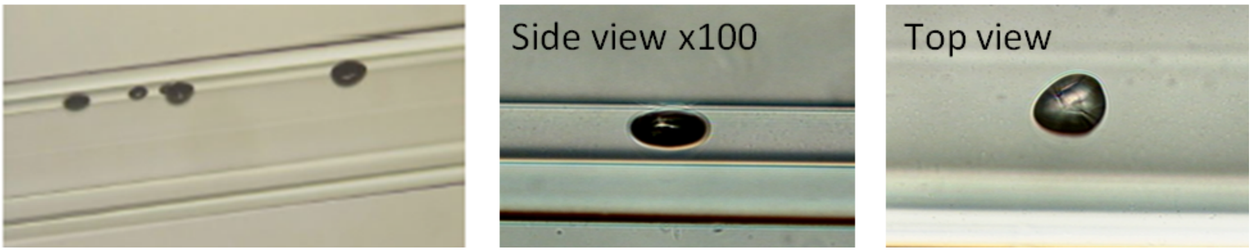

(A) Primary coating cavitation

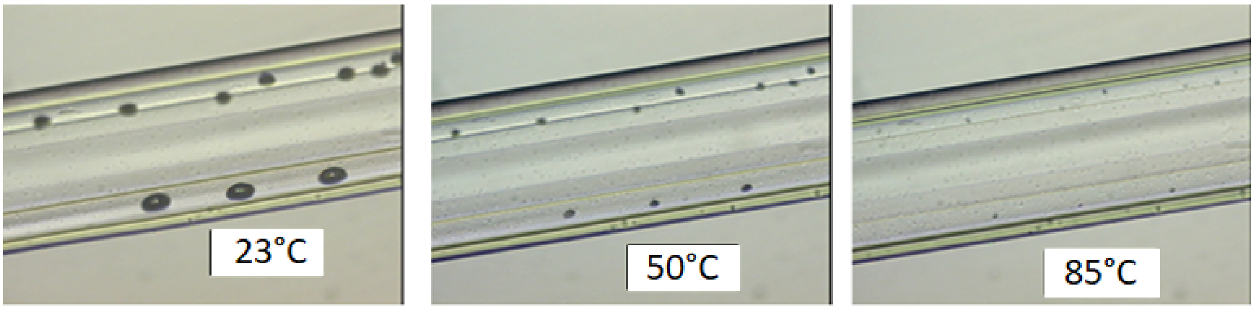

(B) Closing of cavities upon heating

FIGURE 1.3: Apparition of cavities in the primary coating - Courtesy of Covestro. (A) The cavities are internal cohesive ruptures of the primary coating. (B) Upon heating, the internal stresses in the coating are released leading to a closing of the cavities.

1.3 Scope of this manuscript

In this study, we will present in the first two chapters the chemistry of the network, its polymerisation process and the influence of the formulation on the material properties: the Young's modulus, the fracture energy and the strain hardening. As the polymerisation process used is an intense UV light flash, its influence on the microstructure of the network will also be investigated.

Chapter 3 will focus on the description of the hydrostatic traction set-up that was designed and built for this study and the description of the FEM modelling that allows for an analysis of the pressure applied locally. Finally, in Chapter 4, we will focus on the main results of the cavitation behaviour in the soft and thin confined layers: the thickness and the formulation effects, especially the role of strain hardening, on the cavitation growth. The relevant state of the art for each chapter will be found in their introduction.

Chapter 2

Model acrylate networks: Structure and properties

As described in the introduction, the aim of this work is to reproduce the polymerisation process used in the industry to form model networks with similar architecture and to investigate their properties. This chapter looks into the process of free radical polymerisation by UV and the influence of the process parameters on the network's formation.

2.1 Free radical polymerisation and formation of networks

Photopolymerisation by UV is a well studied polymerisation technique that won an important place in industry for a wide range of applications, such as microcircuits, thin coatings, 3D printing, adhesives, stereolithography and even dental prosthetics [22]. What all of these applications have in common is a requirement for fast polymerisation, with low to no solvent release and a polymerisation of a relatively thin layer of material. In this way, UV polymerisation checks all boxes as it allows for an almost instantaneous transformation of a liquid polymer melt to a solid [23]. The limitation of UV radiation is the absorption of the radiation by the polymer melt, which prevents the production of thick samples, however it is cheaper than thermal curing for example, because of the smaller polymerisation time and the lower energy consumption, especially with the use of LED UV lamps (170 W for the Phoseon Firejet UV lamp compared to 50W (60°C) to 250 W (320°C) for an oven of 30 L). The polymerisation mechanism can be either a free radical one, for acrylate monomers, or a cationic one, for vinyl ethers or epoxies. We will focus on the free radical polymerisation, its mechanism and the impact of the chemistry and UV polymerisation process on the structure of the networks, especially in the focus of a particular application: the primary coating of optical fibres.

2.1.1 Free radical polymerisation mechanism

The free radical polymerisation mechanism in a polymer melt (i.e solvent free) can be described in three steps ([24],[25]):

- **initiation** (2.1): absorption of a photon by the photoinitiator named PI_2, which leads to the production of a radical. All activated photoinitiators will not lead to the second step of initiation. Only a fraction will attack a double bond on a monomer, leading to an activated monomer. The kinetic limiting step is the dissociation of the PI_2, i.e $k_i >> k_d$ with k being the reaction rate constant of the respective chemical reactions.

- **propagation** (2.2): chain growth by successive attacks of the activated chain on new monomers. The radical site will always be at the end of the chain.

- **termination**, 4 possibles mechanisms: *disproportionation* (2.3), where 2 radical polymer chains terminate each other by one stealing a hydrogen from the other, leading to an unsaturated polymer $P_m^=$ and a saturated one P_n^H (mostly observed in the case of high temperature polymerisation, such as rubber vulcanisation), *combination* (2.4), where 2 radical polymer chains (or an activated photoinitiator $PI\cdot$) form a C-C bound with their radicals, *trapped radicals (vitrification)*, where propagating radicals become trapped without access to new monomers or other radicals, and *oxidation* (2.5), when a radical chain interacts with an O_2 molecule.

The reactions steps occurring during the radical polymerisation are:

$$\begin{aligned}
&\textit{initiation} && (2.1)\\
PI_2 &\xrightarrow{k_d} 2\,PI\cdot\\
PI\cdot + M &\xrightarrow{k_i} P_1\cdot\\
&\textit{propagation} && (2.2)\\
P_n\cdot + M &\xrightarrow{k_p} P_{n+1}\cdot\\
&\textit{termination by disproportionation} && (2.3)\\
P_n\cdot + P_m\cdot &\xrightarrow{k_{td}} P_n^H + P_m^=\\
&\textit{termination by combination} && (2.4)\\
P_n\cdot + P_m\cdot &\xrightarrow{k_{tc}} P_{n+m}\\
&\textit{termination by oxidation} && (2.5)\\
PI\cdot + O_2 &\xrightarrow{k_O} PIO_2\cdot
\end{aligned}$$

As seen in the last termination mechanism, the concentration of O_2 in the reactants will induce an inhibition of the polymerisation, as it consumes the activated photoinitiator. When polymerising in an O_2 rich environment, the photopolymerisation cannot propagate because $k_O.[O_2] >> k_p.[M]$, so the photoinitiator is eaten by O_2 before reacting with the monomers. The resulting peroxide radical is not very reactive and will not continue the propagation. The propagation step can therefore only take place once the monomers can compete favorably with the oxygen. This inhibition by O_2 will have the biggest impact for low illumination powers, while for high illumination powers, the polymerisation rate is high enough so that the O_2 can not be replaced in the polymer melt [25]. Based on modelling of the polymerisation on a reaction-diffusion model in a mostly inert atmosphere ($O_2 \sim 10^{-6}$ mol/L), the conversion rate R_p can be computed as a function of the UV intensity. At high UV intensities, the computed R_p follows the prediction: $R_p \propto \sqrt{I_0}$, with I_0 the UV intensity, but a deviation appears at lower intensities. The threshold for significant oxygen inhibition was determined at 3 mW/cm^2 for a system of diacrylates films of 10 μm [26].

This description of the polymerisation considers the most important steps, but as the name of free radical polymerisation implies, there is absolutely no control of the propagation of the radical. Many more secondary reactions can happen with the radicals, which are described in several reviews about free radical photopolymerisation ([27], [28]). One of the reactions that may change the kinetics, but mostly will change the polymer chain, is the **transfer reaction**. The mechanism is shown on Figure 2.1. This mechanism of radical transfer can occur intrachain (polymer backbiting) or interchains. In any case, it leads to the branching of polymer chains and to the creation of tertiary radicals which have a higher stability and hence a lower reaction rate [27]. The branching of polymer chains can also be caused by hydrogen abstraction from one $PI\cdot$ on a polymer chain, leading to a radical in the middle of a chain and a deactivated photoinitiator PIH. This is especially observed in the case of free radical photopolymerisation at high UV intensities. These tertiary radicals can even separate in two macromonomers, one with a saturated end and one with an insaturated one, leading to a termination by scission of a chain.

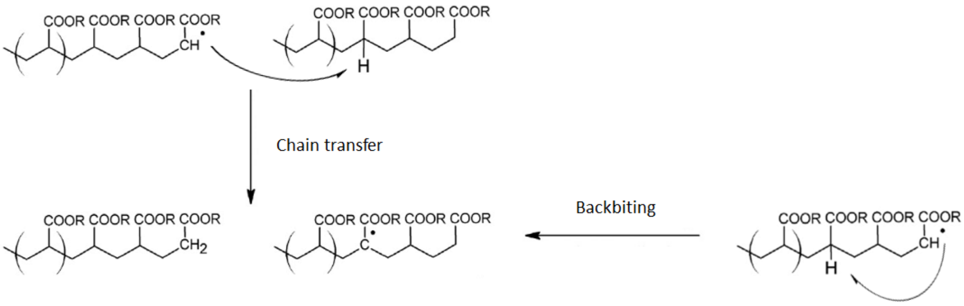

FIGURE 2.1: Potential secondary reactions in polymerisation of acrylates - taken (and simplified) from [27]

This change in the mechanism of polymer growth may impact the kinetics, as in addition to the lower reaction rate, the reactive site moves from the chain end of the polymer to a random place. The chain ends of the polymer have a greater mobility, hence the movement of the radical out of this position will induce a steric hindrance in the polymerisation. To add to the complexity, the kinetics of polymerisation depends on the chemical function of the monomer used. We will focus on the kinetic differences between the acrylate and methacrylate monomers. First, activated methacrylates will form a tertiary radical, more substituted than an activated acrylate. This will lead to a stabilization of the methacrylates, and therefore should lead to a decrease of reaction rate.

2.1.2 Polymerisation kinetics

The technique used for the determination of the polymerisation rates is PLP-SEC (pulsed laser polymerisation size exclusion chromatography), which is mostly developed by Olaj and co-workers [29]. Of course, the measurement will depend on many parameters, such as the pulse frequency [30]. Also, the branched chains originating from chain transfer reaction will also be measured [31], which may be an issue for the measurement of k_p. We will just summarize here the results obtained when all those issues have been taken care of.

Barner-Kowollik et al. investigated the variation in reaction rate when the chemical function changes from methacrylate to acrylate, the impact of the size of the monomers and the solvent effects [32]. Their results are summarized on Figure 2.2 and address our 3 questions: the effect of monomer function, size and kinetic hindrance. First, let's compare the polymerisation rate values from Figure 2.2 (B) and (C), i.e comparing the polymerisation rates of acrylates and methacrylates. The scale of the two figures is quite different: k_p(50°C) for acrylates range from 20 000 to 35 000 L.mol^{-1}.s^{-1} while for methacrylates, it ranges from 650 to 1250 L.mol^{-1}.s^{-1}! Even increasing the temperature from 50°C to 100°C for methacrylates only increases by a factor 3 the reaction rates. The polymerisation kinetics of acrylates is therefore 30 times faster than the one of methacrylates. Then, looking at Figure 2.2 (A), the effect of the length of the side chain of the monomer is reported. The larger the acrylate side chain, the faster the polymerisation rate. The same behaviour is observed for methacrylates. Finally, Figure 2.2 (B) and (C) display the effect of branching monomers in the case of acrylates and methacrylates. For methacrylates, there is globally no impact of the monomer's own steric hindrance on k_p. For acrylates, there is no distinctive correlation between steric hindrance and k_p. Now these measurements are done in conditions where transfer reactions can be neglected, the polymerisation is induced by laser pulses at high frequencies (up to 500 Hz), so the result on a monomer's own steric hindrance is not a good indicator for the effect of chain transfer on the kinetics.

Lovell et al. studied chain transfer reactions by ^{13}C NMR measurement of the free radical polymerisation in bulk of vinyl acetate and could determine the %mol of branched chains as a function of conversion, which can be directly linked to the polymerisation time [33]. It revealed

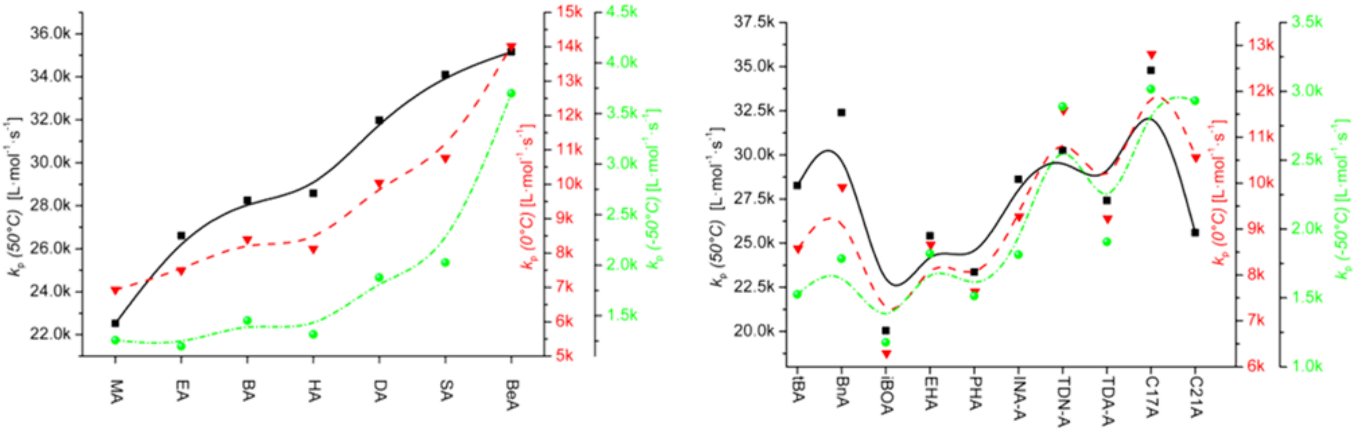

(A) Effect of linear chain length on k_p

(B) Branching of acrylates monomers

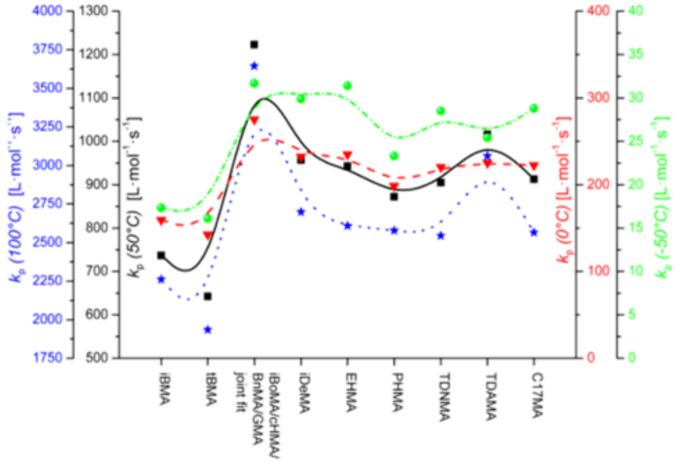

(C) Branching of methacrylates monomers

FIGURE 2.2: Influence of the monomer chemical function, size and structure on the polymerisation rate coefficient k_p for bulk polymerisations - taken from [32]. The colors characterize the temperature at which the constants are measured. (blue = 100°C, black = 50°C, red = 0°C, green = -50°C). (A) The acrylate monomers are ranked left to right in increasing linear ester side chain length. (B) & (C) The monomers are ranked left to right in increasing steric hindrance.

that the percentage of branched chains increases with conversion, first linearly, and then saturates at higher conversions.

2.1.3 Network formation

The two first parts only considered the growth of linear polymer chains with possible branching. This is the case when monofunctional monomers react together. However, when multifunctional monomers react together, a network is created as chemical crosslinks form. As the polymer chains grow and bind together, the viscosity of the medium increases and the chain movements are increasingly restricted. The study of the network growth includes many considerations, such as the evolution of the reaction rate with chain growth, the affinity between all reagents and their diffusivity as conversion (and hence viscosity) increases, which impacts the propagation and termination reactions. We will address some of those points, especially regarding the conversion, kinetics of network formation and chemical affinity.

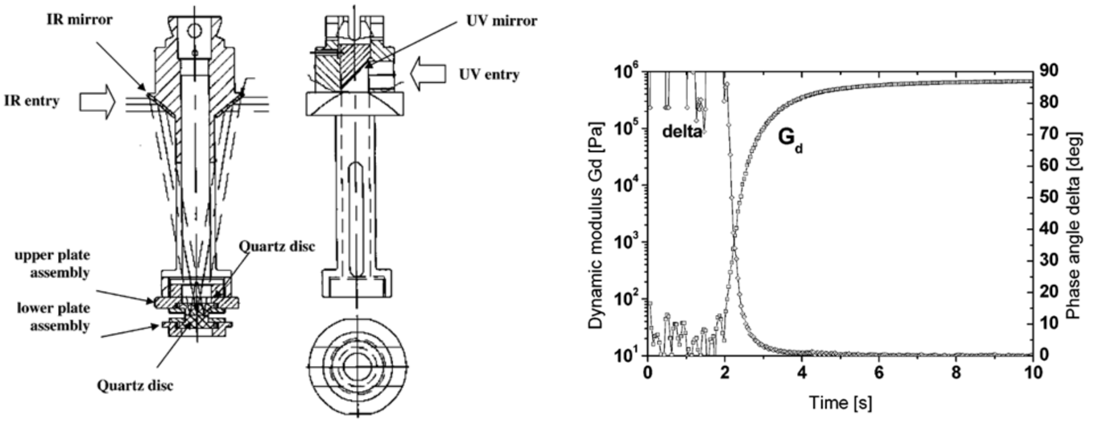

(A) Schematic of the DMA/UV/IR set-up

(B) Increase of dynamic modulus μ^* as illumination starts at 1.575s

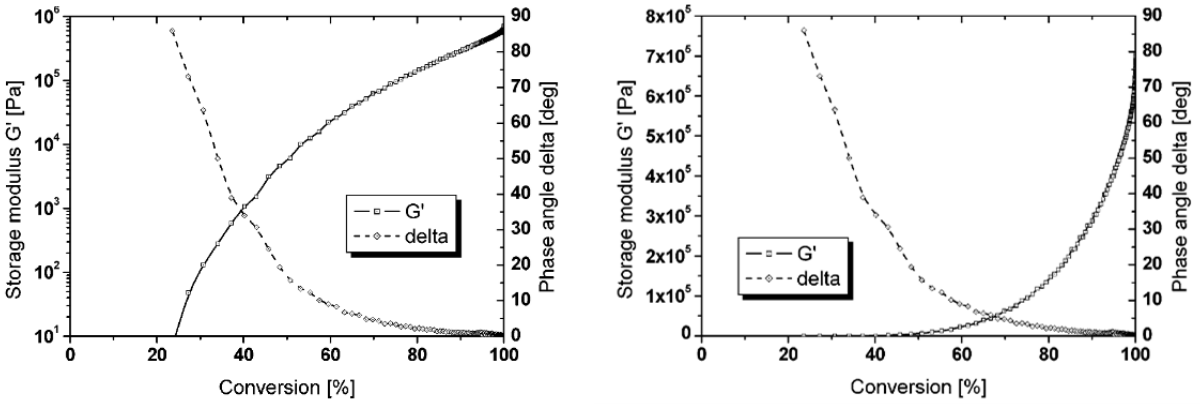

(C) Network builds up as conversion increases, log scale (left) and linear scale (right)

FIGURE 2.3: DMA/UV/IR measurement of UV curable networks - taken from [34]. (A) Schematic drawing of the set-up allowing for simultaneous UV illumination, IR measurement to follow the conversion and DMA testing between the two quartz plates that are mounted in a rheometer. The tested network consists of a mix of 49%(w/w) of PPG3100 diacrylate, 49%(w/w) of ethoxylated nonylphenol acrylate and 1%(w/w) of ketone PI. (B) Variation of dynamic modulus (μ^*) and phase angle (delta) with time, as illumination starts at 1.575s. (C) Variation of Storage modulus ($\mu' = \mu^* cos(\delta)$) with conversion. The unsaturated bond conversion is computed from the disappearance of the corresponding IR peak.

The monitoring of the network formation is possible via DMA and IR measurements while illuminating. Considering the quick polymerisation rates of acrylates, a set-up allowing for the simultaneous measurement of both the conversion and the network build is necessary. The viscosity increases dramatically with conversion as not only the polymer chains grow, but also a network is forming. The conversion rate will therefore vary with conversion: at first it will increase, reach a maximum when the diluted O_2 inhibition has been overcome. Figure 2.3 represents the variation of storage modulus with conversion. At first, the viscosity of the mix is too low (< 1 Pa.s) to make any valid measurement. When conversion rises, the modulus increases and the network becomes more and more elastic, leading to a decrease of the phase angle delta. The determination of the gelation point can be accurately done by testing the moment where $\tan(\delta)$ doesn't vary with frequency, or when μ' and μ'' show the same dependency with frequency (known as the Winter-Chambon criterion [35]). However, in the set-up proposed by Steeman et al. [34], the sample can only be tested at one frequency, leading to the following description of the gelation point: a drop of the phase angle below 45°. This is a sign that the tested material evolves from a viscous liquid (i.e highly dissipative) to an elastic solid. A striking property of the acrylate network (by chain growth polymerisation) is the build up of an elastic network with a conversion rate only just above 20%, while other polymerisation mechanisms (like step-growth polymerisation) display a network build up only for larger conversion rates (thiol-ene case, 65% conversion rate [36]). It is also interesting to compare the increase in modulus both on a linear and on a log scale. While an elastic network can be detected at low conversions, the biggest increase occurs for conversions above 80%, where the growth is exponential. So, while the conversion rate of the polymerisation decreases when the gelation point is passed, the network forms at high conversion rates. Hence the criterion of maximal polymerisation rate does not seem crucial to form an elastic network, but is important to ensure a complete conversion of the acrylate functions.

The structure of the networks will be highly dependent on the size of the monomers and their functionality. When polymerizing monomers with di- or tri-acrylate functions, the gel point is reached at lower conversion rates than for monoacrylates [37]. However, in the case of the copolymerisation of a multiunsaturated monomer with monounsaturated monomers, the gelation point can be shifted towards higher conversion rates. This phenomenon is due to the formation of short cycles in the growing polymer chains when incorporating a multiunsaturated monomer in the chain growth. The radical at the end of the polymer chain can either propagate, make a crosslink with an another chain that also contains a pendant double bond, or form a cycle by attacking its own pendant double bond. When conversion is low, the probability of finding another chain is low, so the probability of forming cycles is higher. Therefore, hard clusters form, diminishing the mobility and possibly trapping other pendant chains. The creation of these clusters will delay the formation of a macrogel. This effect will strongly depend on the concentration of multiunsaturated monomers and on their size and flexibility [38]. This formation of hard clusters can even be observed in critical cases where the highly crosslinked microgels formed lose solubility in the monomer solution. The macrogel is formed by interconnection of the dense microgels. The resulting network therefore consists of hard domains that are linked by softer, less crosslinked regions, and even free monomer if the network vitrified before reaching a high enough conversion [39].

The presence of domains where mobility is lower can also create a lot of pendant unsaturated bonds that did not react, or even trapped radicals. Anseth et al studied the variation of the trapped radicals concentration during conversion for different formulations with varying light intensity and molecular weight of the dimethylacrylate [40]. It results that the higher the molecular weight of the bifunctionalized oligomer, the lower the concentration of trapped radicals as the gelation point is reached at larger conversion rates. It means that the higher the chain mobility is in the medium, the higher is the probability for a termination of the radicals by disproportionation or by recombination, and the lower is the probability of trapping radicals. When considering the effect of illumination power on one dimethacrylate, the higher the illumination power, the higher the absolute concentration of trapped radicals in the medium, but the ratio between trapped radicals and total radical concentration during the conversion is lower. When high conversions are reached, all remaining radicals are considered trapped, so the ratio tends towards 1. This means that while higher light intensities lead to more radicals in the medium than lower light intensities, it also shifts the reactions towards bimolecular termination. Low light intensities lead to a small radical concentration and the rate of termination by trapping increases compared to the bimolecular termination.

The life time of the trapped radicals remaining after the polymerisation can by quite long (over one hour). The kinetics of long-term termination of those trapped radicals is higher for loosely crosslinked networks, so for longer dimethacrylates and lower double bond conversion during the polymerisation. This again is linked with the chain mobility: the higher the mobility, the more probable the termination of the radicals, the quicker the termination kinetics. The presence of trapped radicals that react over time can lead to dark curing. It means that polymerisation and crosslinking continue even if the illumination is stopped, which leads to an increase of the modulus or even a brittleness of the network. It is important to note, however, that all these experiments were done on reagents that were degased, to prevent the presence of O_2. In systems where the termination by oxidation can take place, one can expect the trapped radical concentration to quickly decrease.

2.1.4 Commercial resins and network's structure

In most industrial applications, the UV curable resins consist of a diacrylate functionalized oligomer, which will act as the backbone of the polymer network, mixed with the photoinitiator. Acrylate monomers are added to adjust the viscosity ([21],[37]). Based on the functionality of the monomers, the gelation point and the final properties can be changed: by increasing the functionality, the polymerisation rate increases, and so does the crosslink density, which was already observed for pure monomer formulations, but also the hardness and solvent resistance increases as the flexibility decreases in polyurethane-acrylate networks [41]. Considering the application of optical fibre coatings, the requirements are listed in Table 1.1. The systems will therefore form a copolymer, which brings new considerations, such as the compatibility between the components. Based on these types of formulations, the use of high molecular weight oligomers with diacrylate functions should prevent the growth of microgels [42]. However, some microgel formation during the network formation can still be detected.

Brett et al. studied the polymerisation of two formulations: one out of polyether urethane diacrylate (oligomer) mixed with an acrylate monomer (EHA) (named LT, low T_g), and another with both an oligomer, a monofunctional acrylate and a diacrylate monomer (named HT, high T_g) [43]. The network formation was followed by grazing-incidence small-angle X-ray scattering (GISAXS) at different polymerisation times. The HT formulation produced several inclusions during its polymerisation, which is can easily be rationalized since the diacrylate can react quickly and form those nanogels. However, the LT resin also showed domains that grow during the polymerisation, but reached bigger sizes than for the HT formulation. The initial domains are due to spinodal decomposition, then this heterogeneity increases during polymerisation as the growing polymer chains crosslink and lose their mobility and diffusivity. However, the T_g being low for LT, the network is still quite mobile during polymerisation at room temperature and the initial heterogeneities grow to a large scale. In the case of HT, domains with denser crosslinks appear due to the higher concentration of reactive functions in the mix, and the domains loose their mobility as the T_g is higher than room temperature. We can conclude that the network formation in the oligomer/monomers formulation will be heterogeneous, and the polymerisation at high radiation energies, producing many radicals at the same time, could increase even more this heterogeneity.

To add to these kinetic considerations, the differences in chemical functions will also impact the gelation. Even if the reaction rates of methacrylates is lower than acrylates [32], some formulations can mix acrylates and methacrylates. The network formation will depend on the reaction coefficients between the different chemical functions. Bevington and Harris [44] studied the reactivity ratios between different acrylate and methacrylate monomers towards methyl methacrylate (MA) via isotope tracing. The results are summarized in Table 2.1.

Monomer A	Monomer B	r_A	r_B
Methyl methacrylate	n-Butyl methacrylate	0.79	1.27
	Isobuthyl methacrylate	0.91	1.09
	n-Butyl acrylate	1.74	0.20
	Isobutyl acrylate	1.71	0.20

TABLE 2.1: Reactivity ratios between acrylates and methacrylates - adapted from [44] (with data extracted from [45] and [46]).

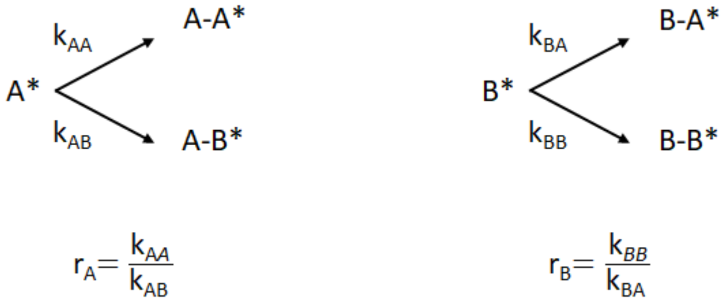

FIGURE 2.4: Reactivity coefficients for polymerisation

The reactivity coefficient r_A and r_B determine the affinity between the components. When monomers A and B are mixed, they can make blocky copolymers (A-A-A-A-B-B-B-B), alternating polymers (A-B-A-B-A-B-A-B) or random copolymers (A-A-B-A-A-B-B-B-A-A-B-A). The structure of the final polymer depends on the ratios of the reaction constants as shown on Figure 2.4. When $r_A > 1$, then the monomer A reacts preferably with itself than with B, when $r_A < 1$, it reacts preferably with B, and reciprocally for monomer B. All the coefficients compare the affinity of MA towards either acrylate or methacrylate monomers with the same structure. Globally, the reaction ratios between methacrylates are the same, $r_A \sim r_B$, meaning that there is no preference in the polymerisation, so the methacrylates together would form a random polymer. However, for the same general structure, but with acrylate functions, there is a significant increase of r_A and a drastic decrease of r_B, going to 0.20! So MMA prefers to react with itself rather than with acrylates BUT the acrylates prefer to react with the MMA rather than with themselves. This change of reactivity is quite interesting. This also means that in the case of a mixing of a dimethacrylate oligomer and acrylate monomers, the chain growth would add the oligomer faster, as all the chemical functions present would rather react with a methacrylate function, leading in principle to an earlier gelation point of the network than with a pure acrylate system. Also, if methacrylate monomers are added with a diacrylate oligomer, it may lead to a slower network build up, as the methacrylate monomers react more slowly and they would rather form their own linear chain that react with the oligomer to form a network.

Finally, an important phenomenon during free radical polymerisation is volume shrinkage. When polymerisation takes place, the Van der Waals bonds between monomers are changed into covalent bonds, leading to a smaller distance between the molecules and a configuration change, hence a volume shrinkage, i.e. an increase in density [47]. When the resin is coated on a substrate, the volume shrinkage is frustrated, leading to internal stresses build up. This shrinkage can cause defects in several applications, like dental restorations [48] or optical lenses [49]. In the case of optical cable coatings, they lead to internal stresses that can lead to cavitation, as described in the introduction.

Let's first consider how the volume shrinkage appears during the polymerisation and induces residual stresses. When the polymerisation takes place, the resin should decrease in volume. However, the kinetics of the volume shrinkage is much lower than the polymerisation rate, all the more so when using high UV intensities. It means that there is a competition between the polymerisation rate and the volume shrinkage: each polymerisation event should lead to a decrease in volume, but when it goes too fast, the volume shrinkage cannot keep up [41]. A lot of polymerisation events are taking place in a bigger volume than what thermodynamic equilibrium requests. Temporary excess free volume is created during polymerisation, improving the propagation as the chains are more mobile. However, the equilibrium state is for a lower volume, so shrinkage should happen at longer timescales. If the network is too stiff, it is impossible, and the excess free volume is trapped. Stress build up or relaxation in the material depends on the chemistry and the structure, especially the chain mobility, i.e the crosslinking density, entanglements and T_g [47]. It will also depend on the modulus of the final material. In the extreme case, if the acrylate resin undergoes vitrification, meaning that the temperature at which the polymerisation takes place is lower than the T_g, then stress relaxation becomes slow and the polymerisation stresses may become significant. When kept in the rubbery state, the internal stresses should relax. Several studies have been conducted to investigate the effect of the monomer (in pure monomer formulations) and the process on the volume shrinkage ([47], [50]). Internal stress measurements can be done during polymerisation via cantilever deflection [51]. It was shown that stress increases with the light intensity as the polymerisation rate is higher, and more excess free volume is created. The monomer size impacts the stress build up as the bigger the chain, the lower the volume density of crosslinks, hence the bigger mobility and the lower the stress. In the same spirit, the higher the functionality, the earlier the gelation (and vitrification) and hence the higher the stress build up. In any case, the stress is very low for materials in the rubbery state (low modulus and quick relaxation), and internal stresses are mainly observed for materials that undergo vitrification. This is true for bulk polymerisation, while confined polymer layers can be subject to internal stresses.

2.1.5 Conclusion on the polymerisation protocol and the components effect on the network

Let us now summarize the different effects described in this quick state of the art of radical polymerisation. Considering that a basic formulation for industrial resins consist of a bulk UV polymerisation of a mix of oligomer, photoinitiator and acrylate monomers:

- **Effect of light intensity**: Higher conversion rate, more radicals are formed at the same time so less effect of O_2 inhibition, possibly more chain heterogeneities, quicker gelation point so more volume shrinkage and more stress build up

- **Effect of the functionality**: The conversion rate increases with the functionality, leading to an earlier gelation point, possibly with creation of heterogeneous phases due to highly crosslinked regions and more trapped radicals

- **Difference between acrylates and methacrylates**: Methacrylates have a slower reaction rate than acrylates and react more favourably with themselves than with acrylates, when acrylates react preferably on methacrylates. The additional CH_3 on methacylates brings a larger stiffness to the chains, that leads to a higher T_g and less flexible networks, also leading to a lower conversion rate than acrylates and a lower volume shrinkage.

- **Effect of the length of the monomer or the oligomer**: Longer chains lead to more flexibility of the reactive ends, and decrease the probability of self-cycling, preventing the formation of microgels during polymerisation. Longer monomers lead to a higher conversion rate and the presence of oligomer lead to a rubbery network that should prevent a high build up of internal stresses due to polymerisation.

2.2 Formulations, polymerisation and conversion

2.2.1 Formulations of the networks

This study's goal is to produce networks as close as possible to the commercial networks. The main requirement for such a mix is to polymerise quickly, in a flash of intense UV light to ensure fast production of the coated glass fibre. The building blocks of the networks were proposed by DSM (then Covestro) and are close to the ones used in industry. They consist of a 8000 g/mol polypropylene glycol (named in the following PPG) oligomer difunctionalized with an acrylate (OL HEA) or a methacrylate (OL HEMA) ending, which DSM (then Covestro) synthesized. They are mixed with acrylate monomers: 2-ethylhexyl acrylate (EHA) and 2-phenoxyethyl acrylate (PEA). The ratios used in this work are 70%w of oligomer and 30%w of acrylate monomers, as this ensures a decrease of viscosity of the mix compared to the oligomer alone. Since the polymerisation will happen in a flash, 1%w of photoinitiator (BAPO - phosphine oxide, phenylbis(2,4,6-trimethylbenzoyl)) was used, which is a rather large amount of photoinitiator. BAPO is a cleavage type photoninitiator, meaning it will break in 2 (or more) radical moieties when absorbing a photon, leading to the initiation of the radical polymerisation. It has been proven that BAPO insures a minimum curing time with a maximum conversion, even for thick samples [23]. Both the acrylate monomers and the photoinitiator were bought from Sigma-Aldrich and used without any purification. The mass and molar composition of a model network can be seen in Table 2.2. This formulation is coherent with the requirements of a primary coating for optic fibers: a PPG backbone which ensures a low T_g material with a high durability, while the acrylates provide good optical properties [21].

The preparation of the polymer mixes is done at room temperature, under the hood in amber glass bottles to protect the mixes from the external UV. 1%w of photoinitiator is first added to the viscous oligomer. The acrylate monomers are then added at the nominal ratios with pasteur pipettes and the mix is kept under agitation until complete homogenization. Due to the high viscosity of the oligomer, a rare earth magnetic stirrer has to be used, insuring a high magnetic force and a good mixing. Other mixing methods could be used, such as mixing on a roller bench overnight or with a speed mixer. The mixing has to be done under normal atmosphere because the oligomers are only non-reactive in presence of O_2. When put under an inert atmosphere (such as N_2), the inhibitors present in the oligomer would be deactivated and the oligomer would jellify. A resting time is needed to allow for the diffusion of the air bubbles out of the polymer mix before it can be used for polymerisation. The resulting polymer mixes are yellow due to the BAPO absorption in the visible light.

Since no purification is performed, the final mixes contain all inhibitors from the oligomer and the acrylate monomers; namely monomethyl ether hydroquinone for the EHA and hydroquinone and monomethyl ether hydroquinone for the PEA. Adding to the fact that they are kept protected from the external UV light and conserved at low temperature, the mixes are considered stable in time. This was confirmed by the consistent mechanical properties over time of the different polymerized samples coming from the same polymer batch.

2.2.2 Preparation of the films and polymerisation

To produce the flash UV polymerisation, a Phoseon Firejet FJ801 395 nm lamp is used. The LED lamps allow for a high intensity in short flashes (as short as 0.1s) for a 10 x 10 cm^2 surface, in a narrow UV wavelength window (more than 90% of the light intensity is in between 380 and 420 nm). This range corresponds to the maximum absorbance of the BAPO (Figure 2.6). It can

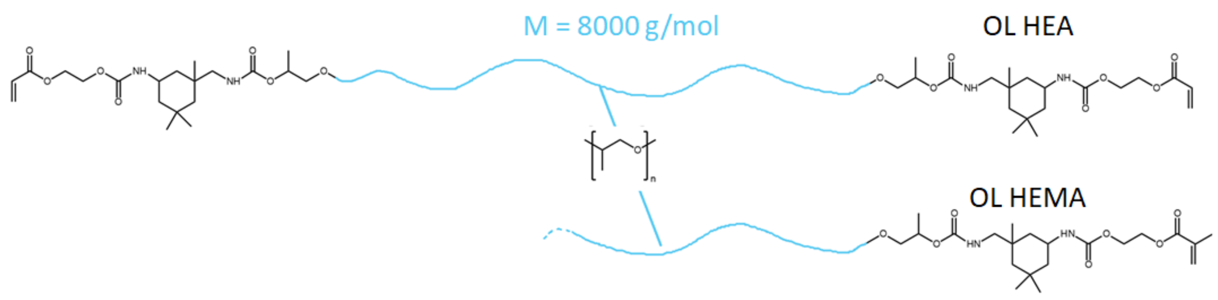

(A) PPG8000 oligomer with the acrylate (OL HEA) and methacrylate (OL HEMA) end functions

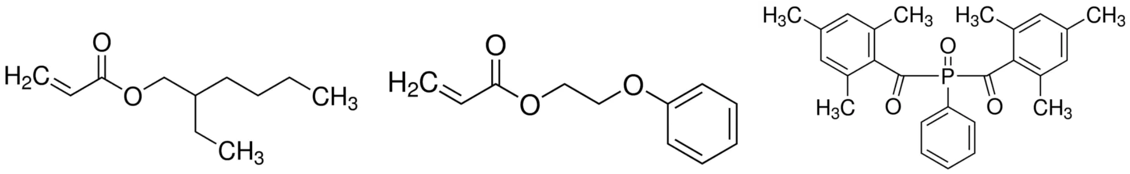

(B) 2-ethylhexyl acrylate (EHA) (C) 2-phenoxyethyl acrylate (PEA) (D) BAPO

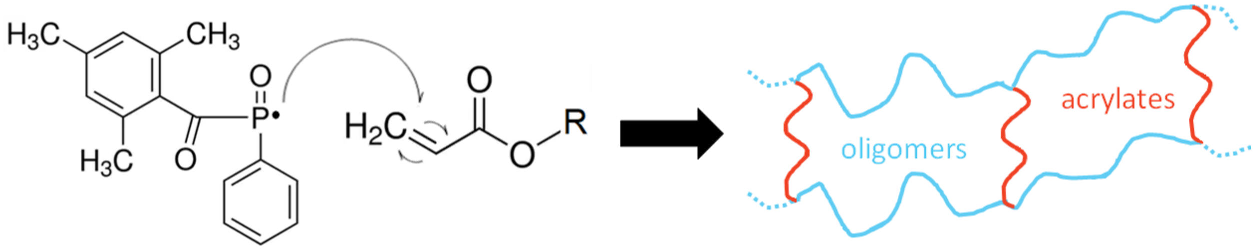

(E) Initiation: attack of the cleaved photoinitiator on a monomer, the propagation leads to the network formation

FIGURE 2.5: Building blocs for model networks and model network's structure

be controlled in time and in lamp power. The lamp was calibrated with a UV meter to determine the corresponding energy (A.2). The lamp shines towards the inside of a polymerisation chamber which allows to fill the atmosphere with nitrogen before polymerising, in order to limit the inhibition of surface polymerisation from the O_2 [52], as displayed on Figure 2.7.

In order to test the mechanical properties of the network in bulk, the polymer mixes are spread onto a 2 mm thick glass slide with a doctor blade which allows various thicknesses. The mix being still quite viscous, it will stay on the glass slide and not flow too much. Because the lamp shines through the glass slide and the whole spread polymer, the thickness of the polymer layer can not be too thick to avoid a gradient of light intensity in the polymer layer and therefore a gradient of conversion and crosslinking. The resulting thickness of the produced film (which is thinner than the gap of the doctor blade) range from around 50 μm to 800 μm. Once the polymer is spread on the glass slide, it is put inside the polymerisation chamber and kept under a constant flow of N_2 for around 5s before the illumination and during the polymerisation. The top and sides of the polymerisation chamber are made of aluminum, the bottom is a PMMA slab through which the UV light is transmitted. Once the lamp shuts off, the nitrogen flow is interrupted and the polymer film on the glass slide is taken out of the polymerisation chamber. When sufficient conversion has been reached, the network is transparent: the yellow color from the polymer mix has disappeared as a majority (if not all) of the BAPO has reacted. It can then be detached from the glass slide by gently detaching the corners with a razor blade. The resulting network is slightly sticky so it is

Component	Molecular mass (g/mol)	%w	%mol
OL HEA	8635	70	4.77
EHA	184.28	15	47.90
PEA	192.21	15	45.92
BAPO	418.46	1	1.41

TABLE 2.2: Composition of a mix of 70%w OL HEA, 15%w EHA and 15%w PEA

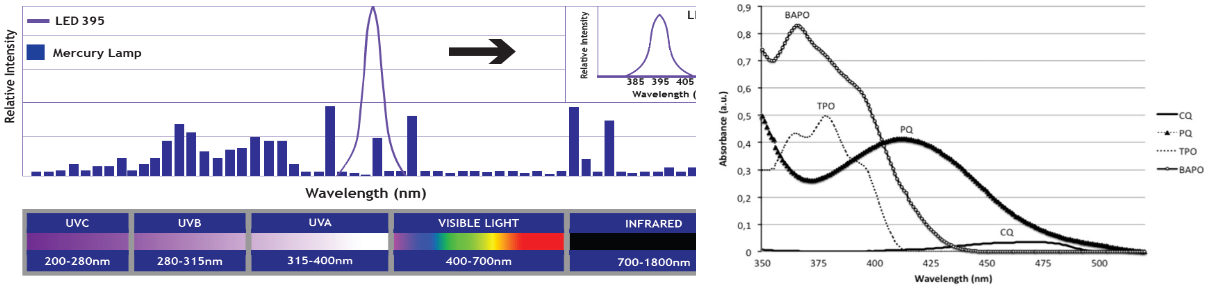

(A) Phoseon Firejet FJ801 395 nm characteristics (Source: Phoseon Firejet Product Overview)

(B) Light absorption profiles of photoinitiators [53]

FIGURE 2.6: UV lamp characteristics and photoinitiator absorption

covered with polyethylene (PE) 6 μm powder to make the manipulations for mechanical testing easier.

Considering the polymerisation protocol, one could argue that a lot of remaining O_2 could inhibit the reaction: the polymer mixes are not degassed before polymerisation and the reaction is carried out under nitrogen flux, but in a polymerisation chamber that is not hermetic. However, the high concentration of photoinitiator and the high UV power will lead to a big concentration of radicals in the polymer mixes. Some of those radicals will not initiate the polymerisation but rather consume the diluted O_2, leading to a good conversion of the acrylates either way [25].

2.2.3 Polymerisation protocol and degree of conversion

While the conversion can be quickly seen through the yellowish color of the resulting networks, a better measurement of the conversion can be achieved by measuring the infrared (IR) absorption of the cured samples. When polymerising, two functions of the acrylate group change: the C=C bond is converted into a single bond, and that will lead to an environment change for the C=O bond. These changes can be followed by comparing the absorption spectra of the cured networks and of the raw polymer mix.

2.2.3.1 Determination of the degree of conversion (DC)

The ATR method is based on the total reflection of the infrared light between the diamond and the sample. Only an evanescent wave will travel through the sample, and will quickly be attenuated. For our type of resin, with a refractive index of around 1.5, the testing depth over the wavelength range will vary from 0.2 to 2.5 μm. We will use these measurements to determine the surface properties of the cured networks, but they can't be used for a quantification of the degree of conversion, as the network surface state may not be representative of the bulk conversion state because of the

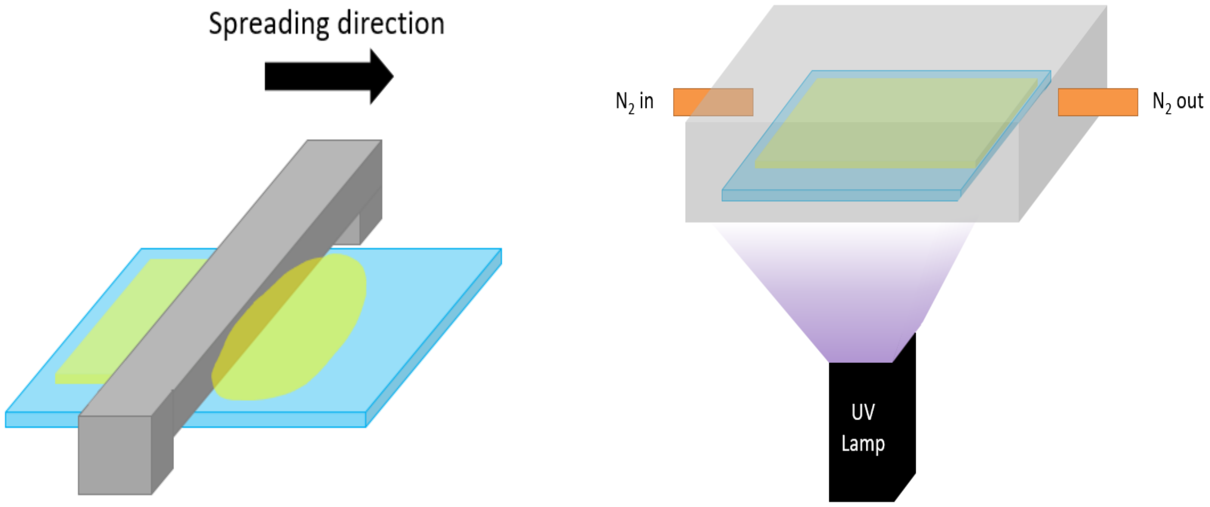

(A) Spreading of polymer with a doctor blade (B) Polymerisation of films under N_2 flow

FIGURE 2.7: Production and polymerisation of polymer films

depth dependent absorption of the UV and O_2 concentration. The transmission spectra, on the other hand, probes a section of the sample of around 1 mm^2, and the transmitted intensity is measured. As the light shines through samples of larger thicknesses (from 100 to 500 μm), some of the wavelengths will be completely absorbed by the most concentrated functions, such as C-H and C=O. This will lead to a saturated signal, but will also act as a magnifier for the less concentrated bonds that are present in the resin. To determine the degree of conversion for example, the disappearance of the C=C bond can be monitored with a good accuracy. All IR spectra were done on a Brucker Tensor 27. Both ATR (Attenuated Total Reflectance) and Transmission methods were used in a range of 4000 to 600 cm^{-1} with a resolution of 4 cm^{-1} and 32 scans co-addition.

In order to determine an illumination protocol that leads to a sufficient degree of conversion in a short time, several polymerisation conditions of a mix of OL HEA 15% EHA 15% PEA have been tested with different lamp powers and an illumination of 1s (see Table A.2). The change of polymerisation energy will lead to different degrees of conversion, named DC in the following. To limit all post-cure reactions of the acrylates, the samples are kept in the dark and their IR absorption is tested less than 1h after their polymerisation. We measure the change in the stretching peak of the C=C acrylate bond (at around 1637 cm^{-1}) in the transmission spectrum as it has already been proven to be a good indicator of the conversion of such acrylate resins [43]. The comparison with the raw polymer mix allows for the measurement of the conversion: the C=C peak of the unreacted mix corresponds to 100% of acrylate functions, so comparing the height of the same peak in the polymerised networks will quantify the remaining non reacted functions. The transmission spectra of the unreacted mix is done by squeezing a drop of the uncured resin between 2 NaCl pellets. Since the exact thickness of the uncured resin is unknown, and all cured networks have a different thickness, a normalization of the spectra is needed before any comparison can be made. The large band at around 3500 cm^{-1}, due to the N-H bond present in the functionalization of the oligomer, can be used, as this bond does not change during the polymerisation. This signal is saturating for the raw polymer mix (Figure 2.8 (A)), so it is normalized by the benzene peak at 692 cm^{-1}, present in the PEA. The decrease of the C=C acrylate peak with an increasing polymerisation energy can be seen on Figure 2.8 (B). The corresponding degree of conversion is computed as:

$$DC = \frac{C = C \text{ peak polymer mix} - C = C \text{ peak polymer network}}{C = C \text{ peak polymer mix}} \tag{2.6}$$

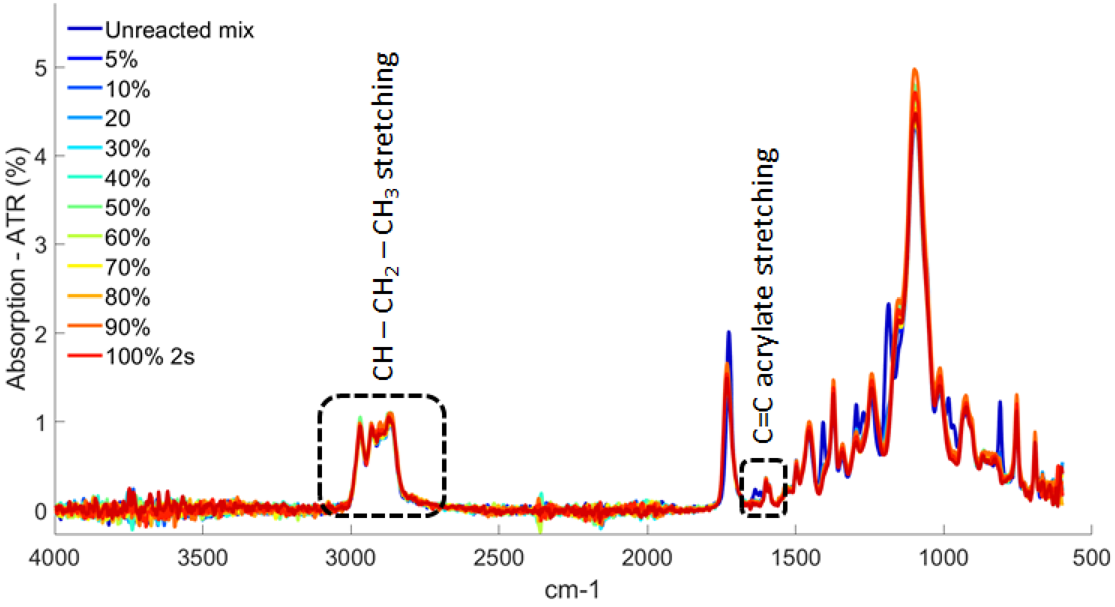

(A) IR ATR spectra of the raw polymer mix (in dark blue) and the different polymerised network

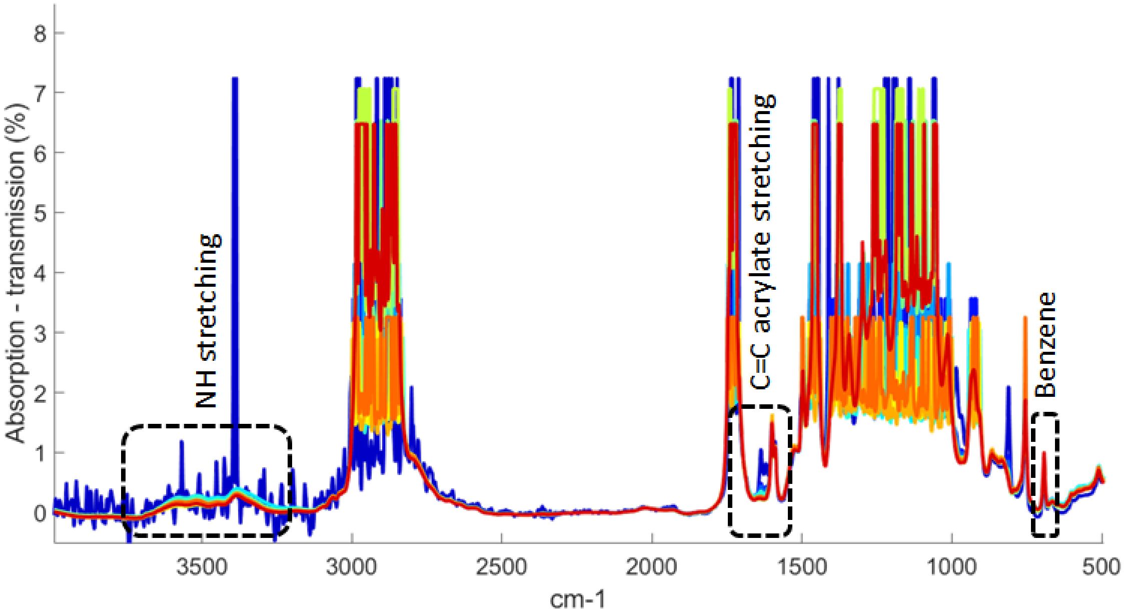

(B) IR transmission spectra of the raw polymer mix (in dark blue) and the different polymerised network

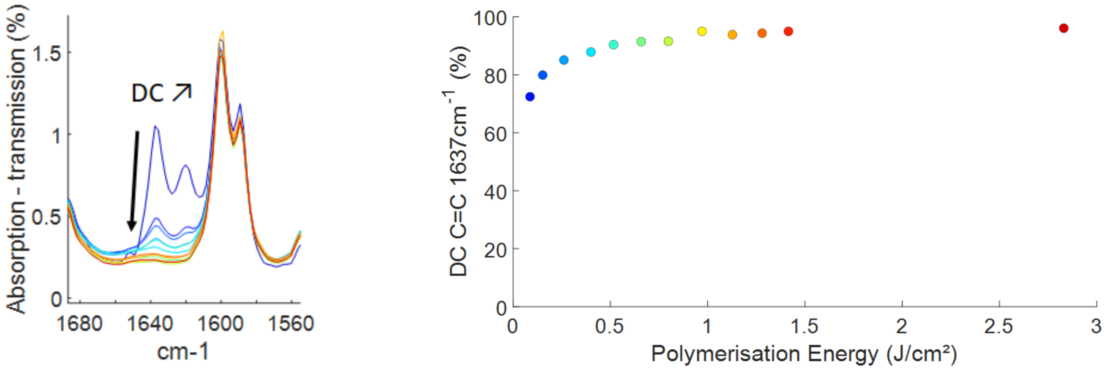

(C) Zoom on 1637 cm $^{-1}$

(D) Degree of conversion of the acrylates as a function of polymerisation energy

FIGURE 2.8: Study of the degree of conversion as a function of polymerisation energy. As the polymerisation energy increases, the conversion increases, which is seen through a decrease of the C=C absorption peak at 1637 cm^{-1}. The conversion reaches a plateau at around 1 J/cm^2, which corresponds to a polymerisation protocol of 70% of lamp power for 1s of illumination

Considering that the polymerisation process only lasts for 1s, the DC reaches very high values even for the lowest energy, which corresponds to 87 mW/cm^2 for 1s. A plateau of conversion of 95% is reached for illuminations above 1 J/cm^2, which corresponds to the energy level used in the industry. This limit of conversion is not only due to the short polymerisation time, but also to the increase in viscosity. It is also possible that some double bonds are pendant in the network, if only one side of the oligomer reacts or in the case of a termination by disproportionation. Those pendant double bonds will be considered on this computation and act as "unreacted" functions. As the polymerisation is taking place, the polymer chains grow and create crosslinks between each other, leading to a significant increase in viscosity. Once the gelation point of the network is reached, the chain movements are highly restricted, inhibiting the reaction of the remaining acrylate functions [34]. In the following, the protocol of 70% of lamp power for 1s of illumination will be used for all polymerisations, as it leads to a sufficient DC in a short time.

2.2.3.2 Homogeneity of the conversion and characterization of the extracted material

As seen on Figure 2.7, the UV light shines through the whole sample during the polymerisation process. While the average conversion is ensured with a 1 J/cm^2 polymerisation energy, we checked the homogeneity of conversion between the 2 network's surfaces by ATR, as they receive a different amount of UV light. No significant difference between the 2 spectra can be seen, even for thicknesses reaching 500 μm. We can therefore conclude that the conversion is homogeneous over the thickness of the samples. The conversion and homogeneity of the networks are equivalent between all formulations (see Table 2.8 for a comparison between OL HEA and OL HEMA with 30% PEA).

The conversion and the homogeneity of the networks can also be determined by conducting equilibrium swelling experiments on the networks. According to the Flory-Rehner theory [54], crosslinked networks will reach a swelling equilibrium in a good solvent when the stretching of the chains due to the swelling matches the osmotic pressure due to the entropy and enthalpy of mixing of the solvent molecules with the network. For each formulation, samples have been weighted to determine their initial mass m_i and immersed in ethyl acetate ($\rho_{solvent} = 0.902$ g/mL) for 1 week at room temperature until equilibrium was reached. The swollen mass m_s was measured after a quick drying of the swollen sample. Finally, the samples were dried overnight under the hood and then 1h under vacuum to determine their dry mass m_d. The swelling in mass Q_m, in volume Q_v and the extracted amount of material m_{ext} can be determined by:

$$Q_m = \frac{m_s}{m_d} \qquad Q_v = 1 + \left[(Q_m - 1) * \frac{\rho_{polymer}}{\rho_{solvent}} \right] \qquad m_{ext} = \frac{m_i - m_d}{m_i} \tag{2.7}$$

Given the small thickness of the samples, the direct measurement of the density of the network is not easy. The density is therefore determined by immersing the networks in water with increasing amount of NaCl. The density of the network is found when the sample starts to float. The density of the OL HEA 15%EHA 15%PEA is measured at 1.042 and it is supposed to be similar for all formulations.

A first observation of the swollen samples shows that the swelling is homogeneous and that the samples are all transparent. This leads to the conclusion that if there are swelling heterogeneities in the networks, they are small enough not to induce visible light diffraction. The results of the swelling experiments are summarized in Table 2.3:

Formulation		m_{ext} (%)	Q_m	Q_v	N
OL HEA	15% EHA 15% PEA	4.92 ± 1.42	4.25 ± 0.11	4.75 ± 0.12	64
	30% EHA	5.18 ± 1.42	4.66 ± 0.11	5.23 ± 0.12	82
	30% PEA	3.84 ± 1.42	3.66 ± 0.11	4.07 ± 0.12	42
OL HEMA	15% EHA 15% PEA	10.87 ± 1.42	4.46 ± 0.11	5.00 ± 0.12	73
	30% EHA	13.55 ± 1.42	4.67 ± 0.11	5.24 ± 0.12	83
	30% PEA	6.30 ± 1.42	3.90 ± 0.11	4.35 ± 0.12	50

TABLE 2.3: Swelling coefficients and extractable material. All swelling experiments were done in ethyl acetate. The standard deviation values were computed for the OL HEA 15% EHA 15% PEA formulation with 3 samples, it is estimated that the deviation is the same for all formulations. N is the mean number of monomer in the elastic chains - θ solvent definition.

A small percentage of the initial mass can be extracted from the networks. This is consistent with the conversion saturating at 95%. In appendix A.3, H-NMR spectra and SEC measurements of the extracted materials are presented. It is shown that the extractables consist of both unreacted monomers and oligomers and small chains that did not crosslink with the main network.

The value N represents the average number of monomers in an elastic chain forming the network. This is based on the balance between osmotic pressure at equilibrium and elastic energy in the network swollen in a θ solvent (for more details see Rubinstein and Colby [55]), that states that:

$$N \simeq Q_v^{8/3} \tag{2.8}$$

It can seem strange to use the θ solvent description to extract N, as the swelling solvent is supposed to be a good solvent for the polymer. The quality of a solvent is defined by the parameter χ characterizing the interactions between the polymer chain and the solvent:

- PPG: $\chi_{ethyl\ acetate} = 0.57$ [56]
- Poly(methyl acrylate): $\chi_{ethyl\ acetate} = 0.43$ [57]

The interaction between the PPG and the ethyl acetate is not that good, while the ethyl acetate can be considered a good solvent for acrylates ($\chi < 0.5$). In this way, the θ solvent description seems to be acceptable, as it describes a solvent that has the same affinity with the polymer as the polymer with itself. Based on our formulations, the network is made out of both PPG chains and acrylate chains, so this mean value of N represents the mean chain length between the oligomer chains and the one formed by the acrylate monomers. Furthermore, it does not directly represent the number of monomers between crosslinks. If there are many trapped entanglements between the crosslinking points, N will represent the mean number of monomers between the trapped entanglements.

2.2.3.3 Glass transition temperature and micro-heterogeneities

The glass transition temperature of each network is measured via DSC on a TA Instrument DSC Q200. Around 10 mg of polymer network are put in an hermetic aluminium sample pan and submitted to temperature sweeps at a given rate. The result is the Heat flux the DSC has to produce in order to follow the set temperature sweep. The thermal response of the sample pan itself is subtracted as the sample is put in the oven next to a reference empty pan. All formulations are tested over a temperature range from -100°C to 100°C, with a temperature sweep of either 20°C/min or 30°C/min, with a "Heat-Cool-Heat" procedure. The first heating part will erase all the thermal memory of the sample, the second one will be used to measure the glass transition temperature. This transition is endothermic and is characterized by a sudden change in the heat-flow curve, as can be seen on Figure 2.9. The faster heating rate was used for the samples with 70% of oligomer and 30% of PEA because they all showed a second drop at higher temperature than expected. Increasing the temperature range allowed for an increased heat flux and therefore a better measurement of this second T_g. The T_g of all formulations can be seen in Table 2.4.

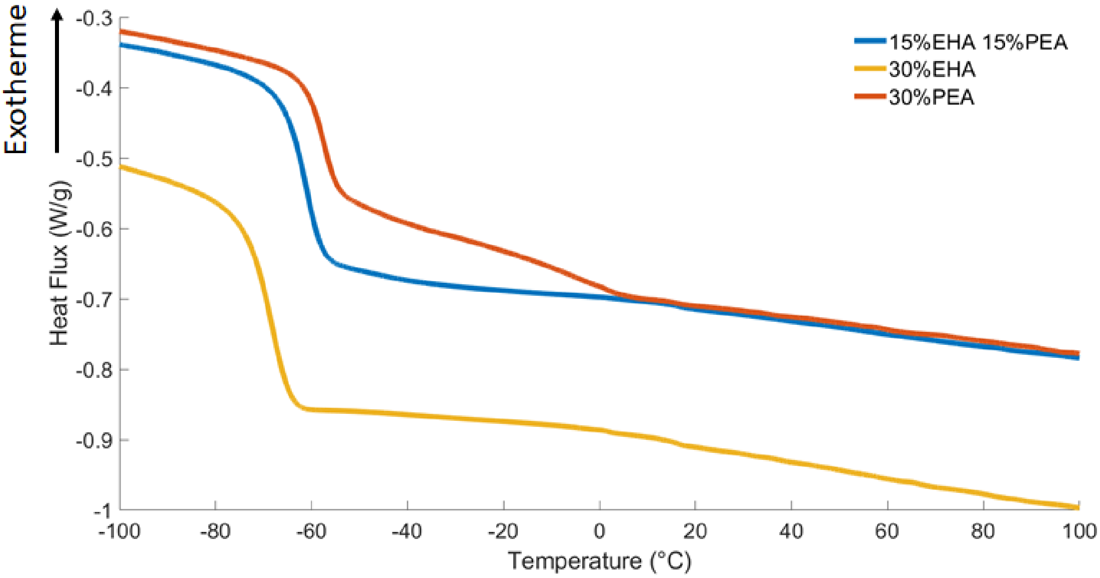

FIGURE 2.9: DSC measurement of 3 formulations with OL HEMA. The temperature sweep is 30°C/min. The second bump on the 30% PEA curves shows the presence of harder domains in the network.

Formulation		Temperature sweep (°C/min)	T_g (°C)
OL HEA	15% EHA 15% PEA	20	-57
	30% EHA		-63
	30% PEA	30	-56 & 5.43
OL HEMA	15% EHA 15% PEA	20	-62.8
	30% EHA		-70.3
	30% PEA	30	-59 & -3.26

TABLE 2.4: Glass transition temperature of each formulation. Each formulation contains 1%w of BAPO.

Formulation	Temperature sweep (°C/min)	T_g (°C)
OL HEA	20	-60.70
OL HEMA		-59.44
EHA + 2%mol BDA	20	-83
PEA + 0%mol BDA		7.7
PEA + 2%mol BDA		9.7

TABLE 2.5: Glass transition temperature of each component. The oligomer is difunctional so it can form a network on its own. EHA needs the addition of BDA as a crosslinker, while PEA can form a network on its own. Because of the low viscosity of the monomers, their respective networks are polymerised in a mold described in Annex A.4 and with a protocol of 70% power during 5s, corresponding to 5 J/cm^2.

The fact that the formulations with 30% PEA have a second T_g is quite interesting. The glass transition temperature of pure PEA is around 8°C (slightly varying with crosslinking density). The PEA is able to form a network without the addition of a crosslinking agent due to the high rate of transfer reactions during the radical polymerisation, while no significant chain crosslinking is observed for EHA without crosslinker. In the 30% PEA formulations, the spinodal separation of the monomer and the oligomer could be more important due to the poor solubility of the aromatic cycle. Because PEA is also able to crosslink on its own and the monomer is more mobile than the oligomer, the original heterogeneities could grow into harder nodules. This is close to the chemical clusters described by Dusek [38] and observed by Krzeminski et al. with AFM and DSC characterizations of aromatic diacrylate polymerisations ([39], [58]). Based on the T_g of the heterogeneities and the T_g of pure PEA, it appears that there is a mix with a high concentration of oligomer in the matrix, and a high concentration of PEA in the heterogeneities, hence leading to a shift of the T_gs. In order to validate this hypothesis of rich PEA hard nodules in a softer rich oligomer matrix, a more precise testing of the micro-structure is needed.

2.2.3.4 AFM testing of the surfaces

One method to characterize surfaces at the microscale is to probe them by AFM (Atomic Force Microscopy). These experiments were conducted by Bruno Bresson in the SIMM laboratory. The principle of the AFM measurement is to probe a surface by measuring the deflection of a cantilever when the probe approaches and interacts with the sample surface. In all the following observations, triangular tips of stiffness of $\sim$ 0.4 N/m were calibrated with a 1 kHz approach-retract experiment on a glass slide, considered as being of "infinite stiffness" in comparison with the samples of interest. The samples are tested following a QNM (PeakForce Quantitative Nanomechanics) method: each point is tested at 1 kHz by a force controlled approach-retreat of the probe. The height, adhesion and modulus of the tested region can be measured. The Young's modulus is obtained in real time with a DMT fit (Derjaguin–Muller–Toporov [59]) of the retraction curve between 70% of the maximum force and 10% of the minimum force, with a tip angle of 18°. The minimum of the force represents the sample's adhesion force. The DMT model is based on the approximation of the contact between the tip and the sample as still behaving like the Hertzian model of contact and taking into account the adhesion between the 2 surfaces. The whole surface is scanned at 0.5 Hz. This method is described on Figure 2.10.

This calculation is highly dependant on the radius of the probing tip, which should be measured independently from the AFM measurements. In our case, the radius was fitted by testing a reference PDMS surface of known modulus. This technique is subject to uncertainties as the modulus measurement can also depend on the frequency or the set force. Indeed we obtain an effective tip radius of around 20 nm, while the apparent resolution of our images seems to be closer to 2 nm. This contradiction is not yet understood, so the following measurements will only be used as a comparison between samples and not a quantitative measurement of the modulus, which is enough for our observations.

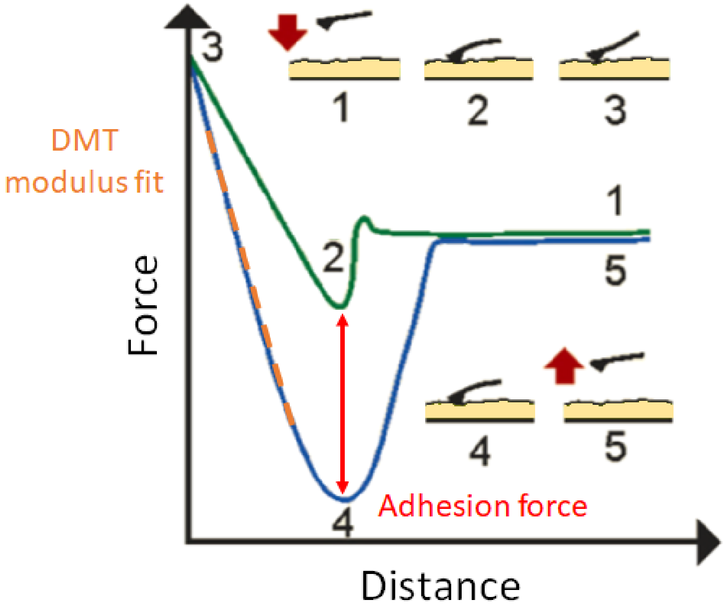

FIGURE 2.10: QNM surface probing method

As shown on Figure 2.11, only the formulation with 30% PEA shows small heterogeneities of harder modulus, of around 20 nm of diameter. These hard zones are also linked to the higher zones in the height measurement. Because the experiment is force-controlled, one explanation for this observation is that softer regions will deform more than harder ones. Both formulations of OL HEA 30% EHA and 15% EHA 15% PEA are homogeneous, the softer network is also the stickier one. This observation of heterogeneities was confirmed by an observation of the same surface with a variation of the applied force and over a temperature range from 0°C to 40°C. Over this range of conditions, the heterogeneities remained. It was also verified that this observation is representative of the bulk of the polymer by scanning the inside of a polymer sample. This was done by preparing a new sample with the same polymerisation protocol, cooling it in liquid nitrogen and breaking it, thus creating a new surface representative of the bulk. With the same AFM probing parameters, the exact same hard nodules have been observed, as can be seen in Appendix A.5. It was also verified that pure PEA networks show no heterogeneities. The formulation of OL HEMA 30% PEA shows the same heterogeneities, showing that a change of oligomer functionalization does not have an impact on the formation of heterogeneities .

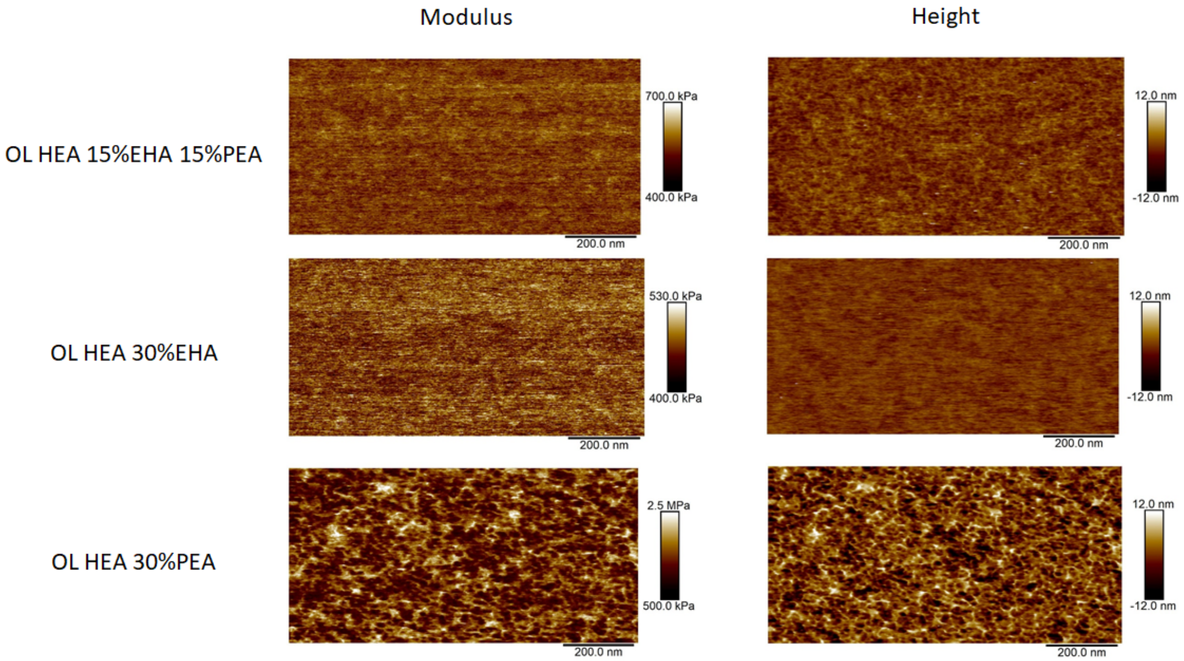

FIGURE 2.11: AFM surface probing of all formulations with OL HEA, QNM mode, set force of 800 pN, 0.5 Hz, 512 pts/ligne. Only the OL HEA 30% PEA sample shows a micro-structure of harder nodules.

These observations are consistent with the double T_g that we observe in DSC experiments. We can conclude that all formulations with 30%w of PEA are heterogeneous. The small heterogeneities appear to be zones where only PEA polymerises, suggesting a partial phase separation between the oligomer and the monomer. This phase separation seems to be attenuated or even to disappear when the PEA is mixed with EHA. A further characterization of these hard nodules could be done by small angle scattering which could give a better idea of their shape [43].

2.3 Influence of the polymerisation protocol and of the chemistry on the micro-structure

The AFM observation of the 3 different formulations of networks revealed a micro-structure of the samples with 30% of PEA that was not expected. The fact that the PEA does not homogenize sufficiently with both the acrylate or the methacrylate oligomer could be due to the rapid polymerisation process that we use. As the polymerisation takes place in 1s, with a high intensity and a high concentration of photoinitiator, a slight change in chemical affinity or reactivity could lead to this phase separation. We looked into ways to vary the polymerisation protocol and the chemical affinity between the components to observe how the heterogeneities evolve. This work was conducted by two interns: Ana Goulée (licence professionnelle chimie/formulation - Sorbonne Université) and Ludovic Dulac (Master 2 Chimie Paris Centre - Sorbonne Université).

2.3.1 Changing the chemical affinity and reactivity

The first lever available to change the reactivity was already partially described in 2.2.3.4: changing the functionalization from acrylate to methacrylate. As discussed in 2.1, acrylates and methacrylates have different reaction rates due to the metastability of the radicals formed on methacrylates [44]. However, both the formulations of OL HEA and OL HEMA showed heterogeneities when polymerised with only PEA. The reactivity change between the two oligomers was therefore not enough to influence the polymerisation of PEA. If the result of the heterogeneity is really a faster growth of the polyPEA chains and a formation of a microgel, it is not surprising that the kinetics of polymerisation of the oligomer would play only a small role, even if the acrylates functions preferably react with methacrylate functions. In order to test the effect of the polymerisation kinetics further, we decided to also slow down the monomer's reaction rate, i.e. using PEMA (2-Phenoxyethyl methacrylate) instead of PEA. Formulations of 70%w of oligomer (either the methacrylate functionalized or the acrylate) and 30% of PEMA were prepared with 1% of BAPO, using the same mixing protocol, and the same polymerisation protocol: 1 J/cm^2 with 1s of illumination.

The result of these polymerisations was striking: no network was formed with the OL HEA 30% PEMA or the OL HEMA 30% PEMA formulations! The change in reactivity between the PEA and the PEMA was important enough so that after 1s of UV illumination, for a total of 1 J/cm^2 polymerisation energy, only a viscosity increase of the mixture could be qualitatively observed. To test the effect of a potential dark curing which can take place when trapped radicals are present in the network, so that the radical polymerisation can take place even after the illumination stops, the samples were kept in the polymerisation chamber under constant nitrogen flux for 1 to 20 min after the 1s illumination. This had no influence on the networks formation, samples that did not lead to a network would stay in the viscous liquid state, even after longer times in inert atmospheres. This implies that no dark curing happens in the networks.

2.3.2 Influence on the UV illumination power at the same total energy

This drastic change in reactivity of the components led to the use of the second lever influencing the network's construction: the UV illumination time. The usual protocol was chosen to deliver a high dose of UV in a flash in order to reproduce the industrial conditions, but it is quite different from standard free radical polymerisations. This powerful illumination over a short time leads to the almost instantaneous complete activation of the photoinitiator, and therefore to a large number of polymerisation sites. This leads to a high conversion rate, but also possibly to more heterogeneities as a lot of chains start and grow at the same time.

The cleanest way to test the effect of a longer polymerisation time with the same total applied radiation energy would be to polymerise the networks in a glove box in a controlled inert atmosphere, with a low UV intensity as described in several acrylate polymerisation studies ([11], [60], [61]). However, the oligomers used are not stable and gelify in a nitrogen atmosphere, as their inhibitors only work in the presence of O_2. The only solution was then to change the polymerisation protocols using the Firejet lamp, which gave a smaller range of polymerisation times.

2.3.2.1 Influence of the chemical function on network formation

In this study, the polymerisation protocols are described with first the lamp power (in %) and the illumination time (in seconds). The same formulations were polymerised with 4 different protocols, each of them resulting in an illumination energy of 1 J/cm^2 but with different illumination times: (70% 1s), (35% 2.1s), (15% 4.9s), (5% 11.5s). In each case, the polymer film was introduced in the polymerisation chamber and the nitrogen flow was started 1 min before the illumination started and kept for 1 to 10 min after the illumination ended. While the time of nitrogen flow after the illumination showed to have close to no impact on the structure of the network, the observations made about the influence of the illumination time are summarized in Table 2.6.

Polymerisation protocol	70% 1s	35% 2.1s	15% 4.9s	5% 11.5s
OL HEA - 30% PEA	✓	✓	✓	✓
OL HEA - 30% PEMA	-	-	±	✓
OL HEMA - 30% PEA	✓	✓	✓	✓
OL HEMA - 30% PEMA	-	±	✓	✓

TABLE 2.6: Influence of the illumination time on the network's structure - Comparison of the reactivity of PEA and PEMA, total energy of polymerisation: 1 J/cm^2. The protocols that do not lead to network formation are identified by -, ± means that a viscous network is formed, ✓ indicates the formation of a network which can be handled and tested.

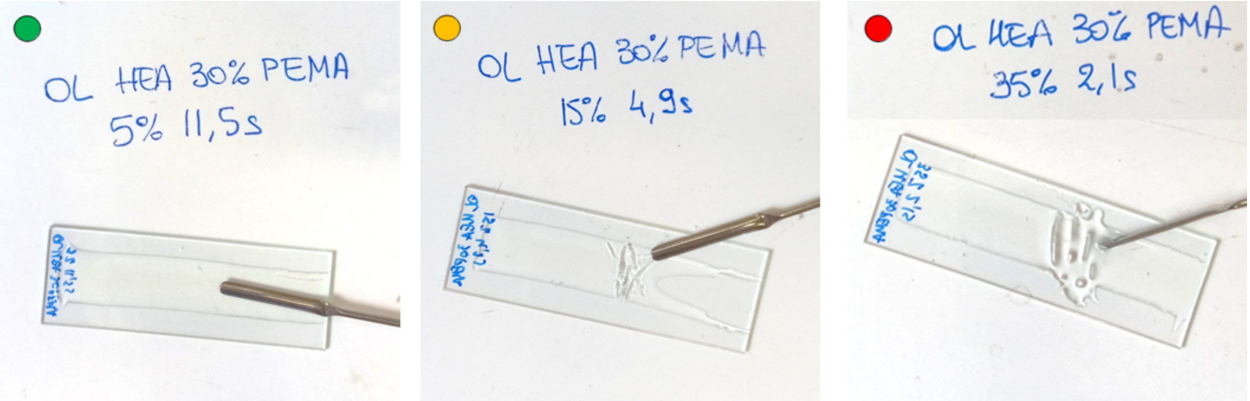

(A) Difference of network's formation for OL HEA 30% PEMA with illumination time. For each condition, the sample's surface is scratched with a spatula.

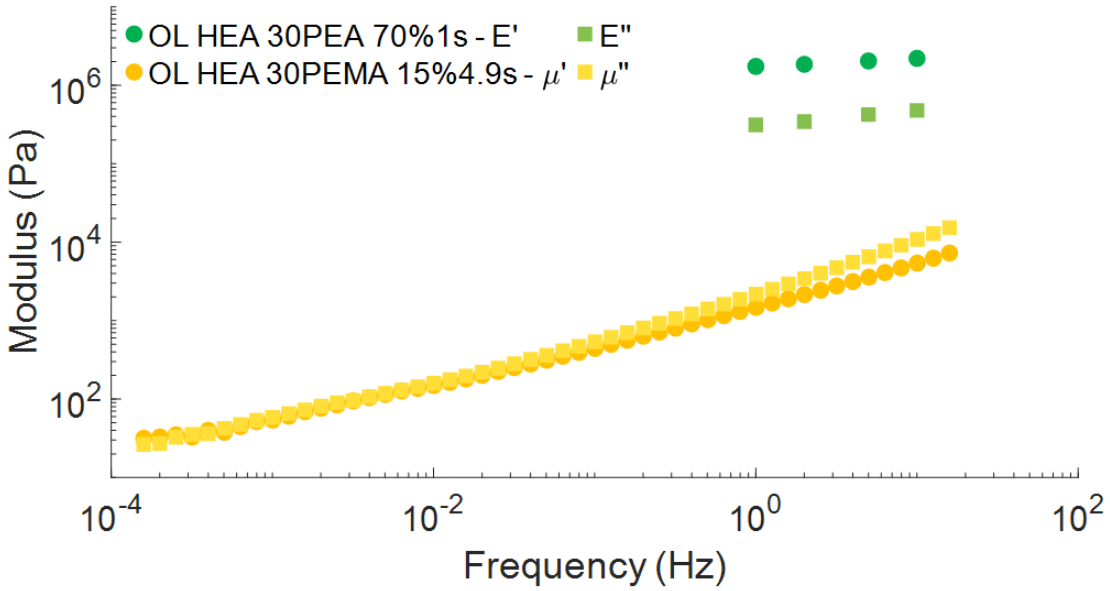

(B) Comparison of the rheology of a green network and a yellow one at 25°C. The elastomeric network (OL HEA 30% PEA 70% 1s) is tested in DMA in tension mode (Strain 2%, Static force 0.03 N). The viscous network (OL HEA 30% PEMA 15% 4.9s) is tested in parallel plates rheology with a roughened plate surface geometry (strain 0.8%, axial Force 0 N)

FIGURE 2.12: Network formation with different illumination times and formulations. (A) For the PEMA based formulations, the longest illumination time leads to the formation of a network. Decreasing the illumination time leads to a shift towards a more gel-like structure or even a viscous liquid. (B) The difference between the elastomeric network and the gel-like structure lies in the difference between the elastic (μ') and dissipative responses (μ'').

The increase of the illumination time has a significant effect on the network structure, as can be seen on Figure 2.12: with an increase of illumination times, the resulting product shifts from a viscous liquid to a very brittle gel and finally to an elastomeric network. When testing the response in small strains, by either DMA for the elastomeric network or parallel plates rheology for the gel-like structure (experiments conducted by Guylaine Ducouret - SIMM laboratory), the difference of network structure is obvious. For the elastomeric network, the elastic response at 25°C is higher than the viscous one, and the elastic modulus is around 1 MPa. For the gel-like structure, the viscous response μ" is higher than the elastic response for a wide range of frequencies, and both moduli are around 10^4 Pa, 2 orders of magnitude below the elastomeric network. This shows that the yellow conditions do not lead to the correct formation of a network, but still there is enough crosslinking and entanglements to form a gel.

It could be argued that these networks are not well produced because the PEMA monomer has a lower solubility in the oligomers, just as the PEA was not soluble. Just as adding EHA leads to the solubilization of PEA in the oligomer matrix, adding EHMA could help to dissolve the PEMA into the oligomer matrix and form the network. Formulations of 15% of PEMA and 15% of EHMA and 30% of EHMA have been polymerised with the same polymerisation protocols, the results are summarized in Figure 2.13.

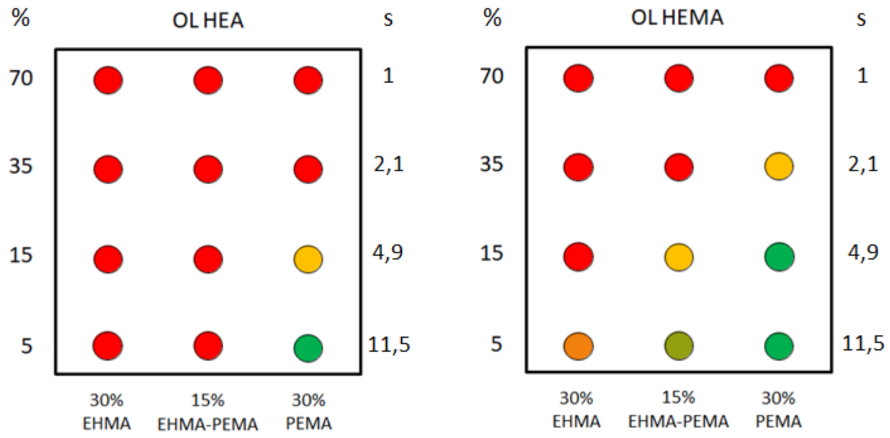

FIGURE 2.13: Structures of networks based on methacrylate monomers. The same color code as in Table 2.6 is used: red means production of a viscous liquid, yellow means the formation of a brittle network, green means the production of an elastomeric network. The addition of EHMA in the formulation inhibits the formation of a network.

Surprisingly, adding EHMA in the formulations does not lead to a better network formation. In fact, it is quite the contrary, as for the OL HEA formulation with the (5% 11.5s) illumination protocol, the formulations based on EHMA do not form a network while they do when pure PEMA is used. This behaviour is not well understood, but suggests that the reactivity with EHMA is lower than with PEMA, and therefore leads to a quicker termination of the polymerisation rather than a propagation. It shows also that the network formation is more favourable when mixing a methacrylate functionalized PPG oligomer with methacrylate monomers, than mixing an acrylate oligomer with the same methacrylate monomers. The ratios of chemical affinity between acrylates and methacrylates lead to a more favourable polymerisation of methacrylates on each other, while acrylates favour a reaction with methacrylates [44]. Therefore, even if the rate of reaction is slower, the networks formed with only methacrylate functionalized building blocks will be more homogeneous and more prone to form a network than the one with a mixed acrylate/methacrylate functionalization.

2.3.2.2 Influence of chemical function on the polymer chain growth

The difference of reactivity between the acrylates and methacrylates can also be observed by polymerizing only monomers with 1%w BAPO and measure the molecular weight of the resulting polymers chains. Once the mix of monomer is polymerised, with a lamp protocol of (70% 5s) corresponding to a polymerisation energy of 5 J/cm^2, the resulting viscous liquid is dissolved in THF at a precisely determined concentration of around 2.5 mg/mL. The resulting solution is then stirred for 24h to ensure homogeneity and complete dissolution and tested on a Viscotek GPC-max VE2001 SEC (Size exclusion chromatography). All SEC experiments were done by Mohamed Hanafi in the SIMM laboratory. The principle of this measurement is to separate the different polymer chains by size as they travel through the column: they interact with the grains filling the column that have different levels of porosity. The smaller the polymer chain, the more interactions and the more time spent in the column as the polymer chain can travel through all the pores, while higher molecular weight chains can't enter the pores and will be flushed out of the column quicker. Three sensors at the bottom of the column measure the properties of the out-coming flow: a refractometer, a viscometer and a light scattering system.

Single polymer chains of EHA and EHMA have been polymerised with a total energy of 5 J/cm^2 (using the mold and protocol for pure monomer polymerisation, see A.4), the resulting mass distribution of the chains can be seen on Figure 2.14. The comparative study between PEA and PEMA at the same illumination energy could not be conducted because the PEA 1%w BAPO formulation forms a network at each polymerisation protocol, as discussed in Section 2.2.3.3, and PEMA makes a network at the longest illumination time. A first observation is the important peak at large retention volumes for both formulations that is due to the monomers (184.28 g/mol for EHA and 198.30 g/mol for EHMA). This is to be expected as no purification is made between the polymerisation and the characterization. The EHA polymerisations lead to a good detection of the polymer peak and a differentiation from the monomer. The EHMA formulations, on the other hand, lead to only small polymer chains rendering the mass characterization difficult. Only an estimated value of M$_n$ can be computed in that case, which is enough to make a comparison between the acrylate and the methacrylate monomer, as well as the influence of the polymerisation time. The results of the SEC measurements are summarized in Table 2.7.

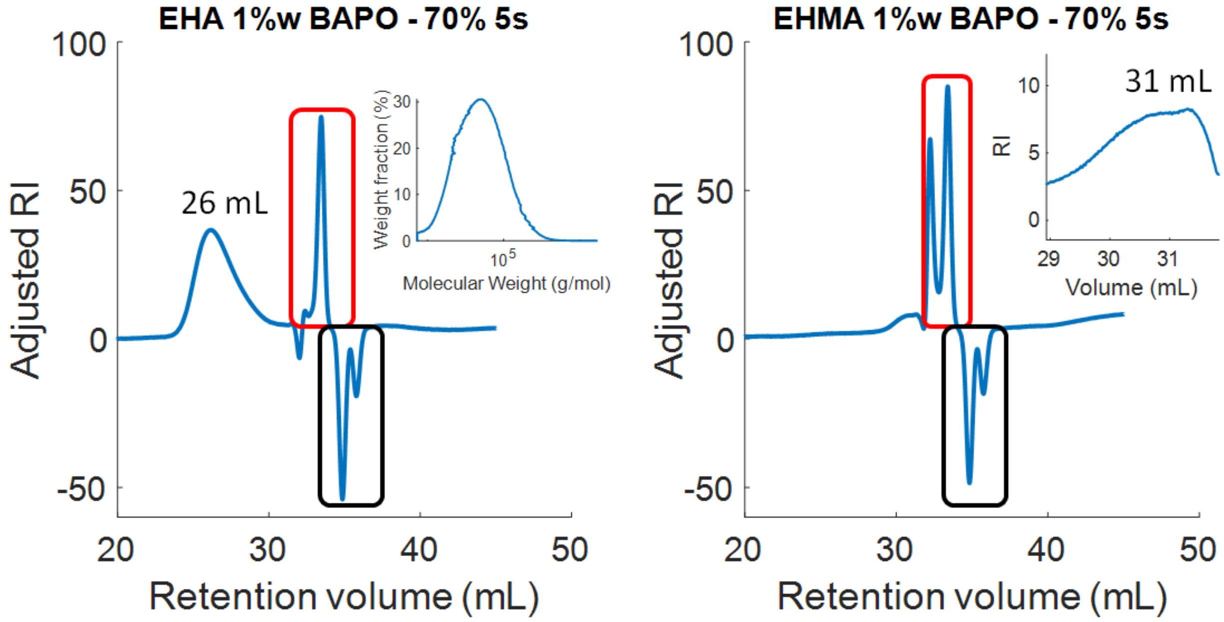

FIGURE 2.14: SEC measurement of EHA (left) and EHMA (right) polymer chains produced at 5 J/cm^2 in 5s - Refractometer. Left insert: Molecular weight distribution corresponding to the polymer chains (retention peak centred at 26 mL), Right insert: zoom on the polymer chain peak for EHMA. The variation of the refractive index (RI) with the retention volume indicates the change in polymer concentration for each specific volume, which is linked with the polymer size. The negative peaks (marked in black) are the solvent peaks and the intense positive peaks (marked in red) at large retention volumes are indicators of small masses, hence monomers or dimers.

The difference in reactivity between the acrylate and the methacrylate leads to a striking difference in the polymer molar mass: for the same polymerisation protocol, EHA leads to the production of chains of around 49 900 g/mol, i.e 270 repetition units, while EHMA make chains of 5000 g/mol, i.e 25 repetitions. For the same total polymerisation energy, increasing the polymerisation time leads to an increase of the average polymer chain length. In both polymerisation processes, the polydispersity is quite high. It is not surprising that free radical polymerisation in such protocols leads to a wide dispersion of polymer chain mass. The effect of the polymerisation time on the chain length is most probably due to the rate at which the photoinitiators are activated. In the case of the high intensity, all photoinitiators are activated at the same time, leading to many initiations and simultaneous polymerisations. The concentration of radicals increases, enhancing the probability of a termination by combination or disproportionation when 2 radicals

Formulation	Polymerisation protocol	M (g/mol)	Number of monomers	Ip
EHA	70% 5s	49 898	271	1.87
	5% 56.8s	169 040	917	2.01
EHMA	70% 5s	$\sim$ 5 000	25	X
	5% 56.8s	$\sim$ 10 000	50	

TABLE 2.7: Influence of the illumination time on the polymer chain's length. Each polymerisation protocol provides a total polymerisation energy of 5 J/cm^2. The monomers are all mixed with 1%w of BAPO as photoinitiator. For the EHA formulation, the mass is Mw which represents the weight average molecular mass and Ip is the polydispersity index = Mw/Mn. For the EHMA formulations, the mass is Mn: the number average molecular mass.

meet. When a lower intensity is used, only fewer photoinitiators are activated at the same time, leading to a higher probability of propagation before a termination can happen.

2.3.3 Influence of the polymerisation protocol on the micro-structure

Now that the effects of the chemical function, the polymerisation power and time on the network formation aspect have been studied, it is interesting to explore the effects on the micro-structure and the possible effect on the formation of heterogeneities in the case of PEA and PEMA. Due to handling difficulties, only the elastomeric networks (marked as ✓) have been tested in IR absorption, swelling measurements and DSC.

2.3.3.1 Effect on the swelling and extractable

The comparison in equilibrium swelling and degree of conversion between the PEA and PEMA networks synthesized at different polymerising times are summarized in Table 2.8. First, let's look at the oligomer functionalization effect on the properties of the networks with 30% PEA: the conversion of the acrylate functions is always almost complete for all polymerisation times. These formulations follow the same conversion behaviour as the polymerisation of the OL HEA 15% EHA 15% PEA, as described on Figure 2.8. The only notable difference between OL HEA and OL HEMA is a slight increase of extractable mass in the OL HEMA 30% PEA formulations. This could be due to the fact that methacrylate oligomers have an increased reactivity on themselves than with the acrylate monomer, leading to more unreacted PEA.

Now let's look at the effect of the functionalization of the monomer, from PEA to PEMA. First, the degrees of conversion of the methacrylate functions are much lower than with the PEA formulations. The formulations with PEMA also have a larger quantity of extractibles and a larger swelling of the networks. This is all going in the same direction: with a lower reactivity of the methacrylate function, it is not surprising that more chains are not linked to the main network, and that more monomers and oligomers did not get converted at all. Again, the difference of reactivity between the OL HEA and OL HEMA with the PEMA is clear since, with the polymerisation protocol (5% 11.5s), the extractible mass for OL HEA is 4.5 times larger than with OL HEMA.

Formulation		Polymerisation protocol	Q_m	m_{ext} (%)	DC (1635 cm^{-1}) ± 1%
OL HEA	30% PEA	70% 1s	3.66	3.84	99
		35% 2.1s	3.7	3.7	98
		15% 4.9s	3.6	3.1	**100**
		5% 11.5s	3.6	3	**100**
OL HEMA	30% PEA	70% 1s	3.9	6.3	93
		35% 2.1s	3.8	5.9	98
		15% 4.9s	3.8	5.4	99
		5% 11.5s	3.7	6.2	**100**
OL HEA	30% PEMA	5% 11.5 s	11	40	72
OL HEMA	30% PEMA	15% 4.9 s	9.4	33.8	58
		5% 11.5s	5.3	8.9	90

TABLE 2.8: Influence of the polymerisation protocol on the structure's formation and conversion - Difference between PEA and PEMA formulations. The swelling measurements are done in ethyl acetate with the same protocol as described in Section 2.2.3.2. The 100% DC correspond to IR trans spectra in which no residual signal of the unreacted acrylates could be detected.

2.3.3.2 Effect on the heterogeneities

The polymerisation protocol has a distinctive effect on the network formation, so it should also have an impact on the formation of heterogeneities. To test the presence of these hard nodules, T_g measurements via DSC testing have been done on all resulting networks. Again, a protocol of 30°C/min was used to insure a good detection of the possible second bump in the heat flow. The temperature sweeps are shown on Figure 2.15 and the T_gs are summarized in Table 2.9. The difference in heat capacity (HC) between the lower and the higher T_g is about one order of magnitude, explaining why a fast heating/cooling rate is needed for a good detection: only a small polymer mass is responsible for this transition. This leads to a small second bump on the DSC curve, as can be seen on Figure 2.15 (A). To emphasize the variations of the signal, the derivative of the heat flux is computed, and the whole curve is normalized by its total area. This allows for a better observation of the second bump at higher temperatures, revealing the presence of harder nodules. In both the OL HEA and OL HEMA formulations, the second bump is of smaller amplitude and the PEMA leads to a wider peak compared to the PEA ones. This is coherent with the fact that the second T_g in PEMA formulations is less visible on DSC sweeps. It could be a sign of a better incorporation of the PEMA within the matrix, leading to smaller hard nodules, and therefore to a more dilute signal in the total temperature sweep.

Formulation		Protocol	$T_{g,1}$ (°C)	$T_{g,2}$ (°C)	α(monomer,$T_{g,2}$)
OL HEA	30% PEA	70% 1s	-55.25	3.41	94.9
		5% 11.5s	-54.23	5.59	97.3
OL HEMA	30% PEA	70% 1s	-56.19	3.39	94.7
		5% 11.5s	-53.81	1.03	91.9
OL HEA	30% PEMA	5% 11.5s	-56.59	13.32	78.6
OL HEMA	30% PEMA	5% 11.5s	-57.74	13.43	78.4

TABLE 2.9: Influence of the formulation and of the polymerisation protocol on the network's heterogeneities. All DSC measurements were done at a 30°C/min thermal ramp to insure the detection of the second T_g. The formulations with PEA were tested between -100°C and 30°C, the ones with PEMA were tested between -100°C and 100°C.

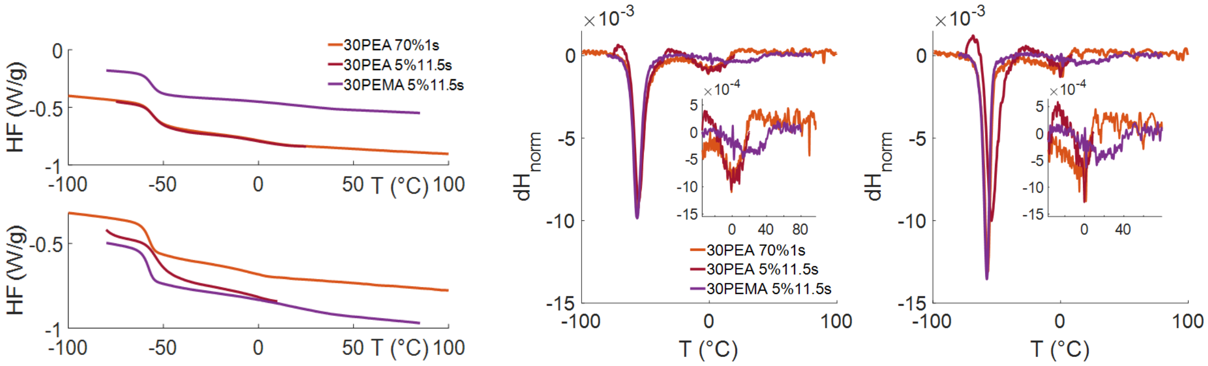

(A) DSC sweeps of OL HEA (top) and OL HEMA (bottom) formulations with either 30% PEA or PEMA

(B) Normalized derivative of the Heat flux. Left: OL HEA, Right: OL HEMA. Insert: zoom on the Heat Flux variation at higher temperatures.

FIGURE 2.15: Effect of the protocol and the formulation on the presence of hard heterogeneities. (A) DSC measurements of the PEA and PEMA formulations for each oligomer. Even with a temperature sweep of 30°C/min, the second T_g is hard to determine, especially for the PEMA formulations. (B) dHF/dT is computed and normalized by the total area of the resulting curve. The insert shows the region of the second T_g. This computation allows for a better visualization of the presence of the heterogeneities.

Formulation	Protocol	T_g (°C)
PEA 2%mol BDA	70% 5s	9.7
PEMA 2%mol BDA	5% 56.8s	42.68

TABLE 2.10: T_g of pure PEA and PEMA. All formulations contain 1%w of BAPO and the DSC temperature sweeps are at 30°C/min. The protocols used are leading to the formation of networks.

Our hypothesis describes the hard nodules as a PEA rich phase, and the matrix as an oligomer rich phase. If we consider that both components are soluble in each phase, then the Fox equation can be applied to both phases. This law states that for a mixture of 2 miscible components i and j, the resulting T_g can be computed as:

$$\frac{1}{T_g} = \frac{\alpha_i}{T_{g,i}} + \frac{\alpha_j}{T_{g,j}} \tag{2.9}$$

where α_i is the weight fraction of the component i, and $\alpha_i + \alpha_j = 1$. Based on this equation, the weight fraction of PEA (respectively PEMA) in the phase of high T_g can be computed. The pure T_g of each oligomer is reported in Table 2.5 and the pure T_g of PEA and PEMA in Table 2.10. As described in section 2.2.3.3 (and Appendix A.4), the pure monomer networks are polymerised in a mold due to their low viscosity.

In addition to the DSC measurements, the surfaces of the different formulations are probed by AFM. Two effects have to be considered independently: the polymerisation time (Figure 2.16 (A)) and the chemical reactivity.

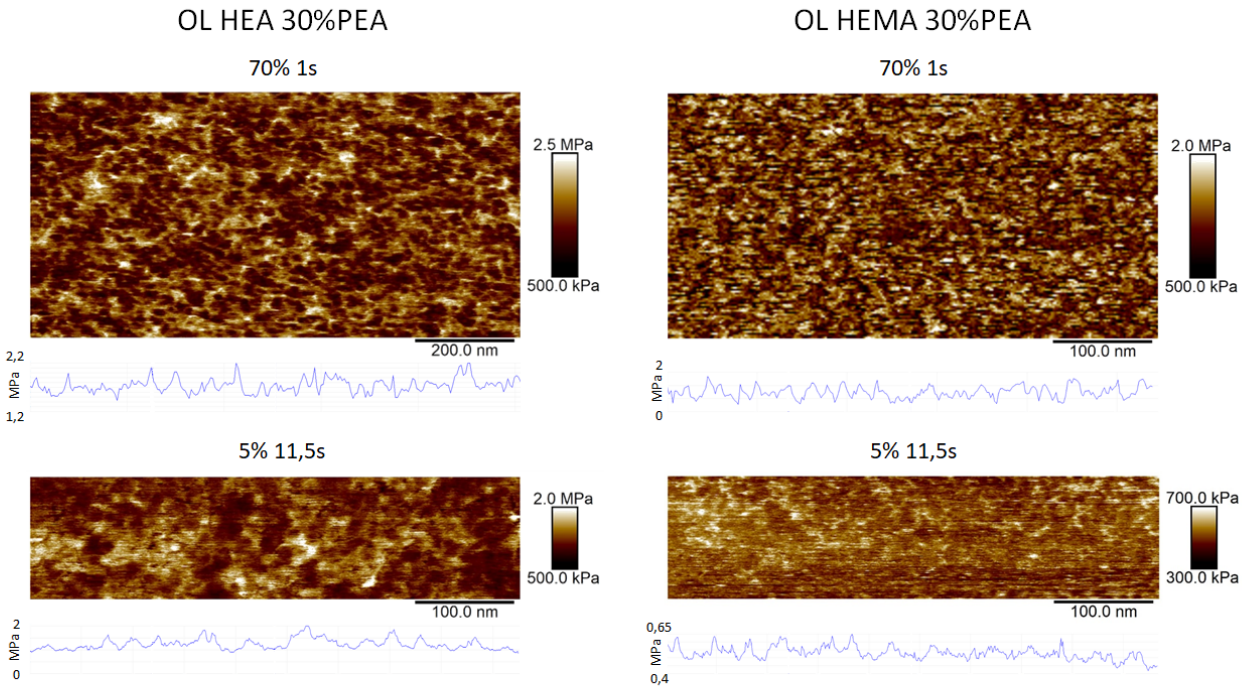

(A) Networks based on PEA formulations

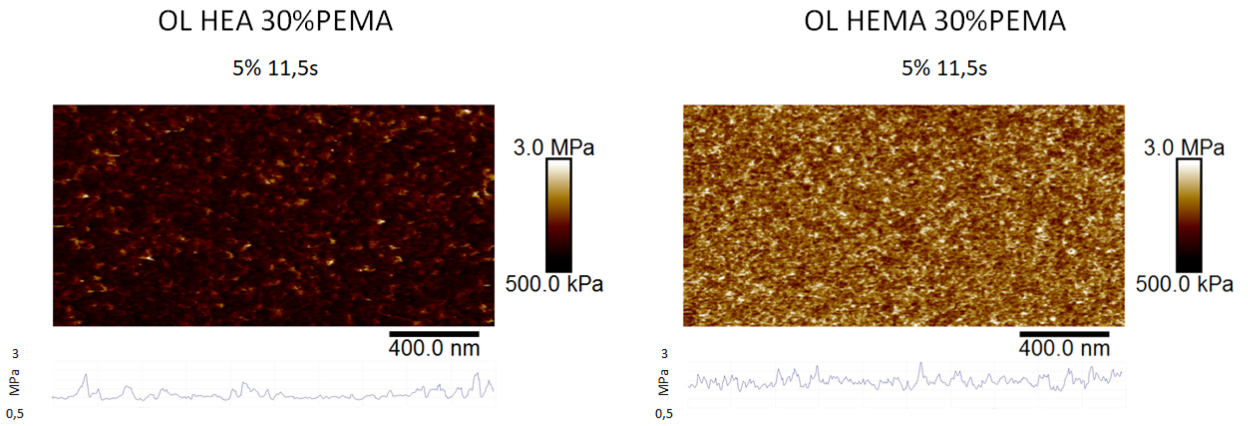

(B) Networks based on PEMA formulations

FIGURE 2.16: Modulus measurement by AFM - Effect of the oligomer functionalization and polymerisation protocol. All measurements are done by the QNM technique with a set force of 800 pN at 0.5 Hz, 512 points by line on the sample's surfaces. The blue curves correspond to a slice of the modulus diagonally of each image, with the same parameters

In all formulations and for all polymerisation times, there are hard nodules. Considering the PEA incorporation, a longer polymerisation time leads to a bigger homogenization of the PEA. This can also be observed on the spatial modulus evolution along the scanned area in AFM, which is described by the curves underneath each AFM image. The variations for the PEMA formulations are less intense than for the PEA ones. Then, the OL HEMA formulations leads to smaller and seemingly more numerous hard nodules. Finally, when polymerising a methacrylate monomer, the PEMA, the behaviour seems to be very similar to the acrylate. Therefore, we can see that while the differences in reactivity between the PEMA and the PEA lead to different dynamics of network formation, they do not change significantly the micro-structure.

2.4 Take home messages

- The formulations we study here consist of 70%w of a PPG di(meth)acrylate functionalized oligomer (synthesized by DSM, then Covestro) with 30%w of acrylate monomers (EHA and/or PEA) with 1%w of photoinitiator (BAPO). These formulations are a good model for the industrial resins.
- The networks are polymerised by an intense UV light. The effect of the light intensity and the polymerisation time has been investigated and the reference polymerisation protocol leading to the maximum conversion consists of 1s of illumination at 70% lamp power, for a total illumination energy of 1 J/cm^2. Polymer films of thickness from 50 μm to 800 μm can be polymerised with no issue of conversion gradient in the thickness.
- The network formation in our polymerisation process is highly dependant on the chemical function of the monomer. When using methacrylate monomers instead of acrylate ones, the highest light intensities (and shorter illumination times) do not lead to the formation of a network.
- The formulation containing 30% PEA presented a microstructure that was investigated with AFM measurements. The hard nodules observed are attributed to PEA rich zones in a softer matrix made mostly from the oligomer.

Chapter 3

Mechanical properties

In Chapter 2, the building blocks of the networks were described. All networks are chemically crosslinked PPG oligomers and acrylate chains. Based on the polymerisation protocols (high UV energy, short time), the chain length between crosslinks is polydisperse and there is a high probability of looping or dangling chains in the network. This chapter aims at characterizing the mechanical properties of such networks and at investigating their differences based on the chemical formulation.

3.1 Introduction

Everyone has once played with a rubber band. It can deform to several times its initial length without needing a large force, and all the deformation is reversible. This behaviour of elastomeric networks is very interesting and differs from metals and ceramics, as described on Figure 3.1. This difference of mechanical behaviour is due to the structure of the different networks and the mobility of their chemical and physical bonds. Brittle materials can show no significant network deformation, leading to the breaking of the material at small elongations. In the case of ductile materials, movements are allowed in the ordered structure by the motion of dislocations to respond to the deformation, but this new order leads to an irreversible deformation of the material once the stress is released. Rubbers show a more complex behaviour, because they can endure large reversible deformations without bond breakage.

3.1.1 Molecular interpretation of the non-linear elasticity

To better understand polymer physics and the link between molecular physics and bulk behaviour, the study of the book "Polymer Physics" from Rubinstein and Colby is recommended [55]. The discussion in this part is inspired from their study.

Let's consider a polymer chain of N monomers of a length a in a stress-free state. This polymer chain can take several configurations that depend on the interactions between monomers and on the general stiffness of the backbone. In the ideal state, there are no interactions and the chain follows a random walk. The probability that the chain has an end-to-end vector of $\vec{R}$ follows a Gaussian function with a most probable square end-to-end distance of $R_0^2 = N_{C-C} l_{C-C}^2$ with N_{C-C} the number of Carbon-Carbon bonds and l_{C-C} the bond length. A chain in that state is called a Gaussian chain. In the case of a chemical network, the polymer chains are irreversibly linked together at crosslinking points. It is also necessary to implement the fact that monomers interact with each other and that the chains are not in a pure ideal conformation. The constraints on the random walk are described by a structure factor C_∞, and the value of R_0 becomes:

$$R_0 = \sqrt{C_\infty N_{C-C}} l_{C-C} \tag{3.1}$$

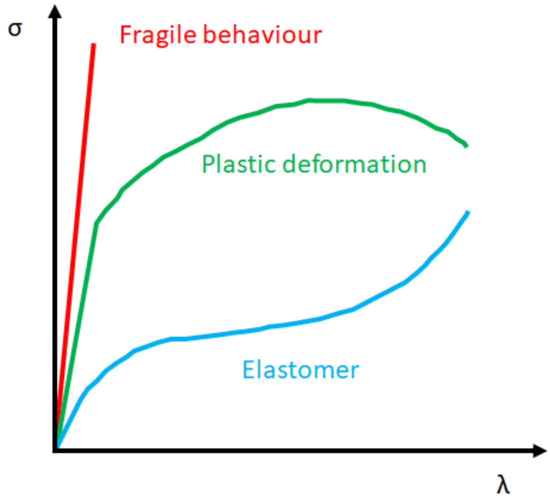

FIGURE 3.1: Difference in mechanical response of model materials. Fragile materials, such as ceramics have a high elastic modulus but low deformation at break. Ductile materials, such as metals or semi-crystalline polymers, present a plastic behaviour: they endure bigger deformations but past a threshold, the deformation will not be completely recovered. Rubbers have an elastomeric behaviour showing a strain softening and strain hardening behaviour, and can withstand deformations of several hundreds %.

The value of C_∞ varies for each polymer depending on the stiffness and the possible interactions (steric hindrance, H-H bonds, ...) between the side chains. It is greater than 1, showing that the behaviour deviates from the random walk and increases the size of the random coil. The easiest description of the mechanics of such a network is to consider that all the elastic strands between the crosslinks behave as gaussian chains. This is the affine model, as described on Figure 3.2 (A). In this model, the crosslinking points are assumed to be fixed in space, directly linking the elastic chain to a fictitious homogeneous elastic background. The macroscopic deformation applied on the block of rubber is directly transmitted to each of the elastic strands, so each strand has the same deformation equal to the macroscopic deformation. The material is also assumed incompressible (for elastomers) and isotropic.

Let's consider a block of rubber of initial dimensions L_{x0}, L_{y0} and L_{z0}. Under deformation, it will deform to the new dimensions L_x, L_y and L_z. The stretches describing these deformations are called λ: $\lambda_i = L_i/L_{i0}$. When the block is under deformations of λ_x, λ_y and λ_z in each of the 3 space directions, the incompressibility implies that:

$$V_0 = L_{x0}.L_{z0}.L_{z0} = V = L_x.L_z.L_z = \lambda_x L_{x0}.\lambda_y L_{z0}.\lambda_z L_{z0} \Rightarrow \lambda_x \lambda_y \lambda_z = 1 \tag{3.2}$$

In an uniaxial stress state, the stress on the x axis is computed as the ratio of the force f_x divided by the perpendicular area, either in the deformed state, leading to the true stress $\sigma_{T,x}$, or in the undeformed state, leading to the nominal stress $\sigma_{N,x}$:

$$\begin{aligned} \sigma_{N,x} &= \frac{f_x}{L_{y,0}L_{z,0}} \\ \sigma_{T,x} &= \frac{f_x}{L_y L_z} = \frac{f_x}{\lambda_y \lambda_z L_{y,0} L_{z,0}} = \lambda_x \sigma_{N,x} \end{aligned} \tag{3.3}$$

In the affine model, the free energy of the network can be computed from the sum of the free energy of each of the n elastic strands forming the network, and the force applied in each direction

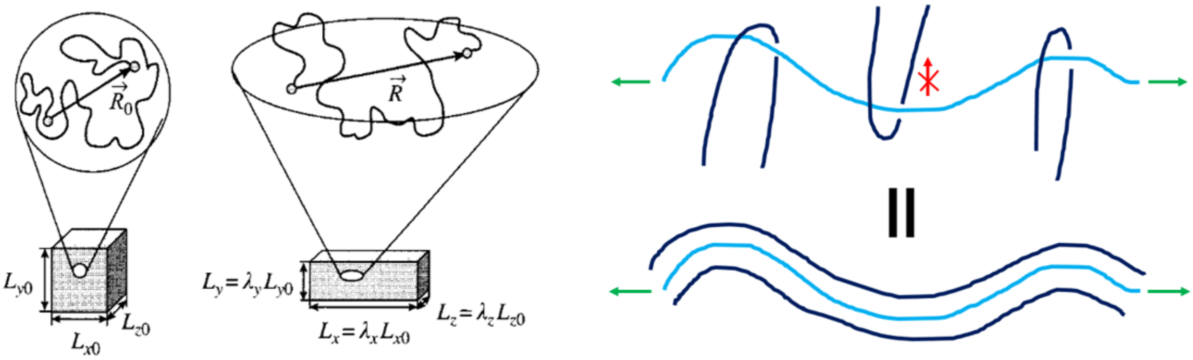

(A) Affine model - Deformation of a network

(B) Entanglements description by the Edwards tube model

FIGURE 3.2: Affine model of deformation and schematics of entanglements. (A) In the affine model, the macroscopic deformations applied on a block of rubber is the same as the microscopic deformation applied on each elastic chain, and the crosslinks are fixed in space [55]. (B) When a polymer chain is entangled with other chains, it restricts its movements in the normal direction, as described by the red arrows. The dynamics of this polymer chain can be described as flowing through a tube (Edwards tube model [62])

is the derivative of the free energy:

$$\begin{aligned}
\Delta F_{network} &= \frac{nkT}{2}(\lambda_x^2+\lambda_y^2+\lambda_z^2-3) \\
f_x &= \frac{\partial \Delta F_{network}}{\partial x} = \frac{\partial \Delta F_{network}}{\partial \lambda_x L_{x,0}} = \frac{nkT}{2L_{x,0}}\frac{\partial(\lambda_x^2+\lambda_y^2+\lambda_z^2-3)}{\partial \lambda_x} \\
\sigma_{N,x} &= \frac{f_x}{L_{y,0}L_{z,0}} = \frac{nkT}{2V}\frac{\partial(\lambda_x^2+\lambda_y^2+\lambda_z^2-3)}{\partial \lambda_x}
\end{aligned} \tag{3.4}$$

The isotropy and incompressibility of the material leads to a direct relationship between the stretches in all directions:

$$\begin{aligned}
\lambda_x &= \frac{1}{\lambda_y\lambda_z} = \lambda \Rightarrow \lambda_y = \lambda_z = \frac{1}{\sqrt{\lambda}} \\
\sigma_N &= \frac{nkT}{V}(\lambda - \frac{1}{\lambda^2}) = \nu kT(\lambda - \frac{1}{\lambda^2})
\end{aligned} \tag{3.5}$$

When the sample is elongated, the polymer chains unfold and extend in the stress direction. This has an entropic cost, as the number of configurations that the polymer chain can take decreases as the end-to-end vector becomes larger, this is why the stress increases with the deformation.

This non-linear elasticity is however not the only reason for the strain softening. In the case of long polymer chains, entanglements can occur in between polymer chains. The entanglements restrict the motion of the polymer chains as described on Figure 3.2 (B): the chain can only slip through the other polymer chains to free itself. At small deformations, the entanglements act as additional crosslinking points. At larger deformations, the chains unfold and flow. The entanglements will move and align in the direction of the stress, leading to strain softening, as the number of effective crosslinks decreases. In the case of a crosslinked network, the chain flow is limited, so the remaining crosslinks at infinitely large strain represent the chemical crosslinking of the networks and the trapped entanglements. This description is considering the non-dissipative softening. However, softening can also be observed at constant strain over time. This is due to the relaxation of dangling chains (attached only to one end), that leads to energy dissipation.

Finally, when the block of rubber is at very high deformations, some of the polymer chains will be stretched close to their maximum extensibility. The cost for further extension becomes enthalpic as it means pulling on the chemical bonds of the polymer backbone. This will happen for chains that are already pre-stretched or very short. In uniaxial traction, it is highly unlikely that the majority of the chains are brought to this extreme extension. However, the statistical description of the entropy of a single chain leaves the Gaussian approximation at intermediate stretches to increase dramatically [63]. The strain hardening comes from the non linearity of the entropy with the extension, following a Langevin function.

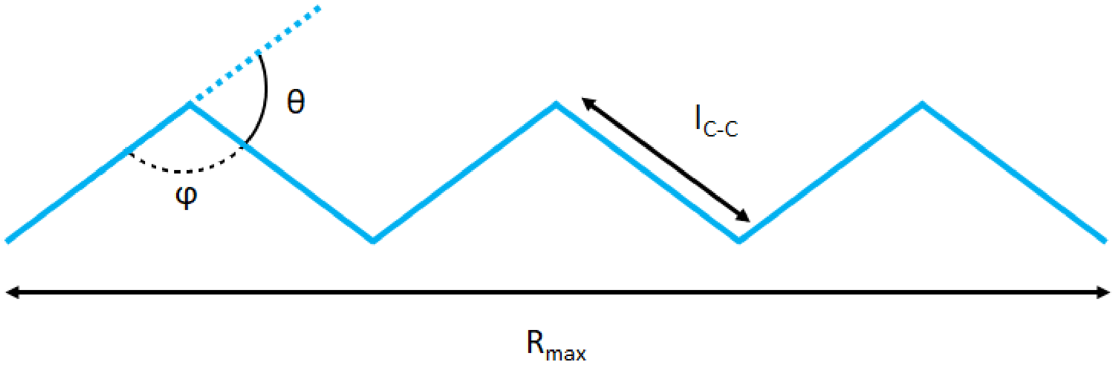

FIGURE 3.3: Maximal extension of a polymer chain with fixed valence angle φ between the C-C bonds

The maximum extension of the polymer chains can be computed by knowing the number of monomers between crosslinks N_x and the length of a monomer. In the case of an acrylate chain, each monomer contribution to the polymer backbone is 2 Carbon-Carbon bonds, hence $N_{C-C} = 2N$. The carbon bonds in such polymer backbones have a valence angle of $\varphi = 109.5°$. As described on Figure 3.3, the maximum length of a polymer chain is:

$$R_{max} = cos(\frac{\theta}{2})N_{C-C}l_{C-C} = cos(\frac{\pi-\varphi}{2})2Nl_{C-C} \tag{3.6}$$

When combining equations 3.1 and 3.6, the theoretical maximum extension of the polymer chain can be computed:

$$\lambda_{max} = \frac{R_{max}}{R_0} = \frac{cos(\frac{\pi-\varphi}{2})2Nl_{C-C}}{\sqrt{C_\infty 2N}l_{C-C}} = cos(\frac{\pi-\varphi}{2})\sqrt{\frac{2N}{C_\infty}} \simeq 0.82\sqrt{\frac{2N}{C_\infty}} \tag{3.7}$$

3.1.2 Modelling the non-linear elasticity

While the mechanics of the polymer network can be explained with the molecular behaviour to some extent, global models have been developed to describe the non-linear elasticity. Let's take now a step back and consider the polymer network from a continuum mechanics point of view. Three strain invariants can be defined:

$$\begin{aligned} I_1 &= \lambda_1^2 + \lambda_2^2 + \lambda_3^2 \\ I_2 &= \lambda_1^2\lambda_2^2 + \lambda_2^2\lambda_3^2 + \lambda_3^2\lambda_1^2 \\ I_3 &= \lambda_1^2\lambda_2^2\lambda_3^2 \end{aligned} \tag{3.8}$$

As already mentioned, the incompressibility of elastomers means that the volume is conserved at all times, therefore $I_3 = 1$. We will define $J_i = I_i - 3$ (i = 1 or 2) to insure a 0 strain in the undeformed state.

3.1.2.1 Strain energy density function: W

The strain energy density W defines the energy stored in the material when it is put under deformations: $W = f(\lambda_1, \lambda_2, \lambda_3) = f(J_1, J_2)$. It was observed that in many cases, $\frac{\partial W}{\partial J_2} << \frac{\partial W}{\partial J_1}$ [64], so we will consider strain energy densities that only include J_1. The simplest model to describe an unfilled rubber is the Neo-Hookean model. It is directly linked to the statistical elasticity model (see equation 3.5).

$$W_{NH} = \frac{E}{6} J_1 \tag{3.9}$$

where E is the Young's modulus. It only describes the elasticity at small strains, as it does not take the strain hardening into account. An addition to this model was proposed by Gent [65]:

$$W_{Gent} = -\frac{E}{6} J_m \ln\left(1 - \frac{J_1}{J_m}\right) \tag{3.10}$$

This model adds a term that describes a strain stiffening behavior, physically related to the finite extensibility of the polymer chains: J_m. It has the advantage of linking the strain energy to material properties, but it is harder to use in modelling as it diverges for $J_1 = J_m$. Yeoh proposed a 3^{rd} degree polynomial model that can include both the strain softening and strain hardening without leading to a divergence [66]:

$$W_{Yeoh} = C_1 J_1 + C_2 J_1^2 + C_3 J_1^3 \tag{3.11}$$

One small draw back of this function is that while C_1 is linked to the Young's modulus, there is no direct identification of C_2 and C_3 to material properties. They both act as fitting parameters of the softening and stiffening with strain.

3.1.2.2 Stress computation

The computation of the stress from W depends on the symmetry of the deformation applied on the polymer. The general expression for the true stresses is [65]:

$$\begin{aligned} \sigma_{T,x} &= \lambda_x \frac{\partial W}{\partial J_1} \frac{\partial J_1}{\partial \lambda_x} + p \\ \sigma_{T,y} &= \lambda_y \frac{\partial W}{\partial J_1} \frac{\partial J_1}{\partial \lambda_y} + p \\ \sigma_{T,z} &= \lambda_z \frac{\partial W}{\partial J_1} \frac{\partial J_1}{\partial \lambda_z} + p \end{aligned} \tag{3.12}$$

where p is an undefined hydrostatic pressure. In the case of an incompressible material, the pressure does not work so it has to be determined from the boundary conditions. As shown before, in a **unixial tension** test in the x direction, $\sigma_{T,y} = \sigma_{T,z} = 0$ and the relation between the stretches is described in equation 3.5 and leads to:

$$\begin{aligned} J_{1,uni} &= \lambda_x^2 + \lambda_y^2 + \lambda_z^2 - 3 = \lambda^2 + \frac{2}{\lambda} - 3 \\ \sigma_{T,uni} &= \lambda \left(\frac{\partial W}{\partial J_1}\right) \left(\frac{\partial J_1}{\partial \lambda}\right) = \left(\frac{\partial W}{\partial J_1}\right) (\lambda^2 - \frac{1}{\lambda}) \end{aligned} \tag{3.13}$$

When testing a polymer sheet **biaxially**, the computation needs to take into account λ_x and λ_y. In a case of non uniform stretching, the rectangular sheet shown on Figure 3.4 (A) is stretched with different ratios in the x and y directions. In this case:

$$\begin{aligned} \lambda_x\lambda_y\lambda_z = 1 \Rightarrow \lambda_z = \frac{1}{\lambda_x\lambda_y} \\ J_{1,bi} = \lambda_x^2 + \lambda_y^2 + \lambda_z^2 - 3 = \lambda_x^2 + \lambda_y^2 + \frac{1}{\lambda_x^2\lambda_y^2} - 3 \end{aligned} \tag{3.14}$$

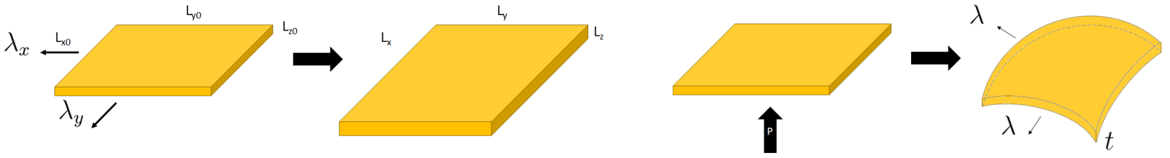

(A) Biaxial stretching of a polymer sheet

(B) Equibiaxial stretching of a membrane by inflation

FIGURE 3.4: Biaxial testing of a polymer sheet. (A) In plane stretching of a polymer sheet: different ratios of deformations in the x and y directions can be obtained. (B) Bulge inflation of a polymer sheet: at the pole of the bulge the stretches are equal.

The stress computation leads to:

$$\begin{aligned} \frac{\partial J_1}{\partial \lambda_x} = 2\lambda_x - \frac{2}{\lambda_x^2\lambda_y^2} \Rightarrow \sigma_{T,x} = 2\left(\frac{\partial W}{\partial J_1}\right)\left(\lambda_x^2 - \frac{1}{\lambda_x^2\lambda_y^2}\right) \\ \frac{\partial J_1}{\partial \lambda_y} = 2\lambda_y - \frac{2}{\lambda_x^2\lambda_y^2} \Rightarrow \sigma_{T,y} = 2\left(\frac{\partial W}{\partial J_1}\right)\left(\lambda_y^2 - \frac{1}{\lambda_x^2\lambda_y^2}\right) \end{aligned} \tag{3.15}$$

In the special case of an equibiaxial stretching, $\lambda_x = \lambda_y = \lambda$, equation 3.15 simplifies into:

$$\begin{aligned} J_{1,bi} = 2\lambda^2 + \frac{1}{\lambda^4} - 3 \\ \sigma_T = 2\left(\frac{\partial W}{\partial J_1}\right)\left(\lambda^2 - \frac{1}{\lambda^4}\right) \end{aligned} \tag{3.16}$$

Based on the stress computation with the Neo-Hookean strain energy density and the statistical elasticity model, we can deduce that:

$$\sigma_N = \nu kT(\lambda - \frac{1}{\lambda^2}) = \frac{E}{3}(\lambda - \frac{1}{\lambda^2}) \Rightarrow E = 3\nu kT \tag{3.17}$$

In the statistical rubber elasticity model, the Young's modulus is linked with the density of elastic chains in the network and the temperature, linking the elasticity to the entropy of each polymer chain. Normalizing the experimental stress with the Neo-Hookean behaviour will allow the visualisation of the difference between the experimental behaviour and the statistical rubber:

$$\sigma_{R,uni} = \frac{\sigma_{N,uni}}{\lambda - \frac{1}{\lambda^2}} \; and \; \sigma_{R,bi} = \frac{\sigma_{N,bi}}{\lambda - \frac{1}{\lambda^5}} \tag{3.18}$$

This expression is also called the Mooney stress. This analysis of the reduced stress leads to Mooney plots where the strain softening and hardening are easier to visualize, as described on Figure 3.5.

Model	$\sigma_{T,uni}$	$\sigma_{T,equibiaxial}$
Neo-Hookean	$\frac{E}{3}\left(\lambda^2-\frac{1}{\lambda}\right)$	$\frac{E}{3}\left(\lambda^2-\frac{1}{\lambda^4}\right)$
Gent	$\frac{E}{3}\frac{\lambda^2-\frac{1}{\lambda}}{1-\frac{J_{1,uni}}{J_m}}$	$\frac{E}{3}\frac{\lambda^2-\frac{1}{\lambda^4}}{1-\frac{J_{1,bi}}{J_m}}$
Yeoh	$2\left(C_1+2J_{1,uni}C_2+3C_3J_{1,uni}^2\right)\left(\lambda^2-\frac{1}{\lambda}\right)$	$2\left(C_1+2J_{1,bi}C_2+3C_3J_{1,bi}^2\right)\left(\lambda^2-\frac{1}{\lambda^4}\right)$

TABLE 3.1: True stress expressions for the different strain energy density functions

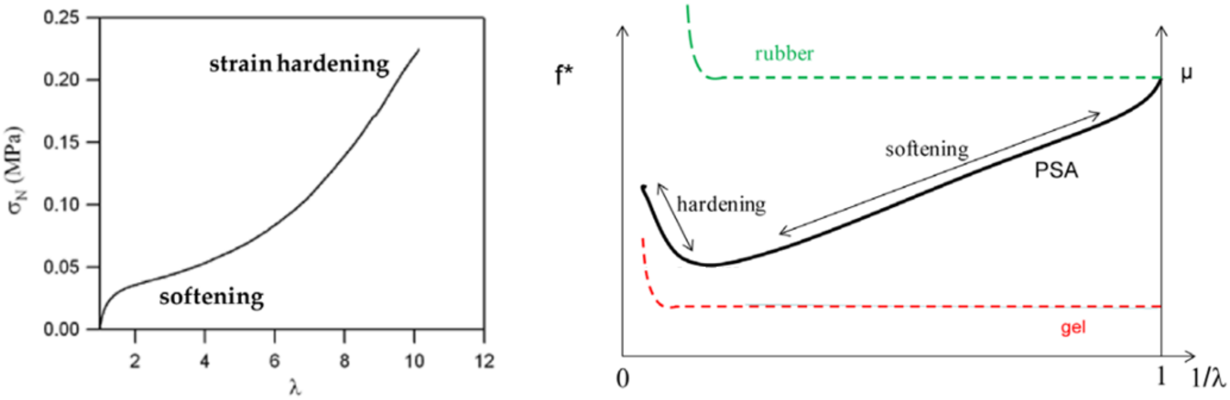

FIGURE 3.5: Mooney plot and critical states of a rubber and a gel - taken from [12]. f* is the Mooney stress. For a pure Neo-Hookean material, the normalization leads to a constant proportional to the Young's modulus until the strain hardening regime is obtained. Any deviation is due to the reversible dissipations of entanglements or irreversible viscoelastic relaxations.

When a polymer network shows more reversible softening than predicted in the Neo-Hookean model, it means that there are a lot of entanglements that can align and slip and as a result reduce the stress during the deformation. Rubinstein and Panyukov proposed a model for the reduced nominal stress in uniaxial tension to compute the relative contributions of the entanglements and crosslinks to the stress [67]:

$$\sigma_{R,uni} = \mu_x + \frac{\mu_e}{0.74\lambda + 0.61\lambda^{-1/2} - 0.35} \tag{3.19}$$

where $\mu_e = E_e/3$ is the contribution due to the entanglements and $\mu_x = E_x/3$ the contribution due to the crosslinks to the stress. This theoretical model was derived based on the "slip-tube model" description of the entanglements. This model builds upon the descriptions of the chain behaviour from the affine model [68], the phantom model [69] and Edwards' tube description of the entanglements [62]. It is a mean field model based on the description of one chain towards the "elastic background". In the affine model, all elastic chains are considered fixed towards the background, while the phantom network model adds a degree of freedom to the crosslinking points. The Edwards tube model (see Figure 3.2 (B)) considers the entanglements that restrain the movements of the elastic chain as a continuum potential along the whole chain, which can also be theorized as virtual chains linking the chain to the background. The resulting potential fluctuates with the deformations of the network: within the idea of softening by movements and rearrangements of the entanglements in the stress direction, the virtual chains are allowed to slip along the elastic chain. They are only restricted to the non overlapping conditions, as entanglements can not slide past each other. This is the description of the slip tube model, as described on Figure 3.6.

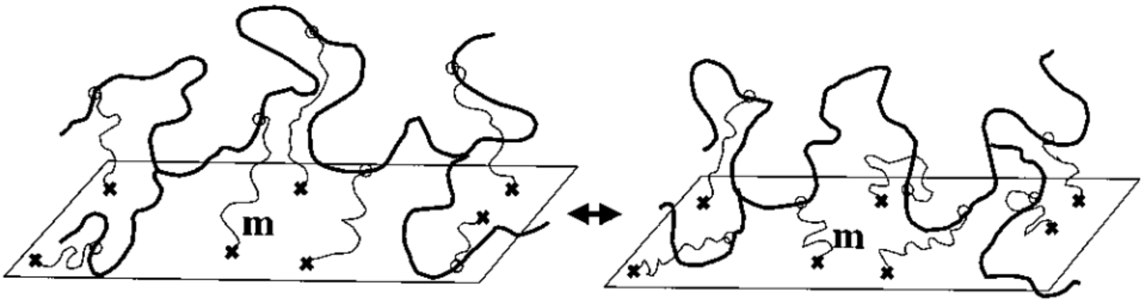

FIGURE 3.6: Slip tube model - Rubinstein and Panyukov. The confining potential acting on the network chain is represented by virtual chains attached to the elastic nonfluctuating background at one end and ending with slip-links at the other (represented as a loop around the elastic chain). These slip-links can slide along the network chain, but cannot pass through each other - taken from [67].

It is important to remember that this model considers all the chains to behave in the same way, with the same type of interactions with each other, as the elastic background is in fact other elastic chains that also deform. This also does not take any time dependant dissipation into account. Rubinstein and Panyukov's model showed good agreement with experimental data from homogeneous elastomeric networks ([61], [70]).

3.1.3 Testing elastomers under large strain deformations

Let's now look more closely at the practical ways of testing the mechanical properties of soft elastomers. The biggest challenge about testing soft and thin films of polymers is achieving clamping conditions that will ensure a good grip on the sample to avoid slippage without breaking it. The uniaxial tensile test is widely used for elastomers, the only requirement for a good testing is to ensure a homogeneous thickness throughout the tested sample. The cutting step in the sample making is crucial: based on the quality of the punch, it may lead to defects at the border of the sample that may lead to fracture at intermediate strains, making the study of the whole non-linear behaviour impossible.

In order to improve the testing of elastomers to study their behaviours at higher deformations, the bulge inflation test can be used. A polymer sheet is clamped either in between metal circles or with rubber bands in an inflation device, and the profile of the bubble is followed as the inflation pressure (or the injected fluid volume) increases. Treloar described the inflation of a vulcanized latex and followed the contour of the polymer bulge by marking the surface of the tested polymer [71]. Knowing the initial length in between each mark, he could compute the local stretches of the whole bulge in both the meridional and the longitudinal direction for different pressures by measuring the deformed length as the arc between the marked points.

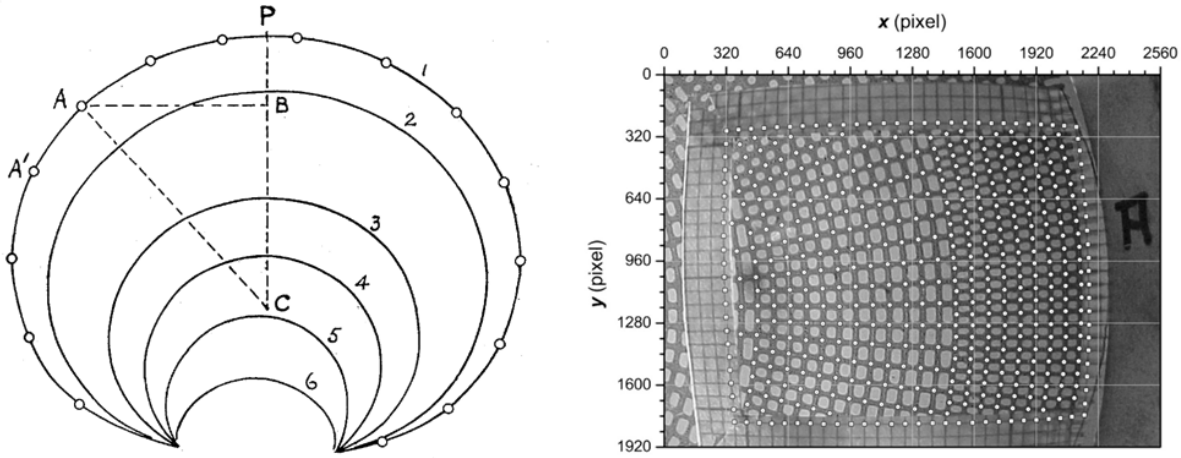

(A) Treloar inflation test - longitudinal sections of inflated sheets [71]

(B) Mott inflation test - photograph of inflated sheet to 26% biaxial strain at the pole [72]

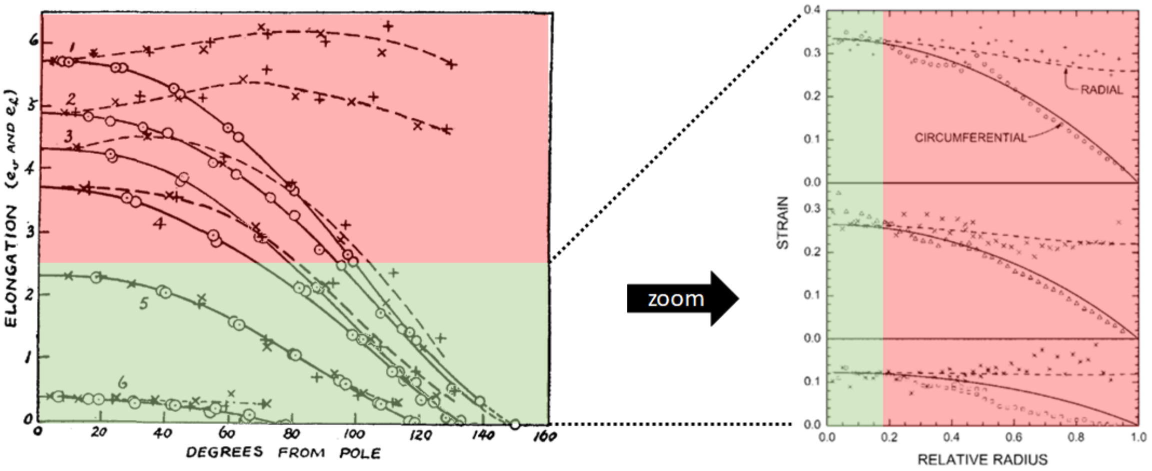

(C) Longitudinal (dotted line) and latitudinal (full line) strains computations from Treloar's experiment (left) and Mott's experiment (right).

FIGURE 3.7: Strains distribution over the bulge contour in inflation test. (A) Inflation of vulcanized latex sheets. Circles were drawn on the flat surface, the white dots on the drawn contours represent the position of these circles in the deformed state in the plane of observation. (B) Inflation of deproteinized natural rubber. A pattern of dots has been stamped on the undeformed sheet, their position is followed during inflation. The white circles on the photograph represent the detected position of the pattern. (C) Resulting strains computations from each method. Treloar assumed the strains to be equibiaxial over the whole bulge for small strains, while a difference in the 2 directions arises at higher inflations. Mott's technique proves more precise for small inflations and shows that even at small deformations, the true equibiaxial strains state is only true at the very vicinity of the bulge's apex.

This study showed that the stretches do not lead to a full biaxial state over the bulge: at high deformations, only the apex of the bulge is stretched in an equibiaxial state, while the polymer near the clamps is under pure shear. Mott et al. proposed an alternative inflation test with a closer look on the displacement at the apex by measuring the displacement of a pattern stamped on the elastomer [72]. This computation led to the left plot on Figure 3.7 (C), which acts as a zoom of the data from Treloar. It appears that even at small inflations, there is a deviation of the 2 stretches over the bulge, meaning that for every state of inflation, the true equibiaxial stretch can only be measured over the apex of the bulge. Several techniques can be used to measure precisely the stretches, such as a direct thickness measurement of the polymer at the bulge via IR absorption or magnetic force [73], but they all imply a specific set-up that can be more difficult to use. The easy method of arc length measurement over the vicinity of the bulge, such as described by Treloar are quite popular as it requires only a way of marking the polymer and a visualization of the bubble profile.

The Hoop (true) stress in a thin membrane under equibiaxial stretches is computed as:

$$\sigma_T = \frac{PR}{2t} = \frac{PR\lambda^2}{2t_0} = \lambda\sigma_N \tag{3.20}$$

where P is the pressure, R the curvature radius and t the thickness. Due to the incompressibility of the material, equation 3.14 applies, linking t to the initial thickness and the stretch. The curvature radius of the bulge is then needed. Treloar stated that close to the apex of the inflated bulge, the curvature can be assumed as spherical, so a circular fit is enough as long as there are specific distances over which it is done to stay within the spherical assumptions. Jerrams et al. showed that the shape of the whole bubble contour is much better described as an ellipse, especially when the bubble inflates over a critical point: when the bubble height becomes close to the diameter of the inflation orifice [74].

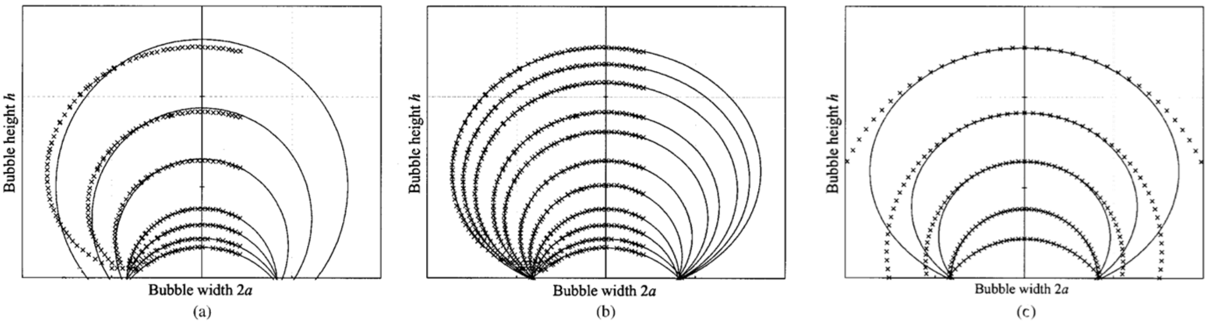

(A) Crosses: experimental contour, (a) approximation to a sphere of the whole contour, (b) approximation of an ellipse, (c) circle of contact at the pole

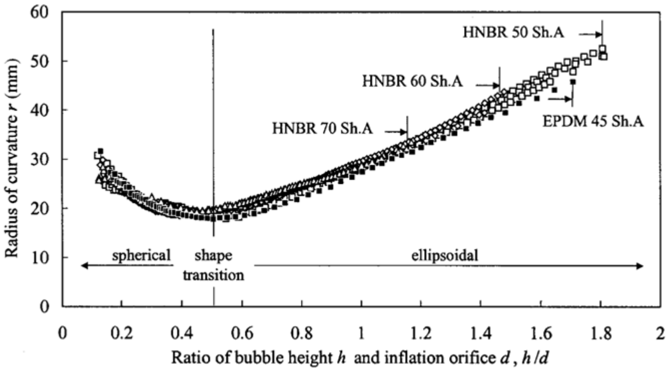

(B) Curvature at the pole evolving from an approximated sphere to a rotation-symmetrical ellipsoid for different materials. HNBR: hydrogenated acrylonitrile–butadiene rubber, EPDM: ethylene–propylenediene rubber

FIGURE 3.8: Shape transition from spherical to ellipsoidal during the inflation - taken from [74]. (A) In order to describe the whole bulge shape, it is necessary to use an ellipse assumption. (B) Investigation of the shape transition between circular and ellipse during the bulge inflation.

In order to compute a realistic radius of curvature, it is therefore necessary to either compute an ellipse trajectory over the whole contour or to make a spherical assumption near the apex. However, as described on Figure 3.8 (A,c), the zone over which the spherical assumption remains relevant varies with the inflation.

As soon as the computation zone is larger than the relevant zone for either the curvature measurement or the stretches measurements, there will be an error. Several studies have investigated the magnitude of the error made depending on the size of the measurement zone for both the stretch and the curvature, by comparing the local biaxial stretch computed by numerical simulation to the results of the spherical assumption. Wang, Fu et al. investigated this error by computing the approximate stress over zones of radius R_s and R_c for the stretch and the curvature respectively in comparison to the initial polymer sheet radius of R_0 [75]. They showed that the error on the true equibiaxial stretch computation is smaller that 5% for $R_s/R_0 < 0.31$. As for the curvature measurement, the error is smaller than 5% for $R_c/R_0 < 0.35$.

Finally, there are cases in which the local curvature and stretch can not be computed, because the bulge is too small for example ([76],[77]). In this case, the mean stretch of the polymer bulge can be computed by assuming that the deformed membrane is the arc of a sphere:

$$\lambda = \frac{\mathcal{L}}{L_0} \tag{3.21}$$

where $\mathcal{L}$ is the length of the arc and L_0 the initial length of the undeformed polymer sheet. By essence, this assumption is false, since it can not describe the biaxial stretches but only approximates the averaged deformation over the whole bulge. The details of the computation are described on Figure 3.9. The approximation made is different whether the bubble diameter is smaller or larger than the half contour of the sphere.

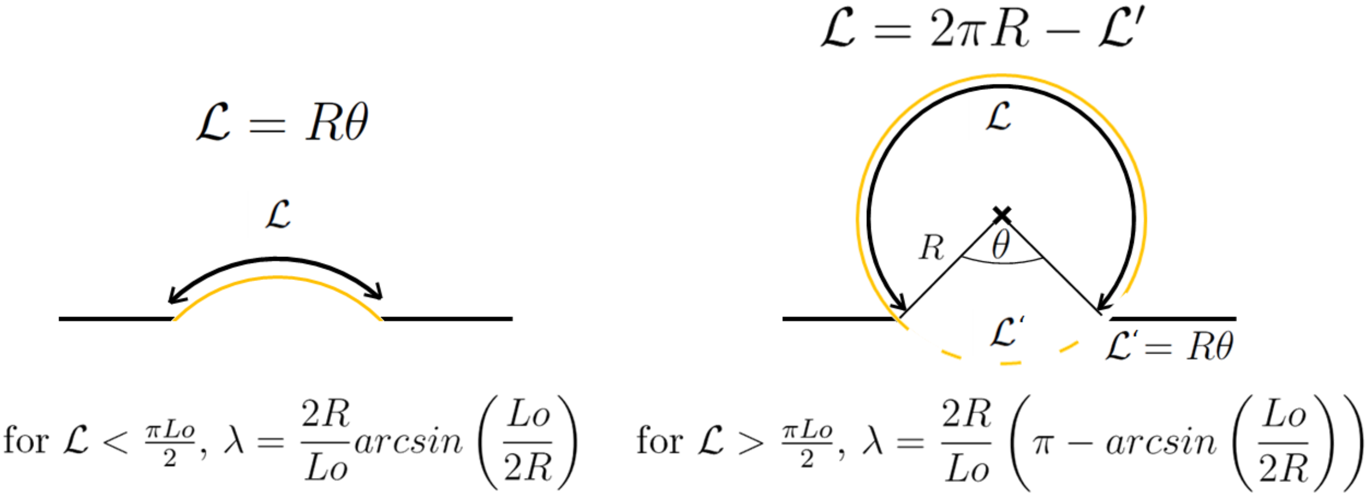

FIGURE 3.9: Contour measurement of the bulge via spherical approximation

3.1.4 Fracture behaviour of elastomers

The fracture study of soft materials is a broad and complex topic. A simplistic picture is the following: in order for the crack to propagate, 2 new surfaces have to be created. This is Griffith's criterion [78] and it works very well for brittle materials, where the cracks are sharp. This criteria is also the basis of Linear Elastic Fracture Mechanics (LEFM). However, soft materials show very different behaviours in fracture, namely the crack propagation can be accompanied by a large degree of blunting.

3.1.4.1 Dissipative mechanisms in fracture

This change of crack shape indicates that a much larger process zone needs to be taken into account when tearing a soft polymer. This process zone is described on Figure 3.10, inspired by Creton's and Cicotti's review on fracture of soft materials [12]. This picture summarizes the different scales at which dissipation occurs in a tearing experiment. When a notched sample is under deformation, the bulk of the polymer deforms homogeneously because of the far field loading. This region only dissipates energy if the material is visco-elastic. At the crack tip, the polymer strands are highly stretched and the crack propagates by breaking chemical bonds. This is the damage zone. At the intermediate scale, various energy dissipation mechanisms can occur. The more dissipation, or the bigger the process zone, the more energy will be needed to propagate the crack, so the higher the tearing energy Γ. Because the process of tearing takes into account all these different types of dissipation, is is not purely a fracture energy. However, as a matter of simplicity, it is often referred as a fracture energy: Γ.

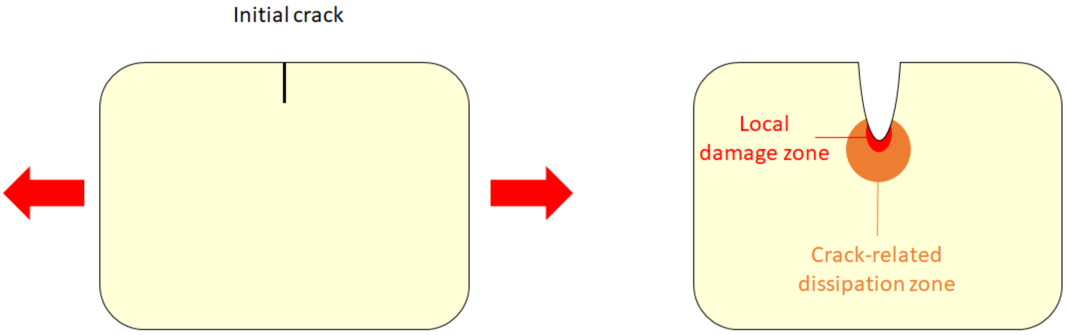

FIGURE 3.10: Stress concentration in a notched sample - taken from [12]. The yellow zone, far from the crack, represents the bulk behaviour reacting to the far field loading, which can lead to a dissipation. Very close to the crack, the polymer is damaged, which leads to the growing of the crack (red zone). The intermediate zone in orange represents the dissipation around the crack tip.

The fact that the fracture energy of soft polymers strongly depends on viscoelastic dissipations implies that the testing conditions such as the temperature and the testing speed will impact the measured value of Γ. It also means that, in conditions where all the viscoelastic dissipation are negligible, the tearing energy should tend towards a threshold. That was observed experimentally by Gent and Ahagon on polybutadiene elastomers at high temperatures and very low tearing rates [79]. This observation corresponds to the idea of a threshold fracture energy of polymers proposed by Lake and Thomas [80]. They propose a computation of the minimal energy needed to propagate a crack, when all viscoelastic dissipation mechanisms are neglected. In this case, the only cost for crack propagation is the rupture of the carbon-carbon bonds of all the chains that are perpendicular to the fracture path. The key hypothesis of the Lake-Thomas model is that in order for the chain to break, it has to reach its maximum extension, leading to an inverse relationship between the fracture energy and the crosslink density of the network:

$$\Gamma_0 = 2N_x U_b \Sigma \tag{3.22}$$

where N_x is the number of monomers between crosslinks, U_b is the energy of a carbon-carbon bond and Σ is the areal density of chains in the fracture plane. In order to add the viscous dissipation to the tearing energy, a simple expression combining the threshold value and the dissipative effects is often proposed ([81],[82]):

$$\Gamma = \Gamma_0 + f(v, T) \tag{3.23}$$

where v is the testing velocity. While it is quite coherent with experimental observations, that do show higher energy of fracture for lower temperatures and higher velocities of testing, it does not completely describe the mechanisms at stake in fracture.

In order to characterize the molecular behaviours in fracture experiments and to decorrelate the viscous dissipations and the fracture events, a detection of bond scission events by mechanophores has been made by Slootman et al [11]. Mecanophores are molecules incorporated and crosslinked in the polymer network that become fluorescent when broken. Through an observation of the broken network by laser scanning confocal microscopy, the density of broken chains and their spatial distribution can be measured.

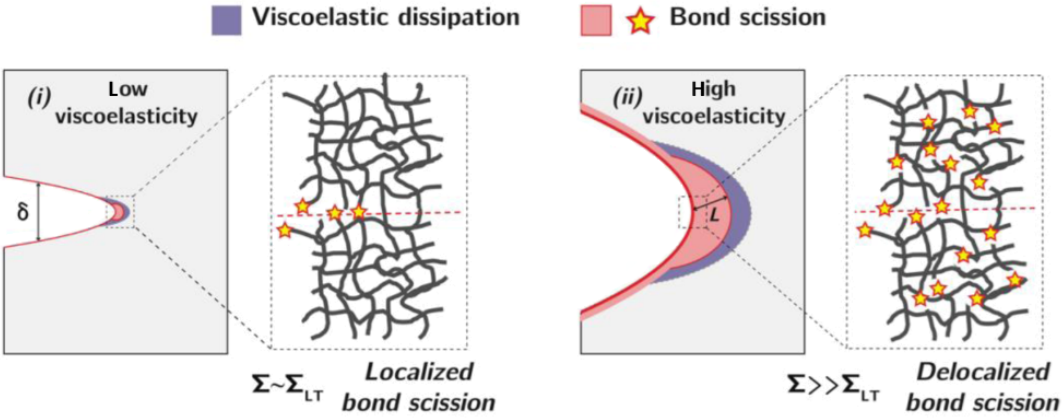

FIGURE 3.11: Schematic coupling between viscoelasticity (in blue) and strand breakage (in red) at crack tip [11]. The zoom shows the localization of bond breakages (yellow stars) in the network. δ is the crack tip opening displacement and L the characteristic spatial extension of bond scission at the crack tip.

This study showed that there is a strong link between the viscous dissipation and the bond breakage. First, depending on the linear viscoelastic behaviour of the elastomer, an increase of crack velocity can increase the viscous dissipation (it is in particular but not only related to E'' dependency with frequency). Then, this increase of dissipation increases the energy needed to propagate the crack which, in turn, causes a larger crack opening. Finally, this causes the zone where bond scission is possible to grow in size.

3.1.4.2 Testing the tearing energy

To measure the tearing energy of polymers, several test geometries can be used, that can lead to constant fracture propagation in simple shear tests, or to uncontrolled fracture, such as the single edge notch test. We will focus on the single edge notch sample tested in uniaxial deformation. The computation of the strain energy release rate in that type of test has been estimated experimentally by Greensmith [83]:

$$G(\lambda) = \frac{6cW(\lambda)}{\sqrt{\lambda}} \tag{3.24}$$

where c is the initial crack size, λ is the stretch and $W(\lambda)$ is the strain energy density computed as the integral of the stress stretch curve of the **un-notched** sample up to λ. The tearing energy Γ is estimated by computing the area until λ_{prop}, the deformation at which the crack begins to propagate. This is determined experimentally by the drop of the stress applied on the notched sample.

3.2 Testing the non-linear elasticity

In Chapter 2, the effect of the polymerisation protocol on the network's formation was investigated. In this chapter, the mechanical properties of the elastomeric networks are tested, so only networks that were polymerized in green conditions will be investigated. For the main part, the focus will be on formulations with 30%w of acrylate monomers EHA and PEA, polymerised with a total energy of 1 J/cm^2 with a lamp protocol of (70% 1s).

3.2.1 Uniaxial tension

3.2.1.1 Testing conditions

Samples in a dumbbell shape are cut from the PE coated polymer sheet with a punch to test them in uniaxial tension. Because the homogeneity of the thickness over the tested sample is crucial, the tensile samples are cut perpendicularly to the spreading direction with the doctor blade. The gauge length is 15 mm and the width 4 mm. The thickness of each sample is measured via a touch probe in the tested region of the dumbbell, and varies between 200 and 800 μm. All experiments are performed on an Instron tensile tester (model 5565) with a 10 N load cell. A video extensometer is used to measure the deformation between 2 white dots that are painted on the samples, approximately 1 cm apart. The samples are fixed in a custom clamp (built in house by the workshop). The sample is held with sand paper to avoid slippage and the clamp is closed with screws fastened at a set torque of 5 cNm. To avoid any pre-stretch, the dumbbells are clamped in a slightly buckled state.

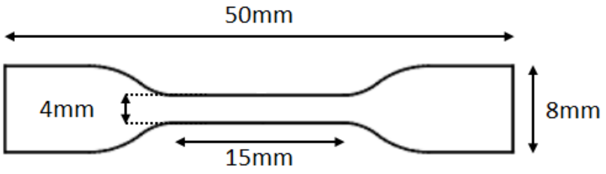

FIGURE 3.12: Schematic of the dumbbells. The shape is designed so that when clamped on the wider parts, the deformation and stress are homogeneous in the thin straight middle part.

For each condition, at least 3 samples are tested so that a mean and a standard deviation can be computed. In standard conditions (and unless written otherwise), the tensile tests are done at a crosshead velocity of 0.1 mm/s, corresponding to an initial stretch rate of 0.67%/s, at room temperature (around 20°C). The raw data consist of the time, the force F, the crosshead displacement and the stretch $\lambda = L/L_0$ where L is the measured distance between the 2 dots at each time and L_0 is the initial measured distance. From this data, the nominal stress is computed by dividing the force by the initial cross section corresponding to the product of the width (w_0) and the thickness (t_0):

$$\sigma_N = \frac{F}{w_0 t_0} \tag{3.25}$$

The stress and strain data are plotted and the initial part of the curve corresponding to the debuckling is discarded. The Young's modulus is then measured by fitting the $\sigma_N = f(\epsilon)$ with $\epsilon = \lambda - 1$ between 0 and 5%, with an affine fit.

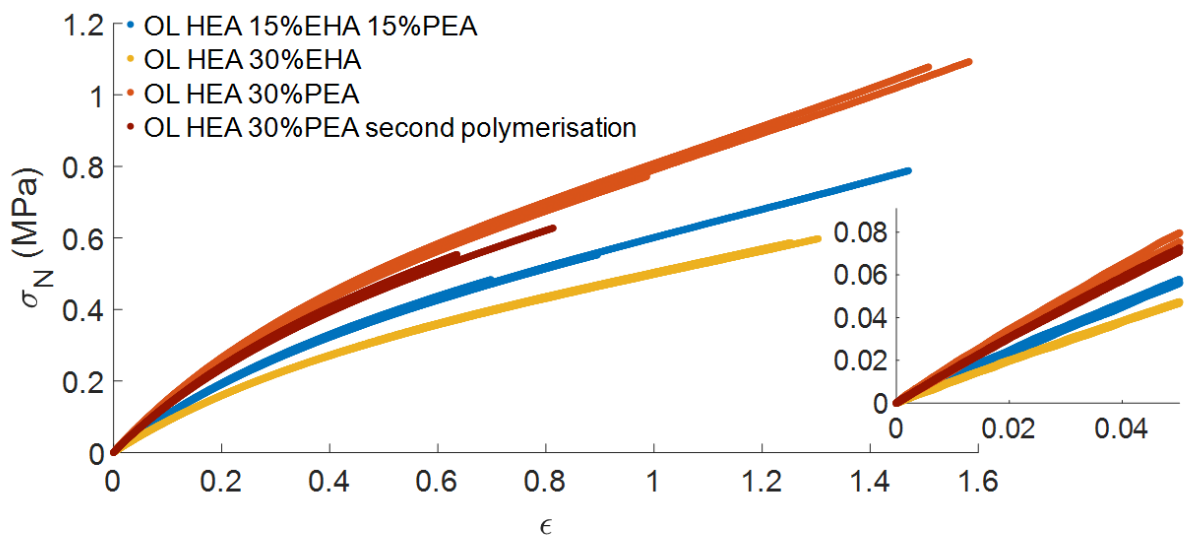

(A) Nominal stress versus strain curves for uniaxial tensile test on different formulations.

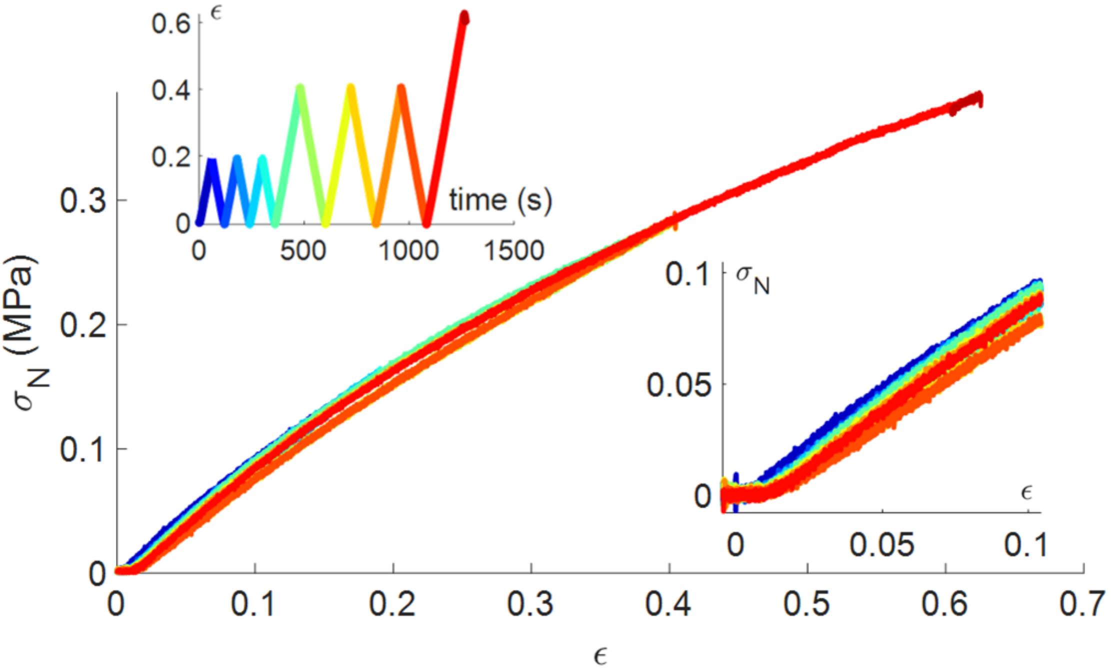

(B) Cyclic behaviour of OL HEA 15% EHA 15% PEA - displacement controlled

FIGURE 3.13: Behaviour in uniaxial traction for the OL HEA formulations - initial stretch rate 0.67%/s. (A) Inter and intra sample variability. The 3 formulations were polymerised and 3 samples were tested. A second sheet of the OL HEA 30% PEA formulation was polymerised on a different day and tested independently. Insert: Zoom on the linear elasticity region. (B) Cyclic testing: Left insert: deformation versus experimental time. Right insert: zoom on the small deformations. 3 cycles up to the same displacement are made.

As can be seen on Figure 3.13, there is a slight difference in the elastic behaviour between samples that were cut from the same polymer sheet and between the different polymerisation events. This can be due to the heterogeneities coming from the flash polymerisation or a flawed determination of the thickness since the polymer sheets are made by spreading a liquid precursor with a doctor blade and may be subject to thickness heterogeneities. But these differences are small compared to the difference in behaviour due to the formulation, making comparisons possible. As can be seen on Figure 3.13 (A), there is only a small error in the linear elasticity domain, leading to only a small error on the determination of the Young's modulus. The maximum deformation obtained in a uniaxial tensile test is around 120%, and varies significantly between samples. It shows that the samples are notch sensitive: the defects while cutting the samples with the punch are large enough so that the strain hardening domain is not accessible. The cyclic testing consist of 3 cycles at the same displacement to test for dissipation and irreversibility. There is almost no hysteresis visible between the different cycles. The main energy dissipation is seen through a small residual strain at the end of the cycle, showing the presence of dissipation mechanisms slower than the testing velocity or a slight slippage in the clamps. The small viscoelasticity present shows that the behaviour of the polymer is mostly hyperelastic.

3.2.1.2 Effect of the formulation on the properties

The Young's modulus of the different networks is computed via a linear fit of the $\sigma_N = f(\epsilon)$ up to 5% deformation for 3 different samples tested under the reference protocol. It was verified that E does not vary significantly with testing velocity (from 0.1 mm/s to 0.5 mm/s) or temperature (from 20°C to 60°C). Since the networks show only softening, it is interesting to represent their behaviour in uniaxial tension in a Mooney plot. The results for all the formulations are presented on Figure 3.14.

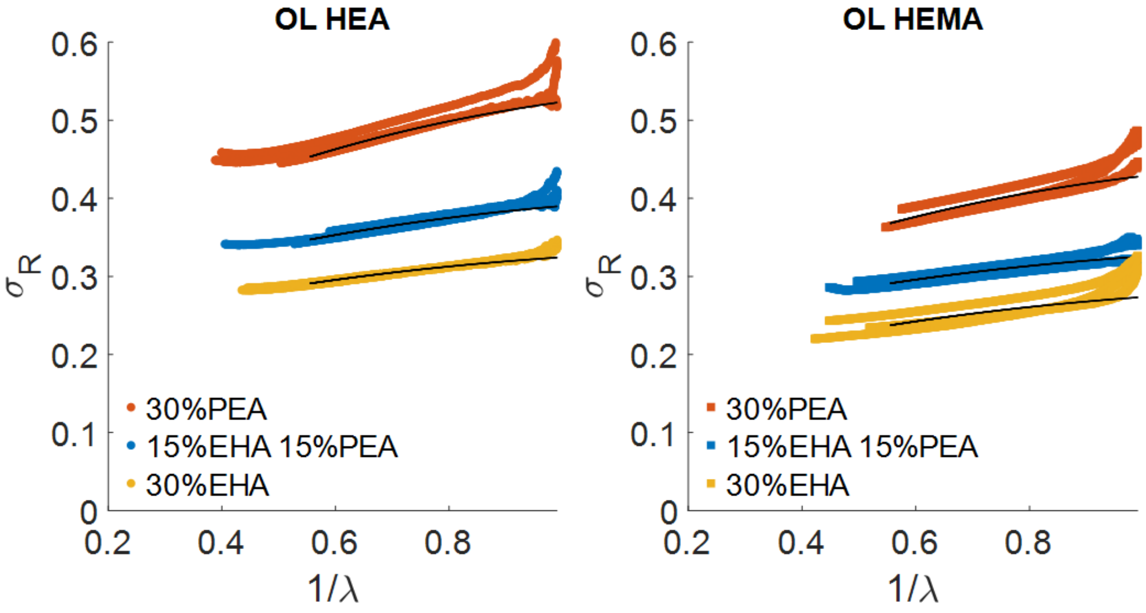

FIGURE 3.14: Mooney plots of the tensile test and Rubinstein and Panyukov fit (black curve, equation: 3.19).

All the formulations based on the acrylate oligomer have a higher Young's modulus compared to formulations based on the methacrylate oligomer, and an increase in PEA content in the formulation increases the modulus. In this representation the strain softening of all formulations is obvious and the onset of strain hardening can be observed, especially for the OL HEA 30% PEA and 15% EHA 15% PEA formulations. Due to small oscillations of the force measurement at small deformations, the behaviour in small strains on the Mooney plot is unreliable. The Rubinstein-Panyukov fit (equation 3.19) is applied to the nominal stress (and not the reduced Mooney stress) to ensure a better fit and only takes the data up to 80% deformation to avoid taking into account the strain hardening regime. The Young's modulus and the results of the Rubinstein-Panyukov fit for all formulations are summarized in Table 3.2. The fit seems to be valid as the moduli reported from the Rubinstein and Panyukov fit are very close to the values measured at small strains. For

Formulation		E (MPa) (tensile test)	E_x (MPa)	E_e (MPa)	$E_x + E_e$
OL HEA	15% 15%	1.156 ± 0.025	0.746 ± 0.017	0.425 ± 0.006	1.171
	30% EHA	0.958 ± 0.007	0.642 ± 0.018	0.332 ± 0.021	0.975
	30% PEA	1.564 ± 0.065	0.877 ± 0.037	0.694 ± 0.035	1.571
OL HEMA	15% 15%	0.967 ± 0.060	0.637 ± 0.015	0.340 ± 0.025	0.978
	30% EHA	0.853 ± 0.023	0.464 ± 0.057	0.357 ± 0.059	0.821
	30% PEA	1.301 ± 0.049	0.689 ± 0.042	0.597 ± 0.022	1.286

TABLE 3.2: Moduli from the tensile test and the Rubinstein and Panyukov modelling

all formulations, there is a significant contribution due to the presence of entanglements in the elasticity: they represent approximately 40% of the elastic modulus. This shows that the average molar mass between crosslink points is larger than the average mass between entanglements. This mass M_e is tabulated and depends on the monomer size and the rigidity and size of its side group:

- PPG8000: M_e = 3000 g/mol [84] $\Rightarrow N_e = 39$
- P(EHA): M_e = 60 000 g/mol [85] $\Rightarrow N_e = 326$

The PEA monomer is rarely studied on its own, it is mostly used as a co-monomer. Therefore, its properties are not well tabulated. However, its monomer molecular mass is close to that of EHA, and its rigidity can be assumed of the same order of magnitude, so we can estimate that their polymerisation behaviour will be close, therefore that their mass between entanglements is the same. This leads to $N_{e,P(PEA)}$ = 312.

Based on the mass of the PPG alone, it was expected to observe some entanglements, as $M_{mol}(PPG) = 2.67 M_e(PPG)$. Given the entanglements contribution, it is also expected that the acrylate chains also entangle. Interestingly, it is for the formulations based on PEA that the entanglements contribution is the highest. This network is also the only one that presents micro-heterogeneities (see Figure 2.11). It could mean that, while the PEA polymerises and crosslinks in those small domains, making hard nodules, the oligomer forming the matrix is more loosely crosslinked, leading to more entanglements.

3.2.2 Biaxial tension

From the tensile data, it is difficult to access the totality of the non-linear behaviour. There is no way to determine the strain hardening because of the sensitivity to cutting defects at the edges of the sample that nucleate macroscopic cracks. To overcome this experimental difficulty and get access to larger deformations, the samples where tested in bulge inflation. All testing where done at the FIBEr laboratory (KU Leuven Core Facility for Biomechanical Experimentation) by Wouter Willekens.

3.2.2.1 Description of the set-up

A sheet of polymer of 3 cm x 3 cm is cut and clamped with a metal ring. The zone inside this circle of L_0 = 2 cm of diameter is the tested area, meaning it will not be influenced by any defects on the cut sides. The inflation test is done by injecting water, the whole set-up is immersed in water to avoid the effect of gravity on the deformation of the bulge. The inflation is volume controlled, increasing cycles of inflations are made with a constant flow rate and steps of 3.5 mL until rupture. For each formulation, 3 samples are tested. The raw data consist of the Pressure P, measured with a sensor in the tank with a precision of 0.2% of the nominal value and the images taken with a camera perpendicular to the bulge, leading to the observation of the bulge contour. The perpendicular view of the set-up does not lead to the complete vision of the polymer bulge as the sample holder is 3 mm thick, as described on Figure 3.15. Hence, for small deformations, the bulge is invisible, and the shape of the bulge contour is always inaccessible.

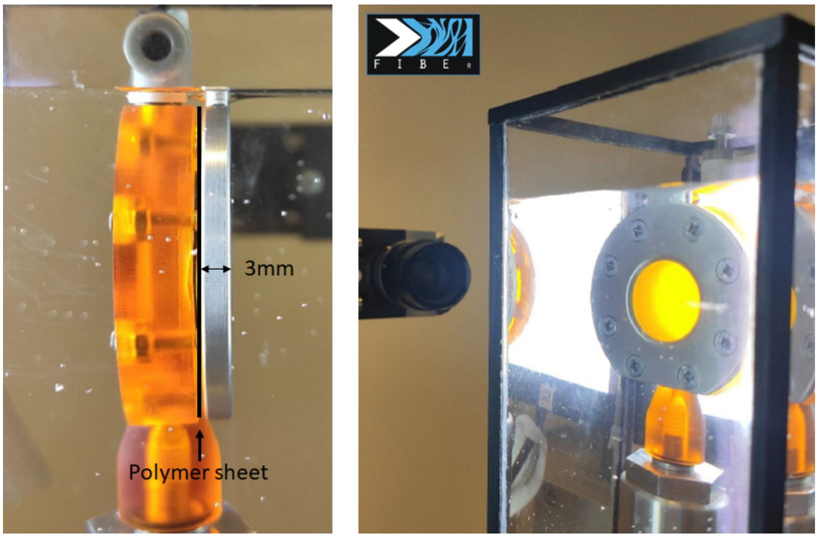

(A) Biaxial inflation set-up

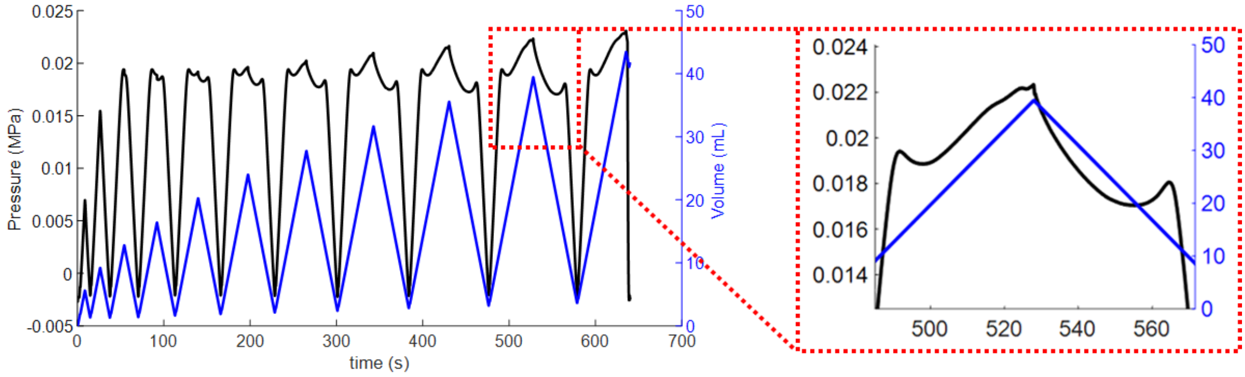

(B) Volume controlled experiment on OL HEMA 30% EHA - until rupture

FIGURE 3.15: Biaxial inflation set-up and volume controlled experiment. (A) The polymer sheet is clamped between the metallic and the plastic part of the set-up, its position is marked by the black line. The contrast of the images is given by a bright light behind the inflation set-up. (B) Injected water volume (in blue) and Pressure (in black) in the inflation of OL HEMA 30% EHA. The experiment is volume controlled, the pressure behaviour is non linear at high volumes of inflation.

From these raw data, the bulge's contour will be extracted from the videos, which will lead to the curvature measurement at each time. The circular curvature will be used for the (mean) stretch computation. The stress computation will rely on the ellipsoidal curvature, the stretch and the pressure. The different computation steps are explained in the following sections.

3.2.2.2 Image analysis - Contour extraction

The contour extraction based on the raw images requires several steps that are made on Image J. First, a black and white threshold is applied on the whole experiment. The image is then cleaned from outliers to erase the signal coming form small air bubbles and dust in the tank. Finally, the contours are extracted by outlining the shape. As can be seen on Figure 3.16 (A), for small deformations, the bulge is invisible, and in the case of big inflations, the bubble overlaps with the reflection of the tank's wall, leading to a loss of these contour points. The computation of the stretch will be hindered, mainly for the small deformations when the bulge barely comes out from the holder, leading to the detection of only a few contour points. The resulting extracted contours can be seen on Figure 3.16 (B) where the detection problems for small deformations (in dark blue) and big deformations (in red) can be observed.

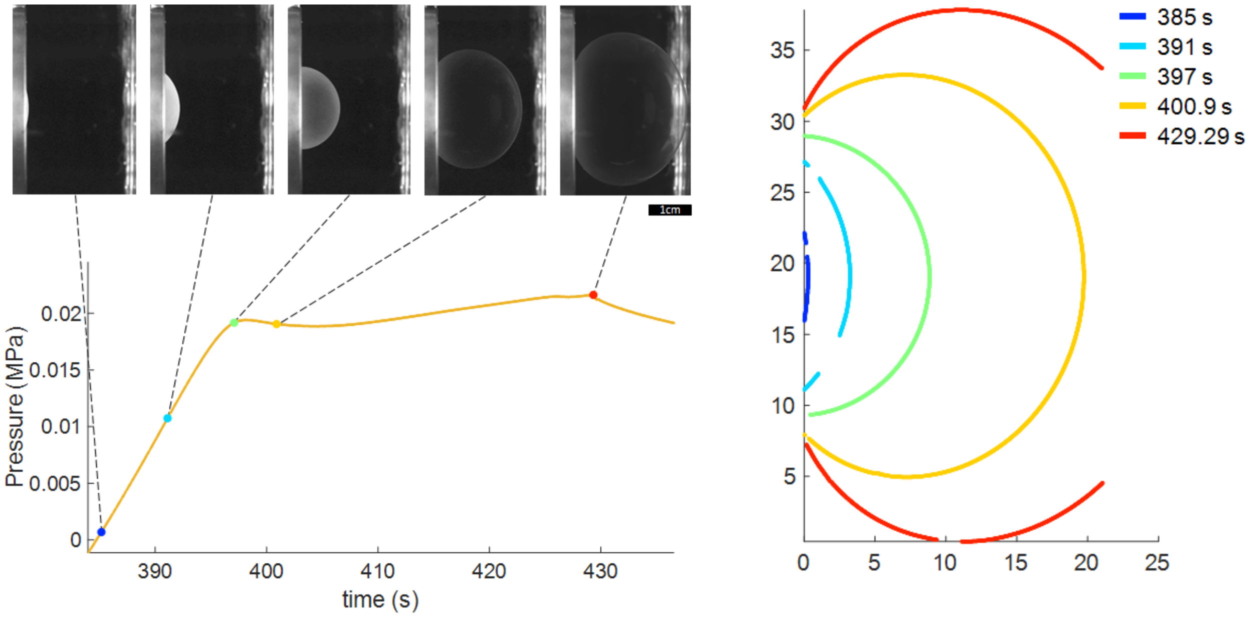

(A) Pressure versus time and corresponding bubble inflations

(B) Extraction of the contours via Image J

FIGURE 3.16: Inflation test of OL HEMA 30% EHA. (A) Inflation of the polymer sheet, Pressure versus time with the corresponding images (scale 1 cm). The pressure increase is not linear with time while the volume increase is. The non linear behaviour starts at the critical inflation of the half sphere state. (B) Extraction of the contours through image analysis. The missing points in some contours represent image detection problems (due to dust, ...) and the largest contour shows the detection problem due to the tank's wall (corresponding to the last picture of (A)).

As was already discussed in Section 3.1.3, the shape of the bulge changes from a spherical shape to an ellipsoidal one, depending on the total deformation. Both fits where applied on the experimental contours, based on the least mean square method. As can be seen on Figure 3.17, corresponding to the study of Jerrams et al. [74], the circular fit describes the experimental contours well for small deformations, while the ellipsoidal fit seems to keep a good agreement with the experimental data up to larger deformations. Even in the case of very large deformations, where the extremity of the contour is lost because of the tank wall, the ellipsoidal fit still gives a good representation of the bubble shape.

From those two approximations, the curvature of the bubble at the apex can be determined. For the circular approximation, it is directly the fitted radius. For the ellipsoidal fit, the radius of curvature at the apex is computed as:

$$R = \frac{a^2}{b} \tag{3.26}$$

where b is the axis of the ellipse in the direction of the bulge inflation and a the axis perpendicular to it.

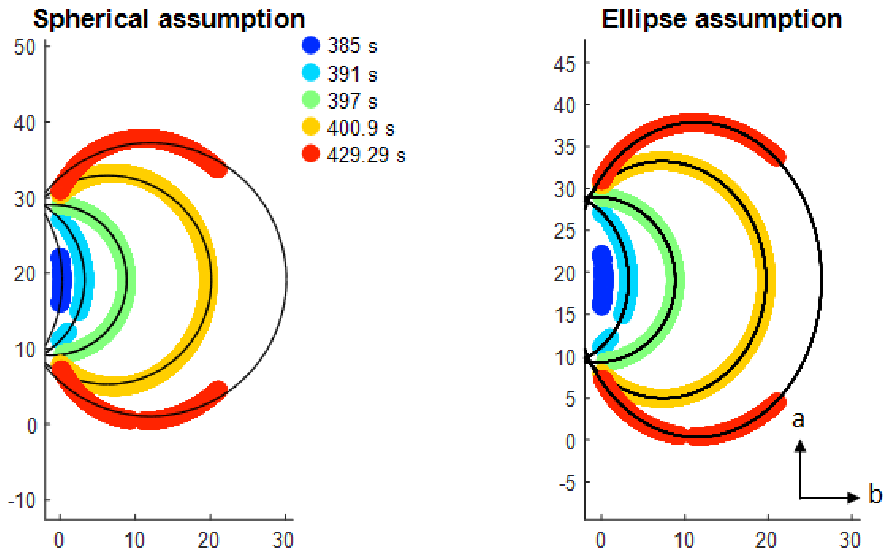

FIGURE 3.17: Comparison of the circular and the ellipse assumption of the bulge inflation. The circular assumption fits well for small deformations but looses the accuracy for the bigger ones. The ellipse fit works well but needs more points than the circular one to work, so the smaller deformations are not well fitted. The fits are based on the least mean square method (Matlab codes: $circfit$ by Andrew Horchler (2022) and $fit\_ellipse$ by Ohad Gal (2022)). The axis a and b are the axis of the ellipse.

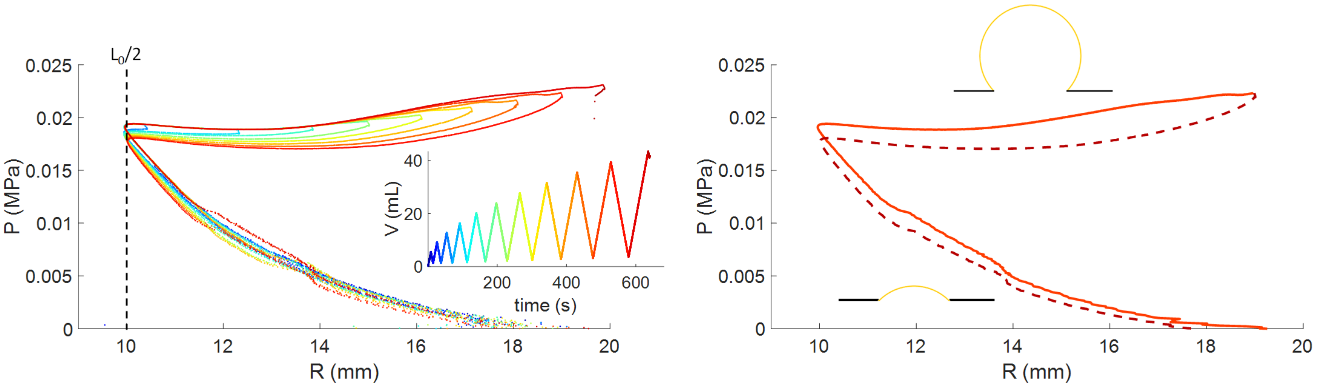

(A) All pressure cycles against the radius

(B) Loading in full line, unloading in broken line

FIGURE 3.18: Pressure behaviour with the curvature radius of the bulge - all cycles (OL HEMA 30% EHA). (A) The radius comes from the spherical fit. Broken line: value of L_0 for the stretch computation. Insert: Volume evolution representing the loading and unloading with time. (B) Last full loading/unloading cycle, the schematics represents the contour's shape in yellow, the sample holder is in black.

In the initial state, the polymer sheet is flat, therefore its radius of curvature is ∞. When the pressure increases, a bulge forms and the curvature is reduced. As can be seen on Figure 3.18, the critical point R = $L_0/2$, when the bulge transitions from under to over the half sphere shape is also the moment when the circular assumption becomes inaccurate. Above the half sphere, the radius of curvature increases again, the bulge is mostly out of the sample holder. This behaviour is qualitatively the same whether the radius plotted is obtained from the circular or the ellipsoidal fit of the profile, the only difference being that the ellipsoidal fit agrees better with the bubble shape, especially for large deformations, so it leads to a greater radius of curvature for the large pressures.

3.2.2.3 Computation of the stretch and stress

In this experiment, there are no marks of any sort on the polymer sheet, so there is no direct determination of the stretch at the pole of the bubble. The region of equibiaxial stresses and stretches is located at the apex and in a close vicinity to it, while due to the substrate constraint, the border of the bulge is subject to shear stresses [72]. However, in our case, the only way to determine a stretch of the bulge is to compute the mean stretch by comparing the total length of the bulge's contour $\mathcal{L}$ and compare it to its initial length L_0. Because of the sample holder's thickness and the possible extraction problem due to the thresholding, it's not possible to extract the actual contour's length from the image analysis. It will therefore be needed to use an approximate value of stretch. The ellipsoidal assumption gives a better description of the bubble shape, but there is no trivial way to measure the length of an arc of ellipse. Therefore, the average cross-sectional stretch of the bulge will be approximated as the measurement of the arc of a circle, based on the circular assumption of the contour. The computation of λ depends on the state of the bubble, whether is is below or over the half sphere. Both cases and the corresponding computation are described on Figure 3.9. The complete computation of λ will rely on the combination of the two expressions depending on the state of inflation. The stress is then computed following Hoop's formula (see equation 3.20). The curvature R for the stress computation is measured with the ellipse assumption over the whole contour as it is the most accurate description.

Through the raw computation of the stress and the stretch, the computed true stress does not equal 0 for the state of no deformation ($\lambda = 1$). This is not physically possible, this error must arise from the difficult analysis of the contours at low inflations. The value of stretch and stress are corrected via a shifting of the stretch values via a linear fit and recomputing the resulting stress, as described in Appendix B.2. The measurement of the nominal stretch at the apex is based on an average over the whole contour and the circular approximation. This does not represent the truly biaxial state of the deformation, and this error impacts the computation of the stress. The error induced by this computation is discussed in Appendix B.2.

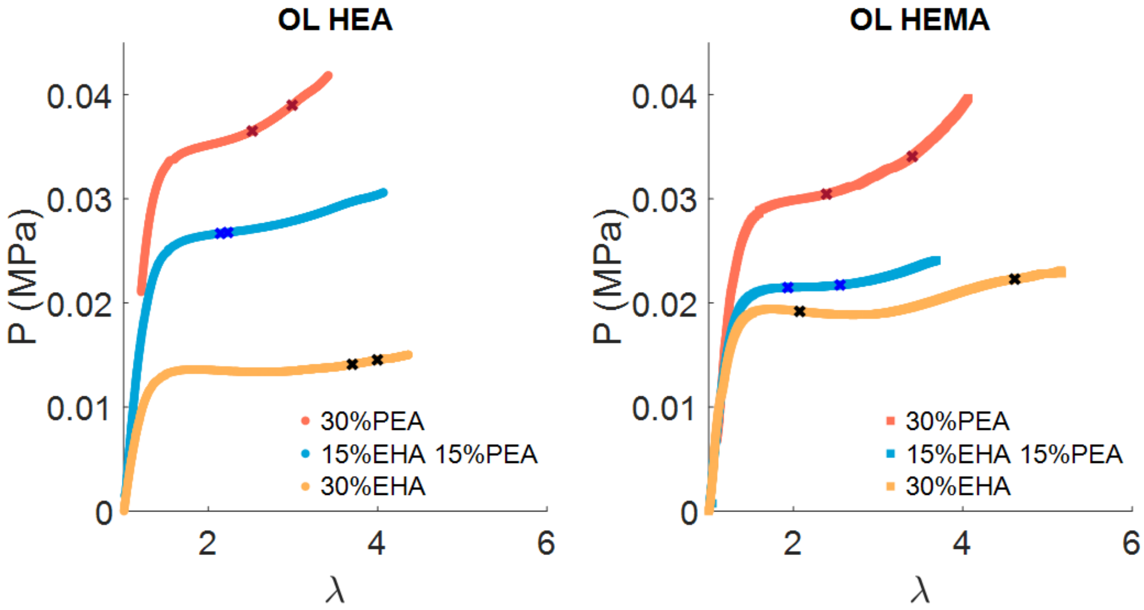

(A) Longest loading curve for all formulations and breaking point of the other two samples.

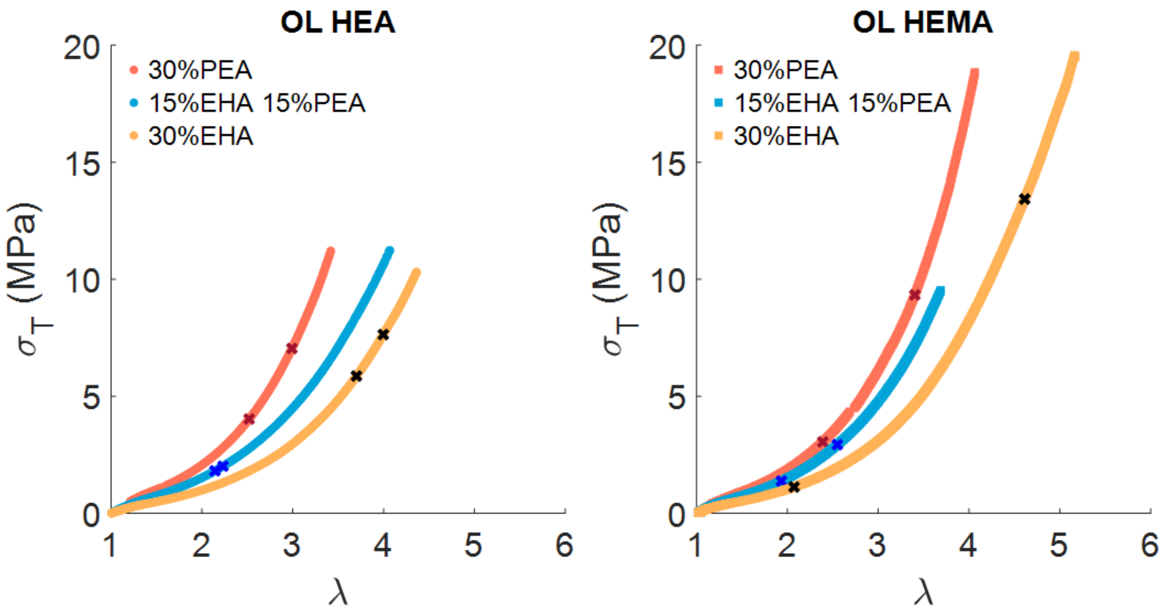

(B) Computed stress with the Hoop equation and the elliptic curvature

FIGURE 3.19: Pressure and True Hoop stress versus mean stretch for all formulations - volume controlled experiment until rupture. Only the longest loading curve is shown for each formulation. The crosses represent the deformation at which the other two samples of each formulation breaks. (A) The sudden change in pressure is linked with the geometrical change from spherical to ellipsoidal shape. Note that the deformation of the OL HEA 30% PEA can not be measured for $\lambda < 1.2$ due to detection problems. For the OL HEMA 30% EHA formulation, the pressure decreases at medium deformations and increases again for larger strains, resulting in an unstable response under controlled pressure.

The behaviour in Pressure and the resulting Hoop stress versus the mean stretch can be seen on Figure 3.19. One very obvious observation is that the extensions obtained from the biaxial inflation are far greater than in tensile tests. The hypothesis under which the tensile samples would break because they are notch sensitive is verified. The pressure vs stretch behaviour varies with deformation: for small deformations, while the bulge is still spherical, the pressure increases linearly with stretch. The change occurs for $\lambda \sim \pi/2$ when the shape shifts from spherical to ellipsoidal. For each formulation, 3 samples coming from separate polymerisation runs are tested, and they show that the behaviour in pressure is reproducible. The complete cycles in pressure and stress for each samples can be seen in Appendix B.2. The cycling at these large deformations shows a small hysteresis between the loading and unloading curve. However the initial strain is completely recovered. Since, in uniaxial traction, there was no visible hysteresis, it would be surprising that our type of network undergoes a dissipative behaviour in biaxial deformations. Therefore we believe that this difference between the loading and the unloading of the curve must be caused by friction of the polymer on the edge of the clamp.

Surprisingly, the samples based on 15% EHA and 15% PEA break at a smaller deformations than the other formulations. In the case of the OL HEMA 30% EHA formulations, the behaviour is even more complex: the pressure decreases after the change of shape, and increases for larger deformations. This behaviour can be seen because the experiment is volume controlled. In the case of a pressure controlled experiment, the bubble inflation would undergo an instability, jumping from small to high stretches suddenly. The instability is due to the large strain softening at intermediate strains that is then compensated by the strain hardening. For the other networks, the strain hardening appears sooner, blocking this instability. This non linear behaviour has already been largely studied in the case of the inflation of a balloon ([86], [87]).

3.2.3 Analysis of the elasticity behaviours

The mechanical responses of the networks is better seen on a Mooney plot where the uniaxial and the biaxial data are normalized by their respective Neo-Hookean behaviour in strain (see equation 3.18).

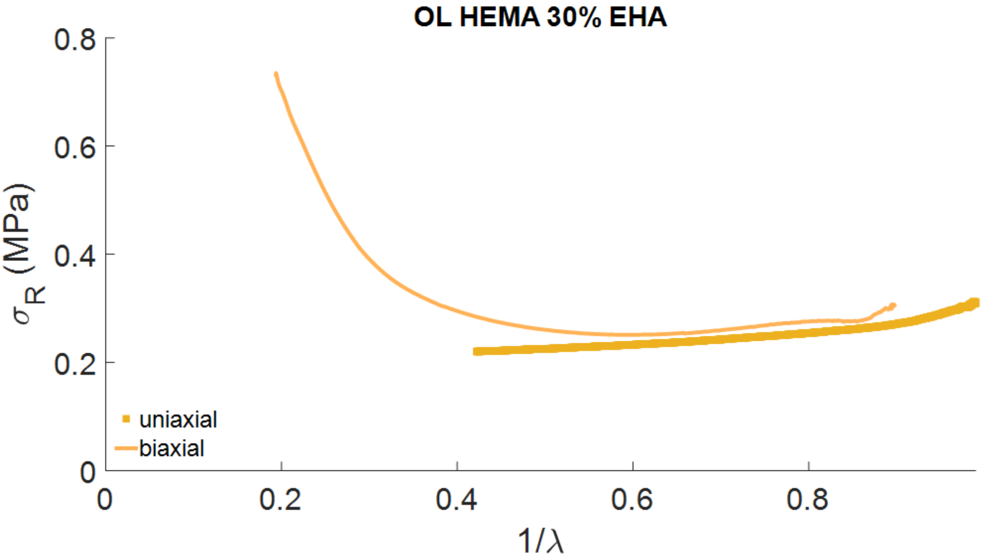

FIGURE 3.20: Mooney plots - comparison of the uniaxial and the biaxial testing. The biaxial data is only shown for $1/\lambda < 0.9$.

In the bulge inflation analysis, the measurement of the small strains is not really reliable, as was explained in Section 3.2.2.3, so only the data for $1/\lambda < 0.9$ is shown. The whole behaviour of all formulations is shown in Appendix B.3. However, the difference in strain hardening between the uniaxial test and the biaxial test is obvious on the Mooney plot. Considering its appearance, it is to be remembered that the abscissa λ for the uniaxial and the biaxial is not the same: for the uniaxial, we consider λ_z in the traction direction while for the biaxial, we consider the in-plane stretches. The appearance of the strain hardening in biaxial is therefore at smaller strains than in uniaxial. A better description of the respective effective stretch in each geometry is by plotting the data against J_1, as described in Appendix B.3, which shows that far greater extensions are obtained in biaxial inflation than in tensile tests. Let's now compare the strain hardening behaviour of the different formulations. This comparison is easier when the Mooney stress is also normalized by the Young modulus of each material. Based on the fitting with Gent model on the biaxial curve with the longest elongation, the corresponding E_{bi} can be computed. This value is used for the normalization of each reduced stress, leading to a dimensionless value σ_R / E_{bi}.

As can be seen on Figure 3.21, the onset of strain hardening does not depend strongly on the oligomer formulation, but on the monomer formulation. The 30% PEA formulation shows an earlier onset of strain hardening than the 30% EHA. The behaviour of the OL HEMA 15% EHA 15% PEA formulation is quite surprising. On Figure 3.19, it was already clear that it failed at lower pressures and stretch than expected, so all these results are coherent but the reason remains unclear.

3.2.3.1 Fitting of the biaxial and the uniaxial test

Based on these two types of tests, the non-linear elastic behaviour of the networks can be investigated. While the uniaxial results could be accounted for by a Neo-Hookean behaviour, the biaxial results clearly showed evidence of a strain hardening. In order to fit correctly the experimental

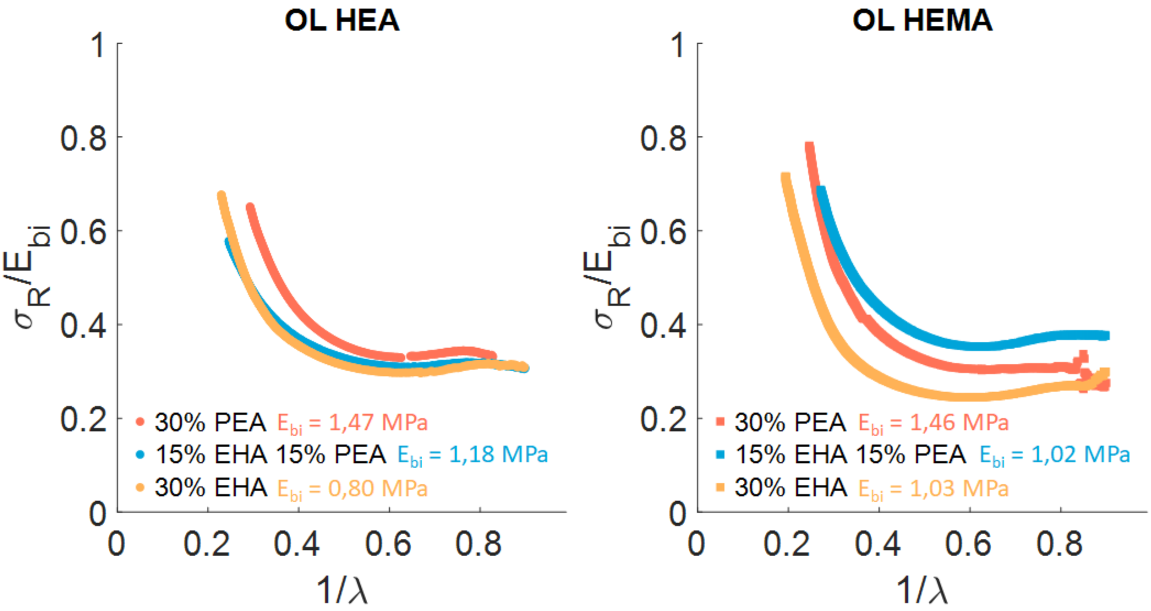

FIGURE 3.21: Mooney plots normalized by the biaxial small strain modulus. The appearance of the strain hardening depends on the monomer formulation, the 30% PEA formulation has an earlier onset of strain hardening.

data, the model will need both a softening and a strain hardening component. The set of data will be fitted with either the Gent or the Yeoh model. The Gent model leads to a direct identification of the fitting parameters with the material parameters: E is the Young's modulus and J_m is proportional to the square of the maximum extensibility. However, in the Gent model, the stress diverges at the maximum extensibility ($J_1 \longrightarrow J_m$) leading to numerical unstabilities. The Yeoh model, on the other hand, does not diverge: it is a 3^{rd} order polynomial in J_1 (see equation 3.11). Therefore, it will be used in the finite elements modelling in the following analysis. The only drawback is the identification of the C_i coefficients with the material behaviour: C_1 represents the small strain elasticity, but the combination of C_2 and C_3 will act on the softening and on the strain hardening (see B.1).

A good constitutive relation is fitted on some tests and correctly predicts the response in other stress states. In order to fit the model, it is therefore interesting to find parameters that will allow the best fit in both the uniaxial and the biaxial testing. The parameters are fitted to the longest uniaxial test and all biaxial tests that extend the polymer over a stretch of 2.5. This should allow for a good fitting of the elastic moduli and of the softening process (highly visible and reliable in uniaxial) while also generating the strain hardening thanks to the biaxial data. The resulting fits are described on Figure 3.22 for the OL HEA formulations.

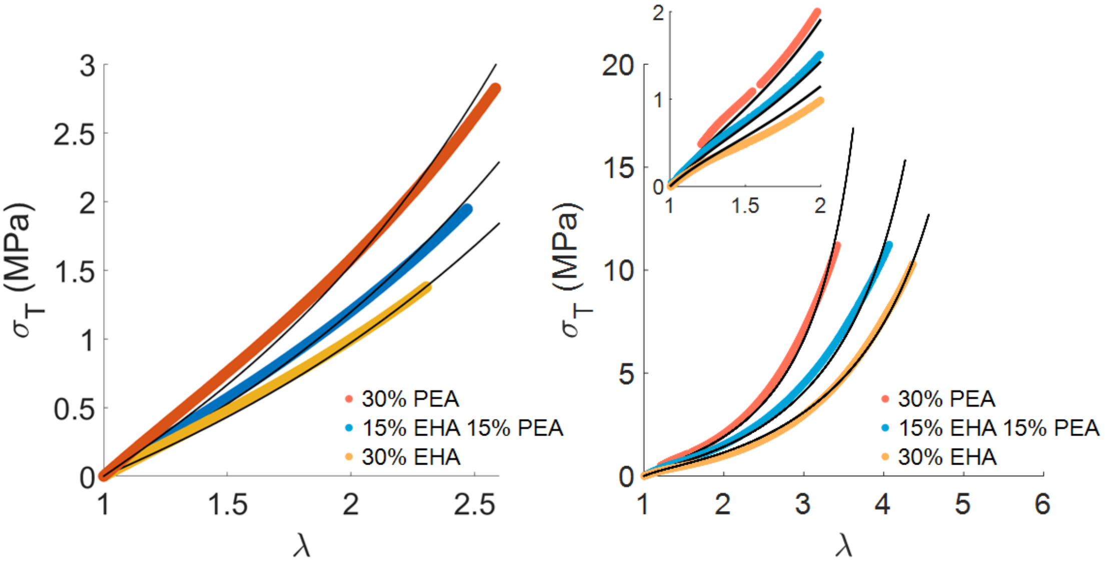

(A) Gent modelling - OL HEA formulations

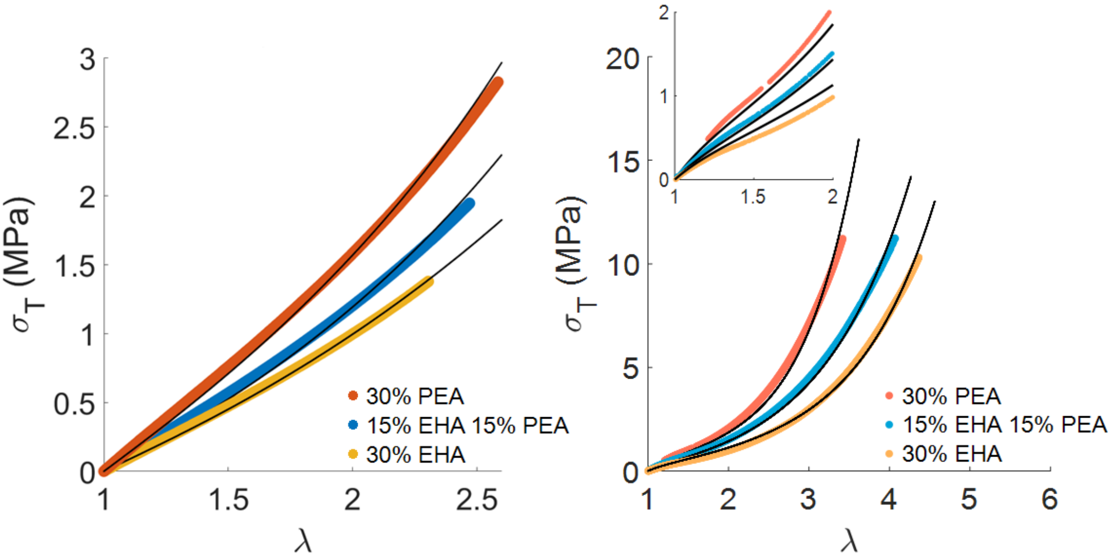

(B) Yeoh modelling - OL HEA formulations

FIGURE 3.22: Gent and Yeoh fits of the networks behaviour. The fits are done with one uniaxial test (left plot) leading to the longest deformation and all biaxial tests (right plot) leading to a stretch longer than 2.5. The fits are shown in thin black lines. The insert is a zoom on the small deformations in biaxial testing.

The fit parameters are summarized in Table 3.3. Both types of fit achieve a globally good description of the material behaviour. The modulus from the Gent fit E_G and the measurement of the Young's modulus from the uniaxial test are in good agreement, E_G is slightly smaller than E from the uniaxial data. In the case of the Yeoh fit, the elastic modulus is determined by $6C_1$, and again, there is a slight underestimation of the modulus. In both cases, the small strain behaviour in biaxial testing is not well fitted, which can be explained by the experimental difficulties of measuring the small deformation region of the bulge inflation test. However, from the shape of the fits and the error estimation (see Appendix B.3), it seems that the Yeoh fit captures well the behaviour of the material both in uniaxial and in biaxial testing. This is not surprising, as it has one more parameter. For all formulations, the error between the experimental data and the fit is always below 40% for the Yeoh fit, while it can reach very large values (up to 80%) for the uniaxial fit in the Gent fit, especially for the OL HEMA formulations (Appendix B.3).

Most importantly, the general trends of the curves have to be considered. More precisely, there are several formulations showing some surprising trends:

- OL HEMA 15% EHA 15% PEA: the Gent fit leads to a smaller finite extensibility than the biaxial curves tend to show. This may be due to relative small extensibilities obtained for this formulation in the bulge inflation. When fitting the longest biaxial stress/stretch curve alone, it leads to $E_G = 1.018$ MPa and $J_m = 41.18$.
- OL HEMA 30% EHA: the Gent fit leads to a higher predicted elastic modulus than the uniaxial data.
- For all formulations and both models, there is no good way to fit the biaxial data in small strains, which is consistent with the Mooney plot

Formulation		Gent		Yeoh			E (MPa)
		E_G (MPa)	J_m	C_1	C_2	C_3	uniaxial
OL HEA	15% 15%	0.989	54.88	0.164	$1.6.10^{-3}$	$3.57.10^{-5}$	1.156
	30% EHA	0.810	69.30	0.142	$-0.2.10^{-3}$	$4.15.10^{-5}$	0.958
	30% PEA	1.241	34.12	0.225	$-0.9.10^{-3}$	$2.66.10^{-4}$	1.564
OL HEMA	15% 15%	0.840	38.01	0.130	$3.7.10^{-3}$	$2.60.10^{-5}$	0.967
	30% EHA	0.842	76.00	0.101	$2.6.10^{-3}$	$1.36.10^{-6}$	0.853
	30% PEA	1.287	46.26	0.181	$4.3.10^{-3}$	$4.63.10^{-5}$	1.301

TABLE 3.3: Fit parameters for Gent and Yeoh

While the modelling of the behaviour is not perfect, given the uncertainties of the experimental analysis of the bulge inflation test, we still obtain a quite good agreement between the uniaxial and the biaxial test. The Gent model especially, while leading to the biggest errors, allows us a good ranking of the strain hardening of the different networks. J_m can directly be linked to the finite extensibility λ_m in uniaxial and biaxial tests (see Table 3.6). The finite extensibility does not seem to depend on the oligomer, but mostly on the acrylate formulation, with the 30% PEA leading to the lowest extensibility. When thinking about the microstructure of the 30% PEA networks again, it has those hard nodules that seem to consist of mostly highly crosslinked PEA. Therefore, while the soft matrix is entangled and could deform largely, the hard nodules have a smaller extensibility or can act as rigid connectors, leading to a lower onset of strain hardening. The 30% EHA formulations have the lowest modulus, the longest chains and therefore the highest onset of strain hardening.

3.2.3.2 Elastic chain density and theoretical maximal extension

The elastic chain density ν can be computed from the value of the Young's modulus E, based on equation 3.17. Based on the affine model, there is direct relationship between the elastic chain density and the average molecular weight between crosslinks:

$$E = 3\nu_{elas}kT = \frac{3\rho RT}{M_x} \tag{3.27}$$

Based on the Rubinstein and Panyukov fitting of the uniaxial data of our networks, we could extract the crosslinks contribution to the modulus. However, the model is based on a phantom model of the elastic network [67]. The link between ν_{elas} and the elastic modulus in the phantom network depends on the functionality f of the chains:

$$E_x = 3\nu_{elas,phan} kT \frac{f-2}{2} = \frac{3\rho RT}{M_x}\left(1 - \frac{2}{f}\right) \tag{3.28}$$

In our systems, the functionality is 4, leading to:

$$\nu_{elas,phan} = 2\nu_{elas,aff} \tag{3.29}$$

These relations can lead to the computation of M_x the average molecular weight between crosslinks and $\nu_{elas,phan}$ the density of elastic chains. However, our networks are based on a mixture of oligomer chains and acrylate-based chains. While the oligomer chains have a definite length, the acrylate chains display a dispersion of chain length. Therefore, there is no direct relation between the computed M_x and the reality of the network. However, we would like to study the link between the strain hardening and the formulation of the networks, taking also into account the bimodality of chain lengths. We will first compute the total elastic chain density in the phantom model. By assuming that all the oligomers are active in the elastic network, meaning that all of them are linked on their 2 chain ends, the density of acrylate chains becomes the difference between the total density of elastic chains and the density of oligomer chains. Finally, by knowing the initial monomer density, the average number of monomers per chain can be determined.

The oligomer concentration is known (70%w), leading to the direct computation of the oligomer density ν_{OL}:

$$\nu_{OL} = \frac{0.7\rho\mathcal{N}_A}{\mathcal{M}_{OL}} \tag{3.30}$$

where $\mathcal{M}_{OL}$ is the molecular mass of the HEA (or HEMA) oligomer and ρ is the network's density: 1042 kg/m^3 (measured by salt water immersion, see Section 2.2.3.2). The density of the acrylate-based chains is then: $\nu_{A\ chains} = \nu_{elas} - \nu_{OL}$. Based on the initial acrylate monomer concentration, the mean number of acrylate per acrylate-based chain $N_{acrylates}$ is computed:

$$N_{acrylates} = \frac{\nu_{A\ monomers}}{\nu_{A\ chains}} \tag{3.31}$$

Formulation		E_x (MPa)	$\nu_{elas,phan}$ (m^{-3})	ν_{OL} (m^{-3})	$\nu_{A\ chains}$ (m^{-3})	$N_{acrylates}$
OL HEA	15% 15%	0,746	1.222.10^{26}	5,085.10^{25}	7.131.10^{25}	14
	30% EHA	0,642	1.051.10^{26}		5.428.10^{25}	19
	30% PEA	0,877	1.436.10^{26}		9.277.10^{25}	11
OL HEMA	15% 15%	0,637	1.043.10^{26}	5,067.10^{25}	5.364.10^{25}	19
	30% EHA	0,464	7.598.10^{25}		2.531.10^{25}	40
	30% PEA	0,689	1.128.10^{26}		6.216.10^{25}	16

TABLE 3.4: Computation of the elastic chain density in the affine model (based on E_x) and determination of the mean acrylate chain length

This analysis is summarized in Table 3.4, E_x is the fitted modulus from Table 3.2 and the density of elastic chains is computed considering the phantom model. It shows that theoretically, the acrylate chains are very small, and therefore very stiff, linking the longer oligomer chains together. The number of monomers in the oligomer chains is known (N_{OL} = 105), leading to the computation of the mean number of monomers in an elastic chain:

$$N_m = \frac{N_{OL}\nu_{OL} + N_{acrylates}\nu_{A,chains}}{\nu_{elas}} \tag{3.32}$$

This mean number can be compared to the extracted value from the swelling experiments (see Section 2.2.3.2), as can be seen on Table 3.5.

Formulation		N_m	$N_{swelling}$
OL HEA	15% EHA 15% PEA	52	64
	30% EHA	61	82
	30% PEA	44	42
OL HEMA	15% EHA 15% PEA	61	73
	30% EHA	83	83
	30% PEA	56	50

TABLE 3.5: Comparison between the molecular prediction and the swelling

It is reassuring that the theoretical computation on the chain length do match (to some extent) the extracted N from the swelling experiment. This implies that the θ solvent description was not bad. However, it is important to note that this computation considers that **all** oligomer chains are active in the elastic network and that all monomers react to also form a network strand. This is of course false, as the polymerisation is not controlled and oligomer chains can also form loops or dangling chains in the network. It was also observed that a portion of oligomer chains and monomers do not crosslink in the network as they can be extracted with a good solvent (see Appendix A.3). However, there is no way to determine the proportion of oligomer chains that actually participate in the elastic network, so there is no way to make a better computation of the acrylate-based chains.

Based on the mean acrylate chain length and the oligomer chain length, it is possible to compute the maximum extensibility of each type of chain family and compare it to the macroscopic λ_m extracted from the J_m fit. The molecular maximum extensibility is computed as described in equation 3.7 as the ratio of the mean square end-to-end distance in the relaxed state R_0 and the maximum end-to-end distance R_{max} computed in the restricted angle assumption. In this computation, the form factor C_∞ of each component is needed:

- $C_\infty(PPG) = 5.76$ [88]
- $C_\infty(PEHA) = 9.5$ [89]
- $C_\infty(PPEMA) = 11.3$ [84] $\Rightarrow C_\infty(PPEA) \sim 11$

C_∞ depends on the rigidity of the monomers, so we assume here that the PEA is slightly less rigid than its methacrylate version. On Table 3.6, the maximal extensibility of the oligomer and the acrylate-based chains from the molecular interpretation based on the computation with E and E_x are compared to the maximum extensibility from the Gent fit.

First of all, the maximum extensibility computation from the J_m value depends on the type of test. The maximum extensibility in uniaxial tension is higher than in equibiaxial tension. This is not surprising: when considering the polymer as the random walk coil at rest, the end-to-end vector will increase more when the deformation is in one direction while an equibiaxial tension will expand the polymer coil in 2D but not increase the end-to-end vector as much, as described on Figure 3.23. This is also seen experimentally as the strain hardening appears at lower stretches in biaxial testing, as can be seen on the reduced stress against the J_1 in each test (See Appendix B.3).

OL HEA		15% EHA 15% PEA	30% EHA	30% PEA
Gent fit	$\lambda_{m,uni}$	7.60	8.49	6.07
	$\lambda_{m,bi}$	5.38	6.01	4.31
Molecular fit	$\lambda_{m,OL}$	5.32	5.32	5.32
	$\lambda_{m,acrylate,E_x}$	1.36	1.63	1.14
	$\lambda_{m,mean,uni}$	3.00	3.42	2.62
OL HEMA		**15% EHA 15% PEA**	**30% EHA**	**30% PEA**
Gent fit	$\lambda_{m,uni}$	6.04	8.98	6.95
	$\lambda_{m,bi}$	4.29	6.36	4.93
Molecular fit	$\lambda_{m,OL}$	5.32	5.32	5.32
	$\lambda_{m,acrylate,E_x}$	1.56	2.39	1.39
	$\lambda_{m,mean,uni}$	3.39	4.34	3.15

TABLE 3.6: Comparison of the macroscopic maximal extensibility and the molecular interpretation, for the assumption based on E_x

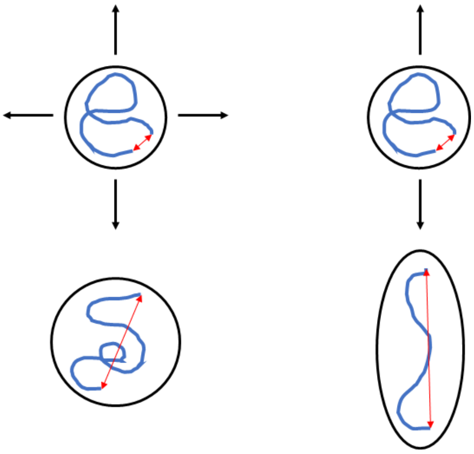

FIGURE 3.23: Variation of end-to-end vector under uniaxial and biaxial deformation. The end-to-end vector is marked in red.

The results from Table 3.6 show that the molecular interpretation of the maximum extensibility does not correspond to the macroscopic measurement. Based on our assumptions of a complete conversion and defect-free crosslinking of the network, the acrylate chains are quite small, leading to a mean predicted maximum extension that is less than half of the measured one. This same analysis was made in several studies with more reproducible networks (simple formulation and more controlled polymerisation) and the experimental maximum extensibility could be predicted with this theoretical model [60]. The fact that this computation does not fit the macroscopic extensibility in this type of networks shows that our formulations lead to heterogeneous networks and chain lengths. The population of oligomer chains and acrylate-based chains leads to a complicated architecture of the network and theoretical predictions are not straightforward. If we consider the polymerisation process again, a viscous oligomer and monomer mix is polymerized at high speeds via UV thanks to a high quantity of photoinitiator. Many chains initiate and propagate at the same time, leading most probably to many dangling chains or small loops, therefore enhancing the heterogeneity in chain length and decreasing the number of effective elastic chains. The discrepancy between the molecular interpretation of the chain lengths and the actual macroscopic measurement of the maximum extensibility is therefore not that surprising.

3.2.4 Modelling the biaxial deformation and validating the strain energy function

The biaxial inflation of the polymer films proved very useful to describe the strain hardening. However, the analysis done here is based on the pretty strong approximation that the total stretch over the bulge is biaxial. This is false, yes, but is this analysis completely rubbish? Let's see how this approximation on the data analysis, and therefore on the strain energy density parameters, lead to a discrepancy between the material properties and the reality.

We modelled the membrane inflation in a volume controlled experiment in FEM on Abaqus. Considering the geometry, an axisymmetric description of the membrane is sufficient. The polymer film is modelled by Shell elements: SAX1. This is a simple 2 node element, making the membrane just as a line. The ouput are displayed either on the upper or lower surface of the membrane. Because we are dealing with thin shells, there is no stress or stretch difference between the 2 surfaces. The inflation is done via Fluid elements (FAX2) that fill the cavity underneath the membrane. The Abaqus model and inflation technique was proposed by Pierre-Yves Corbel (ENSTA Bretagne).

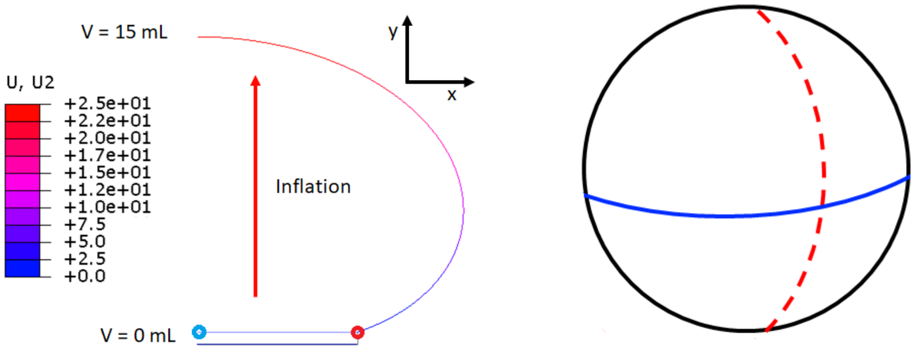

(A) Model evolution between the initial state (V = 0 mL) and an intermediate inflation

(B) Meridian direction in red, Hoop direction in blue on a sphere

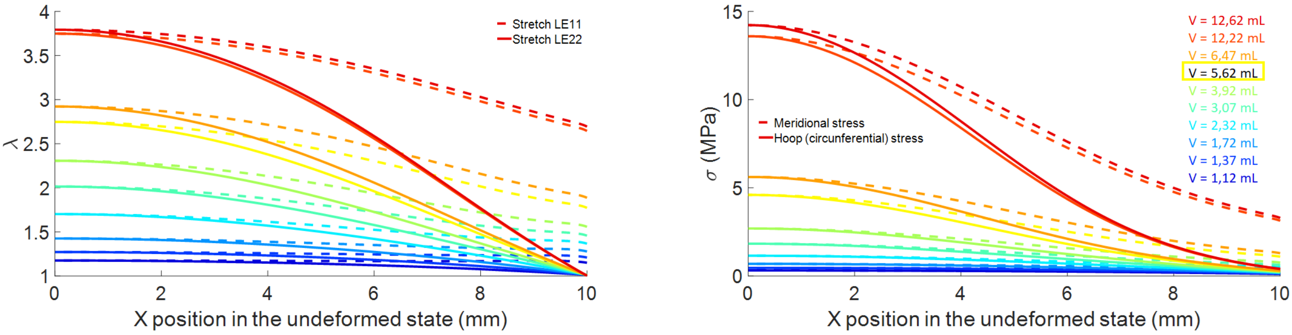

(C) Evolution of the meridian and circumferential stretch

(D) Evolution of the meridian and circumferential stress

FIGURE 3.24: Abaqus model for the bubble inflation - Biaxial Stress and stretch evolution. (A) U2 is the displacement in mm in the y direction. The red circled point is fixed in X and Y but can rotate. The blue circled point is fixed on the Y axis. The line below the membrane displays the limit of the cavity. V: volume of inflation. (B) Description of the two directions for the stretch and the stress. (C) and (D) Evolution of the stretch and stress over the bulge for different inflation volumes. Material parameters of OL HEMA 30% PEA 3: $C_1 = 0.181$, $C_2 = 4.3.10^{-3}$, $C_3 = 4.63.10^{-5}$, t = 352 μm.

The membrane is described by its thickness t, a Poisson's coefficient of $\nu = 0.499$ and a Yeoh constitutive equation. The coefficients used are described in Table 3.3 and come from the fitting of our computation of the stretch and stress, which is approximate. It is not possible to use the Gent model as it diverges for stretches close the maximum extension. The boundary conditions fix the external membrane point in x and y displacements, while the rotation is free. The membrane apex is fixed on the axisymmetric axis. Two typical cases are considered: OL HEMA 30% PEA and OL HEMA 30% EHA. These are two extreme behaviours, where the first shows an early strain hardening while the second shows an instability in the pressure behaviour due to its larger softening.

As expected, the truly biaxial zone is around the apex of the sphere. Let's now compare the modelling with our experimental data. The experimental stress and stretch are computed as a mean over the whole bulge, while we'll only consider the biaxial stretch and stress at the very apex of the modelled bulge. The comparison for the two extreme formulations is displayed on Figure 3.25.

As can be seen on the stress curve (Figure 3.25 (B)), the Abaqus modelling follows exactly the experimental behaviour. This is reassuring: the Yeoh parameters were extracted from fitting the experimental stress versus stretch curve with a truly biaxial material law. Then, these coefficients are put in the Abaqus model and the truly biaxial behaviour is extracted. So the fact that the fit is perfect it is at least confirming that the modelling works well. But the interesting curve is the evolution of the Pressure with the stretch (Figure 3.25 (A)). For both formulations, the computed Pressure does not follow the experimental one. While for the 30% PEA formulation, the behaviours are still quite similar, and the disparities could be induced by the difference of λ, the behaviour of the 30% EHA formulation differs greatly. The instability in Pressure, that is better displayed on the insert of Figure 3.25 (A), is not present in the computed pressure.

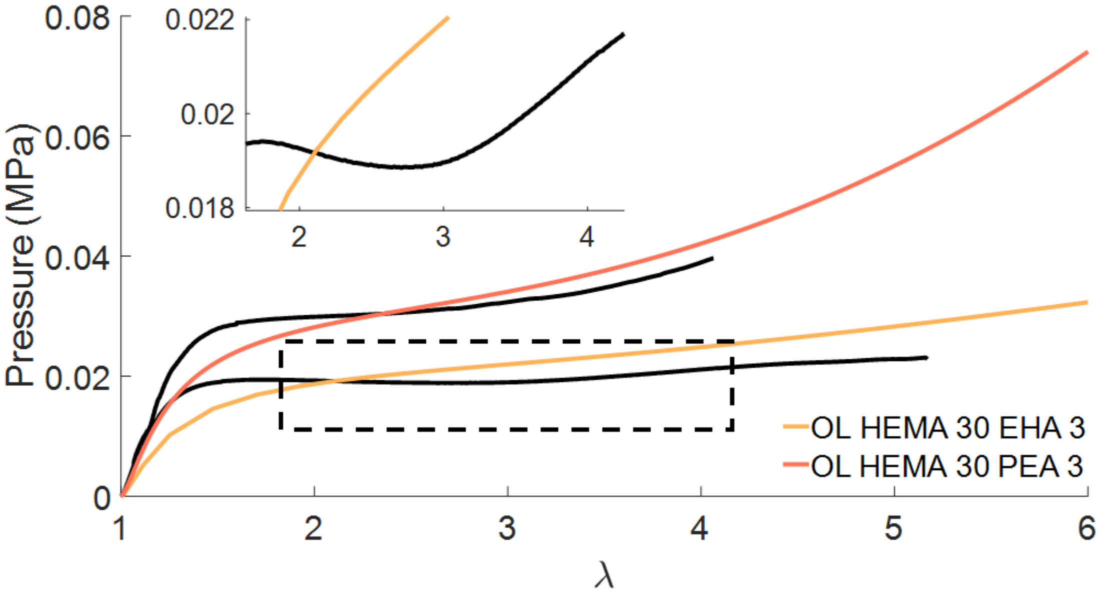

(A) Pressure evolution with λ

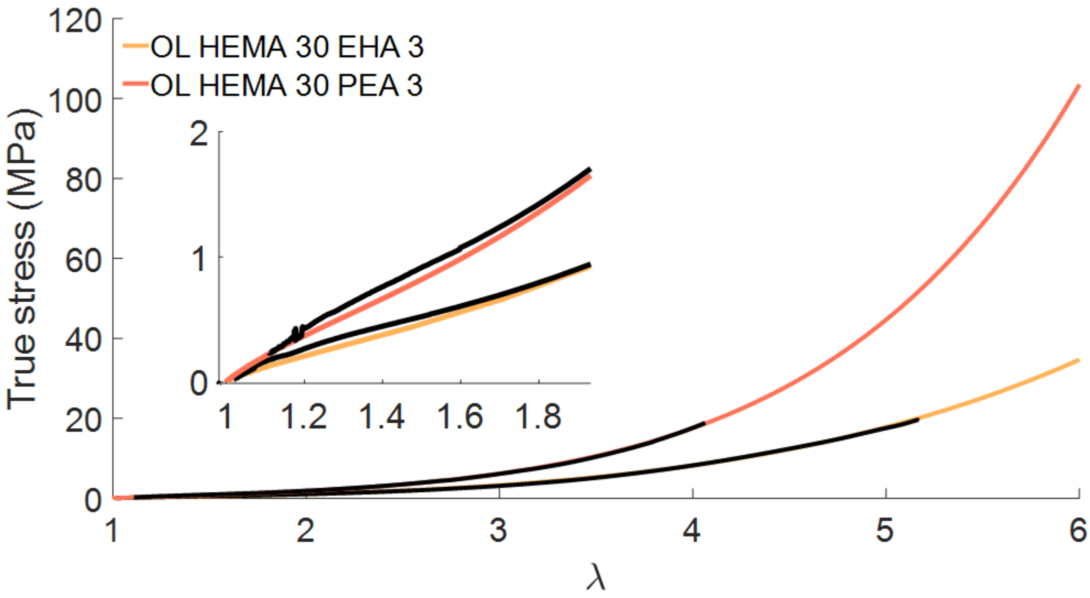

(B) Stress evolution with λ

FIGURE 3.25: Modelling of the bubble inflation and comparison with the experiment. OL HEMA 30% PEA 3: t = 0.352 mm, OL HEMA 30% EHA 3: t = 0.419 mm. Only the longest elongation is displayed from the experimental data. (A) Abaqus model (in color): P: pressure inside the cavity, λ: stretch at the apex of the inflated membrane (exp(LE1)). Experiments (in black): λ is measured over the whole contour and represents the mean stretch. Insert: zoom on the pressure instability during the inflation of OL HEMA 30% EHA. (B) The stretch from Abaqus is S11 at the apex, the experimental stress is computed with the mean stretch and the elliptic curvature. Insert: zoom on the small deformation region.

This leads us to the first conclusion that yes, inflation of polymer membranes is not that simple. The Pressure evolution can show several subtleties and the rough computation that was done on our experiments is not detailed enough to encapsulate these behaviours. At least, the silver lining is that for materials that have a more simple behaviour, like OL HEMA 30% PEA, the rough computation is not that off in predicting the pressure evolution. Also, this modelling allows us to determine the errors made when computing the mean stretch instead of actually measuring the true biaxial stretch at the apex. The error made with this approximation is described in Appendix B.2.

However, if we look at the raw data that we studied, we overlooked how full of information the bubble profiles were. The particular shapes in which the bubble deforms during the inflation are coming from the various stretch situations over the bulge, that vary from the perfect biaxial to pure shear. One could then wonder, why only analyze the apex of the sphere to stay in the truly biaxial stretching situation, when the whole geometry is so rich in informations? Furthermore, when fitting the material parameters on a mechanical test result (may it be the uniaxial, biaxial, shear, ...), the idea is always to achieve a good material description that could predict the material's behaviour in other testing geometries. One could then assume that simply fitting the experimental contours in bubble inflation could result in a good material constitutive equation since the mechanical test explores several degrees of multiaxiality in just one experiment.

Thanks to our Abaqus modelling, we could extract the computed bubble contours for various pressures and compare it to the experimental contours. Let's first consider the OL HEMA 30% PEA 3. The displayed contours represent the whole bulge inflation, as the last contour at P = 0.0396 MPa is close to the sample's rupture.

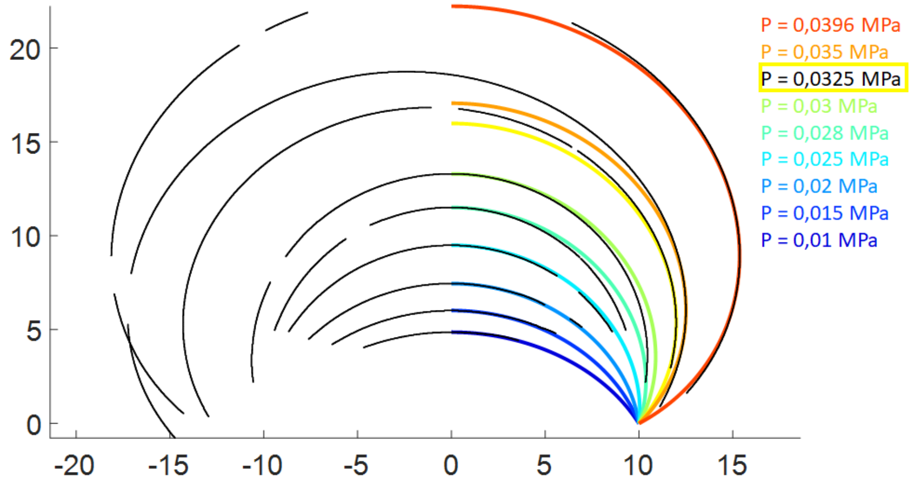

FIGURE 3.26: Contour modelling versus experiment - OL HEMA 30% PEA 3 - Yeoh parameters from the experimental data. The experimental contours are in black, the computed ones in the various colors. To help the eye observing the curvature difference between the computed inflation and the experimental one, the experimental contours are shifted: the small contours are shifted to match the maximum deflection of the computed bulge, the larger ones to match the maximum displacement in X.

The modelled evolution of the pressure was already quite good for this formulation, and this is confirmed by the the contour comparison on Figure 3.26. Yet there is still some discrepancy, especially when the pressure increases and the bubble becomes ellipsoidal. However, when the contours of OL HEMA 30% EHA 3 are observed with the initial Yeoh parameters, the computed bubble shape is quite off (Figure 3.27 (A)). In the small inflation domain, the computed bubble shape is close to the experimental values, but the lack of instability in the model makes it impossible to compare the inflation at larger stretches. This again shows us that our inflation analysis was incomplete, but the modelling can be used to play a little with the material parameters. Based on Figure 3.25 (A), it was obvious that the material parameters did not capture the softening very well. By lowering C_2 and increasing C_3 to compensate, we could observe a computed Pressure with an instability! Figure 3.27 (C) displays the new computed behaviour, that is much closer to the experiment. However, it is still not perfect, as described by the evolution of the contours: the instability in pressure does not appear at the same moment than in the experiment. This shows us that our initial parameters were not the best to describe the material's behaviour, but they were good starting points to try and tweak for the perfect fit.

This leads us to the second, and more interesting, conclusion: the inflation modelling offers a great potential! Based only on a side view of the bubble inflation, the extraction of the bubble contours can lead to the complete fitting of the materials constitutive equation, including the complex interaction between softening and hardening. This would require the design of a loop between the Abaqus modelling which would output the pressure, volume and contours to be fitted externally with the experimental data. The starting point for the parameter value can be easily computed with the rough image analysis we described. This would be experimentally much simpler than the exact measurement of the true biaxial stretch, as it only requires the Pressure and the bubble contour. Of course, it would need a bigger work in programming, that we did not have the time to do during this study, but once coded, any type of deformed bulge could be well modelled and be fitted with a robust material law. By testing different material constitutive equations in this optimisation of the contours, it could also be a way to discriminate between them and find the best description of the material.

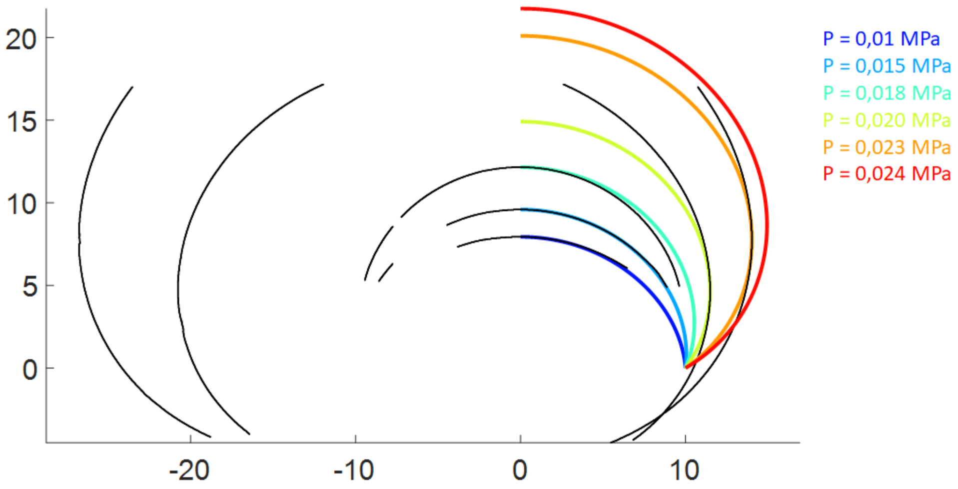

(A) Yeoh parameters from the experimental data

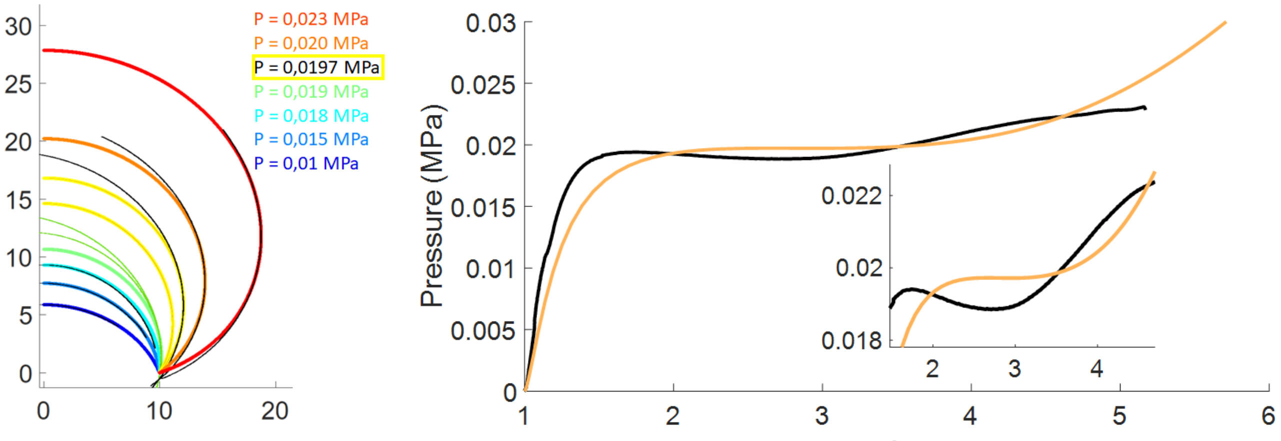

(B) Effect of slightly shifted Yeoh parameters on the contours

(C) Effect of slightly shifted Yeoh parameters on the Pressure versus stretch

FIGURE 3.27: Contour comparison between the modelling (in colors) and the experiment (in black) - OL HEMA 30% EHA 3. (A) The simulation was done with the initial experimental parameters from the bulge inflation experiment, as no instability in pressure was observed, the modelled contours do not reproduce the experimental bulge. (B) and (C) Computation made with : $C_1 = 0.12$, $C_2 = 2.5.10^{-4}$, $C_3 = 2.72.10^{-5}$. (B) Green contours: instability of the experimental bulge, the same pressure leads to 2 inflations. Yellow lines: instability of the Abaqus model at P = 0.0197 MPa. (C) Comparison of the computed pressure with the experimental one. The model shows an instability in pressure at slightly shifted values of λ compared to the experiment.

3.3 Fracture properties

The fracture energy, defined in Section 3.1.4 was determined via single notched samples of a dumbbell shape. A pre-crack of around 1 mm in length is cut on one side with a sharp razor blade. The cut was then observed with an optical microscope to determine the exact length c (Figure 3.28 (A)). The samples were tested at different velocities (0.5, 0.1, 0.01 and 0.001 mm/s) to test the effect of the pulling velocity on the rupture energy. For each velocity, except for the slowest one, at least 3 samples were tested.

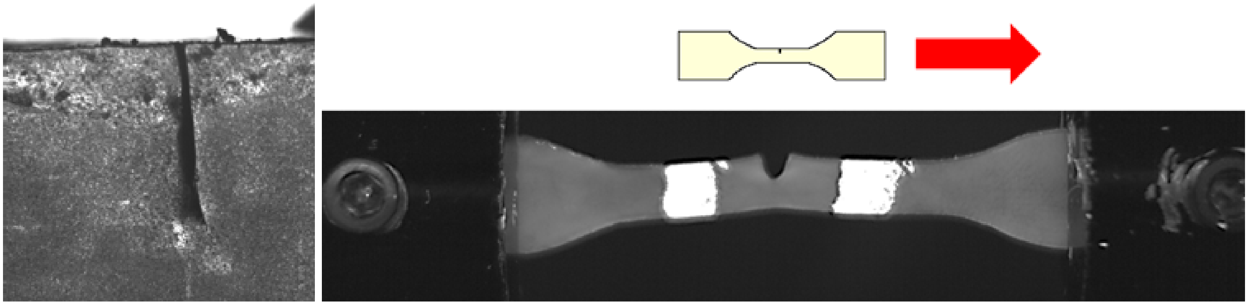

(A) Initial crack ~ 1mm (B) Opening of the crack during deformation

FIGURE 3.28: Notch evolution during the fracture test

The fracture energy is computed from the stress/stretch curves. Greensmith's approximation of the fracture energy relies on the computation of the strain energy density of the un-notched sample [83]. However, because of the dispersion observed in the tensile data between polymerisation batches, it did not seem relevant to use an un-notched curve for the fracture energy measurement. So $W(\lambda_{prop})$ is computed by the area of the **notched sample** until the crack propagates. This leads to a small underestimation of the fracture energy. The resulting testing curves are displayed on Figure 3.29 and the area used for the computation of $W(\lambda_{prop})$ is displayed. The resulting fracture energies depending on the formulation and the initial testing stretch rate are displayed in Table 3.7. The fracture tests of all formulations are displayed in Appendix B.4.

Based on the stress curve, the mean velocity of the crack propagation can be measured. The dumbbell is 4 mm wide, and the initial length of the cut is known, so the total length over which the crack propagates is known. The time needed to fracture can be estimated by using the time between the maximum force and the last data point. This leads to the global plots of the fracture energy Γ_c versus the initial stretch rate and the mean crack velocity, as seen on Figure 3.30.

As discussed in Section 3.1.4, there is a strong dependence of the fracture energy on the viscous dissipation mechanisms: Γ_c increases with the mean crack velocity. The variation of the fracture energy with velocity does not depend strongly on the oligomer, but mostly on the monomer composition. A power law can be determined between the fracture energy Γ_c and the mean crack velocity: $\Gamma_c \propto v_{crack}^n$. Because we consider that the oligomer functionalization is not very important on the fracture behaviour, both the OL HEA and OL HEMA are used to determine the power law, leading to the results in Table 3.8. Only one outlier can be seen on the trend: OL HEMA 30% PEA at the lowest velocity appears to have a much lower fracture energy than the other velocities would suggest.

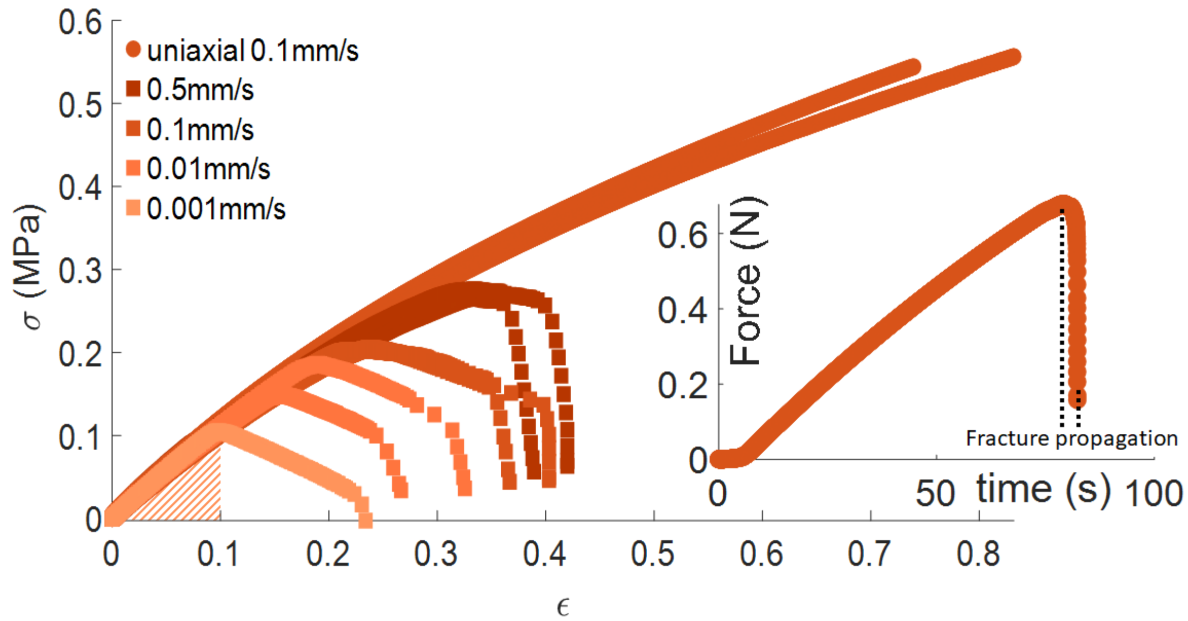

FIGURE 3.29: OL HEMA 30% PEA - Stress-strain curves of notched samples at different stretch rates and comparison with the test carried out on a pristine sample (un-notched). Decreasing the crosshead velocity decreases the fracture energy. The cross-hatched area represents the loading before the fracture propagation and is used for the computation of Γ_c. Insert: Force versus time for the 0.1 mm/s fracture test. The time from the maximum force to the total rupture is used for the computation of the mean crack velocity.

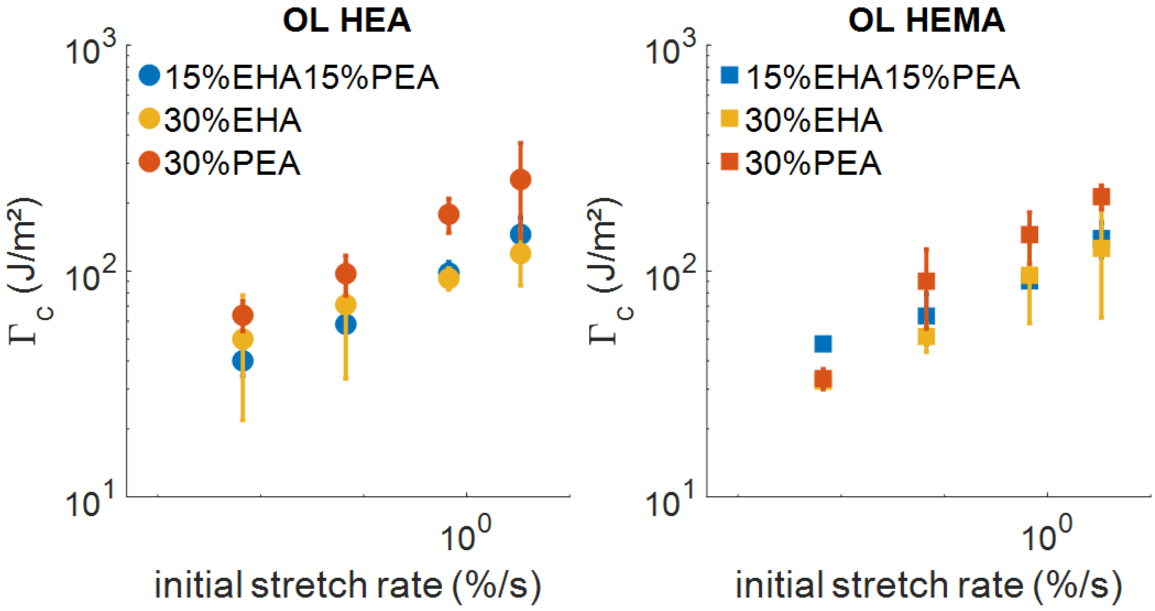

(A) Log-Log plot of the fracture energy versus initial stretch rate

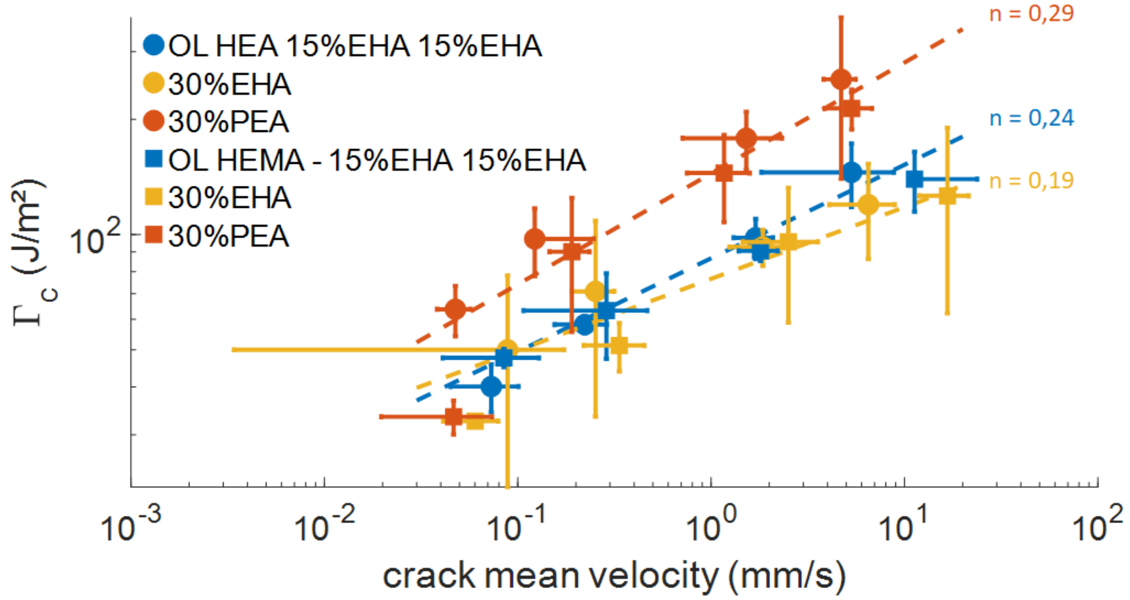

(B) Log-Log plot of the fracture energy versus mean crack velocity

FIGURE 3.30: Viscoelastic behaviour of the fracture energy. Formulations based on OL HEA: circles, formulations based on OL HEMA: squares.

Formulation	%/s	Γ_c (J/m^2)	Formulation	%/s	Γ_c (J/m^2)
OL HEA 15% EHA 15% PEA	3.33	145.32 ± 27.52	OL HEMA 15% EHA 15% PEA	3.33	139.48 ± 24.85
	0.67	98.03 ± 11.74		0.67	90.58 ± 5.27
	0.067	58.17 ± 2.98		0.067	63.26 ± 15.92
	0.0067	40.07 ± 5.74		0.0067	47.63 ± 2.63
OL HEA 30%EHA	3.33	119.62 ± 33.37	OL HEMA 30%EHA	3.33	126.13 ± 63.91
	0.67	92.73 ± 10.02		0.67	95.62 ± 36.80
	0.067	70.99 ± 97.54		0.067	51.29 ± 7.42
	0.0067	49.98 ± 28.09		0.0067	32.55 ± 0.17
OL HEA 30%PEA	3.33	254.26 ± 114.56	OL HEMA 30%PEA	3.33	213.40 ± 25.50
	0.67	178.33 ± 30.83		0.67	144.73 ± 37.08
	0.067	97.35 ± 19.54		0.067	90.13 ± 34.51
	0.0067	63.76 ± 9.56		0.0067	33.40 ± 3.39

TABLE 3.7: Fracture energy depending on the initial stretch rate (%/s)

Formulation	n	T_g OL HEA (°C)	T_g OL HEMA (°C)
15% EHA 15% PEA	0.24 ± 0.02	-57	-63
30% EHA	0.19 ± 0.04	-63	-70
30% PEA	0.29 ± 0.03	-56 & 5	-59 & -3

TABLE 3.8: Power law between Γ_c and v_{crack}. The behaviour is considered the same for both oligomer, only the monomer formulation is taken into account.

In principle, the higher the exponent, the higher the level of viscous dissipation. All samples are at $T \gg T_g$, except for the 30% PEA formulations that have a higher T_g. This is coherent with the measured exponents, showing an increased role of viscous dissipation in the fracture behaviour. Also, Figure 3.31 focuses on the evolution of the crack opening with the testing strain rate. When pulling on single-edge notched samples, the initial crack, cut with the razor blade before the test, opens and then the fracture propagates. The crack propagation is observed by filming the experiment with the extensometer that takes regular pictures of the sample while also measuring the deformation, as explained in Section 3.2.1.1. The faster the crosshead velocity, the wider is the opening before the propagation can be detected. Slootman et al. considered the fracture in elastomeric networks that are comparable, to some extend, to our networks [11]. Their results state that a higher testing velocity leads to a higher process zone around the crack where both viscous dissipation and additional bond fracture happen, leading to an increase of the energy needed to propagate the fracture. This explanation could be fitting for our model networks.

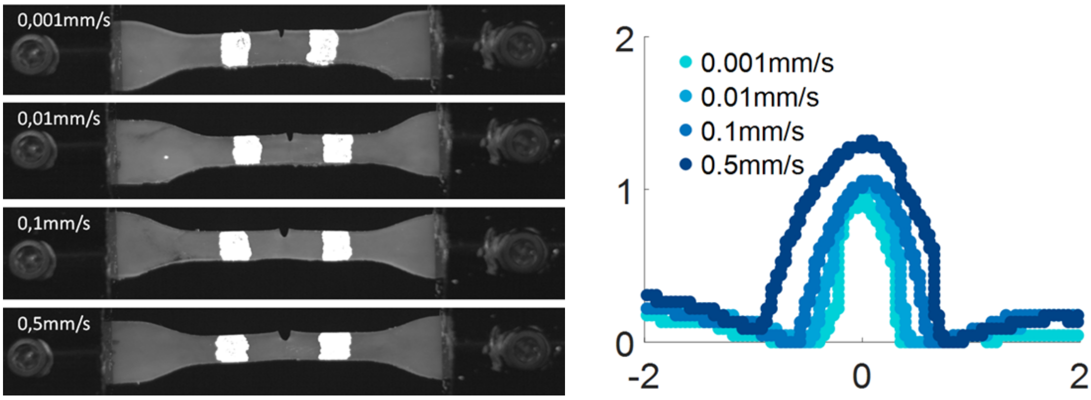

(A) Fracture samples before the crack propagation

(B) Extraction of the crack shape (mm)

FIGURE 3.31: Evolution of the crack shape with the applied strain rate for the OL HEA 15% EHA 15% PEA formulation. The plots of (B) are the extracted contours of the crack opening. When tested at high stretch rates, the opening is more important.

Through the filming of the fracture experiments, it is also possible to analyse the crack propagation velocity. While the mean crack velocity was only computed with the force versus time curve, the film analysis shows that the velocity of propagation is not constant. In fact, it accelerates. This also means that the fracture energy during the propagation varies, as the velocity varies. Either way, the computed Γ_c for each experiments here represents the needed energy to fracture at our considered testing velocities.

3.4 Take home messages

- The uniaxial testing of the different formulations showed that the networks are hyperelastic and present a significant softening. The Young's modulus could be extracted from the small strain test and the softening could be attributed to a significant contribution of the entanglements in the networks. To test the large strain behaviour, the networks were tested in bulge inflation. This allowed for the investigation of the strain hardening.

- The mechanical responses were fitted with two constitutive models: Gent, that allows for a direct quantification of the strain hardening through the J_m parameter but diverges at stretches approaching the finite extensibility, and Yeoh that can be used in finite element modelling.

- The bulge inflation experiment was modelled and showed that while our analysis of the experiment is only approximate, it brings the perspective of a systematic comparison between the modelled inflated bulge and the experimental one for a more robust determination of the constitutive model and its parameter for the material's description.

- The toughness of the materials was measured via single notched test in uniaxial traction. The fracture energy depends on the testing velocity, suggesting a role of the viscous dissipation at the crack tip.

- The material parameters are all linked together. With little surprise, the formulations with the highest Young's modulus are also the toughest and have the highest strain hardening.

Chapter 4

Testing thin elastomeric layers under hydrostatic traction

In this chapter, we will discuss the theory around the cavitation in soft incompressible layers and the different techniques used for its analysis. We will then describe the hydrostatic traction set-up we designed to confine polymer films of a thickness of hundreds of micrometers. Through careful sample preparation, cavitation is induced in the samples through the increase of the hydrostatic pressure. The cavitation resistance is then analysed via image analysis and FEM modelling.

4.1 How can we observe and describe cavitation?

In a nutshell, cavitation in soft solids appears due to their very high bulk modulus K compared to their shear modulus μ. When put under hydrostatic stress, it is energetically more favourable for them to grow a cavity by shear (and therefore by breaking bonds internally) than to deform by changing its volume and decrease its density. Once a cavity opens, elastic energy is released and the increased volume by the opened cavity releases the hydrostatic stress in its surrounding. The questions surrounding cavitation is soft solids are:

- How do these cavities nucleate? Is it around an initial defect in the network, like a less crosslinked region or a dust inclusion, or is it a fracture nucleation?
- How do these cavities grow?

We will try and discuss the different phenomena as described in the literature and the experimental techniques available to analyse the cavitation process.

4.1.1 Theoretical models for cavitation

We will first consider the growth of a cavity. As a thought experiment, let's visualise a block of polymer under hydrostatic stress, containing one spherical cavity. The cavity is supposed to be small enough to not "feel" the size effects, meaning that the cavity can be considered growing in an infinite medium.

One of the first analysis of such a bubble expansion has been proposed by Gent and Lindley [1]. As described on Figure 4.1, they consider the elastic expansion of a spherical cavity in a block of incompressible, Neo-Hookean material under hydrostatic pressure. Thanks to the incompressibility, the external pressure field is equivalent to an internal pressure in the cavity. In this case, the cavity grows purely by elastic deformation of the surrounding network. With λ the deformation of the cavity and E the material's Young's modulus, the pressure can be expressed as:

$$P = \frac{E}{6}\left(5 - \frac{4}{\lambda} - \frac{1}{\lambda^4}\right) \tag{4.1}$$

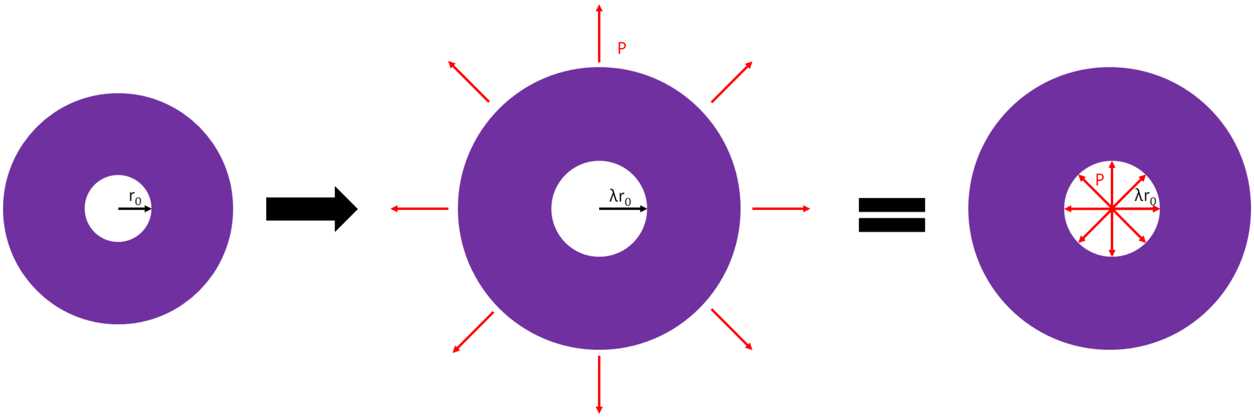

FIGURE 4.1: Gent and Lindley inflation model [1]. The material is considered incompressible and following a Neo-Hookean elastic behaviour. The far-field applied pressure is expending the pre-existing spherical cavity elastically. This is equivalent to considering the pressure to be directly applied inside the cavity.

Based on equation 4.1, for a pressure of $P_m = 5E/6$, $\lambda \longrightarrow \infty$. This means that for pressures over P_m, the cavity is no longer stable and will expand dramatically, but always elastically. This theoretical derivation was describing their results on hydrostatic traction of confined rubber cylinder and is particularly interesting as the cavitation resistance depends solely on the material's elasticity, with no effect of the defect size, unlike usual fracture experiments [1].

While this theoretical result is very simple and attractive, there are two main points that need to be discussed. First of all, the critical growth of a cavity can not be purely elastic. As mentioned in chapter 3.1.2, the Neo-Hookean strain energy density does not take into account the finite extensibility of polymer chains. However, this finite extensibility exists, and the cavity inflation will submit the network surrounding it to large deformations. If the inflation were to be purely elastic, the cavity growth would therefore be limited by the maximum extensibility of those chains. The fact that cavities can grow dramatically implies a fracture process that need to be added to the cavitation model. The second idea is the size effect of the tested sample, and therefore of the defects inside it. Gent and Lindley's model implies that the cavitation behaviour is exactly the same, no matter the size of the initial cavity, which is not physical. This was already underlined by Gent in his *"Cautionary tale"* of cavitation [90]: this simple description depending only of the elasticity of the network works in the presence of big defects, but experimental tests show that small rubber volumes resist to higher pressures than predicted ([7], [91]). Williams and Schapery were the first to try and explain the additional cost needed to expend small spherical defects in an infinite Neo-Hookean medium [92]. However, they did not conclude on the origin of this energetic cost, they only consider a surface energy applied on the cavity. This increased resistance can be explained by the fracture process happening for the growth of cavities, or by their surface tension.

4.1.1.1 Addition of fracture energy

Gent and Wang were one of the firsts to propose the analysis of the cavitation growth by fracture [2]. This analysis comes from the observation that samples with only small cracks cavitate at higher critical pressures than expected. This means that an additional force is exerted on smaller cavities that prevent them from growing. They analyse this phenomena by using Griffith criterion: a fracture can only grow if the released elastic energy is sufficient to overcome the critical energy release rate G_c. Their goal is to compute the energy release rate G for an initially present penny shaped crack, depending on its size, to determine under which applied negative hydrostatic pressure they could grow by fracture.

The steps for computing the energy release rate G of a penny shaped crack in an infinite Neo-Hookean medium is described on Figure 4.2. The basis of their assumption is that spherical cavities in rubber come from penny shaped cracks, and that these penny shapes can be inflated into spheres of the same radius with no additional pressure. Under hydrostatic stress, the cavity of radius r_0 is inflated into a radius of R_0. By comparing the energy released between two configurations of cracks of different radii inflating into the same final cavity volume, they compute the energy release rate of a penny shape in an infinite medium.

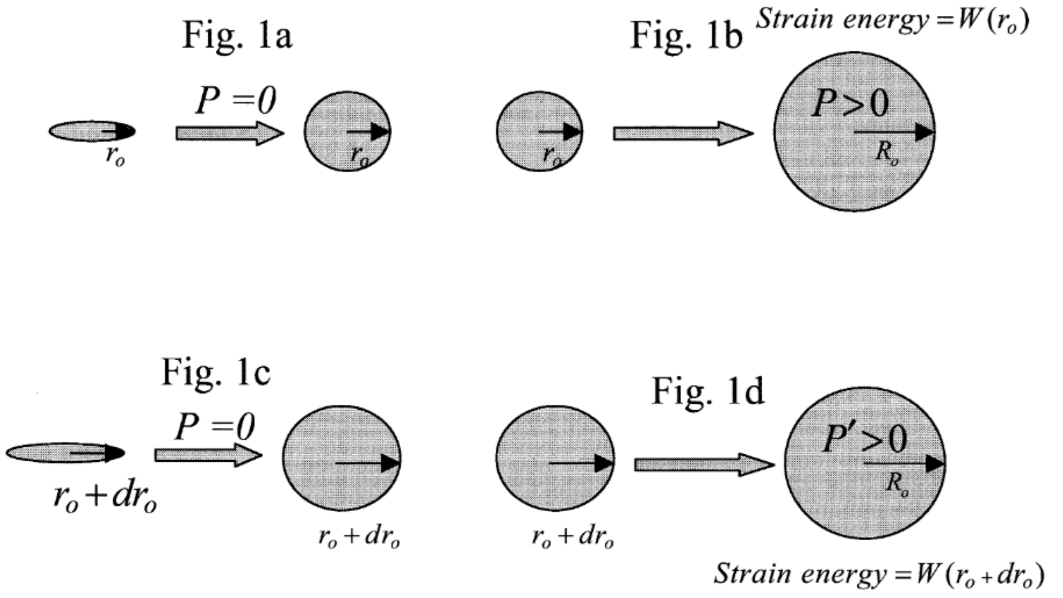

FIGURE 4.2: Growth of a cavity by fracture - Gent and Wang model [2], schematic taken from [93]. The energy release rate is estimated by comparing the strain densities in the case of a growth of a cavity of radius r_0 and the one of radius $r_0 + dr_0$ to the same final volume.

Their analysis leads to a relationship between G, P and λ the expansion ratio of the cavity:

$$\begin{aligned} \lambda &= \frac{R_0}{r_0} \\ P &= \frac{E}{6}\left(5 - \frac{4}{\lambda} - \frac{1}{\lambda^4}\right) \\ G &= \frac{2Er_0}{3}\left(1 + \lambda^2 - \frac{2}{\lambda}\right) \end{aligned} \tag{4.2}$$

This description allows for cracks of intermediate size to propagate into fracture, but very small cracks still don't reach G_c, regardless of the extension applied on their surface. This is justified by the absence of finite chain extensibility in the Neo-Hookean model. However, this computation technique allows for the analytical computation of a penny shape growth that shows the effect of the initial defect size on the critical cavitation pressure. They also derived the range of defect sizes (between 0.5 μm to 1 mm) for which the pressure triggering cavitation lies between 3E and E for defects in usual rubbers (G_c = 100 J/m^2 and E = 2 MPa).

Building on this fracture hypothesis, Lin and Hui proposed to compute numerically the strain energy release rate for various types of non linear elastic behaviours [93]. They used a finite element modelling method to study the growth of penny shaped cracks, this allowed them to not assume the shape of the crack to be spherical. Based on this analysis on Neo-Hookean materials, they could conclude that the Gent and Wang model overestimated G, leading to smaller predicted critical pressures. They could also investigate the influence of material properties on the growth, especially the effect of strain hardening that increases the critical pressure for the same initial defect radius.

In order to separate the elastic expansion from the fracture phenomena in cavitation, Lefèvre, Ravi-Chandar and Lopez-Pamies confronted a FEM modelling of the poker-chip experiment with a material showing only elastic (and hence reversible) deformations to the experimental results from Gent and Lindley [94]. When computing the loading curve of the poker-chips with predesigned spherical cavities, they obtained stresses that were quite different from the experimental curves from Gent and Lindley. However, the evolution of the defects in the modelled network seemed to correspond to the experimental nucleation and growth. Lefèvre et al then concluded that while the cavities growth could be qualitatively reproduced by the deformation of a purely elastic network under hydrostatic stress, the modelled macroscopic loading deviated from the experimental values. This lead them to conclude that a simple elastic and reversible growth of the cavities was not enough to describe the cavitation behaviour in rubbers.

Finally, Kang et al. showed that the fracture component in the cavitation behaviour could lead to an unstable cavity growth [3]. They stated that in many experiments, the difference between elastic cavity growth and fracture propagation is hard to differentiate. Still in the study of a Neo-Hookean material, they modelled a spherical cavity with a ring shaped crack around it. By changing the ratio between the radius of the cavity R and the initial crack size a, they can switch the cavity from a pure bubble ($R \gg a$) to a penny-shaped crack ($a \gg R$). Through a finite element analysis, they could compute the elastic energy release rate G for two different loading modes: either a pressure controlled experiment, or a volume controlled one. In the pressure controlled loading, the cavity inflates but the crack does not propagate until the pressure reaches its critical value of 2.5μ. In a volume controlled loading, the behaviour of the energy release rate is very different. For a fixed inflation volume, G has a non monotonic evolution with crack length a: it reaches its maximum for a specific a/R ratio and decreases again for larger cracks. Therefore, for small initial cracks, when the inflation volume reaches its critical limit (hence when $G = \Gamma$), the crack can suddenly grow without volume change. Past this unstable growth, the crack can only propagate with a volume inflation. This behaviour is summarized on Figure 4.3.

Assuming that the cavitation process involves a fracture event allows to explain, to some extent, why smaller samples, hence with smaller defect sizes, need higher hydrostatic pressures to cavitate. It also opens the door for unstable growth of cavities in the medium. However, it is important to note that these descriptions of cavity growth consider only the fracture mechanism, but not the surface tension of said cavities. But, the smaller the initial defect, the higher the surface to volume ratio, therefore the more important the surface tension will be.

4.1.1.2 Considering the surface tension of small cavities

Gent and Tompkins proposed to add surface tension as an additional stress applied on small defects, explaining why small cavities appeared to never expend in rubbers under hydrostatic

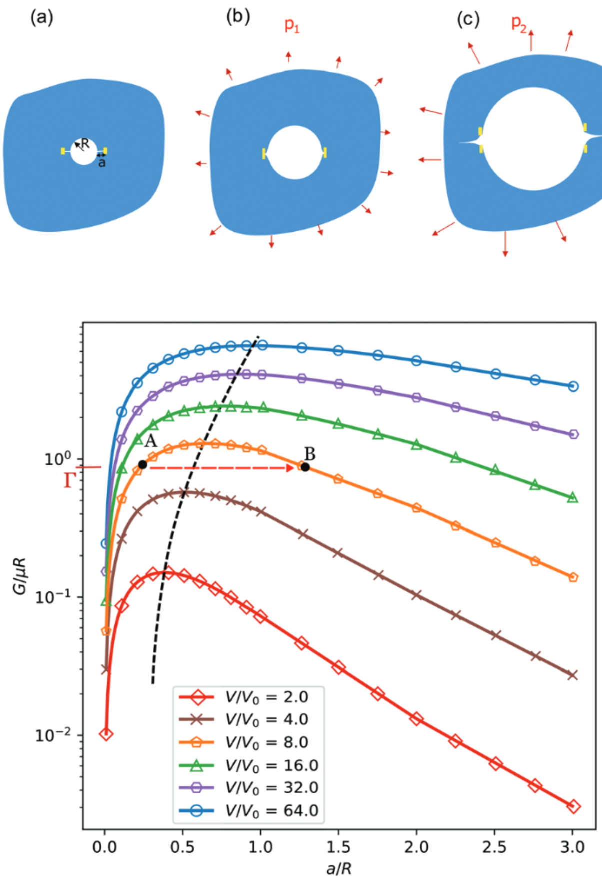

FIGURE 4.3: Dependence of the normalized energy release rate on the size of ring crack for different cavity volumes in a volume controlled experiment - Kang et al. model [3]. The schematics show the initial configuration (a): spherical cavity of radius R and initial ring crack of radius a, (b) under a small hydrostatic pressure, the cavity expends but the crack doesn't propagate, (c) at a large enough loading, the crack propagates with the cavity expansion. Graph: The black dashed curve connects the maximum G values for different cavity volumes. The evolution of the energy release rate is not monotonic with the crack length. Considering a material's toughness Γ and a small initial crack length (corresponding to the abscissa of A), when the inflated volume is high enough ($V/V_0 = 8$), $G = \Gamma$ and the crack will grow unstably from A to B at constant volume V. The crack is then stopped and a further propagation will require an increase of V.

stress [95]. Considereing an infinite Neo-Hookean medium, they buildt from equation 4.1 to:

$$P = \frac{E}{6}\left(5 - \frac{4}{\lambda} - \frac{1}{\lambda^4}\right) + \frac{2\gamma}{r} \tag{4.3}$$

where r is the deformed bubble radius and γ the surface tension, fixed at 0.025 N/m. Let's consider a gas bubble of initial radius r_0 that is trapped in the rubber network during the crosslinking. Around the bubble, the elastic forces are 0. The bubble then shrinks due to the gas diffusion out of the network until the internal pressure drops to 0. Small cavities simply close, but for large enough r_0 (larger than 1.10^{-8} m), the spherical cavity does not disappear but slowly shrinks to a radius $r_1 < r_0$. The value of r_1 depends on the elasticity μ and the surface tension γ. When the block of polymer is put under hydrostatic tensile stress, the surface tension tends to stabilise the cavity, leading to an increase of the critical pressure at which the cavity expands as r_1 decreases, as shown on Figure 4.4.

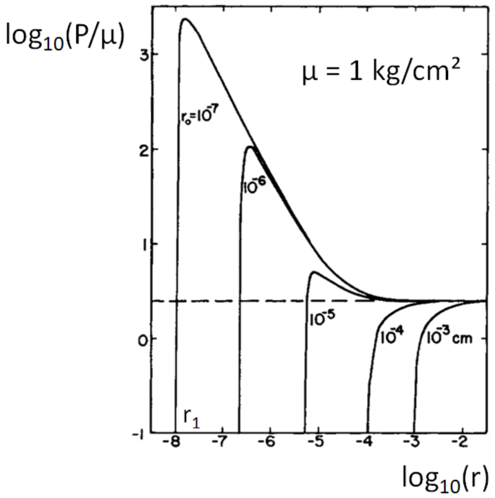

FIGURE 4.4: Inflation pressure P vs. hole radius r for various values of the initial hole radius r_0 - Gent and Tompkins model [95]. The smaller the initial radius r_0, the bigger the pressure needed to expend it. Bigger cavities opens at the critical pressure of 2.5μ as they are not influenced by γ.

The surface tension only impacts small enough bubbles. The effect of surface tension is non negligible for defects sizes under γ/E, which corresponds roughly to 50 nm in rubbers. This shows that the surface tension effect will mostly act on the nucleation of small defects in rubbers, but not on their growth. The value of this critical radius and the overshoot of pressure depends on the elasticity of the medium, and contrary to the intuition, stiffer elastomers show smaller critical pressures for small holes than softer ones. Based on this simple analysis, they suggest that the distribution of defects sizes in a specific sample can be determined by the number of opened cavities for a given applied pressure. Indeed, big defects would open at the standard pressure of 2.5μ, but if the sample does not fail, increasing the pressure over this value would open the smaller ones. They also theorise that the maximum pressure any rubber could sustain would correspond to the pressure needed to open cavities of 1 nm radius. Even if their analysis can not be strictly valid for such small sizes, they imply that this extreme pressure would be of the order of magnitude of 100 MPa. However, the true existence of this limit is a mystery, as it can never be tested experimentally.

It is interesting to note that the increased cavitation resistance was seen on **small samples**, which was explained by the fact that the smaller the sample, the smaller the defects, but the modelling has always been considering **infinite** Neo-Hookean medium. To tackle this, Dollhofer et al. proposed an analysis of an incompressible Neo-Hookean material of finite dimensions [4]. They consider a bubble of initial radius A enclosed in a polymer shell of radius B. Under pressure, the bubble deforms into a radius a and the shell into a radius b. In this case, A is not negligible compared to B. The system is drawn on Figure 4.5. This is justified by the fact that in many experiments on thin films, such as probe tack experiments [96], the cavities opening are not small compared to the film's thickness.

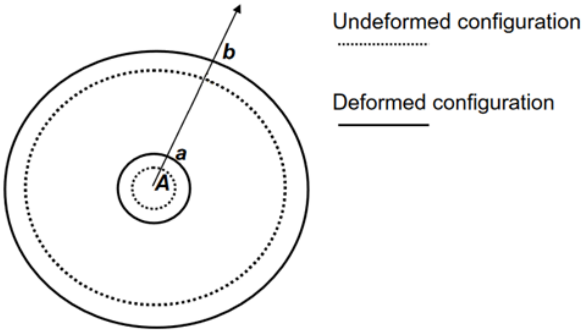

FIGURE 4.5: Cavity expansion in a thin shell

Furthermore, while the other models assumed a constant pressure in the cavity, Dollhofer et al. use a loading method on the shell called "deadload". This means that the force exerted of the shell is constant. However, the pressure inside the cavity changes as it expends, only the integral of the total pressure over the cavity's walls is constant. The inflation of a bubble in a finite shell leads to additional terms in the pressure applied on the cavity surface, which leads to a variation from equation 4.3:

$$P = \frac{E}{6}\left(\frac{4}{\lambda_B} + \frac{1}{\lambda_B^4} - \frac{4}{\lambda} - \frac{1}{\lambda^4}\right) + \frac{2\gamma}{\lambda A} \tag{4.4}$$

where γ is the surface tension, λ is the hoop stretch at the cavity surface and λ_B is the hoop stretch at the outer shell surface. $\lambda A = a$ is the deformed radius of the cavity. Their study is based on a minimization of energy analysis: when loading the sample under hydrostatic pressure, they look for the stable, metastable and unstable deformations of the bubble. A stable position is at the global minimum of the energy curve, a metastable position is at a local minimum and an unstable is at a maximum of the energy curve. If a metastable position exists, an unstable position exists. Dollhofer et al. investigated the evolution of a big defect, (A/B = 0.2, γ not predominant), and a small defect (A/B = 0.01, γ is not negligible) in a dead load type of loading.

The big defect shows a stable growth, the potential energy shows only stable points as the pressure increases, leading to a stable increase of the cavity deformation. For the small cavity now, the energy curves show a very different behaviour as the surface energy plays a bigger role. At rest, the surface tension shrinks the cavity, so the stable position is at $\lambda < 1$. When the loading increases, the stable position moves towards 1, the pressure starts to fight the cavity constriction. At one point, the constricted state of the cavity shifts from stability to metastability, and the energetically stable state becomes the expanded cavity: $\lambda > 1$. This is shown on Figure 4.6 (A). The constricted cavity is first stable (in green), but when the traction increases, the stable position is suddenly at very large strains. It is important to note that the presence of a second stable position at the expanded state is both due to the surface tension and the elastic instability of the swelling of thick elastic shells. The finite size of the sample and the deadload boundary condition alone lead to the blue curve presented on Figure 4.6 (C), with a stable growth that is not linear with the applied pressure. As a reminder, in the idea of Gent and Lindley in an infinite Neo-Hookean medium with imposed cavity pressure, the cavity would grow and explode for pressures above 5E/6.

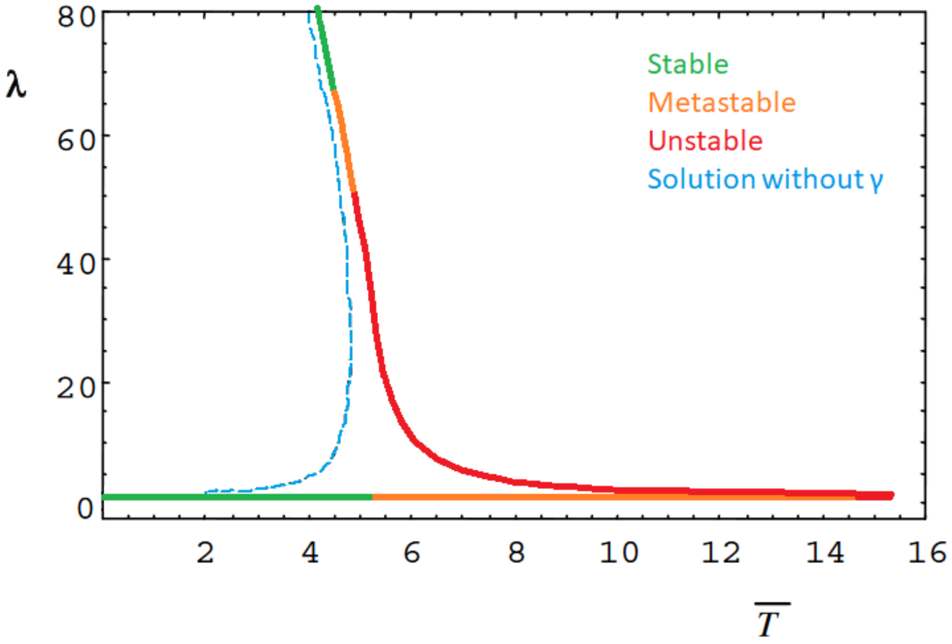

(A) Cavity stretch versus normalized true traction $\overline{T}$

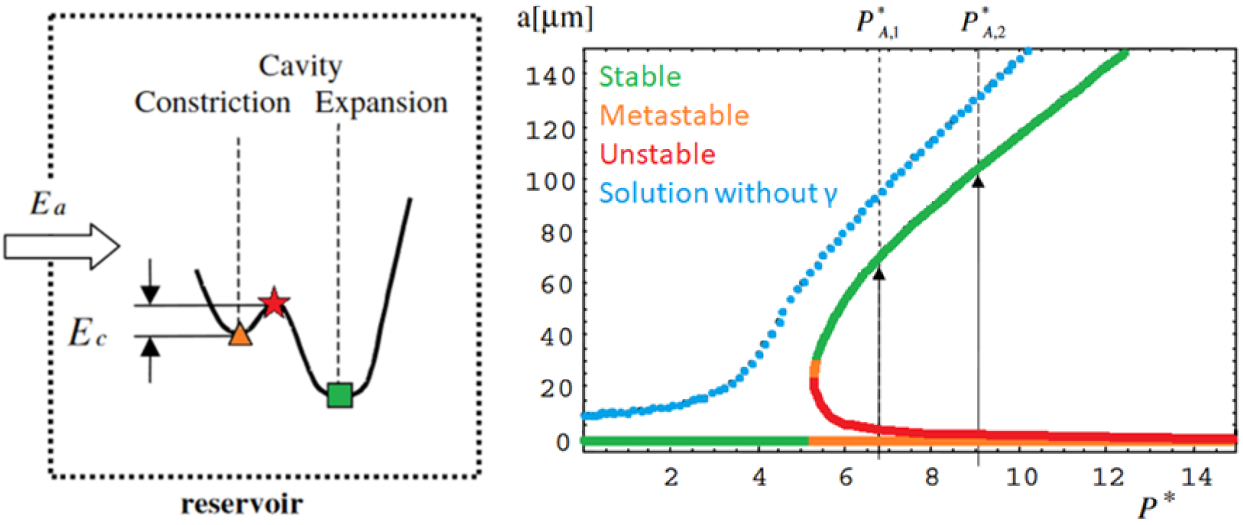

(B) Activation energy issue

(C) Deformed cavity radius versus normalized nominal traction P*

FIGURE 4.6: Cavitation instability for small defects in confined layers - Dollholfer et al. model [4]. Material parameters: E = 0.05 MPa, γ = 0.03 N/m, $B = 50$ μm, $A_{big} = 10$ μm, $A_{small} = 0.5$ μm. (A) The blue broken curve represents the stretch evolution for the big cavity, the surface tension impact on the small cavity leads to a switch to metastability of the constricted cavity ($\lambda < 1$)). (B) E_a is the available energy, E_c the energy barrier. When the constricted position becomes metastable, the transition to the stable expended cavity requires to jump over the potential barrier E_c. This is only possible if $E_a > E_c$. (C) For the big cavity (blue dots), the bubble growth is continuous. For small defects, the jump from constricted to expanded arises depending on the energy barrier and the available energy, as shown by the black arrows.

In an idea of energy minimisation, one could think that as soon as the $\lambda > 1$ solution becomes energetically stable, the cavity would expand directly. But, as shown on Figure 4.6 (B), when a cavity is in a metastable position, it has to overcome a potential energy barrier to be able to jump to the stable solution. This is only possible if enough energy is given to the cavity. Depending on the given energy and the height of the barrier, the jump to the expanded cavity will occur at different critical pressures, as displayed on Figure 4.6 (C). Note that the size of the stable expanded cavity is of the order of magnitude of 100 μm, which is quite large for "just" a surface tension stabilisation. To summarize, given the surface tension effect, a small defect will snap into an expended cavity if two conditions are met:

- the loading pressure is high enough so that the expanded cavity solution is energetically stable, the constricted one becomes metastable.
- The given energy to the system is high enough so that the potential barrier E_c can be overcome.

This type of growth instability has been referred as **snap cavitation**, as an analogy with the snap-through buckling. The analysis of Dollhofer et al. compares quite well to experimental observations in cavitation during probe tack measurements on very soft and viscous materials: Pressure Sensitive Adhesives (PSA). The probe tack technique will be described in more details in Section 4.1.2. In particular, it was used by Chiche et al. to explain the critical cavitation pressure difference between thin and thick layers [96]. They observed the same growth behaviour depending on the size: big defects grow continuously while other bubbles appear suddenly upon loading, meaning that their initial defect size was too small to be detected. Chiche et al. observed that thick layers (240 μm) would show lower critical hydrostatic pressures than thin ones (60 μm). In this test, the sample is loaded under hydrostatic traction, so the given energy to the system is the elastic deformation applied. Basing their discussion on Dollhofer et al. computations, they suggest that the difference lies in the fact that a thin layer will store less elastic energy during the loading compared to the thick one.

Let's imagine one defect of radius r_i in both layers. Its critical pressure to snap is $P_{c,i}$ and the corresponding energy barrier is $En_{c,i}$. In thick layers, the build up of hydrostatic pressure is lower than in thin layers, so the displacement needed to reach $P_{c,i}$ will be high, leading to a huge elastic energy, so the snap to the expended cavity will happen as soon as $P_{c,i}$ is reached. In the thin layer, the hydrostatic stress will be high already for small displacements, so reaching $P_{c,i}$ will be quick, but the stored elastic energy will not be high enough. Therefore, a higher loading of the sample is needed, increasing the stored elastic energy and decreasing the energy barrier. The snap will therefore happen as soon as the given energy is reaching $En'_{c,i}$, the energy barrier at the increased loading $P'_{c,i}$. To summarize, the snapping in the thick layers is limited by the pressure build up, the snapping in the thin layers is limited by the stored energy build up, leading to an increased load before rapid expansion actually occurs.

We can conclude here that the surface tension effect on the cavitation behaviour will always be to increase the needed hydrostatic pressure for the growth of small cavities, but it can also lead to an unstable growth from a closed configuration to a stable expanded cavity. It should be noted that Dollhofer et al did not take into account the fracture energy. In this case, it is justified since the tested materials in the experiments are extremely viscoelastic and only lightly crosslinked so that the cavitation phenomenon is not predominantly a fracture behaviour. In the Gent and Tompkins picture however, they justify that the fracture energy for big defects is unimportant (which is already a big assumption, as discussed in Section 4.1.1.1), but they do not comment on the rubber deformation once small cavities snap, which must produce scission of the polymer chains.

4.1.1.3 Effect of the triaxiality of the applied stress

In the theoretical models we discussed, the loading was always considered purely hydrostatic. However, in the experimental set-ups, that we will shortly review in the next section, the loading may not be purely hydrostatic. Lopez-Pamies et al. proposed a cavitation criteria in rubber considering the sudden elastic growth of its pre-existing defects when put under hydrostatic stress [97]. When considering a Neo-Hookean elastic behaviour, this criteria states that cavitation can occur at the points where:

$$\begin{aligned} &8t_1t_2t_3 - 12\mu(t_1t_2 + t_2t_3 + t_3t_1) + 18\mu^2(t_1 + t_2 + t_3) - 35\mu^3 = 0 \\ &t_i > 2.5\mu \end{aligned} \tag{4.5}$$

where t_i are the principal Cauchy stresses and μ is the shear modulus.
In the case of a purely hydrostatic stress, this results in the same expression that was predicted by Gent and Lindley:

$$\begin{aligned} t_1 = t_2 = t_3 = P \\ \frac{1}{3}(t_1 + t_2 + t_3) - 2.5\mu = 0 \end{aligned} \tag{4.6}$$

However, in the case where there is shear ($\tau_1 = t_2 - t_1$, $\tau_2 = t_3 - t_1$), the criteria states that P must exceed 2.5μ. In that sense, the presence of shear stabilises the rubber as it postpones the validation of the cavitation criteria. Lopez-Pamies et al. showed this difference when considering the impact of shear on the flat against flat geometry [94]. In particular, they showed that if the confinement is high, the difference between the general criteria and the assumption of pure hydrostatic stress ($t_1 = t_2 = t_3$) is small. However in thick poker-chip experiments, the shear becomes non negligible and the general criteria described in equation 4.5 is never met in the center of the polymer. It is only met near the sample's interfaces where there is non-slip conditions between the polymer and the holders. When only considering the pressure field, a sufficient loading of the thick sample will eventually lead to a validation of the hydrostatic criteria (4.6) in the whole thickness of the deformed polymer. This shows how a more general criteria for cavitation is needed, especially when the confinement of the polymer is not that important, leading to significant shear stresses in the network.

This result is coherent with Hou et al. that showed that the minimum of the mean stress at cavitation is found in a pure hydrostatic stress ($t_1 = t_2 = t_3$) [98]. They propose a "cavitation surface" $\mathcal{S}$ that becomes, for Neo-Hookean materials:

$$\mathcal{S} : (4t_1 - t_2 - t_3)(4t_2 - t_3 - t_1)(4t_3 - t_1 - t_2) - 125\mu^3 = 0 \tag{4.7}$$

They also compared their prediction with Gent and Lindley's experimental results on the confined cylinders of rubber [1]. Hou et al. showed that the thickest samples (h = 0.565 cm, D = 2 cm), that never showed any cavitation in the experiments did not meet their cavitation criteria (equation 4.7), while all the thinner ones did.

Considering the cavity growth, Long and Hui investigated via finite element modelling the evolution of the energy release rate of cracks in elastic materials under different types of loadings [99]. They considered an infinite block of Neo-Hokkean material with a unique initial penny shaped crack. This block of polymer is subjected to 2 remote stresses: T is a tension stress normal to the undeformed crack faces, S is a tension stress parallel to the undeformed crack faces. They computed via finite elements analysis the energy release rate for different loading geometries ranging from the uniaxial tension (S/T = 0) to the pure triaxial tension (S/T = 1). They showed that G is always higher for a pure triaxial tension, and the difference between the loading states becomes larger when the average remote tension increases. A sharper strain hardening, i.e a decrease of the finite extensibility of the polymer chains in the material, decreases the energy release rate for the same average stress level in comparison to the Neo-Hookean material.

4.1.1.4 Conclusion on the theoretical models

The models we described here all try to explain the growth of a cavity in a homogeneous medium containing small pre-existing defects. When put under sufficient hydrostatic loading, the defects can grow. The mechanism of this growth is determined by the material properties. At first sight, big defects could simply grow by an elastic expansion that is controlled by the Young's modulus and the strain hardening of the material. However, upon closer inspection, the critical fracture energy of the material is one barrier to over come for this dramatic growth to occur. Furthermore, experimentally testing smaller samples leads to higher measured cavitation pressures ([7], [91]). This means that the effect of the defect size can become crucial.

Both fracture energy and surface tension will hinder the nucleation and the expansion of small defects, therefore leading to a need for an increased hydrostatic pressure for their expansion. In both models, the possibility for an unstable growth of small defects (snap cavitation) was shown ([3], [4]). The importance of a triaxial stress state was underlined by both analytic work on the cavitation criteria ([97], [98]) and finite element modelling on the energy release rate [99]. This gives guide lines for the testing of cavitation: the lowest cavitation resistance should be found in a sample loaded in a purely triaxial traction, which optimises the cavitation criterias we presented (equations 4.5 and 4.7), with the lowest amount of strain hardening, which maximises the energy release rate for the propagation of the penny shaped crack [99].

However, a general model that could describe both the effect of the fracture energy and of the surface tension of the material on its cavitation behaviour is still lacking and such a model could be useful to predict the onset of cavitation over a small volume of a crosslinked elastomer containing (hopefully) small initial defects. Indeed, this type of system would have these two energy barriers to overcome to cavitate.

Finally, the question of the origin of the defects is also still open. In some modelling work which targets growth, the nucleation can be introduced by choosing the position of zero volume cavities of arbitrary shapes [94]. If these defects are small enough, their specific shape and size do not influence their "nucleation" during the loading. This allows for the determination of multiple cavity growth criteria of the samples, even if it is not per se an analysis of the nucleation process.

4.1.2 Different techniques to test materials under hydrostatic pressure

Let's now review the experimental ways to provoke cavitation in polymer networks, and how they are analysed. The biggest differences between the theory that was presented in the last section and the experiments are that:

- The real network's behaviour is not purely Neo-Hookean in most cases, as the finite extensibility of chains will impact the nucleation and growth of cavities.
- The initial defect, or defect distribution, size and shape is not known or controlled.
- The boundary conditions are difficult to control for thin layers, which can add reproducibility problems.

These are some of the reasons why the comparison between the theory and the experimental results is not trivial.

4.1.2.1 True hydrostatic pressure by fluid saturation

In order to provoke cavitation in rubbers, one idea is to saturate them with a fluid and change suddenly the conditions to provoke a change of state of the trapped fluid in the network. For example, Denecour and Gent tested swollen vulcanized rubber sheets under a high temperature differences [100]. If the temperature shock is big enough, the solvent trapped in the network transitions into gas, the vapour bubble expands in the rubber sheet which leads to its inflation into a balloon, and then to its burst. They could draw a linear relation between the solvent vapour pressure at which the bubble formed and the elastic modulus of the swollen networks μ. They find the 2.5μ limit again, which they justify by the presence of large initial defects in the rubber.

Still considering the cavitation growth by liquid saturation, Kim et al. took the approach of phase separation between the network and the swelling solvent [5]. In this experiment, they stretched elastic silicone gels (E = 71 - 800 kPa) and swelled them in fluorinated oil at 40°C. Once the swelling equilibrium was reached, the samples were cooled to room temperature at different temperature ramps, leading to the network/oil phase separation and therefore oil droplets nucleation and growth in the network while still being under the same stretch. All bubbles have an elongated shape due to the elastic deformation of the sample. The bubbles finally shrink once the oil evaporates from the sample. Given the bubble size, they must grow through fracture of the polymer. However, it seems that they display a self-similar growth and shrinkage that is consistent with damage occurring all around the bubble, and not just localized damage. For bigger flaws, the growth transitions to a crack tip and brittle fracture. The two different growing processes are described on Figure 4.7. Kim et al. suggest that the cavity growth is always linked to damage of the network, however it transitions from a ductile damage zone where the bond breakage is distributed around the surface of the cavity to a brittle crack propagation for bigger cavities where the damage is localized to a crack tip. The size transition appearing around the elasto-adhesive length Γ/E. This interesting result suggest that ductile damage could take place in elastomers while it is usually considered only brittle.

The bubble nucleation by saturation can also be provoked by saturating gas in rubber sheets and decreasing rapidly the pressure, like in the experiment of Gent and Tompkins [6]. They attributed the expected critical pressure for cavitation (2.5μ) to the presence of large defects in thick sample pieces. However, smaller test samples did not show any cavitation, which they attributed to a smaller defect sizes distribution. Furthermore, increasing the pressure applied above the critical cavitation pressure increased the number of observed cavities inside the rubber. This observation is displayed in Figure 4.8. They also observed that satellite bubbles would open next to growing bubbles, suggesting that the deformation of the polymer in the vicinity of the cavity lowers the critical stress needed to open a new cavity. Gent and Tompkins also conducted bubble nucleation by saturation experiments in samples held under uniaxial extension, and showed that their critical pressure of cavitation was reduced with an increase of this pre-stretch, which comforted their interpretation of the nucleation of these satellite cavities [6].

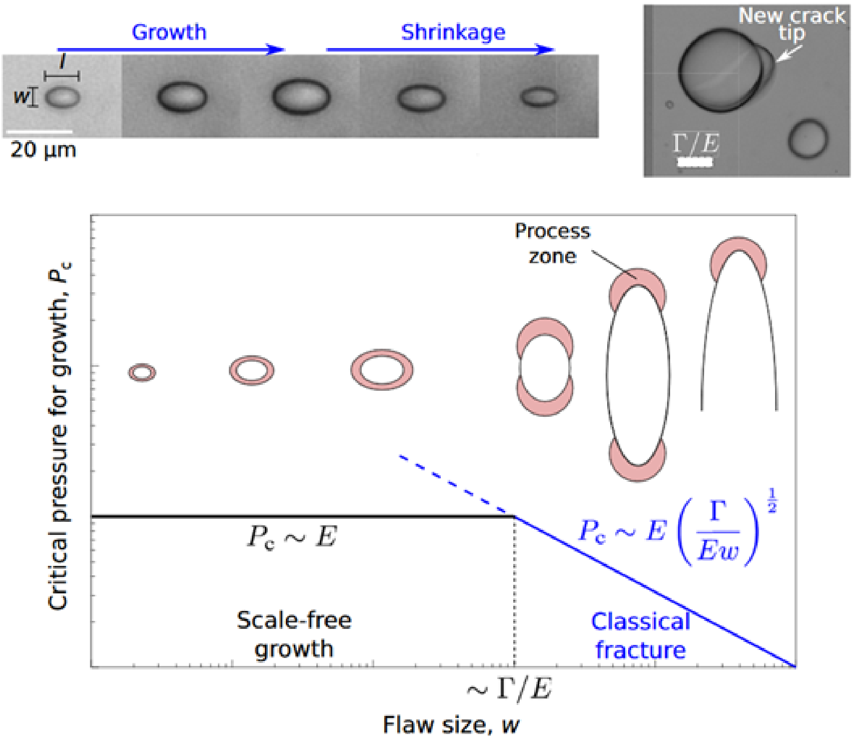

FIGURE 4.7: Transition from scale-free to crack-like growth - Kim et al. idea [5]. The graph represents the suggested behaviour of the cavitation pressure versus the defect size. The scale-free domain (in black) represents a growth behaviour non dependant on Γ, the transition to classical crack propagation occurs for defect sizes larger than Γ/E. Left insert: evolution of a bubble in silicone with E = 333 kPa, pre-stretch of 60%. Growth during the temperature drop, shrinkage due to the oil evaporation. For that system, Γ/E = 102 μm. Right insert: Bubble growth around a large salt crystal, the defect grows by the formation of a crack tip.

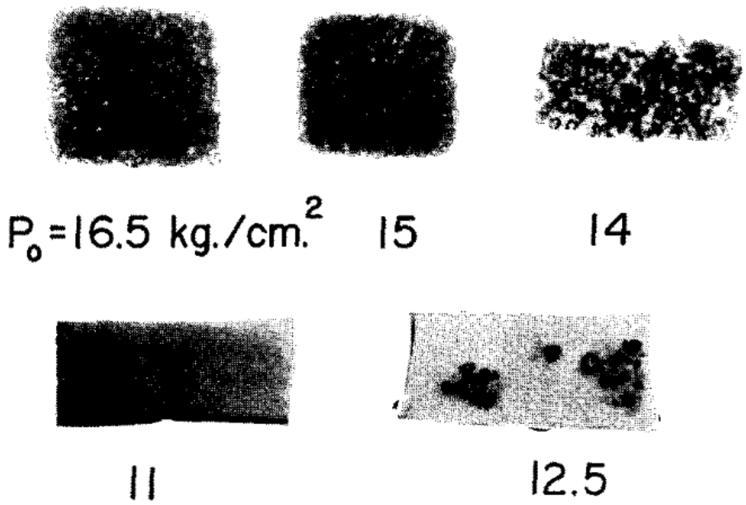

FIGURE 4.8: Number of cavities depending on the applied pressure - Gent and Tompkins [6]. The tested rubber has a shear modulus of μ = 1.9 kg/cm^2.

The molecular damage occurring in the network due to the nucleation and growth of these cavities has been explored more precisely by Morelle et al. [13]. They exposed an elastomeric network (E ≈ 1 MPa, G_c ≈ 180 J/m^2) tagged with Diels Alder mecanophores to high hydrogen gas pressures until saturation was reached and monitored the cavitation behaviour when the pressure dropped. During the pressure drop, the cavities nucleate and grow. By analysing the cavities shape during the de-pressurisation, it appeared that all cavities showed a self-similar growth at first, most of them then transitioning to an anisotropic growth shape while smaller ones kept the spherical shape. This is quite similar to the observation of Kim et al. [5]. The bubble evolution is displayed on Figure 4.9.

When the atmospheric pressure is reached and the sample is back at equilibrium, all cavities are closed and the sample looks undamaged. However, the mecanophores under went a retro Diels Alder reaction when the polymer chains are put under stress, leading to breakage and the formation of a fluorescent moiety. The resulting fluorescence is a marker of polymer chain scission. This is the same method that was used by Slootman et al. (see Section 3.1.4, [11]). This allowed for the post-mortem observation and quantification of the fracture of the closed cavities. Their first observation is that molecular damage is only seen in the sample where cavities appeared. Then, they observed that all cavities show a flower like fracture pattern around a nucleus of high molecular damage. The fracture pattern is also highly planar, which is consistent with a growth through the propagation of penny shaped cracks. This is true, even for small cavities that showed a self-similar growth and shrinkage. We could conclude that Morelle et al. observations are in contradiction with the analysis of Kim et al. However, it is not trivial to discriminate via a post-mortem analysis a closed cavity with damage around its volume and a fracture plane. To be able to discriminate between the two, one would need an observation of the damage in the inflated sample, during the loading.

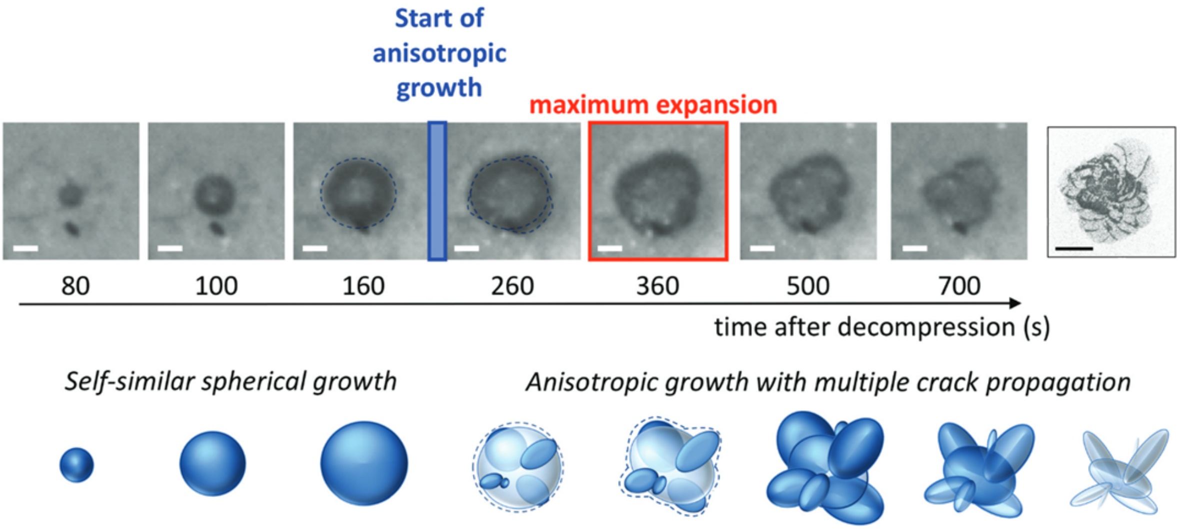

FIGURE 4.9: Optical observation of the cavity growth and explanation - Morelle et al. [13]. First line of pictures: Observation of a cavity during growth, the dashed blue lines highlight the differences in shape. Scale: 100 μm. The blue schematics underneath represent the proposed growth mechanism in the two regimes: self-similar growth and anisotropic growth. Boxed insert: top view of the associated fluorescent damaged region for comparison with the last inflated cavity image. Black scale bar: 100 μm.

However, even if their explanation of the crack growth is different, Kim et al. [5] and Morelle et al. [13] both showed, in experiments with a similar hydrostatic pressure loading, a similar growth of cavity that depends on the pre-stretching of the sample. Cavities show a self-similar growth and then transition into an asymmetric fracture process.

4.1.2.2 Hydrostatic traction on confined layers

The inflation of cavities inside polymer sheets with gas pressure allows for a true nearly triaxial testing of the elastomer. However, it is not possible to follow at each time the actual internal pressure at which the cavities nucleate and grow. Furthermore, it requires longer times as the polymer must reach saturation before it is tested. To be able to follow the hydrostatic stress as the cavitation occurs, several set-ups have been imagined to put a rubber layer under hydrostatic stress. By inducing a traction on a highly confined and incompressible layer, hydrostatic stress will build inside the polymer. Of course, the experimental challenge is to ensure a perfect adhesion (and therefore no slippage) between the polymer and the confining interfaces to test the bulk properties of the material. Different geometries can be used to confine and exert hydrostatic traction on confined layers.

Polymer confined between two rigid beads

Cho and Gent studied the confinement of a transparent silicone rubber confined between two steel spheres or two steel cylinders [7]. The adhesion between the surfaces was insured by a primer. They define the confinement ratio by h/D where h is the confined thickness of polymer and D is the radius of the spheres (respectively the cylinders). These geometries and the transparency of the rubber allowed them to observe the cavity shape and study the impact of the confinement on the hydrostatic pressure for cavitation. With little surprise for us now, they found (again) that large polymer thicknesses led to the usual cavitation limit of 5E/6 while high confinement ratios ($h/D < 0.5\%$) between two spheres would lead to cavitation pressures above 3E, while such an effect was not seen for the cylinder geometry. The difference in the two geometries is not explained in their study.

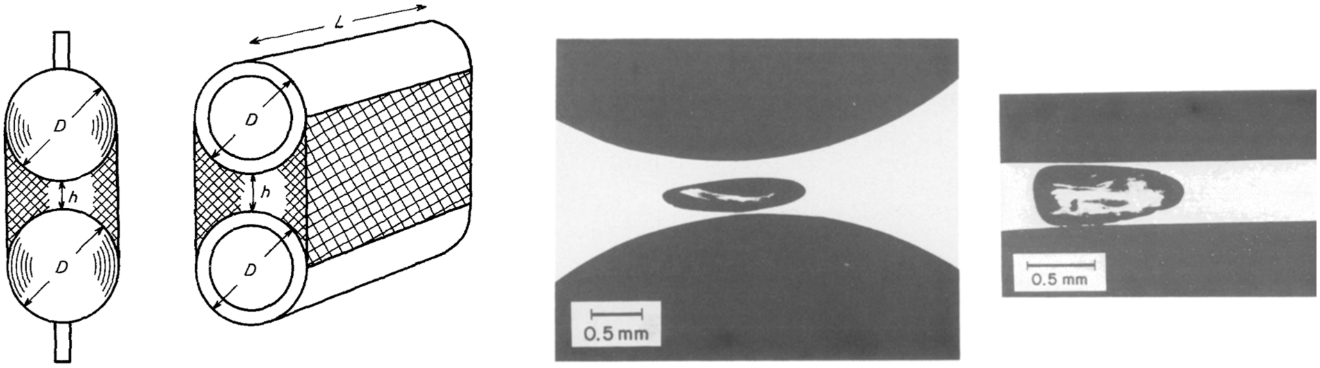

(A) Schematics of the sphere or cylinder confinement

(B) Resulting cavitation in the two confined geometries. Right: spheres, left: cylinders

FIGURE 4.10: Cavitation in confined silicone rubber layers between spheres or cylinders - Cho and Gent [7]. (A) The rubber layer is cross-hatched between the rigid surfaces in white. The specimens were prepared with various polymer heights h, h/D varied between 0.02 to 0.35. (B) Left: Cavity formed at tensile strain e_m of 0.23 between two steel spheres, h/D = 0.045. Right: Cavity formed between two steel cylinders, e_m = 0.08, same h/D.

Many years later, Poulain et al. proposed an updated experiment of confinement between two steel spheres [8]. Thanks to a higher time and spatial resolution, they could observe that the cavities appear in the vicinity of the interfaces, but still in the bulk of the PDMS. In all their systems, a similar cavitation behaviour happens, as described on Figure 4.11. First, cavities nucleate close to the interfaces, then they slowly grow into "micro-cracks", meaning cracks of a micrometer length scale. The conical shape is only due to the stress field between the beads, the unloaded crack is a penny shape. Finally, one crack grows into a macro-crack, the other cavities shrink.

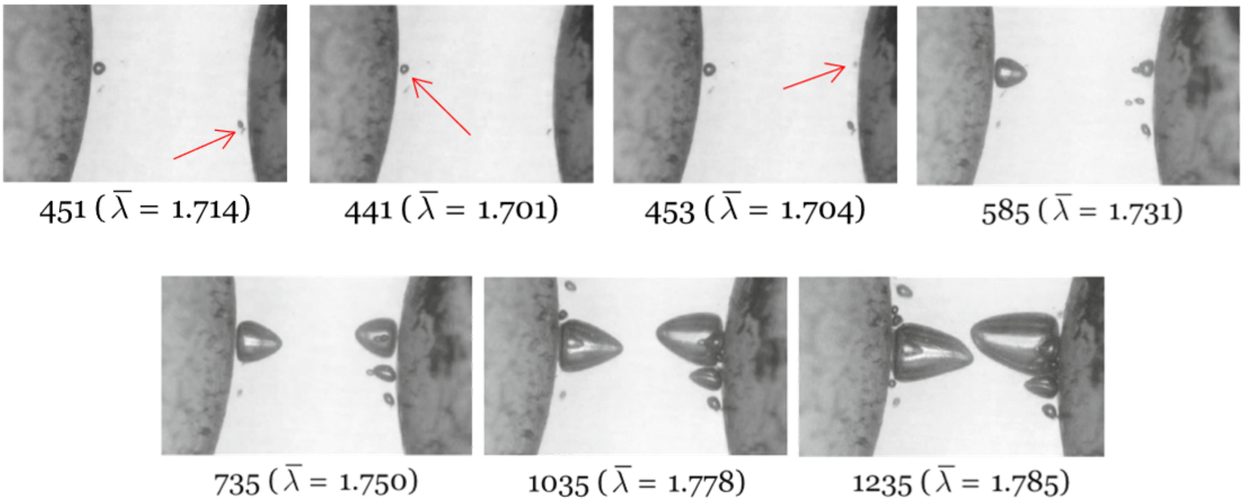

451 ($\bar{\lambda}$ = 1.714) 441 ($\bar{\lambda}$ = 1.701) 453 ($\bar{\lambda}$ = 1.704) 585 ($\bar{\lambda}$ = 1.731)

735 ($\bar{\lambda}$ = 1.750) 1035 ($\bar{\lambda}$ = 1.778) 1235 ($\bar{\lambda}$ = 1.785)

(A) Loading on a 15:1 silicone rubber (Test A) - high strain hardening

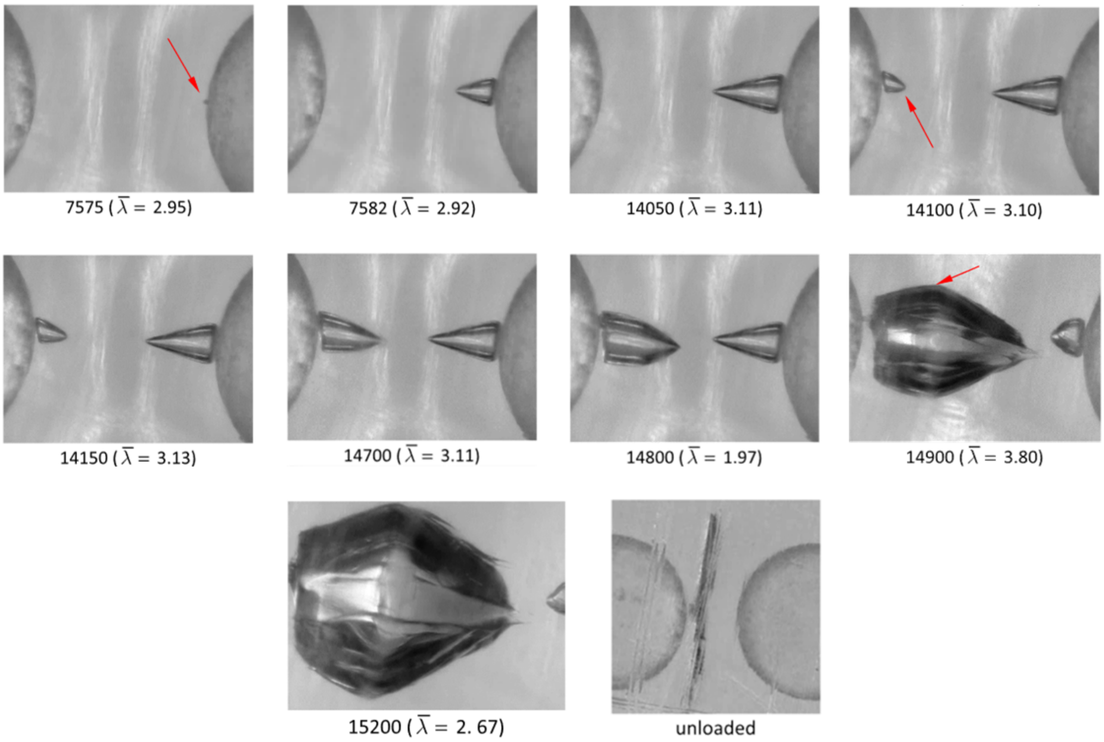

7575 ($\bar{\lambda}$ = 2.95) 7582 ($\bar{\lambda}$ = 2.92) 14050 ($\bar{\lambda}$ = 3.11) 14100 ($\bar{\lambda}$ = 3.10)

14150 ($\bar{\lambda}$ = 3.13) 14700 ($\bar{\lambda}$ = 3.11) 14800 ($\bar{\lambda}$ = 1.97) 14900 ($\bar{\lambda}$ = 3.80)

15200 ($\bar{\lambda}$ = 2. 67) unloaded

(B) Loading on a 45:1 silicone rubber (Test B) - no strain hardening visible in uniaxial testing

FIGURE 4.11: Nucleation, microcrack and macrocrack growth - Poulain et al. [8]. The ratios are PDMS : curing agent. $\bar{\lambda}$: average stretch between the beads. Due to experimental issues, the force during the experiment could not be measured, therefore the loading stress could not be described. (A) $h/D = 0.107$, the red arrows indicate the first three cavities forming, many more appear during the test. One cavity from each interface grows into a micro-crack and they interact with each other. (B) $h/D = 0.210$, the red arrows indicate the only two cavities that appear and, at $\bar{\lambda} = 3.80$, it indicates the crack tip position, which is not at the apex of the cone. From the two micro-cracks, only one cavity becomes a macro-crack that becomes the only visible damage in the unloaded sample.

The interaction between the cracks and the transition to macro-cracks depends on the material properties, as the softer network leads to a much larger macro-crack. This experiment sheds light on the results of Cho and Gent [7], as it appears that the final cavity between the beads did not nucleate in the middle of the confined layer, but probably comes from a nucleation near the interfaces that transited into a crack propagation.

Flat/flat against sphere/flat geometry

Finally, the most well known hydrostatic traction set-up is that of a disk confined between two rigid and flat surfaces. This is the famous geometry, used by Gent and Lindley and named poker-chip, that lead to one of the first descriptions of the critical cavitation pressure [1]. As displayed on Figure 4.12, when put under the same nominal loading, the thinner the test piece, the higher the number of cavities that appear in the sample. This observation is well explained by Kumar and Lopez-Pamies in their phase-field modelling of the poker-chip experiment [101].

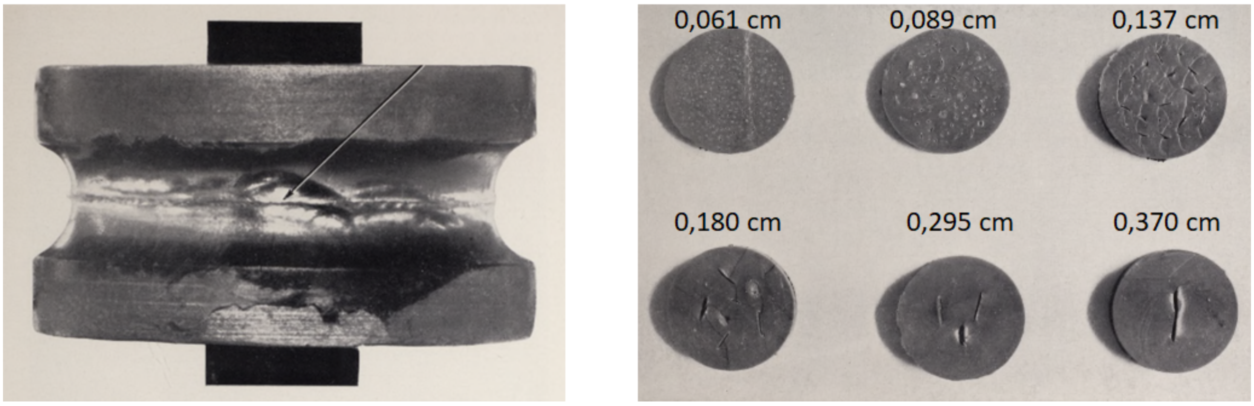

FIGURE 4.12: Poker-chip experiment - Gent and Lindley [1]. Left: Bonded cylinder under tensile stress. (B) Central cross-sections of test pieces of rubber D cut open after being subjected to a tensile stress of 28 kg/cm^2.

The flat/flat geometry is also used in the probe-tack test. This method is used to test the adhesion of viscoelastic PSA [12]. After a contact step where the material is compressed on a flat surface, the sticky and soft material is pulled from it, leading to the force versus stretch curve described on Figure 4.13. Cavities appear at the interface between the material and the surface, grow in the bulk of the layer and finally, the material stretches into fibrils. This is a slightly different behaviour than the one we are interested in, for two reasons: the cavitation is first an adhesion problem here, and their growth is not limited by fracture as the material is only loosely crosslinked.

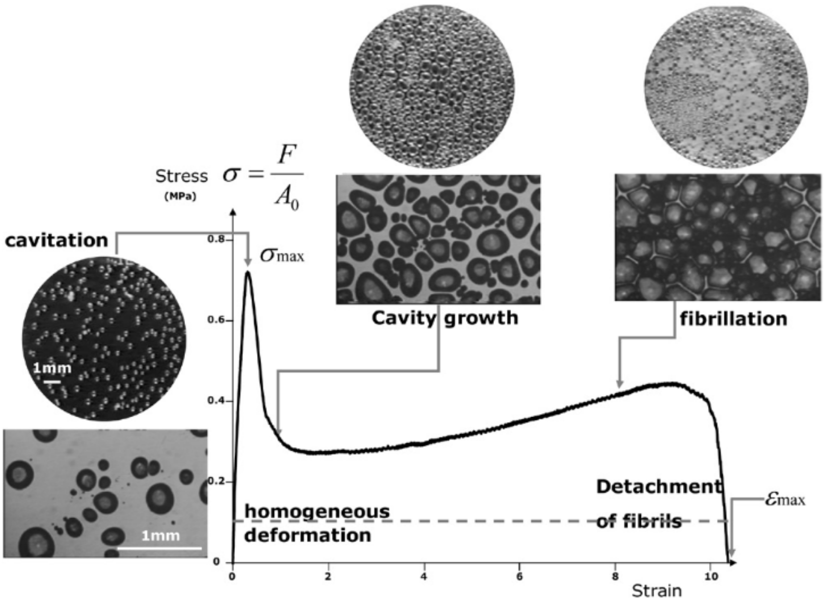

FIGURE 4.13: Debonding process in a probe test [12]. The arrows correspond to the point where each picture was taken.

However, flat against flat geometries lead to a parabolic stress field over the sample [102]. Once a cavity appears in the sample, the stress field becomes nearly flat, allowing for the cavitation of other defects [103]. Cristiano et al. proposed a sphere against flat geometry as an improvement of the flat against flat one [9]. They justify the use of a sphere by the more intense concentration of the hydrostatic stress at the apex of the sphere. This is verified on Figure 4.27. With this set-up, they observed a single cavity opening around the apex and could analyse its behaviour, as displayed on Figure 4.14. The adhesion between the polyurethane network and the glass interfaces was ensured by a silanisation of the glass.

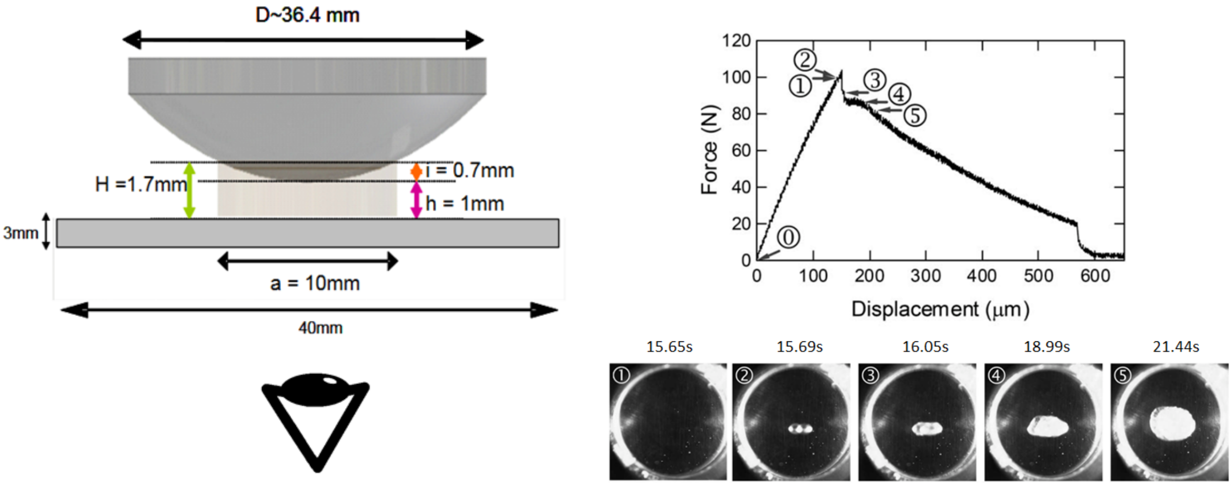

(A) Sphere against Flat geometry - 1 mm confined thickness

(B) Typical force versus displacement plot and cavitation behaviour

FIGURE 4.14: Sphere against flat confinement and cavitation behaviour - Cristiano et al. [9]. (A) A polyurethane network is confined between 2 glass surfaces, the confinement ratios are $h/D = 0.027$ and $h/a = 0.1$. In the loading, the lens is pulled from the glass slide and the cavitation behaviour is observed through the glass slide. (B) The cavity appears suddenly in the sample, no precursor was visible before the burst.

From these experiments and finite element analysis, they could extract the pressure at which the cavity would burst, which was up to 3E. Even with the concentration of hydrostatic stress, one of their tested networks showed several successive cavities growing, suggesting an underlying complex fracture behaviour.

4.1.2.3 Cavitation via imposed defect by needle inflation

The methods described in the first two subsections rely on putting a pristine material under hydrostatic pressure. The nucleation pressure and cavitation growth then depends on the initial defect size, which is rarely known. Another mind-set to test cavitation resistance is then to insert a big defect in the experiment to test the material. This is the idea of needle induced cavitation in soft materials, where a needle is embedded in a soft matrix and fluid (usually water or air) is injected, provoking elastic deformation of the initial defect at the end of the needle and eventually fracture [10]. A typical experiment is described on Figure 4.15.

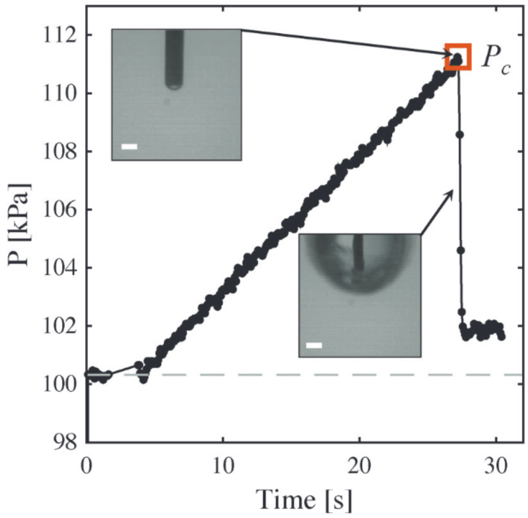

FIGURE 4.15: Characteristic material testing in cavitation rheology - Hutchens et al. [10]. The images show the needle and the bubble just prior to and after the cavitation at the critical pressure P_c. Scale bars: 200 μm.

The large material deformation displayed in Figure 4.15 is only an elastic growth due to the sudden inflation of the defect caused by the needle's insertion. This unstable growth of a large cavity in a Neo-Hookean material with consideration of the surface tension was already presented in Section 4.1.1.2. The critical pressure can lead to the determination of the shear modulus μ:

$$\frac{P_c}{\mu} = \frac{5}{2} + \frac{2\gamma}{\mu A} \tag{4.8}$$

with γ the surface tension between the network and the used fluid (either gas or a liquid) and A is the needle radius, which is assumed to be the inital radius of the void. However, Kundu et al. showed that by changing the material properties, the cavitation behaviour can switch from elastic deformation (which is totally reversible) to irreversible fracture of the material [104]. This transition can also be achieved by changing the needle radius, i.e changing the size of the initial defect.

An analysis of the growth behaviours (either by elastic deformation or fracture propagation) lead Hutchens et al. to map the transition between three behaviours: only fracture propagation, only elastic cavitation and elastic cavitation that transitions to fracture [10]. They showed that the position on the mechanisms map depends on the needle radius, the elastic modulus and surface tension of the soft material with air, but also that strain hardening of the material has an influence. By combining the elastic growth model and the fracture growth model, they could predict in which experimental conditions the elastic modulus or the fracture energy of the soft material can be measured. With these predictions, the cavitation by inflation can be seen as a new rheology tool that allows to test either the elasticity or the fracture properties of the desired soft and brittle material. Cavitation rheology allows for the local testing of the material's elasticity, which allows for the analysis of spatial heterogeneities, which can be quite interesting, especially in biological tissues [105].

4.1.2.4 Conclusion on the experimental set-ups

In this small review of the different cavitation set-ups described in the literature, we could see that very different geometries can be used for the observation of cavitation in samples. However, one key point of this study is to use a polymerisation method that is closed to the industrial process, and polymer layers of comparable thicknesses to the ones used for the optic fibre coating. Therefore, cavitation rheology by needle inflation is not possible, as it requires a large volume of polymer compared to the needle radius. Furthermore, we wish to detect the cavities and the corresponding stress applied, so the saturation experiments (either with gas or with solvents) are also not a good fit. This leads us to the choice of a confined layer tested under hydrostatic traction. This, however, implies the issue of a good adhesion between the polymer and the confining interfaces. Finally, if we want only one cavitation event, the sphere against flat geometry seems to be a better fit. However, this type of set-up will still present some challenges, as the objective will be to produce a confined layer of around 100 μm thickness to approach the thicknesses used industrially. This order of magnitude of thicknesses is achieved in probe tack experiments, where the polymer is doctor bladed or slowly evaporated. In our case, the whole sample needs to be assembled at the controlled thickness before the polymerisation, and then it will be locked in position.

4.2 Producing the cavitation samples

In this study, the elastomeric layers will be tested under hydrostatic traction. As described in Section 4.1, either the flat/flat or the sphere against flat geometry can be used. In the case of the flat punch, for a thin film of incompressible material, the hydrostatic pressure is parabolic in the sample, while the sphere against flat geometry allows for a more pronounced concentration of the hydrostatic stress at the apex of the sphere. In the idea of nucleating only one cavity, and locating it in the sample, the sphere against flat geometry seems more appropriate. Furthermore, one of the drawbacks of the flat/flat geometry is the need for a perfect alignment between the two flat surfaces. If one of the surfaces is slightly tilted compared to the other one, the pressure distribution in the sample will not be uniform and it could even lead to debonding of the sample instead of failure in hydrostatic traction.

Therefore, in this study, the elastomers will be tested in a sphere against flat geometry. In the industrial application, the soft coating that is applied first on the glass fibre is only tens of micrometers thick. The main challenge of this study will therefore be to confine such a thin layer of polymer in a reproducible geometry and thickness and to load it in hydrostatic traction. We will focus on confined thicknesses between 100 and 500 μm. To ensure a high degree of confinement of the elastomer layer, the radius of the sphere is fixed at 3 mm, much bigger than the confined thickness, resulting in a confinement ratio h/D ranging between 0.017 and 0.083, as described on Figure 4.16. The hydrostatic pressure will be induced in the polymer layer by pulling on the half sphere. All set-ups (both for the polymerisation of a layer with a reproducible and controlled thickness and for testing the layer in hydrostatic traction) were designed and build by Ludovic Olanier and Jean-Claude Mancer from the ESPCI workshop.

(A) Total geometry (B) Zoom on the confined region

FIGURE 4.16: Geometry of the sphere against flat confinement for a 500 μm layer. Lens diameter D = 6 mm, polymer thickness h ranging from 100 to 500 μm, polymer spread a, which is not controlled.

4.2.1 Glass surface modification

When testing the samples, the hydrostatic pressure has to build up inside the polymer layer. This implies that the adhesion between the polymer and the glass surfaces has to be stronger than the intrinsic resistance of the polymer network. As was described in Section 2.2.2, the adhesion between usual glass and the polymer networks is quite poor. The cavitation samples are produced from the raw polymer resin precursors by UV inititated free radical polymerisation, so the glass surfaces were silanized with a methacrylate silane (3-(Trimethoxysilyl)propyl methacrylate from Sigma Aldrich) to ensure the chemical reaction between the coated glass surfaces and the polymer network. The surfaces are made of borosilicate, the slide is 2 mm thick (bought from Ediver) and the lens has a radius of 3 mm (bought from Edmund Optics).

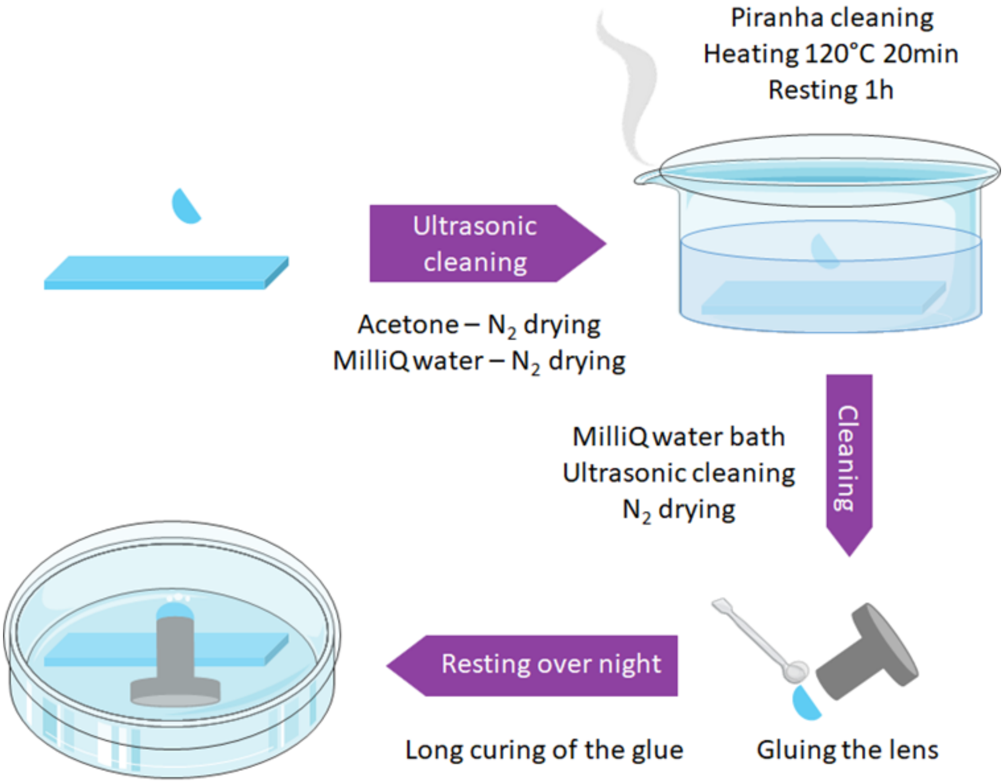

FIGURE 4.17: Cleaning of the surfaces and assembly of the punch

The silanisation of the glass surfaces is a vast topic and a discipline closer to art than science. The results seem to depend on a lot of parameters, such as the chemistry of the silane and the wanted surface state. In our case, we only care about a good adhesion between the surfaces, therefore the silanisation protocol described on Figure 4.17 and 4.18 does not aim at the formation of a monolayer, but at a good silane coverage.

All good silanisations start with clean surfaces. In our study, the cleaning takes place in two steps. First, all surfaces are cleaned successively with acetone (to clean the possible traces of grease) and Milli Q water (to get rid of the remaining dust). Once the glass surfaces are quite clean, they are activated with a Piranha cleaning. The Piranha solution consist of a 70/30 mixture of sulfuric acid (H_2SO_4 - 96%) and hydrogen peroxide (H_2O_2 - 30%). It is a very reactive solution which oxidizes every organic trace left of the glass. The solution is heated at 120°C for 20 minutes to ensure the total reaction of the solution and the production of H_2. The solution bubbles quite profusely during this heating, it can not be left unattended during that time. The whole solution is then left for 1h to cool down. After this step, the glass surfaces are completely activated, which can be seen by the complete wetting of water droplets on the surfaces. The glass lenses are then glued on the aluminium punches with a drop of cyanoacrylate glue (Loctite 434) and the assembly is kept in a closed container at room temperature during the curing of the glue.

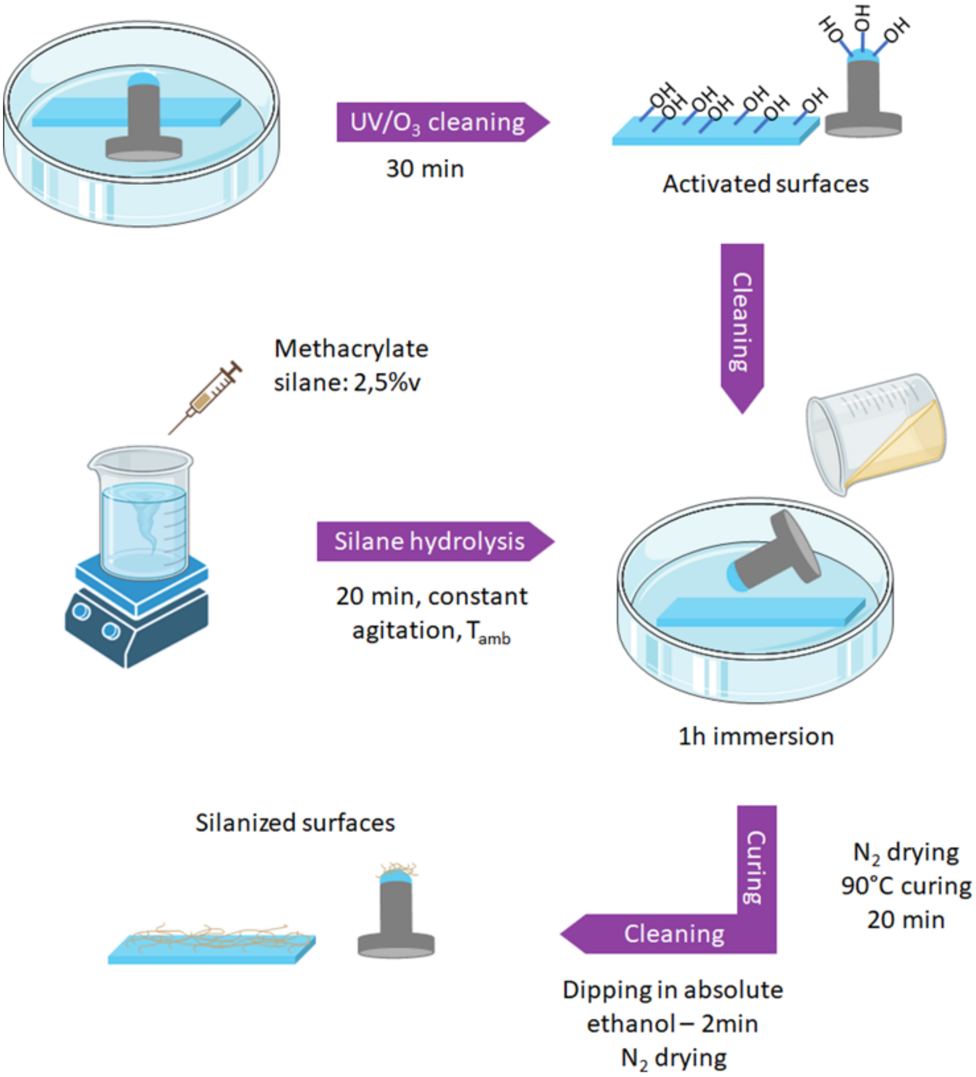

FIGURE 4.18: Silanisation of the glass surfaces

However, the reactivity of these surfaces will decrease over a period of 24h or so. Before the silanisation, the surfaces are activated again via a UV/Ozone plasma (Novascan PSD Pro Series UV Ozone) for 30 minutes. During that time, the silanisation solution is prepared. The methacrylate silane is hydrolysed for 20 minutes at ambient temperature in an ethanol and acidic solution, resulting in a 2.5%v silane solution. The exact composition of the silane solution is described in Appendix C.1. Once prepared, the silane solution is poured on the freshly activated glass slides and lenses. Once all surfaces are covered, the crystallizer is closed to avoid solvent evaporation and left for the reaction to proceed for 1h. The surfaces are then dried with a nitrogen flow. To ensure the chemical bonding between the silane and the surface, the glass slides are cured at 90°C for 20 min, and finally the non-grafted silane is rinsed by a quick dipping in pure ethanol. The dried surfaces are not transparent anymore, several whitish and oily residues remain even after the cleaning. This shows that the hydrolysis of the silane and the long silanisation time leads to a polymerisation of the silane and aggregation on the glass. However, this surface treatment proves adequate for our purpose. The silanized surfaces are kept in a closed box to protect them from dust and they are used the same day.

Remarks on the cleaning process

This cleaning in 2 steps may seem unusual, but it is due to the gluing of the lens to the punch. In fact, after the Piranha cleaning, the surfaces are completely activated and the silanisation could happen directly. However, to glue the lenses, the glass surfaces have to be manipulated, and it seemed that such a handling of the lens surface would deteriorate the silane layer and therefore decrease the adhesion. The 24h hours of glue curing results in a good adhesion between the lens and the punch that will resist to the 1h of immersion in the ethanol silane solution. However, the recommended curing time to maximise the solvent resistance is 1 week, which was not practical for our use. Therefore, there are interactions between the glue and the silane solution, even after the 24h curing, leading to some degradation of the interface that will impact the imaging of the cavitation process by producing an uneven background (see Figure 4.22).

4.2.2 Polymerisation of the samples and testing

The objective of this set-up is to control the thickness of the confined region in a reproducible way. This is achieved by setting the exact distance between the apex of the lens and the glass slide with spacers, as described on Figure 4.19. This has to be done for each sample individually because the glue thickness for each punch may vary and there is a slight thickness variation for each glass slide. The polymerisation holder fixes also the perpendicularity between the punch and the glass slide.

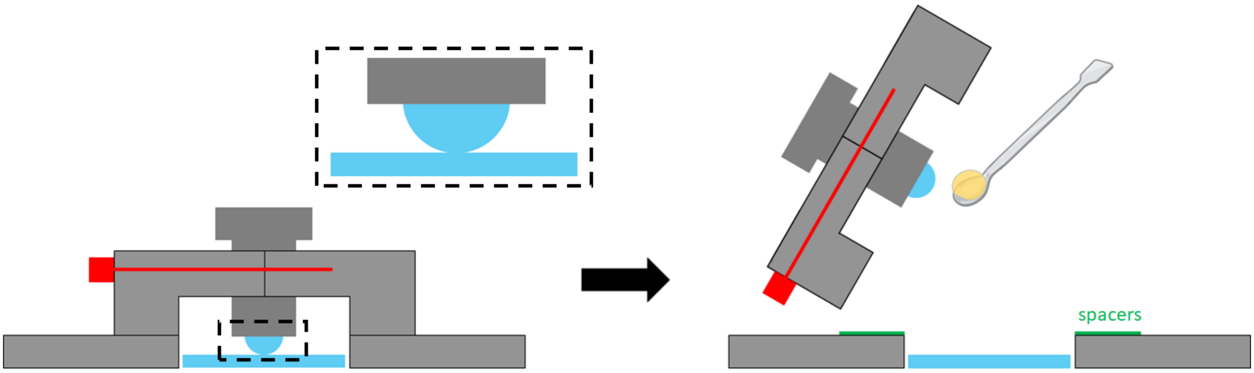

(A) Setting the zero position of the punch and coating the lens

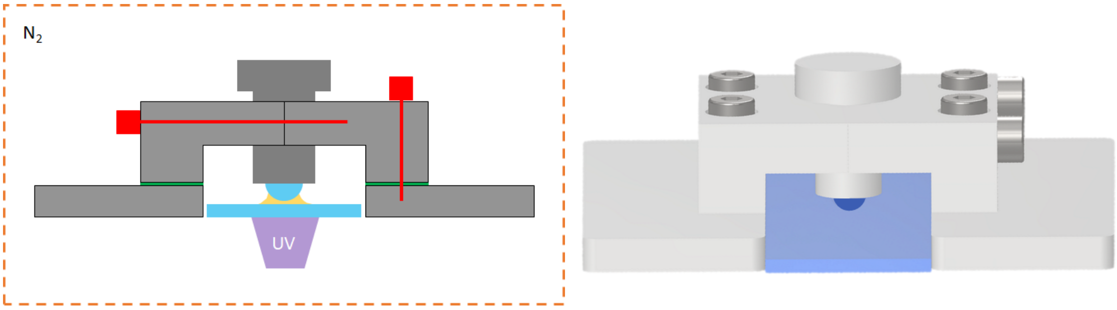

(B) Polymerising with a controlled thickness

(C) Workshop's design

FIGURE 4.19: Cavitation samples: fixing the thickness before polymerising. (A) Left: the lens is in contact with the glass slide. The punch is fixed in position to the holder by screws. Right: Spacers (in green) are placed on the bottom part of the holder and the lens is dabbed with a small amount of polymer resin. (B) The holder is screwed to the bottom part, ensuring that the distance between the lens apex and the glass slide is fixed by the spacer. The polymerisation takes places in the nitrogen chamber and the polymer is cured via UV illumination through the glass slide.

Before polymerisation, both glass surfaces are cleaned again with a nitrogen flow to remove dust. Only a small drop of polymer resin is put on the lens to avoid excessive covering: especially the polymer resin should not reach the aluminium punch. One drawback of this method is that there is no control of the spreading of the resin on the glass slide, which may impact the confinement. Furthermore, no movement of the punch is allowed during polymerisation, while the resin shrinks in volume. This may cause a hydrostatic residual tensile stress (negative pressure) inside the layer. However, no cavities were ever observed after the polymerisation, and the sample is then released from the holder right after the 1s illumination. For thicknesses between 100 μm and 500 μm, the cavitation samples are easy to manipulate (the confined layer can withstand the weight of the glass slide) if no excessive torque is applied on the punch. All samples are tested within 24h of their polymerisation.

Thickness control

Even if the polymerisation set-up is designed to set the gap between the lens and the glass slide, some slight sliding of the punch is still possible before the polymerisation. It was therefore interesting to measure the actual thickness of the complete sample. The optical index of the cured resin is between 1.49 and 1.50, while the refractive index of borosilicate glass is 1.51. This very small difference in refractive index makes the detection of the interface via optical microscope impossible. The polymer resin is however slightly fluorescent and it was therefore possible to measure the thickness by confocal microscopy. The sweeps were done between the glass slide and the lens. This in-situ verification showed that the thickness is accurately controlled with this synthesis method with the expected thickness found in 100 μm and 500 μm samples.

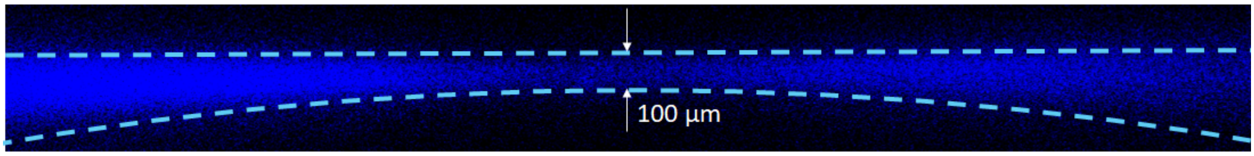

FIGURE 4.20: Confocal in-situ observation of a OL HEA 30% PEA sample, 100 μm thickness, Laser 50 Gain 50. The scan is made through the glass slide. Illumination wavelength: 405 nm, detection window: 450-550 nm. The light blue broken lines represent the estimated positions of the glass surfaces, the fluorescent signal comes from the polymer.

4.3 Observing the cavitation

4.3.1 Description of the hydrostatic traction set-up

The hydrostatic traction set-up is described in Figure 4.21. It consists of 2 parts:

- The mobile part is a fork holding the punch and pulling it away from the glass slide at a controlled speed.
- The fixed part holds the glass slide. It is mounted on a double cantilever of stiffness S that will deflect according to the applied force on the punch. This deflection is measured via a capacitive sensor ($\Delta\delta$) and leads to the Force measurement: $F = S\Delta\delta$.

A capacitive sensor measures the distance between the 2 parts, which is the closest measurement possible to determine the displacement of the lens. This measurement is not impacted by the compliance of the set-up, but it will depend on the glue's stiffness linking the lens to the punch. The displacement resolution is directly the sensor's resolution: 20 nm. The error on the force only comes from the uncertainty on the stiffness measurement, as the sensor's resolution is 1 nm. The double cantilever's stiffness S is calibrated with weights, which leads to $S = 4.166 \pm 0.107.10^6$ N/m. This gives an error of 2.57% on the force measurement.

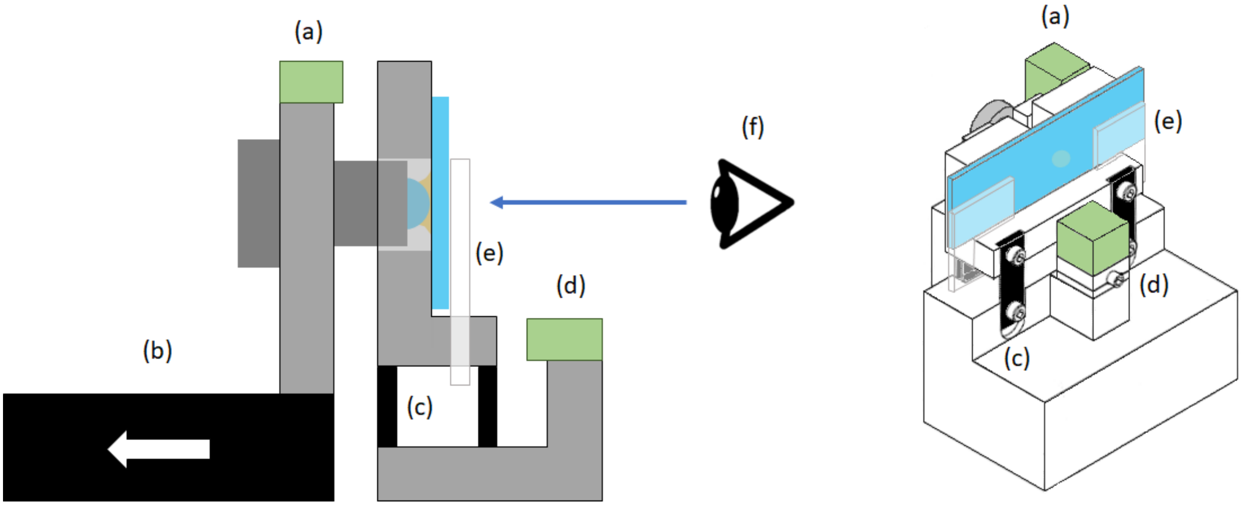

(A) Lateral view of the traction set-up

(B) Tilted view from the set-up

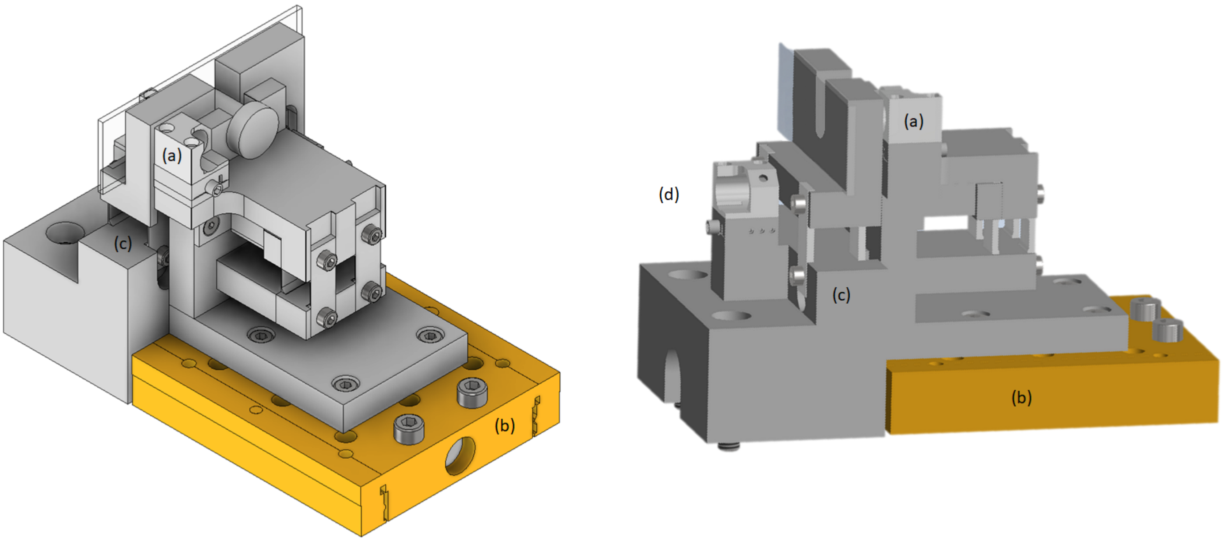

(C) View from the workshop design

FIGURE 4.21: Hydrostatic traction set-up. (A) and (B): (a) Capacitive sensor (1 mm) - displacement measurement. (b) Displacement plate, the movement is controlled by a stepper motor with a 25 mm range. (c) Double cantilever for the force measurement, $S = 4.166.10^6$ N/m (d) Capacitive sensor (50 μm) - force measurement (e) Holders for the glass slide (f) Camera observation (20 fps) with blue light in the observation direction.

The exact list of material used and the calibration of the double cantilever can be found in Appendix C. The data acquisition for the sensors and the camera is performed via a LabView code. Each image acquisition is at 20 fps and the sensor acquisition is at 52.08 Hz. The stepper motor is controlled via its own software.

4.3.2 Experimental procedure and data acquisition

This set-up presents a lot of flat to flat surfaces, which can be tricky. First of all, the alignment between the mobile and the fixed part is verified at the beginning of each set of experiments. The cavitation sample is then slid into the set-up and the contact between the fixed part and the glass slide is made by the 2 holders (marked as (e) on Figure 4.21). The last flat to flat surface is between the mobile part's fork and the punch. Even with a lot of experimental care, the punch may not be completely perpendicular to the glass slide, and this last alignment is made when the traction begins. This will be one source of imprecision on the displacement measurement. The sliding of the punch in the fixed part is also cause of some experimental issues of friction, as described in details in Appendix C.4.

The initial traction position of the mobile part is set just before the rise of the force. The traction tests are then performed at either 5 μm/s or 0.5 μm/s. In the slow experiments, the velocity is increased to 5 μm/s once the fracture propagates dramatically in the sample. All tests are therefore displacement controlled and the resulting raw data is a Force versus displacement curve and the corresponding images.

4.3.3 Typical experimental result of a 500 μm sample

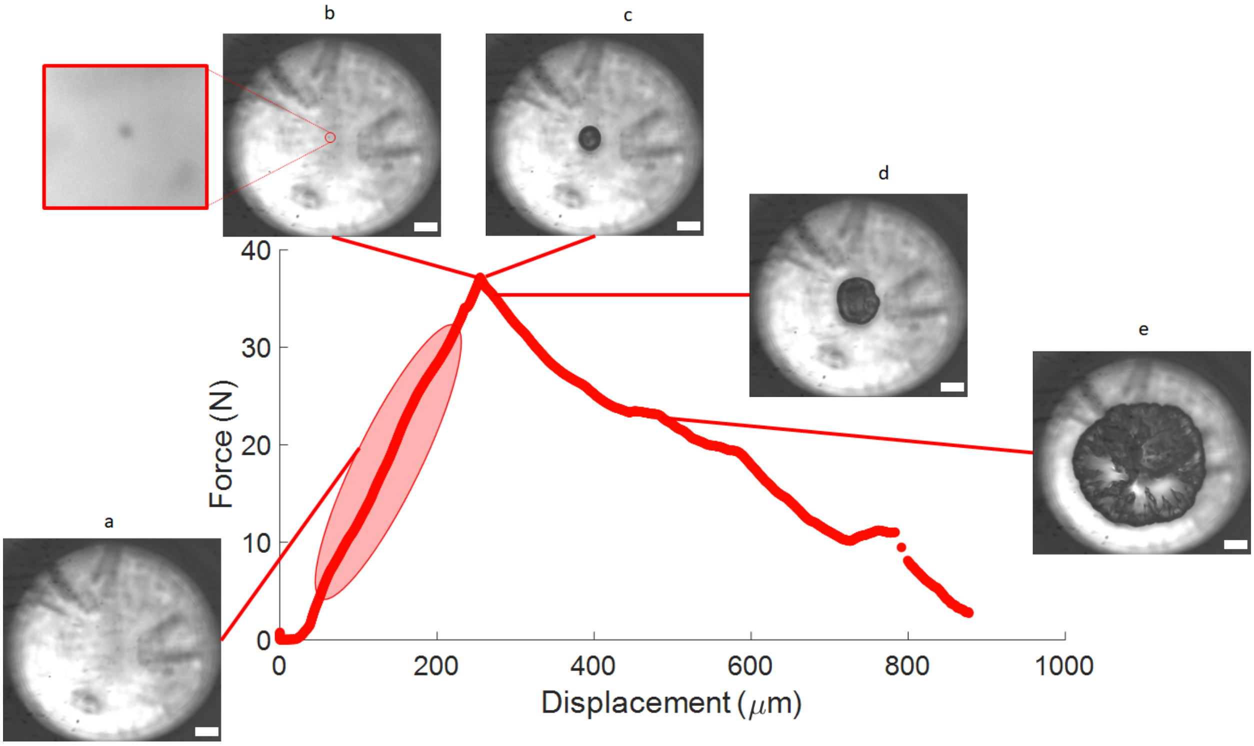

FIGURE 4.22: Typical Force versus displacement for a 500 μm OL HEA 15% EHA 15% PEA sample and corresponding images. Scale bar: 1 mm. Testing velocity of 5 μm/s (a) Elastic loading of the sample. There are some movements in the glue layer responsible for the background but no cavitation. (b) t = 152.57s : First observation of the cavity, diameter of 30 μm. (c) t = 152.62s : The cavity opens dramatically with a diameter of 610 μm. (d) and (e) The cavity propagates directly in a critical fracture of the sample.

A typical cavitation experiment on a 500 μm sample at 5 μm/s is described on Figure 4.22. The accommodation due to the flat/flat contact between the punch and the mobile part can be seen at the beginning of the curve. Furthermore, during the loading of the sample, the glue layer deforms, leading to the changes of the sample's stiffness. These two phenomena lead to a difficult interpretation of the loading curve before the cavitation event. Nothing appears in the elastomer layer during this step. A small crack appears in the layer which dramatically opens in a wide cavity. This implies a great deformation and most likely also a fracture of the polymer around the cavity. The force drops because of the newly created volume leading to the decrease of the sample's stiffness. The punch is being continuously pulled at a constant speed, leading to the transition of the cavity into a critical fracture that tears the sample. This behaviour is coherent with our expectations for the behavior of the thin confined layer in this set-up: one cavity appearing in the bulk of the layer close to the apex of the sphere.

The deformation of the glue is an experimental problem: there is no way to measure which displacement is due to the glue deformation and which is actually applied on the polymer layer. This means that the displacement measurement for the nucleation and explosion of the cavity does not exactly represent the actual deformation of the confined layer. In Figure 4.22, the cavity appears at an effective displacement of the punch of 217 μm, which represents more than 40% deformation of the confined layer. The elastomer being incompressible, it seems a bit high, suggesting that the deformation of the glue layer between the half sphere and the punch and the flat/flat accommodation of the mechanical alignment are not negligible in the traction experiment.

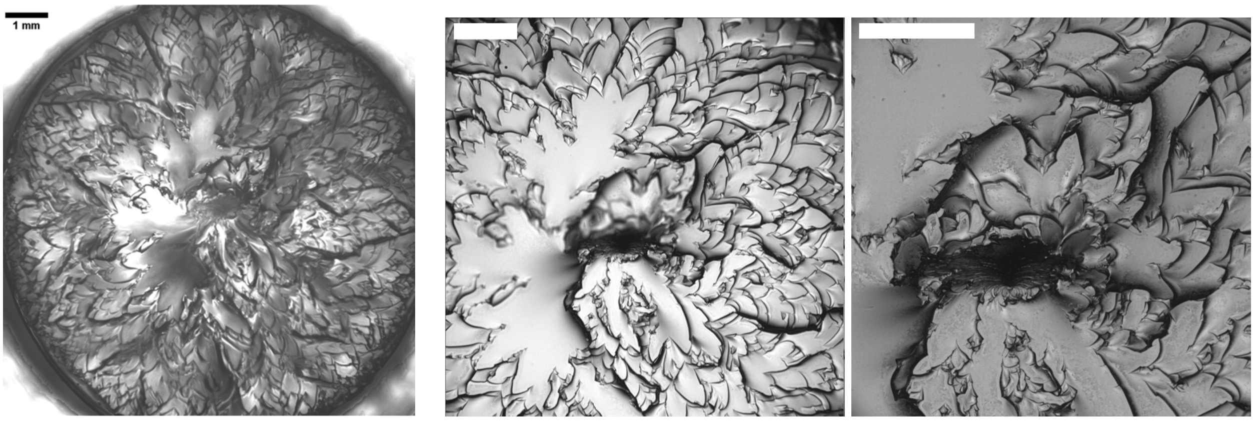

(A) Fractured polymer on the lens - Scale bar: 1 mm

(B) Fractured polymer on the glass slide - Scale bar: 1 mm

(C) Zoom on the nucleation site - Scale bar: 500 μm

FIGURE 4.23: Observation of the fracture surfaces. The fracture surface on the lens side is observed with the set-up's objective, the fracture surface on the glass slide is observed with an optical microscope. The polymer is present on both glass surfaces, meaning that the cavitation really appears inside the polymer layer (inner fracture) and does not come from a delamination at one of the two polymer/glass interfaces.

The presence of the bulk cavitation phenomenon is confirmed by the analysis of the fracture surfaces: there is still some polymer coating both surfaces. The sample's roughness is characteristic of fracture in elastomers: the rougher the surface, the slower the propagation ([106], [107]). A more detailed analysis of the fracture surfaces will be made in Section 5.2.3.3. This roughness is quite high, the images in Figure 4.23 are produced through a stack focusing of different focus planes to see it completely.

4.4 Analysing the cavitation via FEM

Due to the sphere on flat geometry, there is no analytical computation to determine the link between the force applied on the half sphere and the hydrostatic pressure in the confined layer. To analyse the experiments and compute the hydrostatic pressure at which the cavity grows, a finite element modelling is needed. The goal will be to compute the hydrostatic stress distribution in the confined polymer layer and to establish the relationship between the measured force applied on the punch and the local hydrostatic pressure at the location where the cavity appears.

The principle of finite element analysis is to describe the studied part by a mesh. The mesh consist of a set of nodes that delimit the elements. The boundary conditions (external force, displacement, ...) will imply a displacement of the nodes that will deform the elements. The nodes have several degrees of freedom containing the possible displacement and rotation directions. The node displacement is computed by solving the equilibrium equation ($\Sigma F = 0$). To link the movements of the nodes to a stretch and a stress in the material, an interpolation scheme is needed. First, the displacement is interpolated over the whole element, either linearly or quadratically, based on the element definition. The displacement leads directly to the stretch, and the constitutive equation should then provide the stress at each material point. In practice, the stress computation is only carried out accurately at specific points in the elements, which are called integration points. The final consideration is the dynamics of the experiments.

4.4.1 Model definition

The geometry of the cavitation sample is quite simple, and can be represented axisymmetrically in Abaqus. The Y axis is the revolution axis and all computations are done only on a 2D slice, as described on Figure 4.24. The glass modulus (70 GPa) being much larger than the polymer's, both glass surfaces are considered rigid. This implies that their modelling is not necessary as they don't significantly deform.

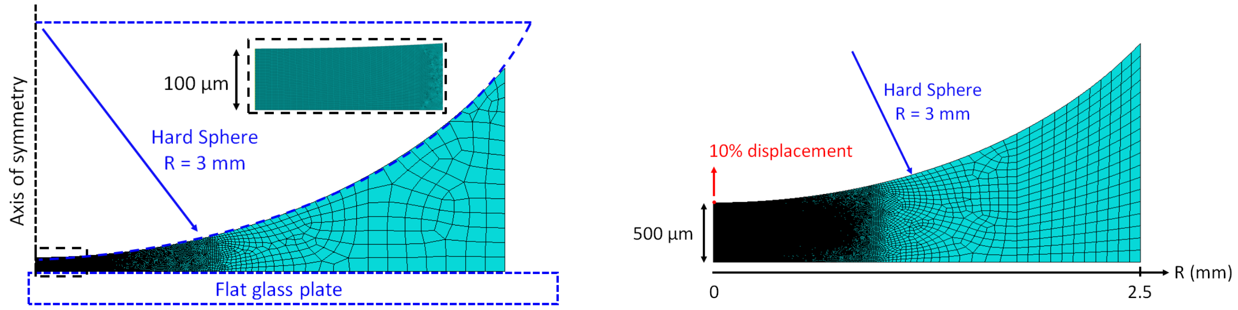

(A) FEM model - 100 μm layer

(B) FEM model - 500 μm layer

FIGURE 4.24: FEM modelling of the confined layer for the 2 extreme thicknesses. (A) The insert shows a zoom on the confined layer. (B) The red point represents the reference for the Force measurement.

The polymer layer is designed with a radius of 2.5 mm on the glass slide. The vertical outer border of the simulation is not exactly realistic relative to the experiment, however the interesting region for us is the confined part. The mesh description varies with R the radius from the apex. From R = 0 to R = 0.2 mm, the mesh consist of squares of 0.001 mm size. For R > 0.2 mm, the mesh size gradually increases to a maximum size of 0.1 mm at R = 2.5 mm.

The material is described with linear elasticity, based on its Young's modulus and Poisson's coefficient: E = 1 MPa and $\nu = 0.499$. Considering the elastomer as nearly incompressible, the displacement at which cavities appear should be quite small, allowing for such an easy description of the material's behaviour and simpler computations (with Standard computation and linear steps). Because the Poisson's ration is very close for 0.5, we use hybrid elements: CAX3H and 4H [108]. These elements have 3 (respectively 4) nodes and are linear. The hybrid elements present therefore an additional degree of freedom representing the pressure while the nodal displacements are used to compute the shear strains and stresses.

To determine the link between the measured macroscopic Force and the local Hydrostatic stress in the layer, the model is submitted to a boundary condition of fixed displacement corresponding to 10% of the confined thickness. The adhesion at the polymer/glass interfaces is considered perfect, therefore the boundary conditions consist of:

- The surface on the glass plate is encastre: no displacement is possible in any direction.
- The upper surface in contact to the half lens moves in the Y direction, no displacement is allowed in the R direction.

4.4.1.1 Hydrostatic pressure distribution in the layer

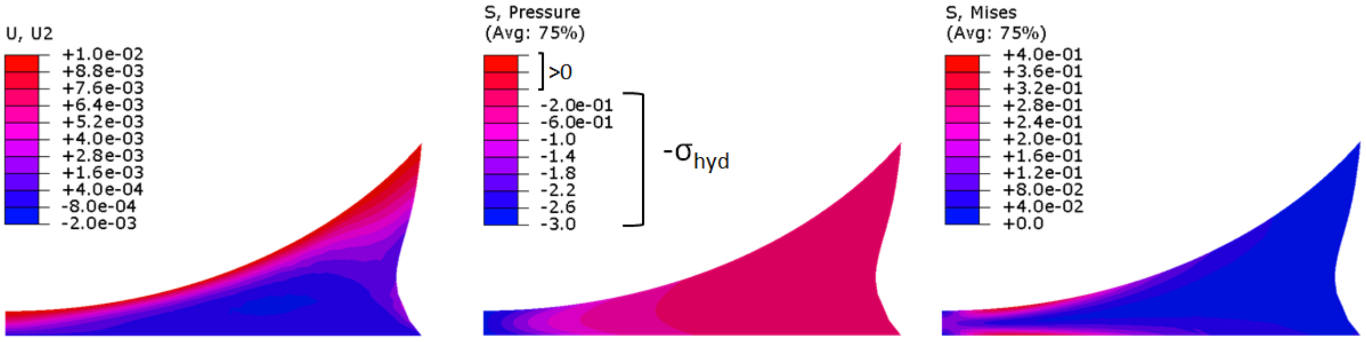

(A) 100 μm layer

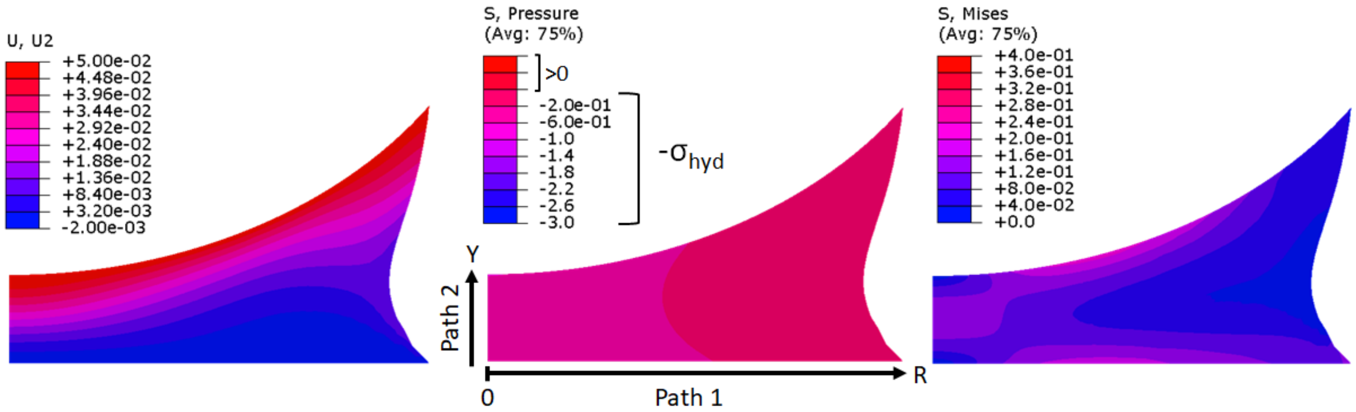

(B) 500 μm layer

FIGURE 4.25: Displacement U2 (Y direction) (mm), Pressure (MPa) and Shear (Mises MPa) outputs in the FEM in confined layer computation for 10% of deformation of the confined region. (B) On the Pressure computation, the 2 paths used for the data extraction are displayed: Path 1 for the evolution with R the distance to the apex, Path 2 for the evolution in the material's thickness at the apex (Y direction).

The FEM computation for layers of 100 μm and 500 μm for 10% displacement can be seen on Figure 4.25. The displacement field in the Y direction serves as a boundary condition verification, as the whole upper layer is displaced by the wanted value: 10 μm and 50 μm respectively. This deformation leads to the build up of a triaxial stress in the layer, as described by the Pressure output. We will fix the following sign convention:

$$\sigma_{hyd} = -P = -\frac{t_1 + t_2 + t_3}{3} \tag{4.9}$$

Finally, the deformation and the fixed surfaces lead to shear stresses in the layer, with interestingly a zone of high shear stresses along the glass interfaces. The center of these "hot spots" for the shear are slightly shifted from the apex. For the thinner layer, it is located at R = 0.41 mm and 0.98 mm for the thicker one.

The pressure field is studied along the 2 paths described on Figure 4.25 (B):

- Path 1 consist of the nodes in contact with the glass slide. The evolution of the stress along it describes the evolution of the stress with the distance to the apex.
- Path 2 is considering the nodes on the axisymmetric axis Y. This allows for the observation of the pressure's evolution along the thickness of the sample, below the apex of the sphere.

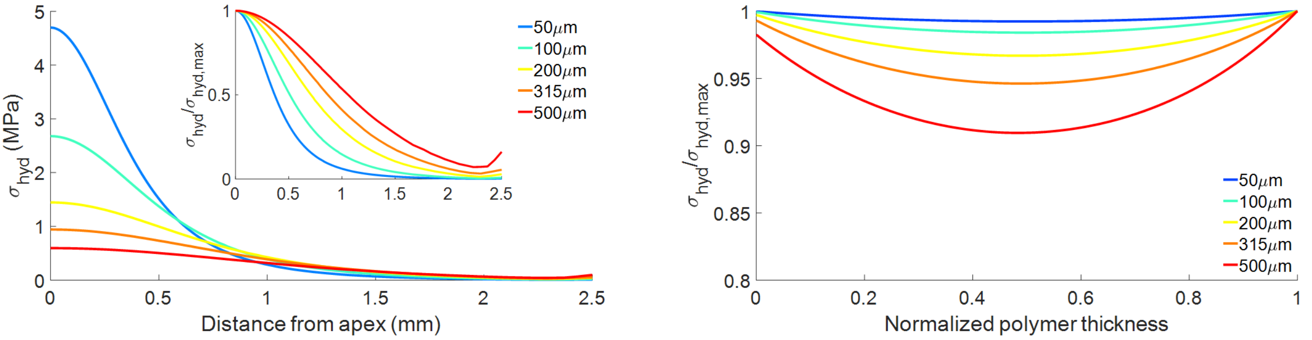

(A) Computation of Path 1: evolution with the radius

(B) Computation of Path 2: evolution with the thickness

FIGURE 4.26: Thickness effect on the pressure field. (A) The insert presents the normalized hydrostatic pressure for each thickness, which underlines the pressure concentration around the apex for the thinner, and more confined, layers. (B) Evolution with the normalized thickness on the Y axis: below 0 is the glass slide, above 1 is the half lens. The highest stress is at the sphere/polymer interface, and it slightly decreases in the middle of the polymer layer.

The thickness impacts greatly the hydrostatic stress distribution with the radius. As expected for the sphere against plan geometry, the hydrostatic pressure is concentrated at the apex of the sphere. The concentration decreases with an increase of the confined thickness, as the overall confinement decreases. The hydrostatic pressure is also not uniform in the polymer thickness, as described on Figure 4.26 (B): its highest value is at the sphere interface and the lowest value is in the middle of the layer. This effect is all the more obvious for the thicker sample. However, the stress variation at the apex is less than 10%, and the exact position on the Y axis of the cavities can not be easily determined. In the following of this study, only the maximum value of the hydrostatic pressure will be considered for each radius R.

The stress concentration can be verified compared to the flat/flat geometry, with a confined thickness of 100 μm on Figure 4.27. While the stress distribution is much more peaked in the sphere against flat geometry, the confinement is much greater in the flat/flat geometry, leading to a higher hydrostatic pressure. However, the whole purpose of the sphere against flat geometry was to obtain this stress concentration, so that goal is achieved. Furthermore, it would be complicated experimentally to polymerise perfect 100 μm thick layers in a flat/flat geometry.

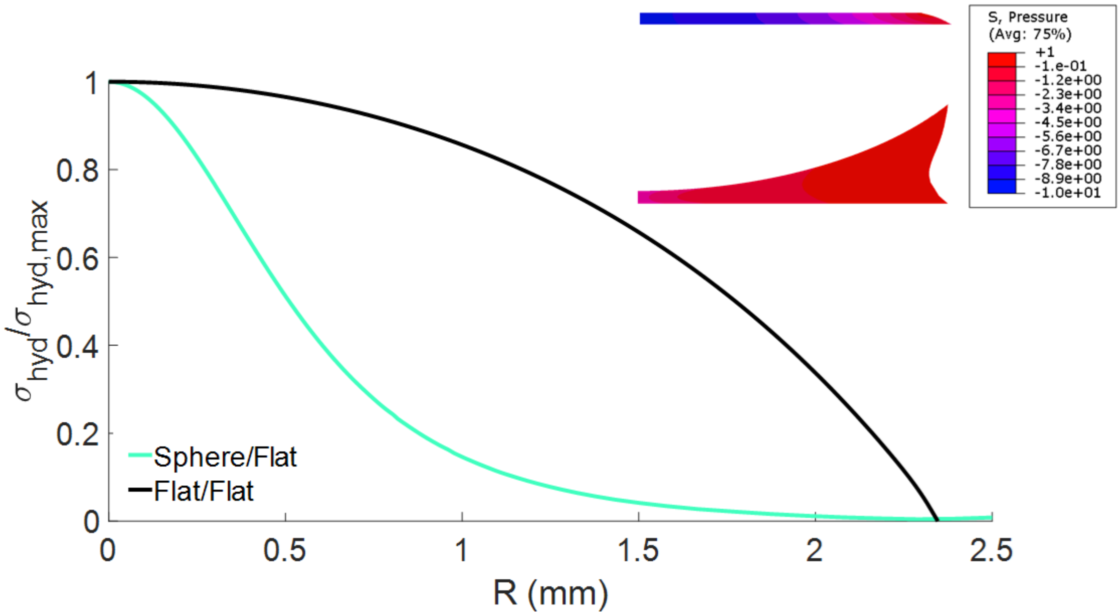

FIGURE 4.27: Hydrostatic stress concentration in the sphere against flat versus the flat/flat geometry for 100 μm layers and 10 μm displacement of the upper surface. The normalized hydrostatic pressure shows the greater concentration of the stress in the sphere against flat geometry, however the stress obtained for the same displacement is much higher in the flat flat geometry.

4.4.1.2 Force and $\sigma_{hyd,max}$ correlation

Based on the linearity of the computation, the relationship between the force and the hydrostatic stress value at the sphere's apex computed for a 10% displacement will be valid for all wanted deformations. A calibration coefficient C (MPa/N) can be computed:

$$\sigma_{hyd,max} = C.F \tag{4.10}$$

that will link the experimental force to the maximum hydrostatic stress in the polymer layer. The dependence of this calibration coefficient to the sample's thickness can be observed on Figure 4.28.

The experimental points over a range of thicknesses from 10 to 1000 μm can be fitted with a power law:

$$C(MPa/N) = 24.h^{-0.806} \tag{4.11}$$

where the thickness is in micrometers and the hydrostatic stress in MPa. This is valid for the material parameter E = 1 MPa and $\nu = 0.499$. This relationship allows us a determination of the **experimental maximum hydrostatic stress** in the layer at each time before the cavitation.

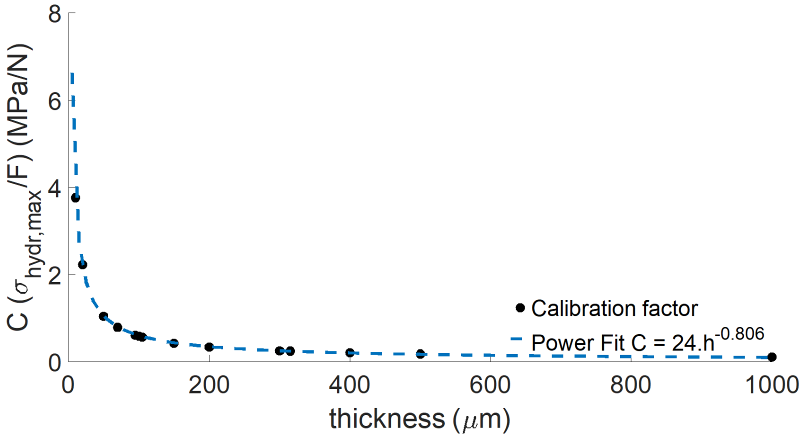

FIGURE 4.28: Calibration coefficient dependence to the polymer thickness - E = 1 MPa and $\nu = 0.499$. The data are fitted with a power law where h is the thickness in μm.

4.4.1.3 Material's influence on the hydrostatic pressure

The Abaqus model was designed with pretty strong material assumptions:

- Elastic linear behaviour of the confined layer with E = 1 MPa
- Incompressible material defined with $\nu = 0.499$
- Fixed length of the polymer spreading and half lens covering of 2.5 mm

Let's discuss and validate each of these assumptions.

Young modulus influence

As described in Chapter 3, the studied materials present a variety of Young's modulus. The computation of the 100 μm layer was done with 2 additional moduli: E = 0.86 MPa and E = 1.16 MPa. As can be seen on Figure 4.29, the maximum hydrostatic stress increases with an increase of modulus, which was expected. As the exerted force increases accordingly, the calibration factor does not vary with E: for 100 μm, it stays at 0,5857.

Poisson's coefficient influence

The Poisson's coefficient defines the incompressibility of the material. A pure incompressible material has $\nu = 0.5$, however it leads to an impossible computation as the Bulk modulus diverges. Thanks to the simplicity of our model, the computation can be done for Poisson's coefficient ranging from 0.49 to 0.4999999, which is the computational limit of Abaqus.

The hydrostatic stress behaviour with ν is described on Figure 4.30: the hydrostatic stress saturates for Poisson's coefficients above 0.4999, and all normalized distributions look alike, with the exception of $\nu = 0.49$. The Poisson's coefficient was initially fixed at $\nu = 0.499$ as it leads to a bulk modulus $K \sim 100$ MPa, a usual value for elastomers. This also ensured that all finite element computations would converge as the Poisson's coefficient was not too high to produce errors. This analysis of Poisson's coefficient impact shows that there is little error made if the actual incompressibility is higher than expected, especially towards the hydrostatic distribution in the layer. The correlation coefficient follows a polynomial law with the Poisson coefficient:

$$C(MPa/N) = 1084.6\nu^2 - 1056.5\nu + 257.7 \tag{4.12}$$

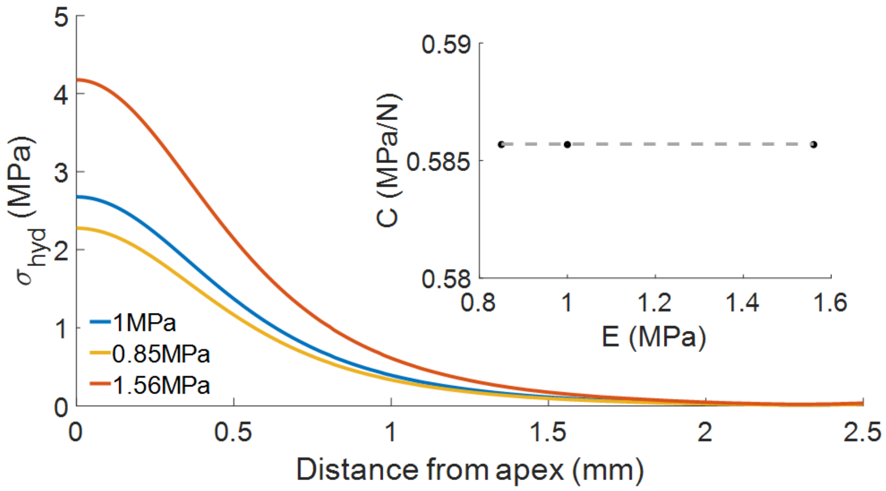

FIGURE 4.29: Modulus effect on the FEM modelling on a 100 μm layer with $\nu = 0.499$. Insert: Evolution of the calibration coefficient with E, grey broken line: C = 0.5857.

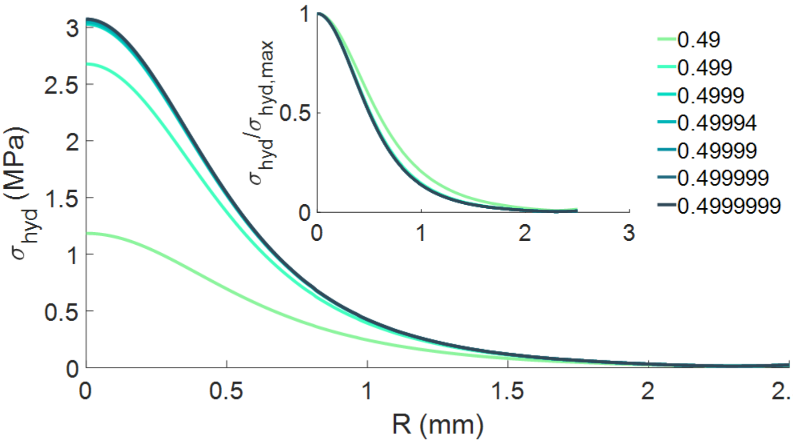

FIGURE 4.30: Poisson's coefficient effect on the FEM modelling with E = 1 MPa. The maximum hydrostatic stress increases with ν but saturates at 0.4999. Insert: normalized hydrostatic stress. Except for $\nu = 0.49$, all distributions have the same profile.

This relation will however not be used in the following as the Poisson's coefficient will stay fixed at 0.499.

Polymer spreading influence

Lastly, the width of the total polymer layer needs to be considered. The 2.5 mm spreading of the polymer layer was taken as a reference as it corresponds to the radius of the fractured surface on the glass slide. However, the actual spreading of the polymer on the half lens and the glass slide is not controlled experimentally. The effect of a change in spreading is studied in Figure 4.31.

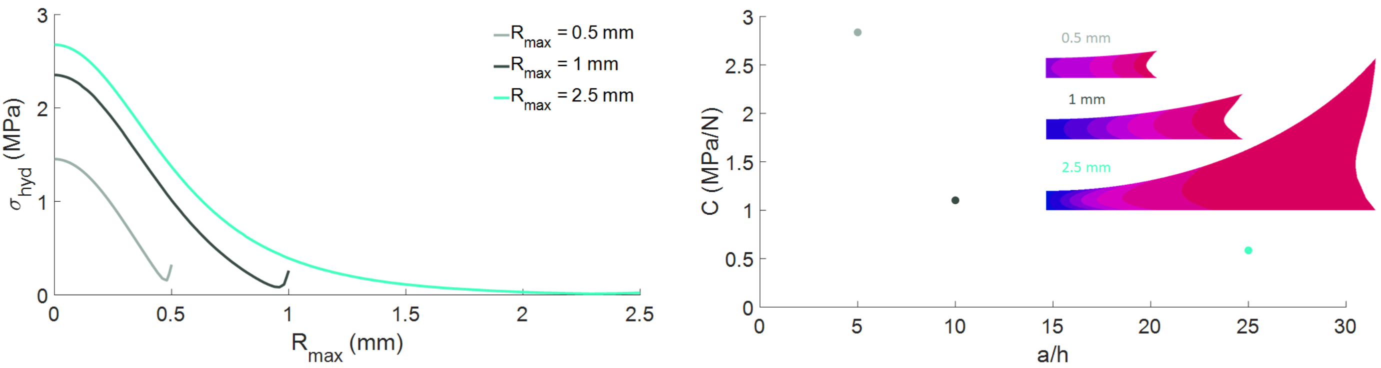

(A) Polymer spreading effect on σ_{hyd}

(B) Calibration coefficient with the spreading

FIGURE 4.31: Polymer spreading effect on the hydrostatic stress and calibration coefficient, 100 μm, E = 1 MPa, $\nu = 0.499$, Path 1. (A) The maximum hydrostatic pressure decreases with the decrease of the polymer length (B) The schematic shows the Pressure field in the different configurations. The pressure is inversely linked to σ_{hyd}, leading to blue being the zone of highest hydrostatic pressure.

Again, this study considers that the polymer drops straight from the half lens to the glass slide, while in reality a meniscus forms. This particular form, that varies between each experiment due to the varying deposed polymer volume, is not easy to model. The fracture surface on the glass slide however present a radius of approximately 2.5 mm, in a quite reproducible fashion. This validates our modelling choice of a 2.5 mm polymer spread.

Conclusion on the material's properties impact on the calibration coefficient

Thickness (μm)	Confinement		C (MPa/N)
	a/h	h/D	
50	100	0.0083	1.0436
100	50	0.0167	0.5857
315	15.87	0.0525	0.2439
500	10	0.0833	0.1777

TABLE 4.1: Confinement and calibration coefficient evolution for the studied layers. Experimental constant: D = 6 mm. Computation constants: $\nu = 0.499$, a = 5 mm

4.4.2 Determination of the local hydrostatic stress

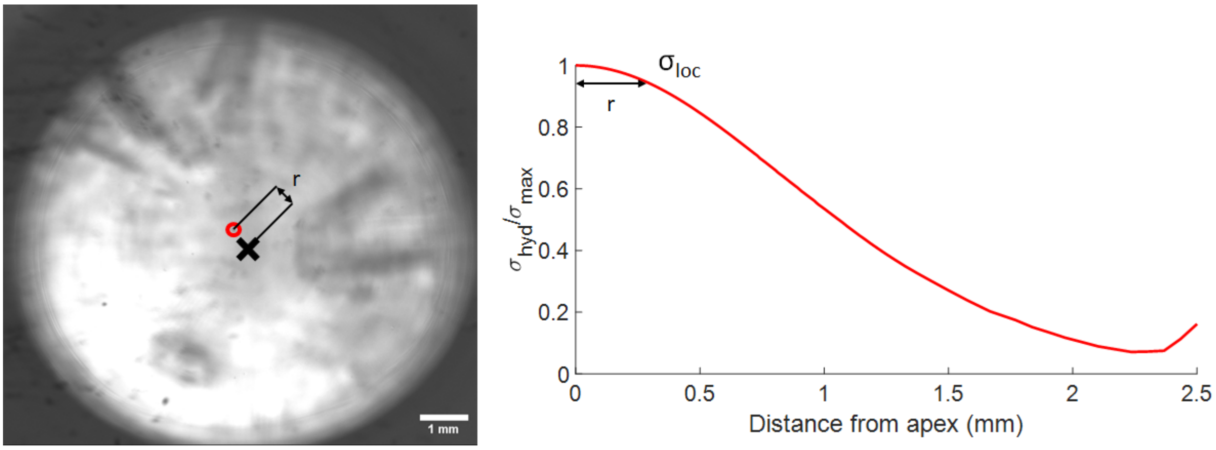

FIGURE 4.32: Determination of $\sigma_{hyd,loc}$ for each nucleation event. Left: red circle: first observation of the cavity in the 500 μm sample, black cross: position of the sphere's apex. r is the radius at which the cavity nucleates. Right: normalized hydrostatic stress distribution. The distance r gives the value of σ_{loc} (as a fraction of σ_{max}.

The FEM analysis provides us with a direct relationship between the force and the maximum hydrostatic stress inside of the layer. However, the cavities in the experiments do not appear exactly at the apex of the sphere. The precise analysis for the determination of the local hydrostatic stress at the cavitation site is described on Figure 4.32. The apex of the sphere is pointed, once all flat/flat accommodations and glue movement in the loading are done. After these various accommodations, the sphere apex is considered to be at the center of the punch. The distance between the center of the cavity and the sphere apex is then computed. Considering the studied sample's thickness, the according normalized stress distribution with radius is then used to determine $\sigma_{loc}/\sigma_{max}$.

Based on the experimental curve and the calibration coefficient, σ_{max} can then be computed with the value of the force at which the cavity bursts. This leads then to the computation of the **local hydrostatic pressure** leading to the material's cavitation. This is truly describing the physical phenomena, therefore, in all the following, only this local hydrostatic stress σ_{loc} will be considered. This computation works because all computations are linear. For each thickness, the normalized hydrostatic stress keeps the same evolution towards the radius, no matter the value of applied deformation. This allows for the direct observation of the ratio $\sigma_{loc}/\sigma_{max}$, no matter the actual force at which the cavity appears in the experiment. It is important to note that this FEM modelling considers the deformation of a perfect layer. The relationship between the hydrostatic stress and the measured force only works for sample that did not cavitate yet. As soon as a cavity bursts in the confined layer, the hydrostatic stress field completely changes.

4.5 Take home messages

- To test the thin layers of elastomer under hydrostatic traction, a sphere against flat geometry has been chosen. Sphere and flat are both made of glass. The tested layer thickness is between 50 to 500 μm. The adhesion between the polymer and the glass is ensured by a silanisation step with a methacrylate silane.

- The thickness of the samples is controlled with a polymerisation set-up. However, it also means that the alignment between the punch and the glass slide is fixed during the polymerisation step. The hydrostatic traction set-up, designed in house, allows for the observation of the cavitation behaviour during loading, as well as the measurement of the force and the displacement. There are still some difficulties with the set-up, such as accommodations during the loading due to the flat against flat interfaces and background issues due to the deformation of the glue.

- Despite the experimental issues, the testing of thin layers under hydrostatic traction worked. The typical cavitation experiment on a 500 μm layer displays one critical cavity opening near the apex of the sphere, characterized by a sudden and significant drop in the force.

- A FEM analysis of the system allowed us to link the macroscopic force to the local hydrostatic pressure of the first cavitation event.

Chapter 5

Analysis of the cavitation behaviour

Chapter 4 described the characteristics of the set-up used to apply hydrostatic traction to thin layers. In this chapter, we will study the effect of the degree of confinement on the cavitation behaviour by testing elastomer layers with a range of polymer thicknesses, and the effect of the network's formulation by testing the different materials described and characterized in Chapter 3. This chapter will consist mainly of the experimental observations of the cavitation behaviours. As a reminder, every time a hydrostatic pressure is mentioned, it refers to the **local** hydrostatic pressure for the **first cavity** opening in the sample since the stress field has been computed only in the absence of cavity.

5.1 Thickness effect

As described in Section 4.3.3, the hydrostatic traction set-up designed produced a cavitation behaviour in 500 μm thick polymer layers as expected: one cavity appearing near to the center of the sample, where the hydrostatic pressure is at its highest, and propagating into a macro-crack. However, the first coating's thickness on industrial optic fibres is around 60 μm. To test the effect of a decrease in thickness, samples of the OL HEA 15% EHA 15% PEA formulation were tested at different confined thicknesses ranging from 50 μm to 500 μm. To facilitate the differentiation between the experiments, we will describe the samples as: Material_thickness_testingvelocity. For example, OLHEA1515_500um_5ums means a 500 μm thick sample of the OL HEA 15% EHA 15% PEA formulation tested at 5 μm/s.

5.1.1 Impact on the critical cavitation pressure

As displayed on Figure 5.1, there seems to be no obvious effect of the thickness on the cavitation pressure for the first cavity. Let's look deeper in the results. There is a large dispersion in the values of critical hydrostatic pressure where the first cavity appears. We tried to improve this by changing slightly the process:

- Assuming that a longer equilibration time will reduce the dispersion, the testing velocity was decreased from 5 μm/s to 0.5 μm/s, in the hope of giving more time to the sample to self-align precisely along the pulling direction, resulting in a more reproducible applied stress field.

- The origin of a few large defects present in the sample could be small aggregates of BAPO (the photoinitiator) that could have not dissolved well. We therefore tried to remove bigger nucleation germs from the mix before polymerisation. The polymer mix was filtrated through a 0.45 μm filter, either by dissolving it in ethyl acetate or by forcing the heated mix through the filter by pressure.

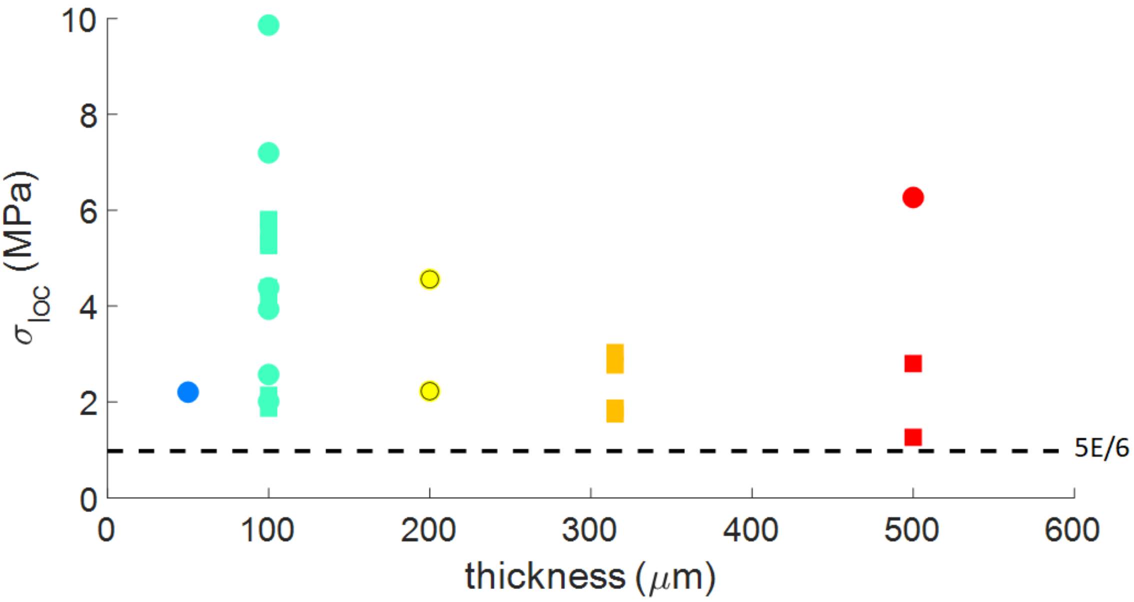

FIGURE 5.1: Thickness influence on the cavitation pressure for the first cavity. Tested network: OL HEA 15% EHA 15% PEA - E = 1.156 MPa. The circles represent tests done at 5 μm/s and squares tests done at 0.5 μm/s. The black dotted line represents Gent and Lindley's theoretical limit of 5E/6.

However, none of these changes helped to decrease significantly the level of dispersion of the hydrostatic pressure of cavitation. This leads us to the conclusion that the cavitation pressure depends on defect sizes that are present in the polymer network.

Then, the results suggest that the 100 μm layer can resist higher pressures before cavitating, however, more samples were tested at that thickness. If we consider the dispersion to be due to different defect sizes, when testing more samples, there are also more chances of testing a sample with fewer defects in the tested volume. Therefore, we can conclude that there is no significant difference with the sample's thickness in the values of hydrostatic pressures needed for the first cavity to appear. This value can be considered as representative both of the polymer and of its defect distribution.

However, the most important observation is that, regardless of the thickness, **all samples resist to a hydrostatic pressure higher than the theoretical limit of 5E/6**. This shows that even if our cavitation process is driven by the defect population, they are all small enough and need a higher stress to open and propagate in the polymer network than the prediction of cavity expansion of Gent and Lindley [1]. Our results are coherent with the observations of Cristiano et al, where they observed cavitation in a similar geometry, on even thicker samples, and obtained cavitation pressures around 3E [9].

5.1.2 Impact on the cavitation behaviour

However, focusing only on the hydrostatic pressure of the first cavity to expand does not describe the whole cavitation behaviour as we observe it. Figure 5.2 displays the loading behaviour of all tested layers of different thicknesses. While no significant effect of the thickness could be detected on the critical hydrostatic pressure for the first cavity to appear optically, there is a great difference in the cavity growth behaviour. The thickest layers display only one drop in the measured force which corresponds to the main (and unique) cavity opening. The intermediate thicknesses (200 μm and 315 μm) either show one or a few growing cavities, so their loading curve can also display these successive force drops. Finally, the thinnest layers display multiple force drops during their loading curves, which is a sign of the appearance of multiple cavities.

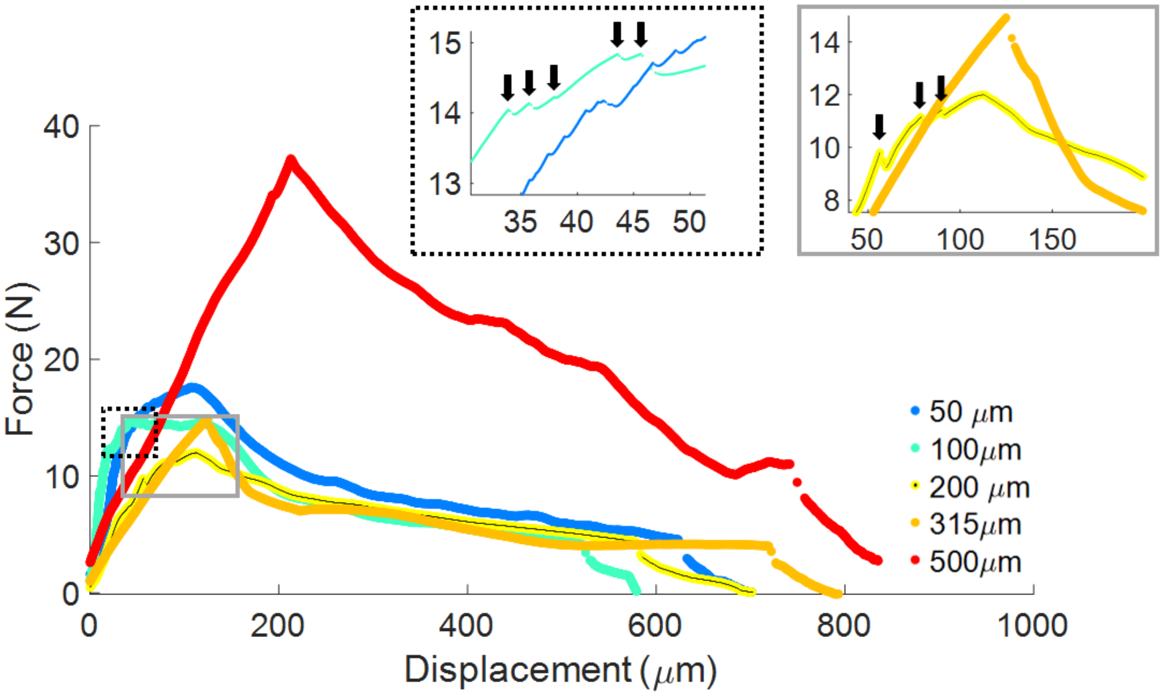

FIGURE 5.2: Influence of the layer thickness on the loading curves. All tests were carried out at 5 μm/s except for 315 μm which was tested at 0.5 μm/s. The loading curves were shifted horizontally to make the 0 displacement correspond to the actual beginning of the sample's loading. Black dotted insert: zoom in on the loading of the two thinnest samples, each curve presents several force drops. Grey insert: zoom on 200 μm and 315 μm samples, the 200 μm shows a few force drops. The force drops on the 100 and the 200 μm samples are marked by the black arrows.

This different cavity nucleation and growth behaviour depending on the thickness was observed by Gent and Lindley in their poker-chip experiment ([1], Figure 4.12), the thinnest samples leading to multiple cavities while the thickest would only lead to a few, or even one. However, their loading curves did not show several force drops corresponding to the successive cavitation events in their thin samples, only a plateau, while their thickest samples did display one force peak. Through modelling of the poker-chip experiment, Kumar and Lopez-Pamies showed that the loading curve of the thin samples should lead to several force drops [101]. They suggested that the difference between the experiment and the modelling could lie either in the viscous dissipation of the rubber (which was not taken into account in the modelling) or in the sensitivity of the force sensor used by Gent and Lindley. Our results seem to show that an increase in force sensitivity makes it possible to detect the sudden force drops. We will now separate the samples in three categories:

- thick samples: 500 μm
- intermediate thicknesses: 200 and 315 μm
- thin samples: 50 and 100 μm

and analyse in more detail their cavitation behaviour and the dynamics of the cavities expansion.

5.1.2.1 Thick samples - catastrophic cavitation

Figure 5.3 is a reminder of the typical loading curve that was presented in the previous chapter. Interestingly, the main cavitation event comes from a precursor that is already apparent but only slightly visible in the immediately preceding frame. Although not completely in focus, we can estimate a 30 μm diameter for this precursor. The expanded cavity has a radius of 304 μm, leading to an approximate in-plane stretch rate for this sudden expansion of:

$$\frac{\lambda}{dt} = \frac{R/R_0}{dt} = \frac{304/15}{0.05} = \frac{20.26}{0.05} = 405\ s^{-1} \tag{5.1}$$

It is important to note that the cavities are seen in 2D, so the shapes observed are the projections of the cavities inside the sample. Therefore, even if the projected cavity seems circular, we can not assume that the open cavity is a sphere, as the polymer is still confined between the glass surfaces. The correct image of this cavity could be more that of an inflated pancake, as drawn on the insert of Figure 5.3.

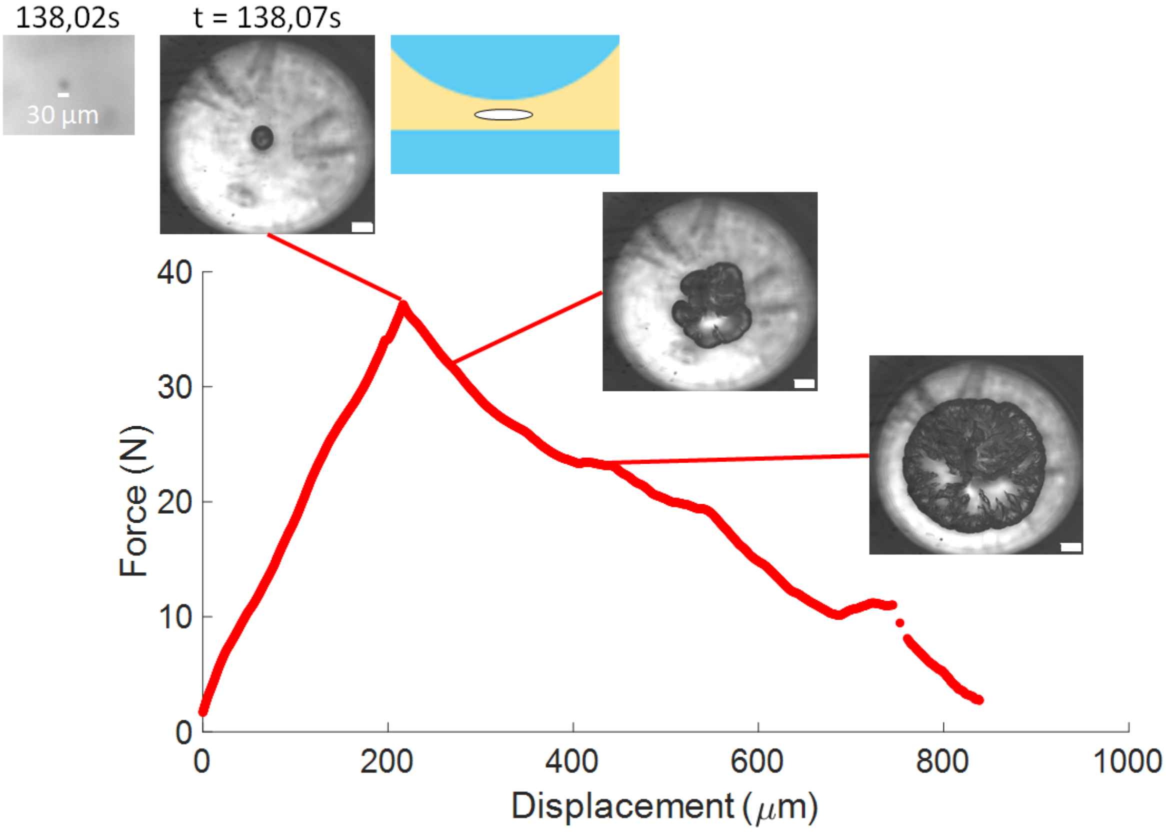

FIGURE 5.3: Loading curve of OLHEA1515_500um_5ums and corresponding cavitation snap and growth. Scale bar: 500 μm. Insert: schematic of our proposition for the shape of the inflated cavity in the confined layer: the projection through the glass slide is circular but the projection in the thickness of the sample is an ellipse.

The stretch applied on the polymer (estimated at ~ 20, we don't know the exact shape and size of the precursor) is too large to only represent elastic deformation of the network surrounding the cavity. As a reminder, in biaxial extension of thin shells, the maximum extensibility for the OL HEA 15% EHA 15% PEA network was found at $\lambda = 5.38$ (see Table 3.6). Of course, in the case of a cavity expansion, the polymer is a 3D matrix, and not a thin membrane, and the loading is closer to plane strain than to plane stress, which changes the elastic response. However, it still shows us how a stretch of 20 or more is well above the elastic deformation domain. This expansion must be provoking fracture or damage in the polymer. However, the stretch rate of 4.10^5 s^{-1} is much higher than the testing velocities used in our material characterizations. As discussed in Section 3.3, the fracture energy measured in the single notched samples in uniaxial traction depended strongly on the testing velocity. This raises the question as to which type of fracture energy should be considered when analysing the fracture behaviour of these cavitation processes.

Let's analyse more closely the dynamics of the cavity growth in the sample. Figure 5.4 displays the evolution of the projected area of the bubble with time and shows corresponding images at key moments of its evolution. The area was measured via an image analysis on Image J (Analyze Particles). The beginning of the experiment is t = 0s. The loading begins at t = 42.91s. 3 domains of cavity growth can be observed:

- The sudden snap of the cavity at 138s. The bubble area grows very suddenly and fast: the cavity's radius evolves from to 30 to 304 μm in 50ms.
- The morphology changes, between 139s and 145s: the initially quite circular crack develops several penny shaped cracks in specific directions away from the apex, where the layer thickness is larger, there is more polymer volume and hence more elastic energy stored.
- The circular crack propagation, after 145s. The different penny shaped cracks merge to form a global crack front that propagates. This propagation is slower than the previous stage.

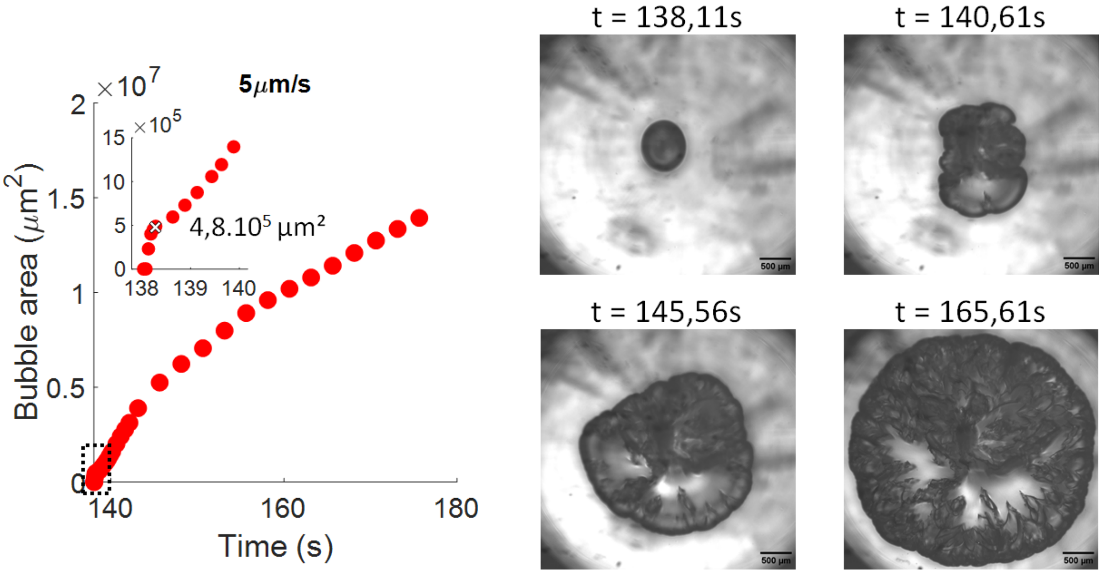

FIGURE 5.4: Thick sample - Following the bubble growth dynamics - OLHEA1515_500um_5ums. Left: Bubble growth with time, Insert: zoom on the snap of the cavity, white cross: transition from the circular shape to the nucleation of several penny-shaped cracks and corresponding area. Right: Corresponding images during the propagation.

The changes of growth rate imply that the cavitation process and the growth process follow different dynamics, and therefore suggest that they are dominated by different mechanisms. This is also suggested by the change of morphology between the initial snapped cavity that appears to have a uniform border (Image at t = 138.11s) and its "destabilization" into several penny shaped cracks that show several crack arrests (Image at t = 140.61s).

The same behaviour can be observed for the slower testing velocity: OLHEA1515_500um_0.5ums, as displayed on Figure 5.5. The corresponding Force versus displacement curve can be seen in Appendix D.1. Again, the cavity snaps open at a stretch rate of 150 s^{-1} (estimated with equation 5.1), destabilises into several cracks and finally becomes circular. A small plateau in bubble area is observed just after the snap for the 0.5 μm/s testing velocity, which was not seen for the faster growing bubble. This can be attributed to the velocity difference: after the snap, the force applied on the cavity decreases, and when the sample is pulled on slower, it takes more time for it to load the cavitated sample again, leading to this apparent stability. This is due to the fact that our set-up is not force controlled, but mostly displacement controlled.

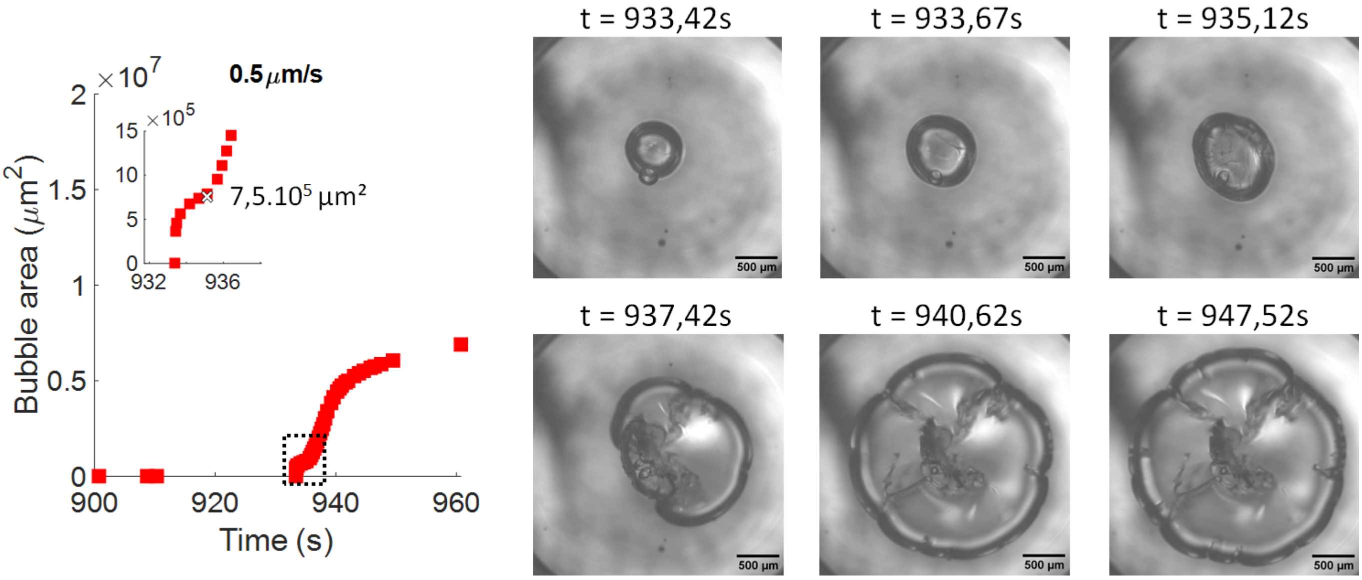

FIGURE 5.5: Thick sample - Following the bubble growth dynamics - OLHEA1515_500um_0.5ums. Left: Bubble growth with time, Insert: zoom on the snap of the cavity, white cross: transition from the circular shape to the nucleation of several penny-shaped cracks and corresponding area. Right: Corresponding images during the propagation.

As a summary, the thick samples have a single cavity that appears in the sample and transitions into a critical fracture by the opening at different places on the periphery of the cavity of penny shaped side cracks. Doing so it goes from a circular shape (probably pancake-like in 3D) into what Morelle et al. described as a raspberry shape [13]. Finally, all penny shaped cracks converge into a final nearly axisymmetric big crack propagating from the apex out throughout the whole sample.

5.1.2.2 Intermediate thickness - few cavitation events

When decreasing the thickness of the sample to 315 μm, an interesting phenomenon arose. Figure 5.6 shows a cavitation behaviour very similar to the one of the thick sample: one cavity snaps in the sample, destabilises into several penny shaped cracks and evolves into a circular crack. The snapping stretch rate is 670 s^{-1}.

Again, as can be seen on the insert of Figure 5.6 (B), there is a significant plateau of bubble growth after the snap. This is to be compared to Figure 5.5, as these samples were tested at the same velocity (0.5 μm/s). The stabilisation plateau of the growth rate of the isotropic cavity seems to be longer for the OLHEA1515_315um_0.5ums_1 sample, and the isotropic cavity continues to grow slowly before transiting to the raspberry shape. This is even visible in the loading curve as an additional peak, shown on the second picture of Figure 5.6 (A). This slow growth before the destabilisation shows that the set-up was again applying an increasing force on the sample. This shows that a new mechanism appears in the 315 μm sample, stabilising the expanded cavity, in comparison to the 500 μm thickness.

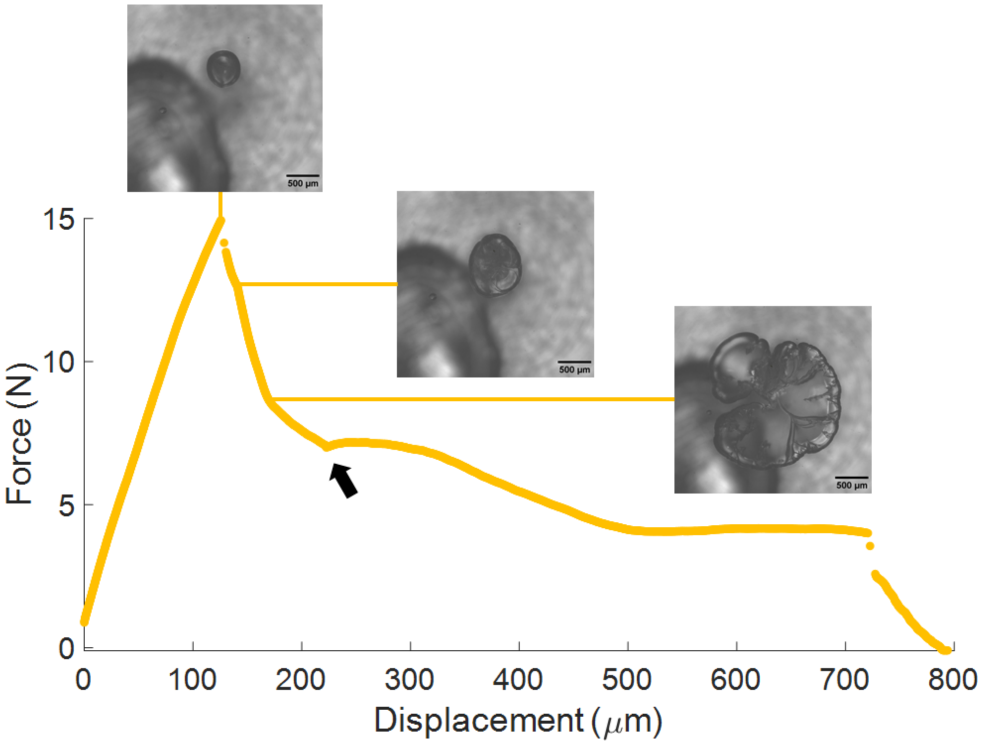

(A) One critical cavity opens and propagates critically

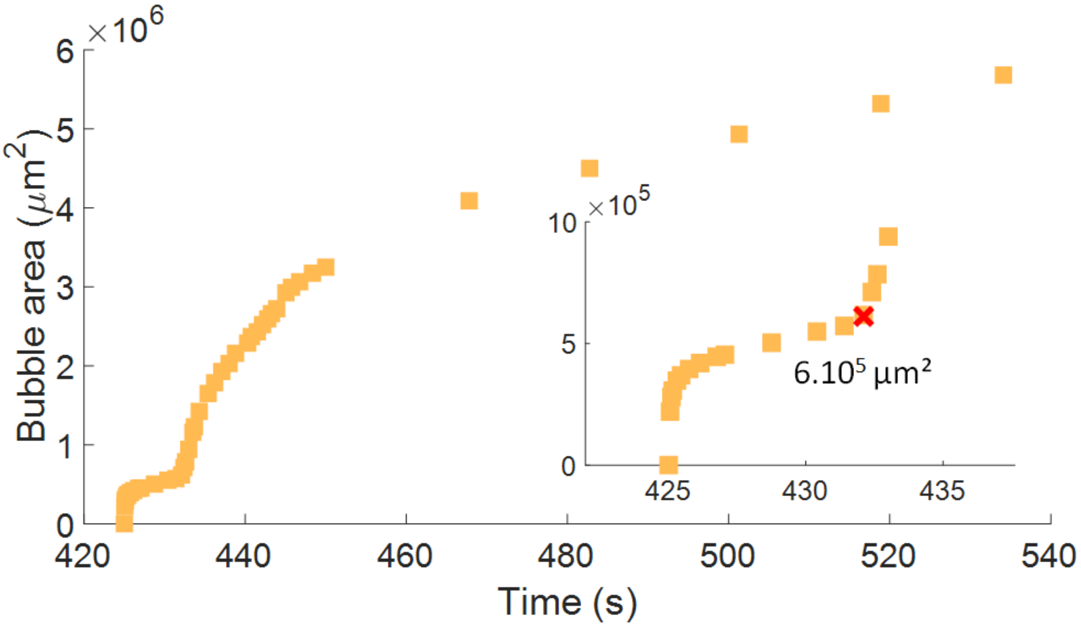

(B) Evolution of the critical cavity's growth

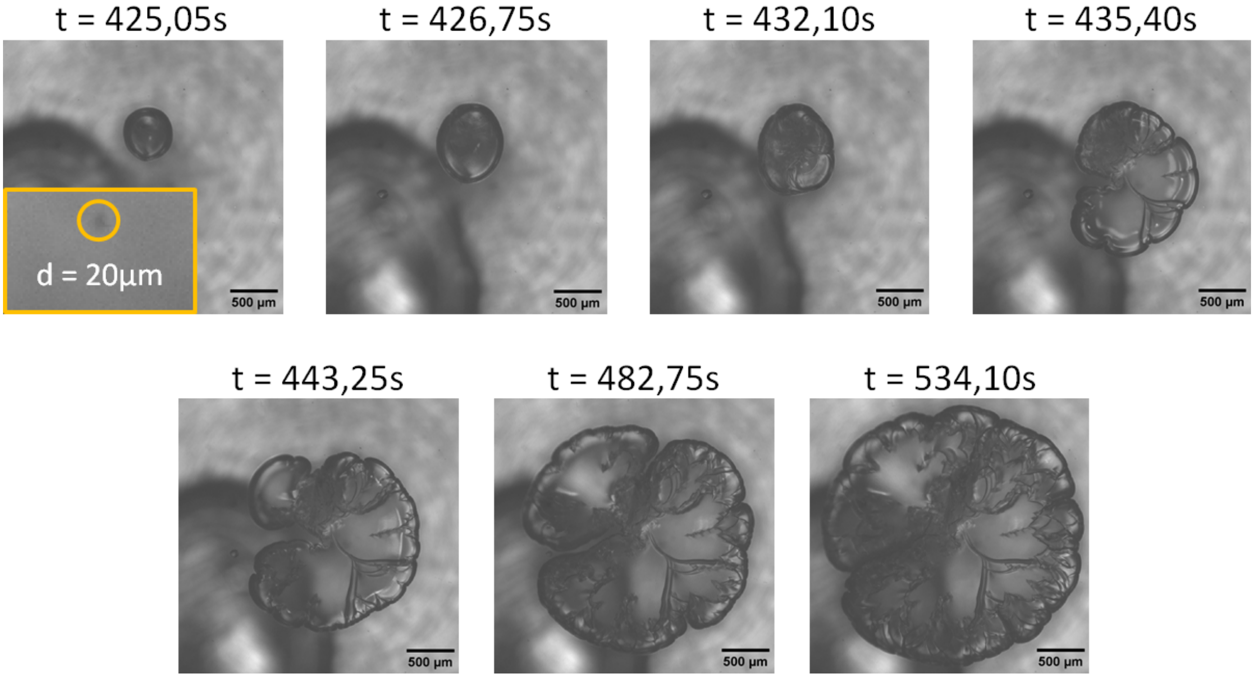

(C) Snap of the cavity, destabilisation into several cracks and global circular fracture

FIGURE 5.6: Cavitation in OLHEA1515_315um_0.5ums_1 with one critical cavitation event. (A) The black arrow indicates the switch to 5 μm/s (propagation of the global fracture). Scale bar: 500 μm. (B) Insert: zoom on the snapping of the cavity. The destabilisation of the crack's front into multiple penny-shapes is marked by the red cross. (C) Insert on the first picture: initial defect seen before the snapping.

This pseudo-stabilisation of the snapped cavity was observed in a more obvious way in another sample of the same thickness, as described on Figure 5.7, sample OLHEA1515_315um_0.5ums_2. This time, the loading curve shows three peaks:

- First peak: the snap open of the first cavity: its precursor is a small defect that slowly grows from an initial diameter of 9 μm to 140 μm and snaps at a larger size with a stretch rate of 63s^{-1}. Although the projected view is a circular shape, the actual inflated cavity in 3D is most likely an inflated pancake.
- Second peak: the snap open of the second cavity: its precursor is also a small defect of 36 μm diameter that snaps at a stretch rate of 254s^{-1}.
- Third peak: the transition of the first cavity into fractures by several penny shaped cracks.

As can be seen on the bubble area evolution on Figure 5.7 (B), the first cavity snaps open, grows again in that stabilisation plateau, but its growth is disturbed by the snapping of the second cavity. However, it still transitions to the penny shaped crack propagation. This sudden growth then closes the second cavity as it tears the polymer under tension that was keeping it open. Once the crack has become circular, it slows down again.

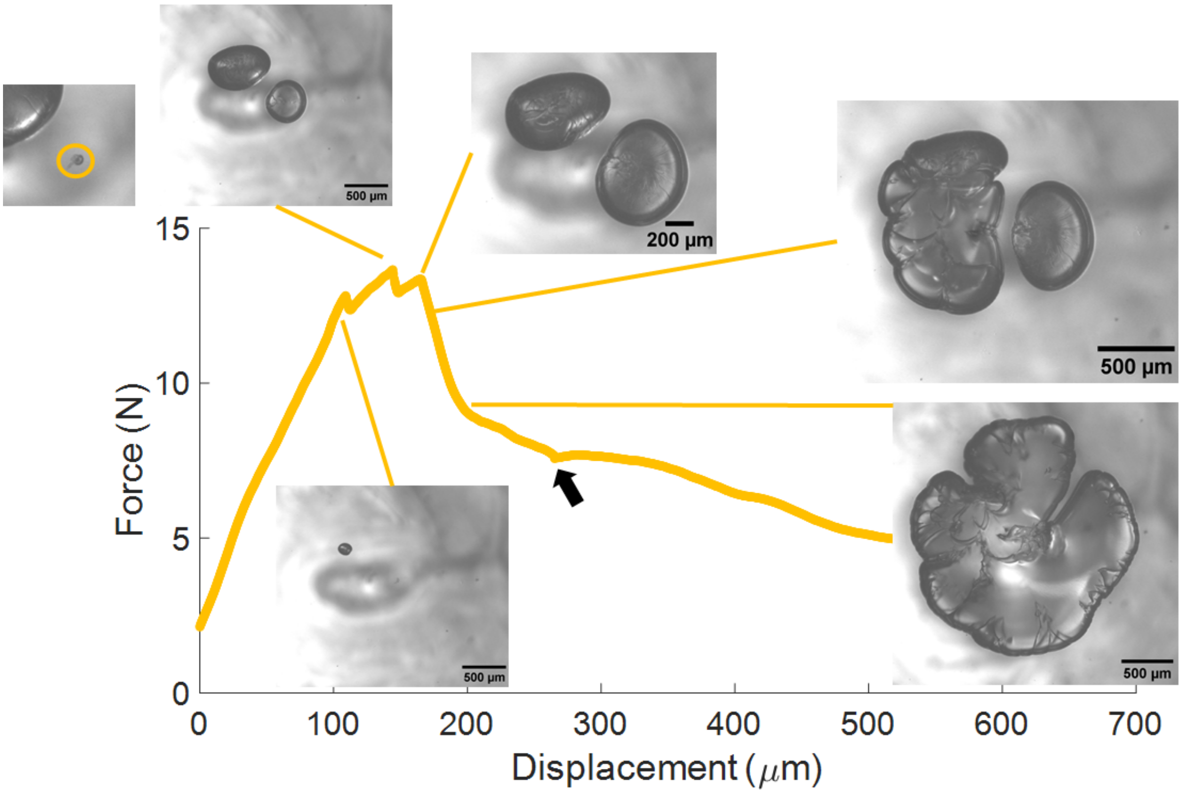

(A) Two cavities appear in the sample, only one becomes critical

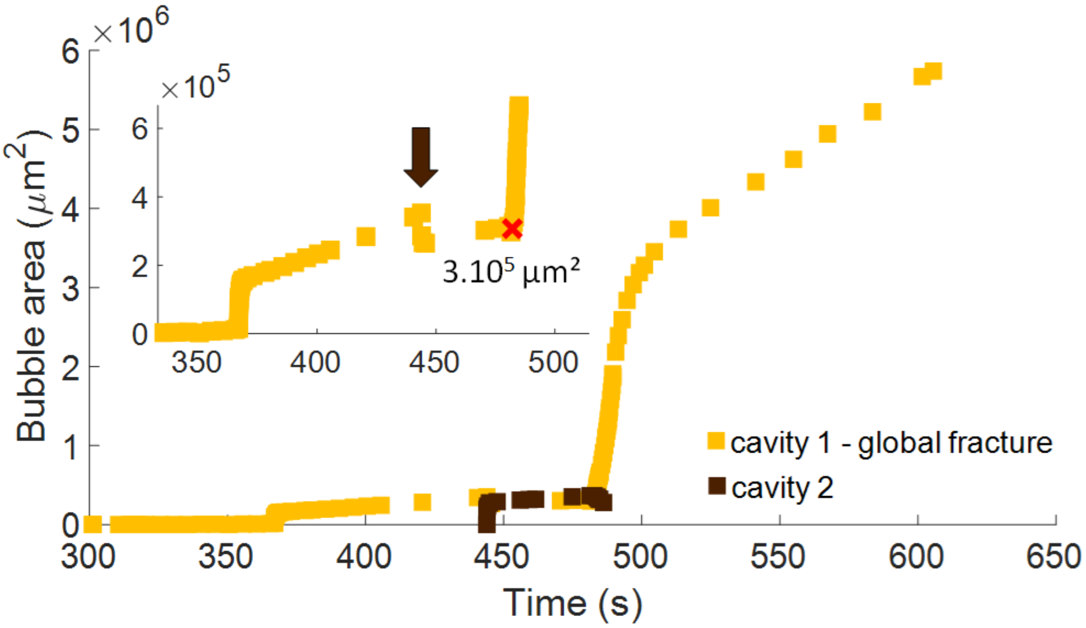

(B) Evolution of the cavities. The brown arrow in the insert shows the moment of the 2^{nd} cavity's snap.

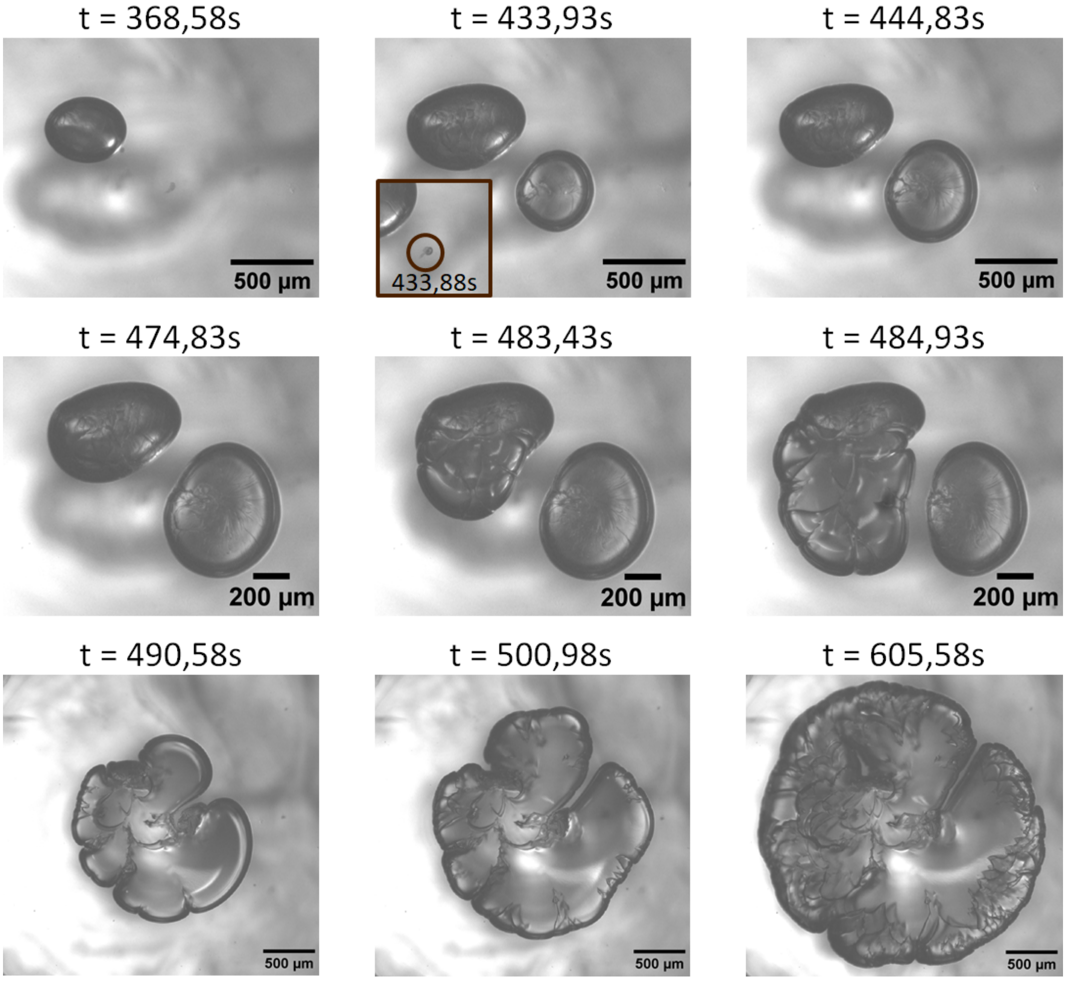

(C) Snap of the two cavities, destabilisation into several cracks and global circular fracture of the 1^{st} one

FIGURE 5.7: Cavitation in OLHEA1515_315um_0.5ums_2 with 2 cavitation events. (A) The black arrow indicates the switch to 5 μm/s (propagation of the global fracture). Scale bar: 500 μm. The first cavity snaps from a slow growing cavity. (B) Insert: zoom on the snapping of the cavity. The destabilisation of the crack's front into multiple penny-shapes is marked by the red cross. The area of transition is smaller than in the sample with only one critical cavity. (C) Insert on the second picture: initial defect seen before the snapping of the 2^{nd} cavity.

When decreasing again the layer thickness, now with a 200 μm sample, this stabilisation effect of the critical cavities is even more pronounced. First, the loading curve displayed on Figure 5.8 (A) shows several force drops, the first one corresponds to two cavities that appear a short time apart from each other, and 350 μm from each other. This distance is quite close, but again, this is only from the projection's observation and the cavities can stem from different positions along the height of the polymer layer. A bubble can also be seen in the polymer, it was present since the beginning and grows with increasing stress. The other peaks correspond to new cavities opening, in total 5 snap in the confined area.

Their growth is described on Figure 5.8 (B) and (C). The cavities 2, 4 and 5 snap open and grow slowly in the pancake shape. They do not seem to nucleate several penny-shaped cracks on their edges. Their position and evolution can be identified on Figure 5.8 (D). The cavities also interact with each other, as the snapping open of one cavity can change the shape of a neighbouring one. Finally, those non critical cavities shrink again as the fracture propagates. This critical fracture arises from cavity 1 and 3. Cavity 1 shows the standard behaviour of snapping, slowly growing and then transiting into the raspberry shape which accelerates the growth. On the other hand, the cavity 3 opens from a pre-existing defect, next to a pre-existing bubble. The growth from the defect seems to accelerate the transition to a fracture, while the bubble's projected area grows linearly and gets eaten by the cavity's expansion. Due to the fact that they are so close, it is not easy to differentiate their growth, so the global area of (cavity 3 + bubble) is displayed on Figure 5.8 (C) with stars. The evolution of cavity 1 can be followed independently and is represented with the black circles.

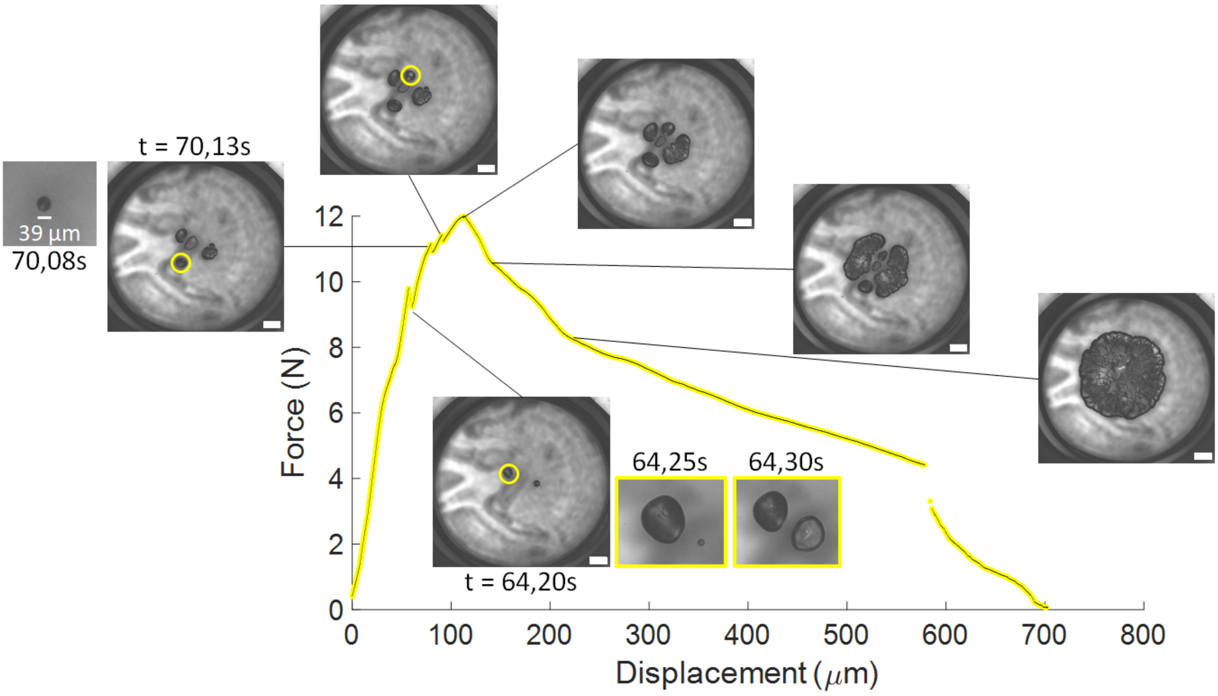

(A) Loading curve of a 200 μm sample and corresponding cavitation events. Scale bar: 500 μm.

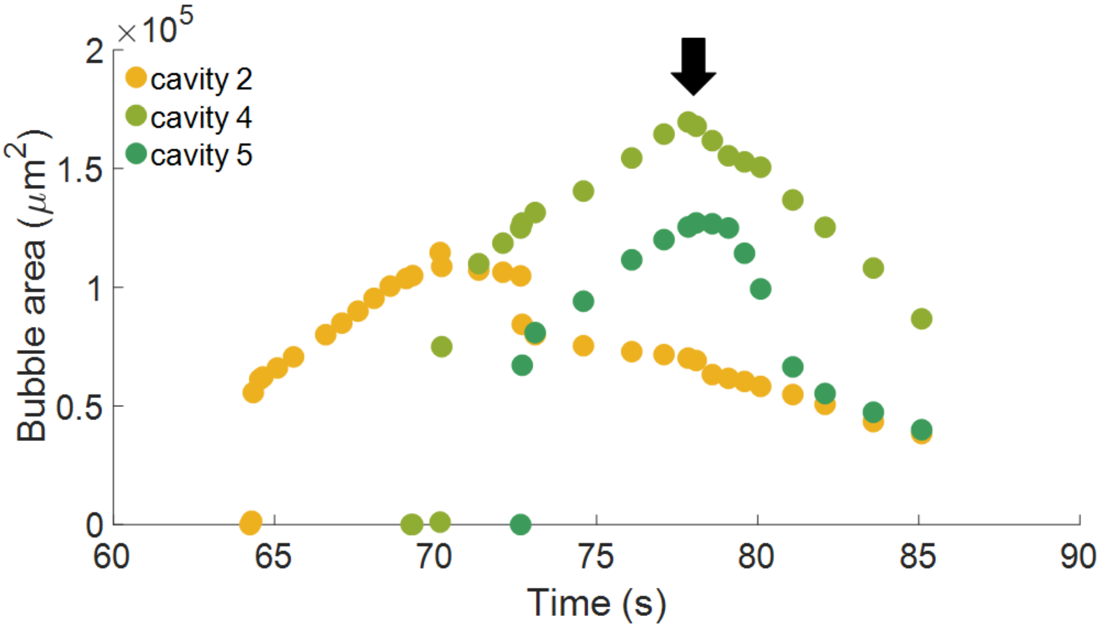

(B) Evolution of the non critical cavities

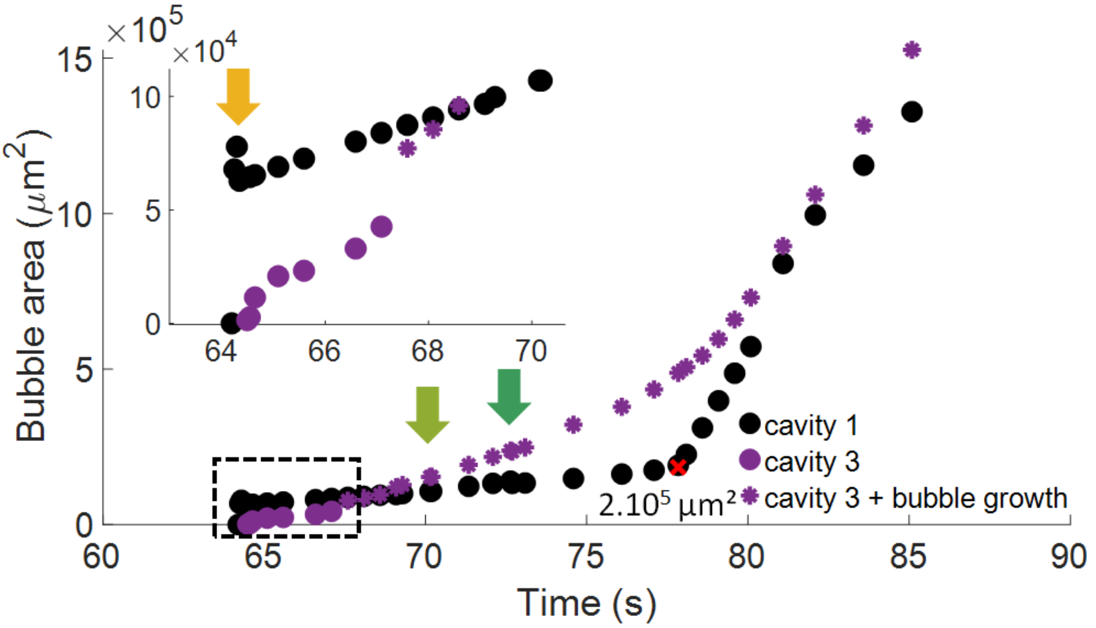

(C) Evolution of the cavities that transit to fracture

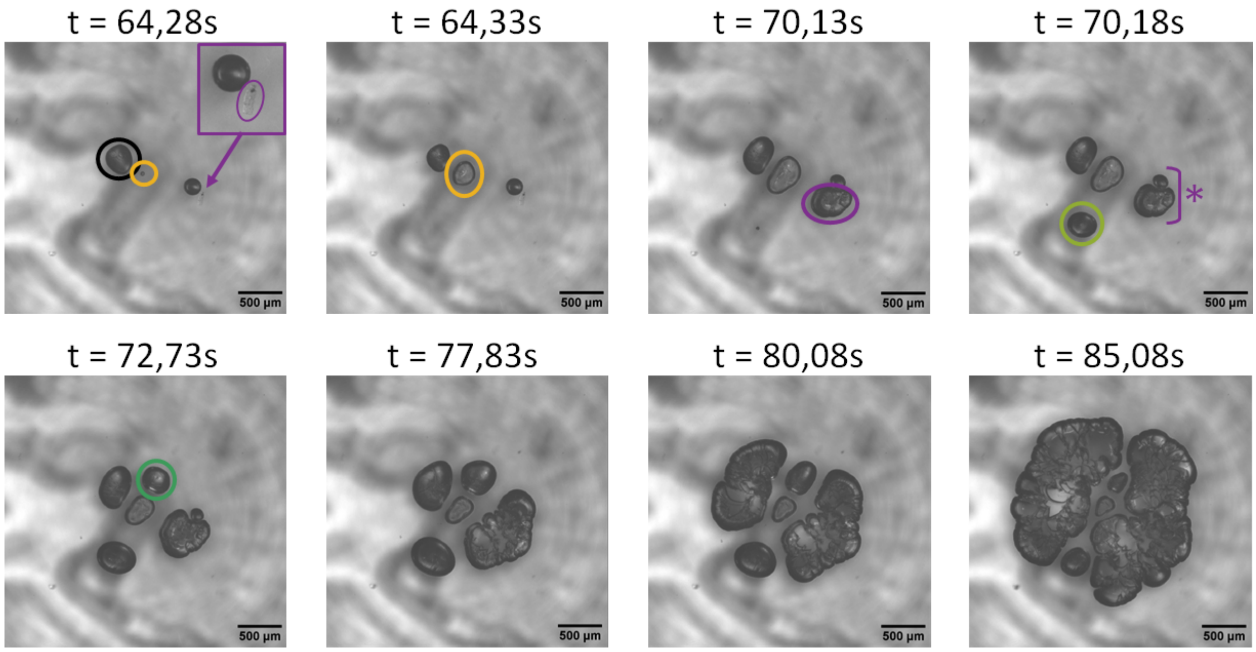

(D) Important cavitation events and labelling of the cavities

FIGURE 5.8: Cavitation in OLHEA1515_200um_5ums. (A) Several cavitation events happen but only 2 cavities evolve into a critical fracture. (B) Evolution of 3 cavities that snap open but shrink in size due to the fracture propagation of the 1st cavity. Black arrow: time at which cavity 1 transitions into the fracture mode. (C) Purple circles: snap of the 3rd cavity. Purples stars: combined area of the 3rd cavity and of the neighbouring defect. Red cross: transition of cavity 1 from single crack to several penny shaped cracks. Insert: zoom on the snapping of the cavities. Coloured arrows: time at which the non critical cavities snap open. (D) The coloured circles indicate which cavities open. Purple insert: the defect that leads to the 3rd cavity is circled, next to the neighbour bubble.

Finally, the estimated stretch rates for the snapping of the cavities is presented in Table 5.1. When no precursor is optically visible before the snap, it was estimated that $R_0 = 2\ \mu$m. As the optical resolution of our objective is 2 μm, it would correspond to an initial defect diameter of 1 pixel. This may be overestimating the initial defect size. The stretch and the stretch rates are then computed as:

$$\lambda = \frac{R}{R_0} \; \& \; \frac{\lambda}{dt} = \frac{\lambda}{t(R) - t(R_0)} \; (s^{-1}) \tag{5.2}$$

Cavity number	Stretch	Stretch rate (s^{-1})
1	73	1460
2	6.3	126
3	3.9	6.39
4	8.6	172
5	73	1460

TABLE 5.1: Estimated snapping stretch rates for the cavities in OLHEA1515_200um_5ums

The other sample tested at 200 μm (OLHEA1515_200um_5ums_2) displayed only two cavitation events, and one that transited to the fracture, much like the 315 μm sample. The intermediate thicknesses seem to present only a few cavitation events, and only one cavity that shifts to the critical fracture. When considering only the cavities that transition into the critical fracture, the intermediate thicknesses seem to allow for a pseudo-stabilisation of the expanded cavity. It can grow, but its front remains uniform, while when the destabilisation starts, different penny shaped cracks propagate and create anisotropy.

5.1.2.3 Thin samples - many cavitation events

Finally, let's analyse the thinnest samples we tested. Their behaviour is very similar, so we will focus on the 100 μm samples. The loading curve of the 50 μm sample is displayed in Appendix D.2. When looking at the Force versus displacement curve displayed on Figure 5.9, it is clear that a much bigger number of cavities open. The cavities expand both during the force increase and beyond the maximum force value: cavities still nucleate during the plateau of the force. This plateau ends when the fracture begins to propagate.

Actually, as the fracture starts to propagate from the cavity in the upper half of the sample, other cavities snap open in the lower half! Because of the large number of cavities and the changing background due to the deformation of the glue in the background, only the growth of a few cavities has been analysed. First, the behaviour of the first four cavities that snap open close to the apex of the sphere is displayed on Figure 5.10.

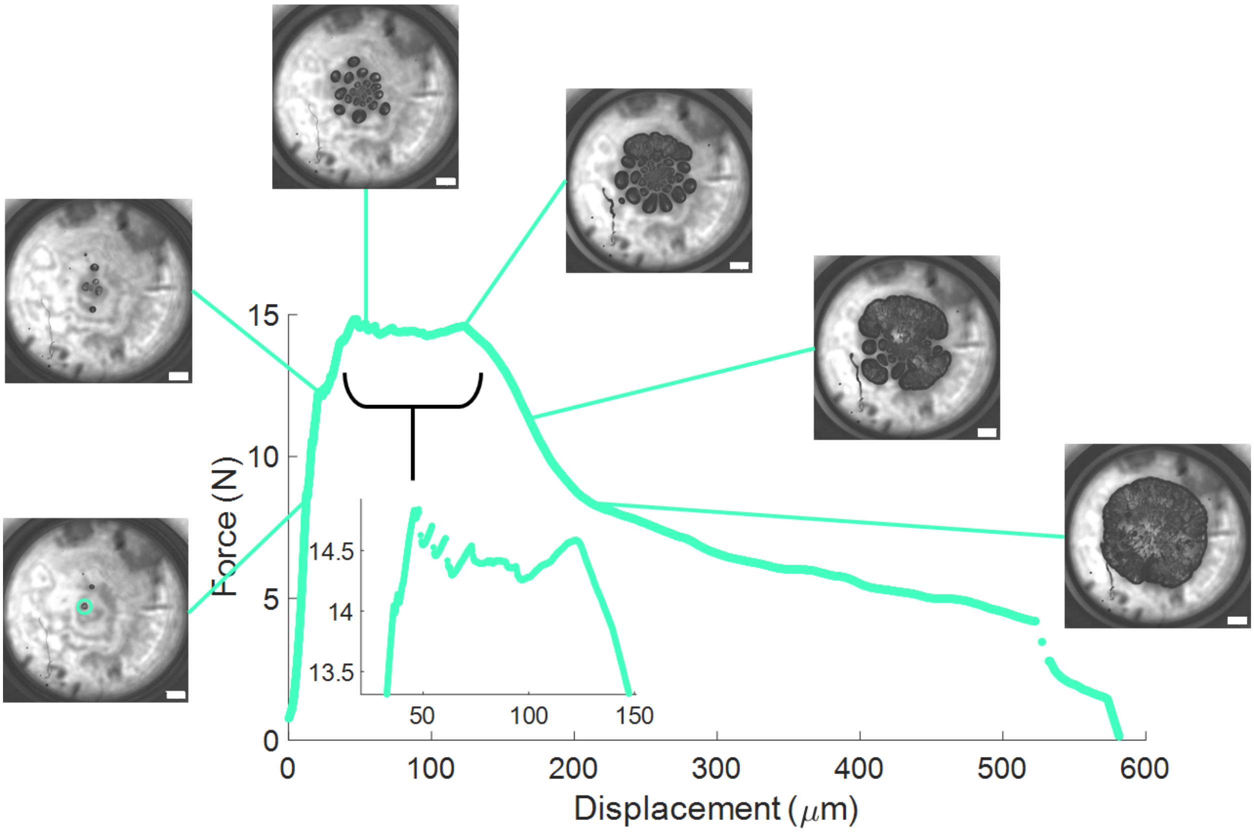

FIGURE 5.9: Loading curve OLHEA1515_100um_5ums and corresponding cavitation events. Scale bar: 500 μm.

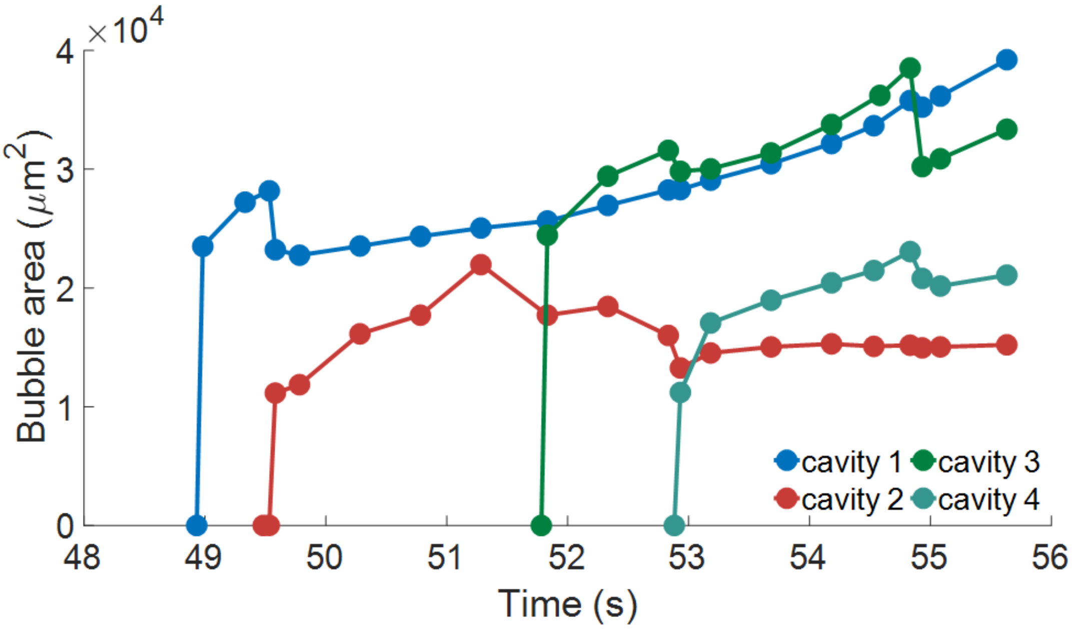

(A) First four cavities evolution and interaction

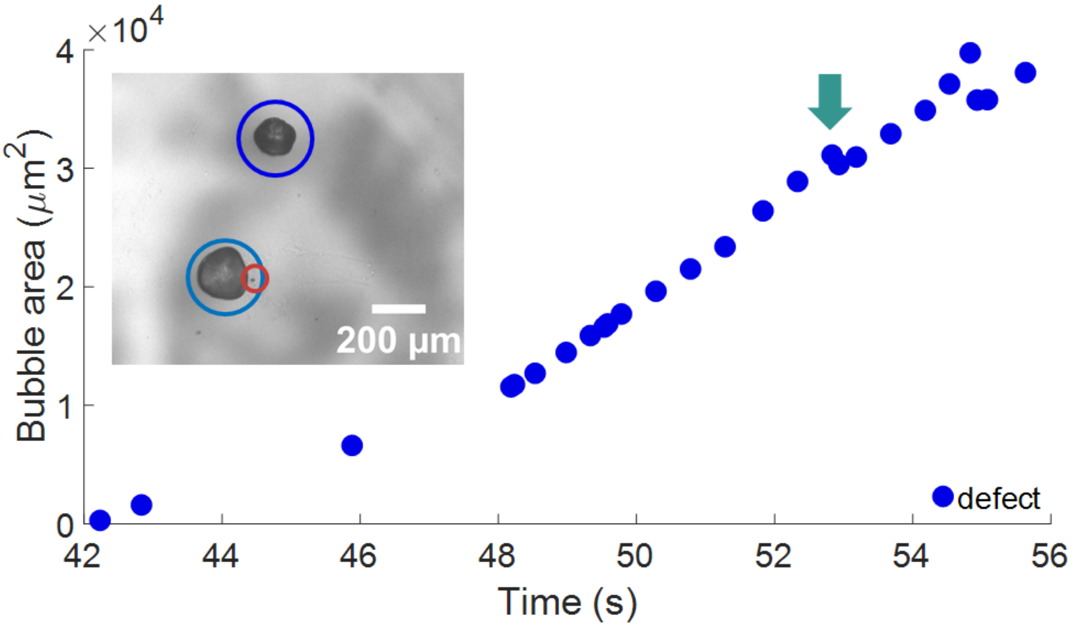

(B) Pre-existing defect's evolution

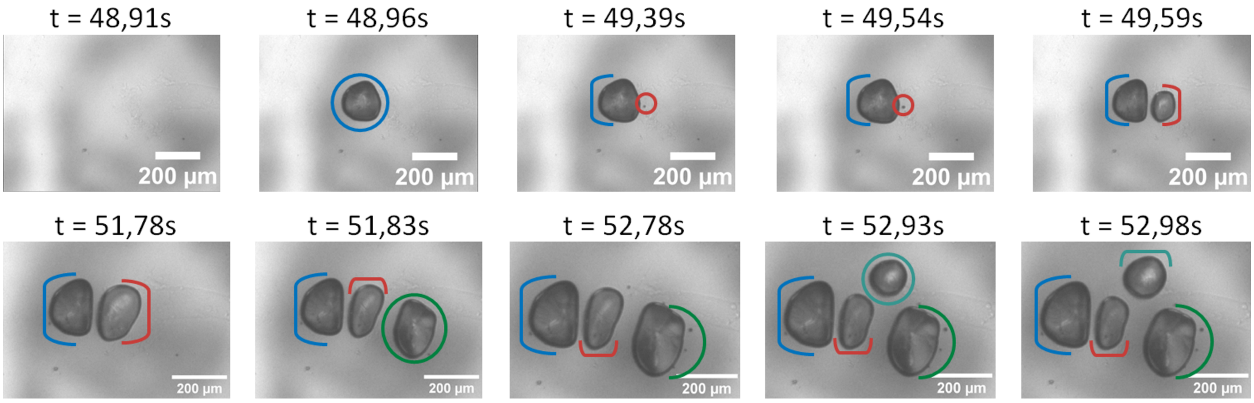

(C) Corresponding images and cavities snapping. Scale bar: 200 μm

FIGURE 5.10: First cavities evolution in a thin sample: OLHEA1515_100um_5ums. (A) The cavities snap and grow slowly, their eventual surface decrease can not be easily analysed. (B) The evolution of the shape and size the pre-existing defect (small bubble) are influenced by the presence of neighbouring cavities, as displayed by the coloured arrow, corresponding to cavity 4.

All cavities interact with each other's growth, and they all snap in the surroundings of the apex. The first 2 cavities snap at only 100 μm distance from each other! In the sample, there is also one pre-existing defect with a linear growth of its projected area, as can be seen on Figure 5.10 (B). The fact that large defects do not present a snapping behaviour but a stable growth was already observed by Chiche et al. in probe tack experiments [96].

Then, the behaviour of the cavities that switch to crack propagation is analysed on Figure 5.11, with both the evolution of the growth and the corresponding cavitation events. Cavity 1′ and 3′ both grow from pre-existing defects opening at approximately 980 μm from the apex. However, 1′ shows a steady growth while 3′ grows suddenly to a small sized cavity. This difference in behaviour can be explained by their initial size: 1′ initiates from a defect of 49 μm in diameter while 3′ grows from an initial diameter is 29 μm. However, since we don't know the exact nature and shape of these pre-existing defects, it is hard to go further in the explanation of this difference.

Cavity 2′ shows a "true" snapping behaviour, and its precursor is barely visible before the snap. As already seen for the critical cavities in the other thicknesses, the cavity grows slowly after the snap and its front remains uniform. Its shape is highly dependant on the other cavities that grow around it. Finally, it destabilises into several cracks, while cavity 1′ has already begun to propagate into fracture.

The difficulty of the observation of the evolution of the first cavity that appears in the vicinity of the apex is well described on Figure 5.11 (B): while it seems that each cavity is well defined for a long period of time, meaning that the polymer walls between them has not broken yet, it is complicated to detect when and where the fracture does happen. It is not clear whether it starts in the confined area, or coming from one of the cavities that transition into fracture.

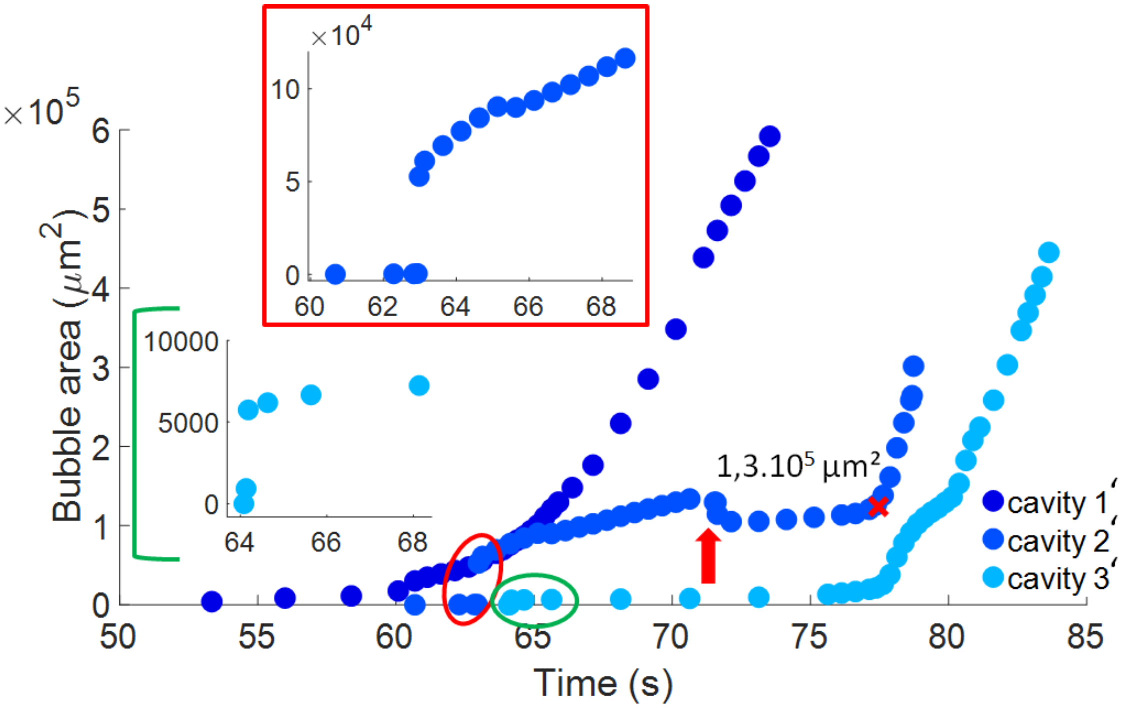

(A) Evolution of the critical cavities

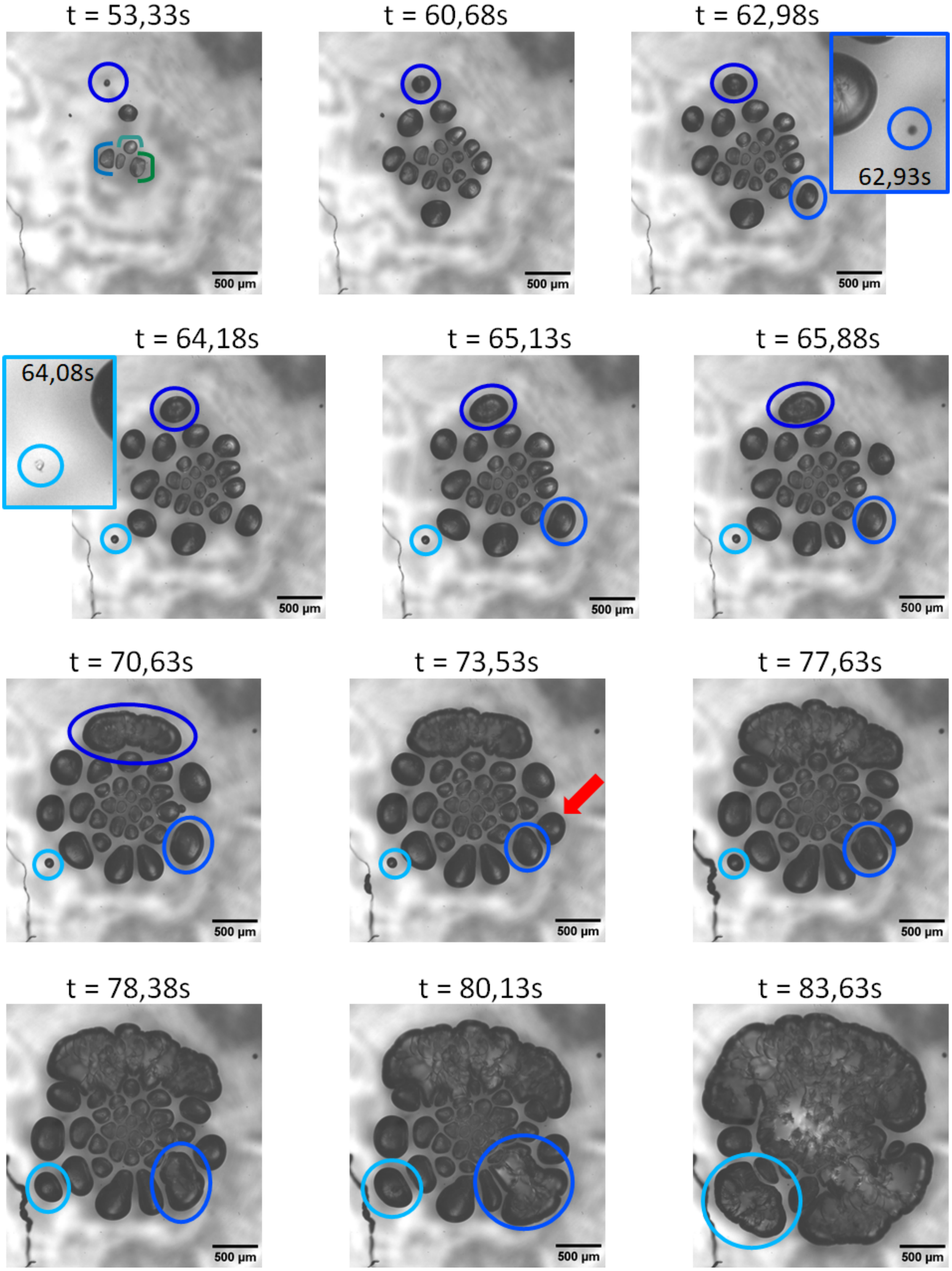

(B) Corresponding cavitation events. Scale bar: 500 μm

FIGURE 5.11: Three critical cavities that fracture the material - OLHEA1515_100um_5ums. (A) Insert: zoom on the snapping behaviour. The 3^{rd} critical cavity opens from a defect, which seems to limit its expanded size. Red arrow: one non-critical cavity opens and disrupts the critical cavity 2′, red cross: area of transition from the single crack to the several penny-shaped cracks. (B) Each cavity is marked by a coloured circle. The 4 first cavities are marked on the first picture (t = 53.33s). The red arrows shows the cavitation event that interacts with cavity 2′.

Again, we can compare this cavitation behaviour with the slower testing speed. The cavitation behaviours is displayed on Figure 5.12, the corresponding Force versus displacement curve can be seen in Appendix D.2. The behaviour observed in OLHEA1515_100um_0.5ums is exactly the same as in OLHEA1515_100um_5ums, the cavitation dynamics does not seem to depend on the testing velocity. The non-critical cavities snap open but finally shrink, the critical cavities snap, reach a plateau and then suddenly grow. The very interesting behaviour here is that several cavities destabilise and propagate into cracks that will converge. This transition from the snapped cavities to the nucleation of multiple penny-shaped cracks appears roughly at the same value of projected area of the expanded cavity: $7.10^4 \mu m^2$. This was not observed in the thicker samples. It is to be noted that when 100 μm samples have a **big** pre-existing defect, they snap directly into critical fracture. The growth of several cavities is a reproducible behaviour of thin layers that do not present obvious defects.

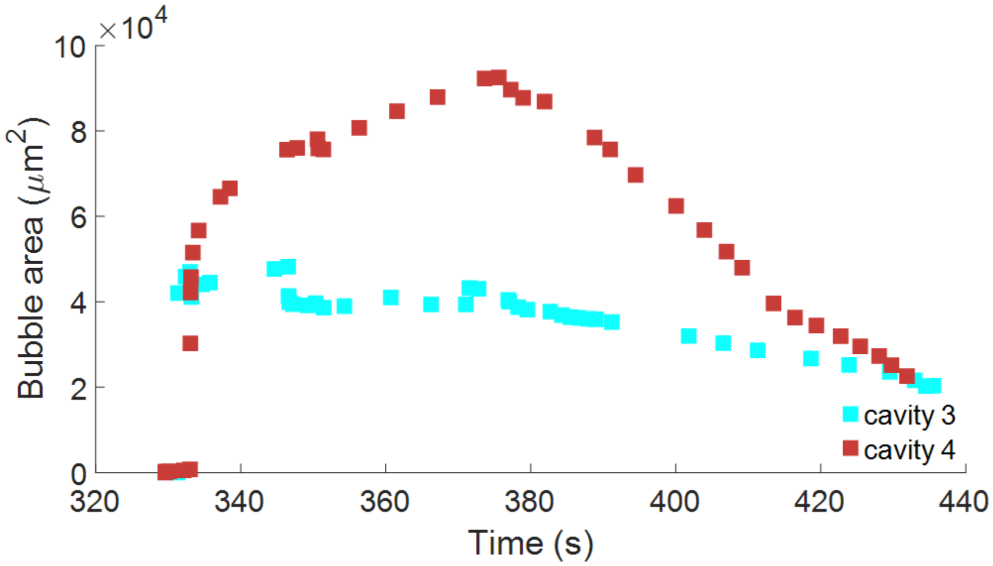

(A) Two non-critical cavities

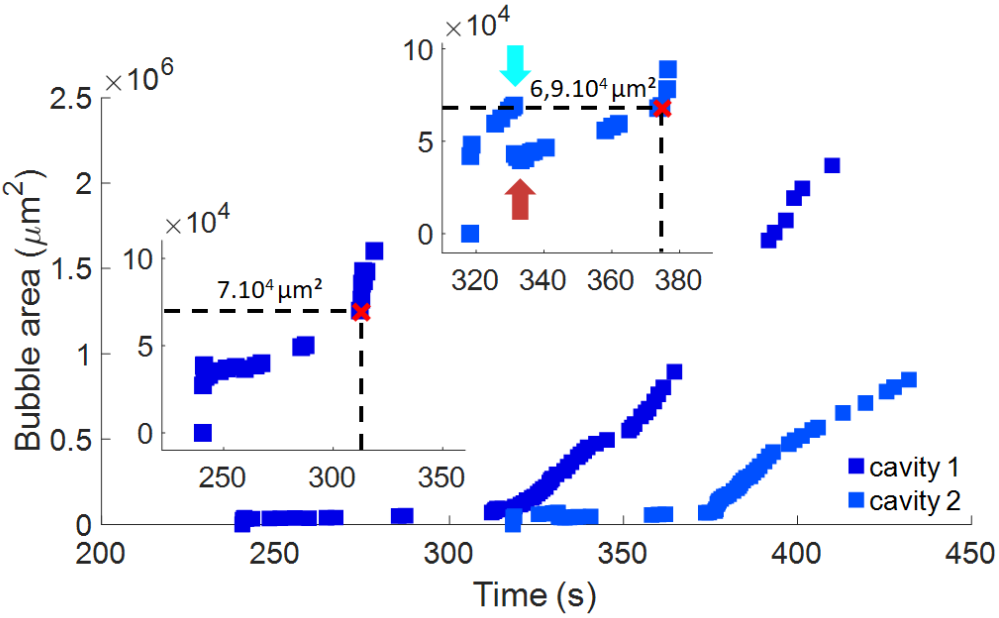

(B) The 2 critical cavities

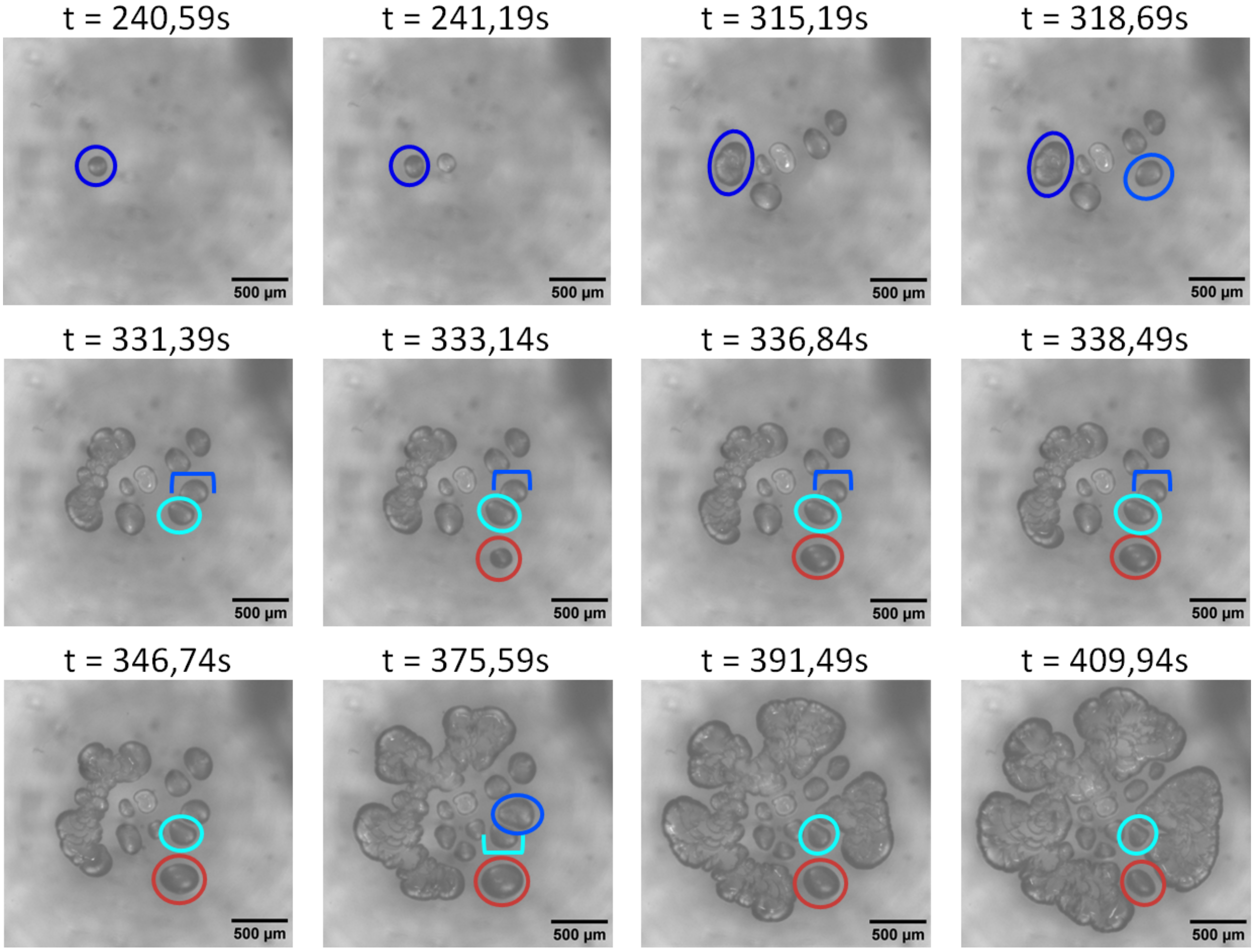

(C) Corresponding cavitation events. Scale bar: 500 μm

FIGURE 5.12: Cavitation behaviour of OLHEA1515_100um_0.5ums. (A) Evolution of 2 cavities that snap, grow slowly and decrease due to the surrounding fracture. (B) The two fracture events come from snapping cavities. Insert: zoom on the snapping behaviour. Arrows: time of the snapping of the non-critical cavities. Dotted black line and red cross: transition from the snapped cavity to the multiple penny shaped-cracks and corresponding area. (C) Observation of the cavitation behaviour. The cavities analyzed on (A) and (B) are marked by their respective colours.

The stretches at the snapping event and the corresponding stretch rates of all analysed cavities in OLHEA1515_100um_0.5ums and OLHEA1515_100um_5ums are summarized in Table 5.2 and Table 5.3. Again, if no precursor is visible, R_0 is assumed to be 2 μm. The first two lines correspond to the critical cavities that present a snap, the other lines describe the non-critical cavities.

Cavity number	Stretch	Stretch rate (s^{-1})
1	55	137
2	62	124
3	58	1160
4	7.4	74

TABLE 5.2: Characteristics of the cavities for OLHEA1515_100um_0.5ums. 1 and 2 were critical.

Cavity number	Stretch	Stretch rate (s^{-1})
2′	11	220
3′	9.5	190
1	44	864
2	31	620
3	44	880
4	30	600

TABLE 5.3: Characteristics of the cavities for OLHEA1515_100um_5ums. 2′ and 3′ were critical.

5.1.3 Closer look on the pseudo-stabilized cavities

It appears that when the thickness of the sample decreases, the expanded cavities reach a metastable state with an inflated pancake shape before transiting to the raspberry type fracture. In order to better understand this cavitation state, we decided to investigate the damage sustained by the cavity during snapping by labeling the sample with mecanophores. We used the π-extended anthracene (Diels Alder Cross-Linker, DACL) as described by Slootman et al. [11]. In a nutshell, the DACL is bifunctionalized with acrylate functions and polymerises and crosslinks with the network. When put under tension, the molecule can undergo a retro Diels Alder reaction when a critical force on the bond is applied and one of the moieties becomes fluorescent reporting therefore for damage. Since the mechanophore is incorporated in a dilute concentration and its scission force is not too much lower than that of a covalent bond, it reports accurately for molecular damage.

The polymer mix tested consisted of the OL HEA 15% EHA 15% PEA formulation. The molar percentage of DACL added consisted of 7.3% of the molar percentage of the HEA oligomer:

$$n(DACL) = 0.073 * n(OL\ HEA)\ (mol) \tag{5.3}$$

To ensure a good dispersion of the DACL in the polymer mix, it was dissolved in dry acetone before its incorporation to the polymer melt. The complete mixing procedure is summarized in Appendix D.3. Then, the cavitation samples were prepared following the usual polymerisation protocol of 70% lamp power and 1s of illumination. After polymerising, the samples were kept in the dark and in the fridge (T = 5°C) before and after testing. It is important to note that the retro Diels Alder leading to fluorescence can also take place if the sample is put under heat or under prolonged UV light, and it was verified that our polymerisation protocol did not induce the activation of the mecanophores. We can then assume that all the fluorescence observed after the testing of the sample is due to polymer chain scission.

To create the cavities, a sample of OL HEA 15% EHA 15% PEA marked with 7.3%mol/mol(OL HEA) DACL with a thickness of 100 μm was tested in the hydrostatic traction set-up at a loading rate of 0.5 μm/s until the first cavitation event was observed. The loading was then stopped and the unloading was made at 5 μm/s until complete unloading of the sample. This sample will be named OLHEA1515_7pc3DACL_100um_0.5ums. After the test, the sample is back to its initial state, the polymer layer is still binding the half sphere to the glass slide, as opposed to the usual tests which were loaded to fracture and where the sample is torn in two. The loading curves and the corresponding cavitation events are displayed on Figure 5.13.

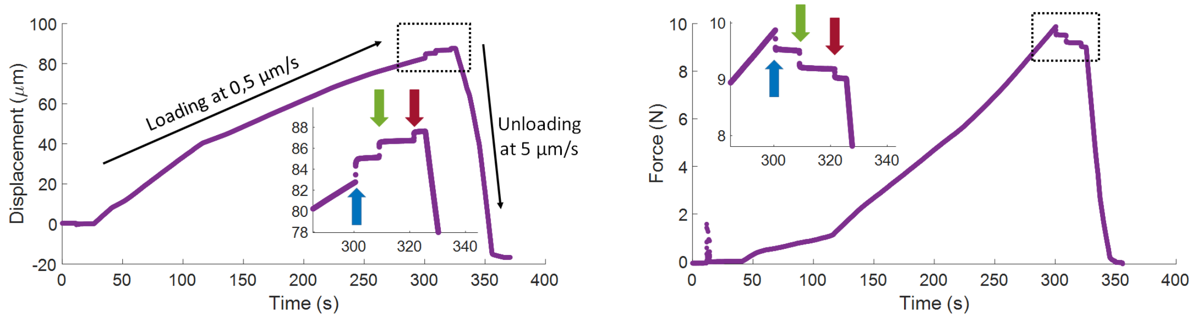

(A) Displacement versus Time

(B) Force versus Time

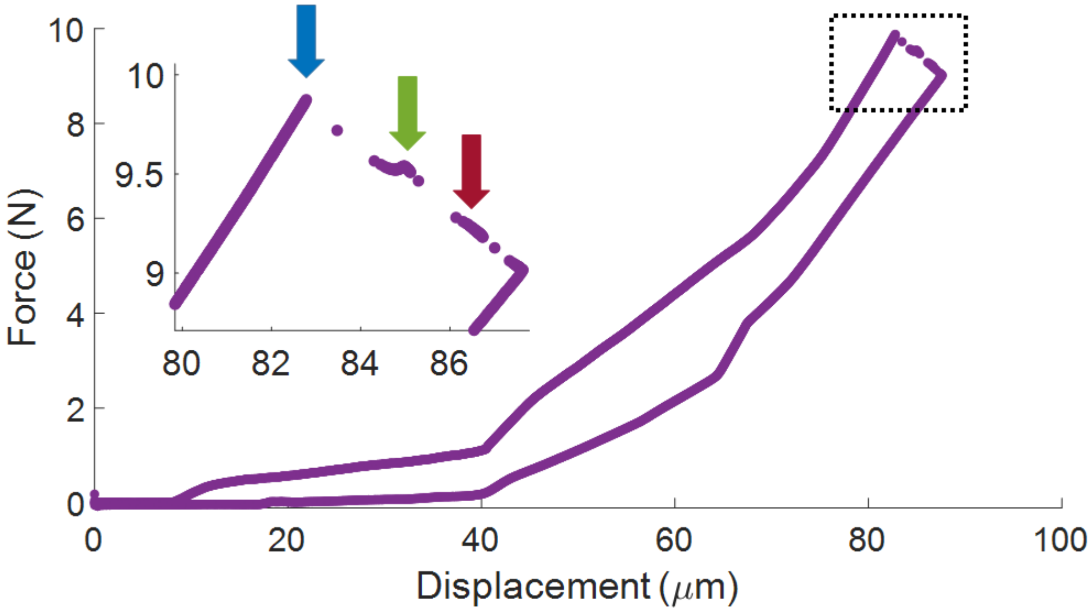

(C) Force versus Displacement to create cavities - complete cycle

FIGURE 5.13: Loading and unloading curves on OLHEA1515_7pc3DACL_100um_0.5ums with no critical fracture. Inserts: zoom on the cavitation events, coloured arrows: specific cavitation events. (A) The loading starts at 26s and the unloading finishes at 353s. The rest of the unloading (t > 353s, Displacement < 0 μm) corresponds to an extra displacement to facilitate the removal of the sample from the set-up. (B) The small jumps of Force at the beginning of the test correspond to the calibration between the sensors and the camera.

As can be seen on Figure 5.13 (A), even if the loading is stopped after the first cavity event, two other cavities appear. They result in a jump in both the displacement and the force, as the opening of each new cavity increases the volume of the sample and releases the stress. Figure 5.13 (C) displays the full loading/unloading cycle. As expected, the unloading cycle is below the loading one, as the material has been damaged by the cavitation. However, no precise analysis can be done on this behaviour as the loading curve is also impacted by the potential deformation of the glue between lens and metal support and by the alignment in the set-up, therefore the force-displacement curve is not purely representative of the polymer's deformation.

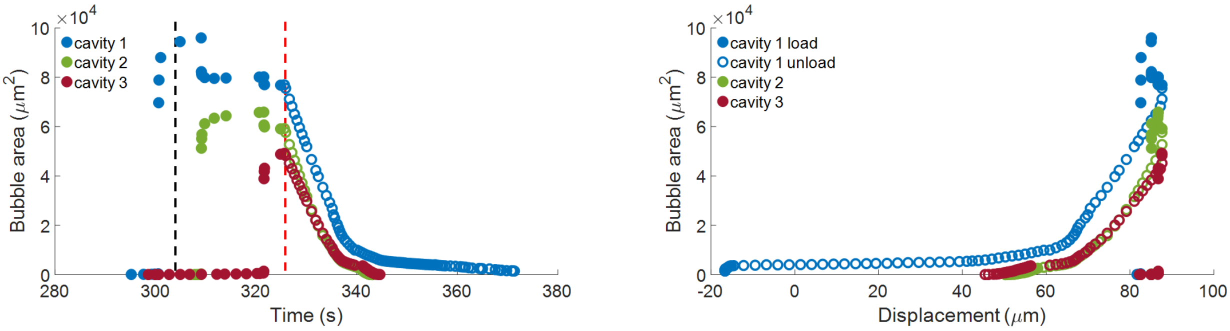

(A) Cavities evolution with time

(B) Cavitation events and evolution during the unloading

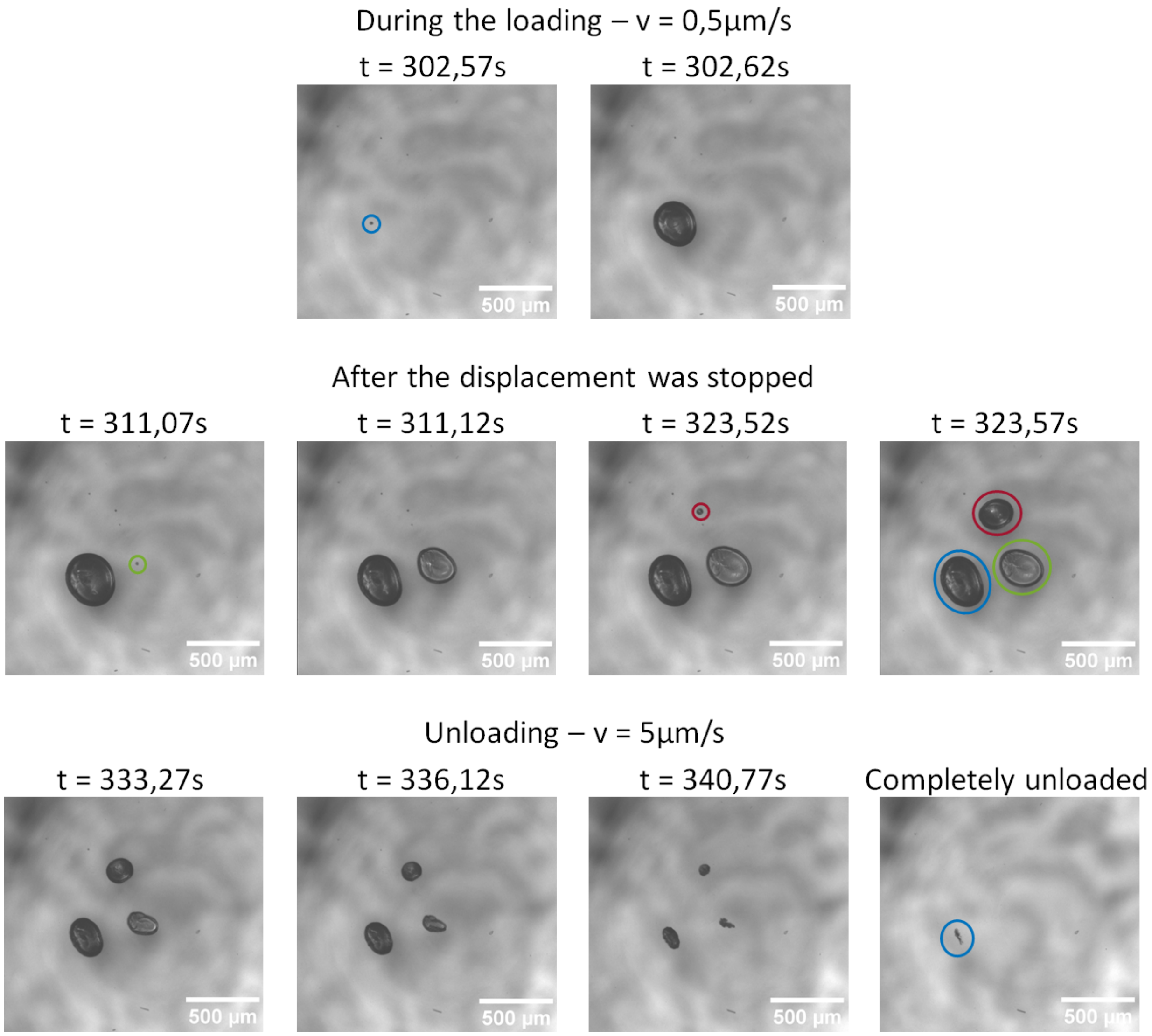

During the loading – v = 0,5µm/s

t = 302,57s t = 302,62s

After the displacement was stopped

t = 311,07s t = 311,12s t = 323,52s t = 323,57s

Unloading – v = 5µm/s

t = 333,27s t = 336,12s t = 340,77s Completely unloaded

(C) Force versus Displacement - complete cycle

FIGURE 5.14: Opening and closing of the pseudo-stable cavities - OLHEA1515_7pc3DACL_100um_0.5ums. (A) Evolution of the cavities area with time. Black dotted line: loading stops. Red dotted line: Unloading starts. (B) Bubble area with the unloading. Cavities 2 and 3 have a very similar behaviour during the closing. (C) Corresponding cavitation events. Scale bar: 500 μm. When the cavities close, it is possible to observe the cracks that formed them. Only the fracture caused by cavity 1 is still visible after the sample's unloading.

Figure 5.14 displays the cavitation dynamics and the cavitation events. Again, all cavities snap open. However, it is quite interesting to note that the last two cavities opened while the loading was stopped. Even if the force on the sample decreased due to the opening of the 1^{st} cavity, other cavities could nucleate and snap open, and quite close to each other. Their position from the apex of the sphere is shown in Table 5.4. We observe that the projection of the cavities is not purely circular but can become elongated, especially during unloading. More important than the area, we define the aspect ratio of the cavities (major axis/minor axis), which is displayed on Figure 5.15.

For each cavity, the snapping event leads to variations of the aspect ratio, which is not surprising, as the precursor of the cavities is very small and its detection and analysis can be flawed. However, the shape of the 3 cavities evolve differently:

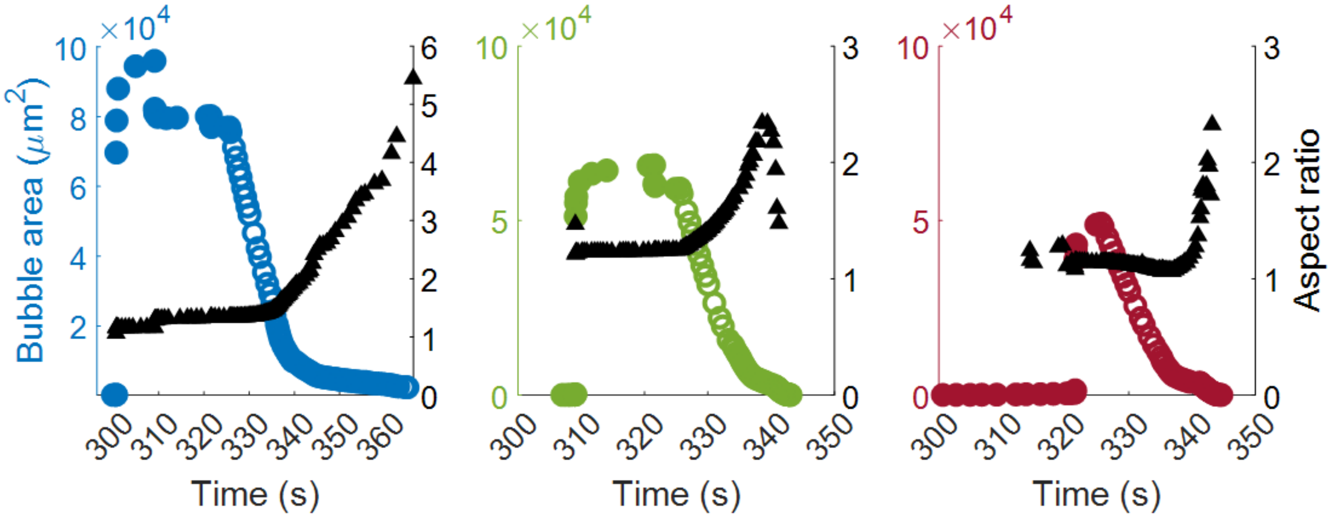

FIGURE 5.15: Aspect ratio's evolution during the cavities evolution - OL-HEA1515_7pc3DACL_100um_0.5ums. The aspect ratio is the ratio: major axis/minor axis. The first cavity is described by the left graph, the second by the middle graph and the third by the right graph.

- 1st cavity: the aspect ratio stays constant after the snap, when the loading is stopped and in the beginning of the unloading. The shape starts to change at t = 335s, which corresponds roughly to the slowing down of the area decrease.
- 2nd cavity: the aspect ratio starts to change as soon as the unloading begins, at 325s, the cavity disappears at t = 343s.
- 3rd cavity: the aspect ratio decreases slowly during the unloading, its strong change starts at 337s, the cavity disappears at t = 344.6s.

The study of the aspect ratio helps to understand if the cavities show a self-similar growth and decrease as was described by Morelle et al [13] and Kim et al. [5]. However, as we see a projection of the cavities, their shape change will also depend on the orientation in space of the crack surface that lead to the inflation of the cavity. Indeed, the behaviour of a cavity that appears parallel to the glass slide and one that appears normal to it will be quite different during the unloading.

To further explore these ideas, this sample was observed by confocal microscopy to identify the extent of polymer damage coming from these cavitation events. The confocal macroscope used is a customized Nikon AZ-100/C2+. The objective is an AZ Plan Fluor 5x, with a focal length of 15 mm with a 3x zoom. This set-up allows for a large working distance that is needed to fit our cavitation sample under the objective. The observation is made through the glass slide. The fluorescence of the DACL is observed via a 405 nm excitation wavelength and the emission was collected between 450 and 550 nm. The resulting observation is displayed on Figure 5.16. The scanned volume is a square of 1392.45 μm size and 200 μm of depth. The pixel size is 1.36 μm.

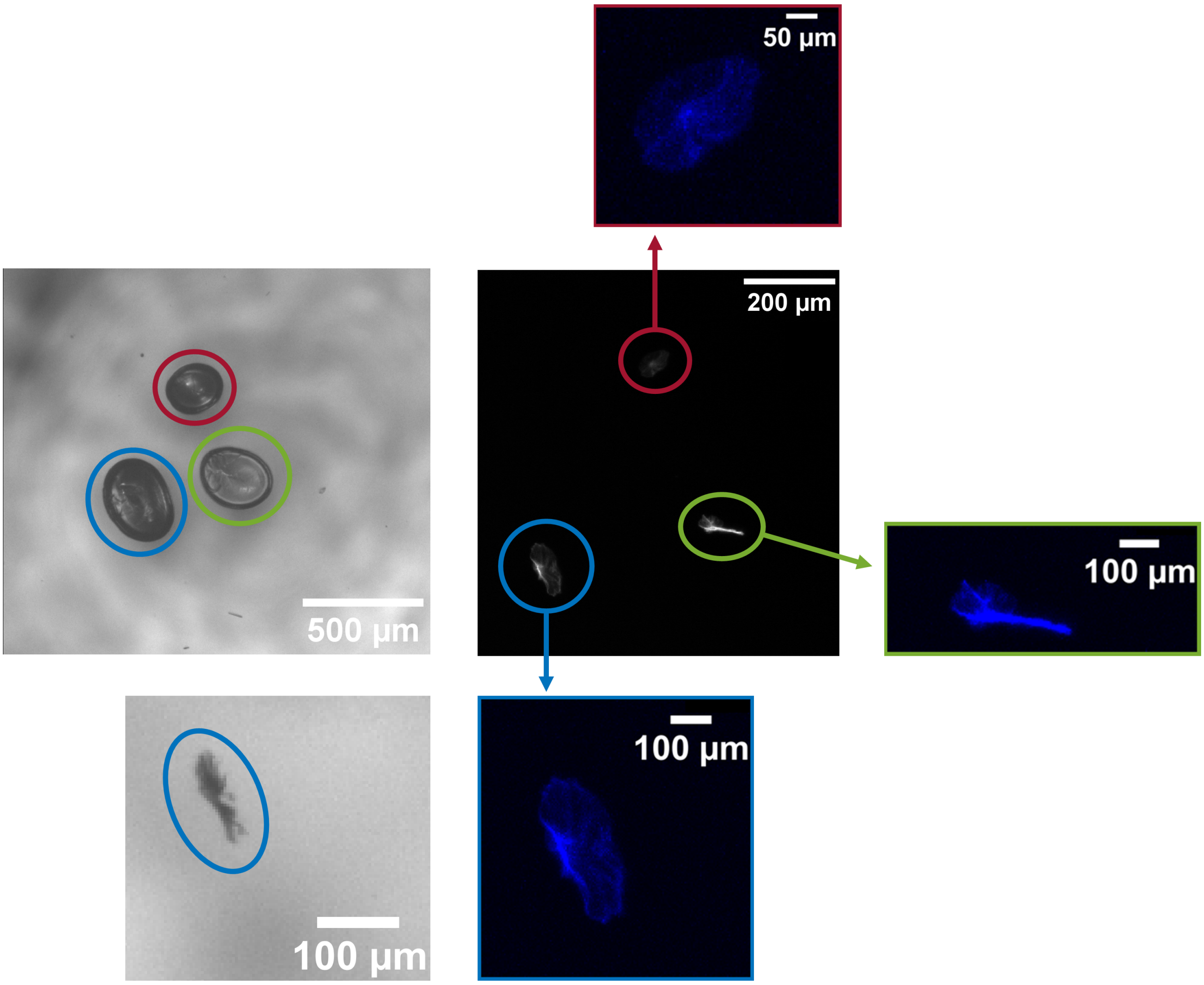

FIGURE 5.16: Comparison between the experimental observations and the confocal imaging. Left: Observation of the inflated cavities during the experiment and the residual damage after the unloading of the 1^{st} cavity. It seems that the cavity was the result of a burst of several cracks. Right: confocal imaging with Laser at 3, Gain at 5, scan over a range in z of 200 μm, each plane is an averaged intensity of 2 scans. All pictures result from an addition of all the z scans into 1 picture. The circles allow for the identification of each cavitation.

First of all, the fluorescent signal observed can be directly linked to the cavities we observed snapping during the experiment and each cavitation event corresponds to a distinctive feature in the confocal image. Even if the cavities 2 and 3 disappeared during the unloading, their respective molecular damage (due to the expansion) was found in the network. This first result confirms our description that the cavities that snapped, but stayed in the pseudo stabilised state provoked damage and fracture in the network. It also seems that all cavities have a nucleus of high molecular damage, which is of higher intensity. However, we did not have time to quantify the damage, so we can not analyse this further.

Then, it does look like the cavities did not open in the same plane, and do not have the same orientation relative to the glass slide. This is especially true for cavity 2, in green, as we see a line of damage, which suggests that the crack actually was perpendicular to the glass slide. If we compare that to the aspect ratio's behaviour, it would explain why cavity 2 shows this rapid change in aspect ratio with the unloading. This difference is summarized in Figure 5.17.

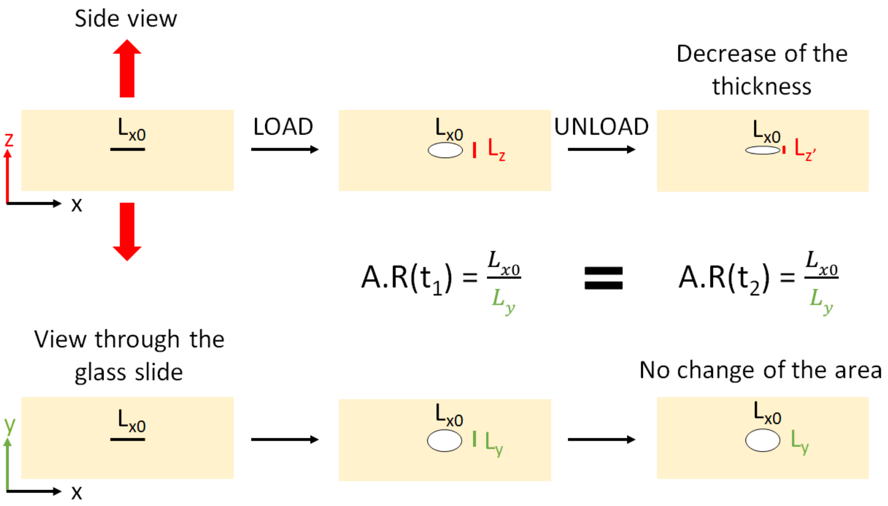

(A) Unloaded crack parallel to the glass slide

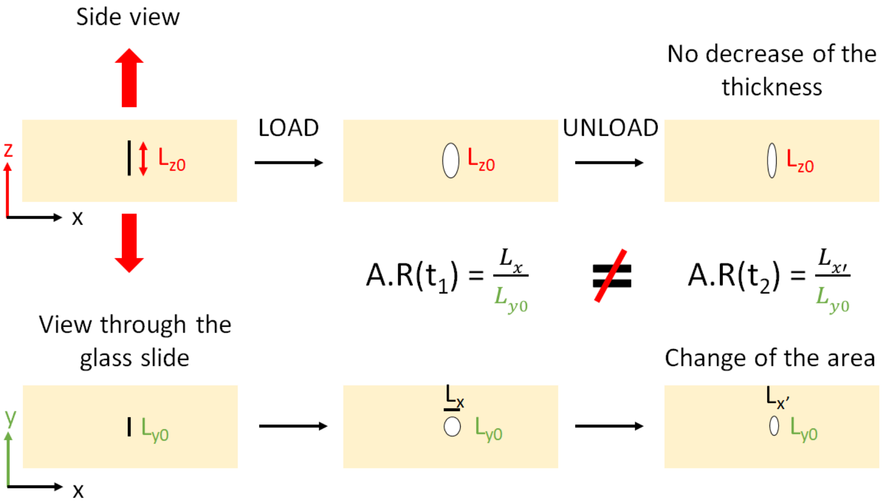

(B) Unloaded crack perpendicular to the glass slide

FIGURE 5.17: Impact of the crack's orientation on the evolution of the Aspect Ratio upon unloading. We consider a circular penny shape in the sample, either parallel (XY plane) or perpendicular (YZ plane) to the glass slide in the network which is under hydrostatic loading. t_1: the penny shaped crack is inflated. t_2: the sample is unloaded, the crack deflates. Depending on the orientation, the aspect ratio does not evolve in the same way.

The confocal microscopy results suggest that cavity 2 was opened perpendicular to the glass slide, hence having an aspect ratio changing rapidly with unloading. It is to be noted that this orientation effect also influences the projected area of the cavities in the view through the glass slide, hence affecting the evolution of the bubble area we described. Therefore, thinking back at the different evolutions of the 500 μm sample with velocity (Figures 5.4 and 5.5), a different crack orientation could also be the cause of the small "stabilisation" observed in projected area for the slowest velocity. However, it can not be the only cause of the long stabilisation in projected area that is observed for the cavities in the thinner layers.

Finally, the confocal microscope images allows also the observation of the cavities position in the thickness of the sample, as shown on Figure 5.18. The scanned depth is twice the size of the layer thickness. This is mostly due to the fact that the glass/polymer interfaces are not very visible under the confocal illumination. Furthermore, even if the polymer layer on its own presents a small fluorecence (see Figure 4.20), the laser parameters used for its observation were much higher (Laser 50 and Gain 50) than the ones used for the mecanophores observation. If we wished to observe the signal coming from the polymer to set the sample's limits, it could lead to photobleaching of the activated DACL. Then, the cavities do not exactly appear at the apex of the sphere, so they appear in regions where the polymer thickness is larger, as described in Table 5.4. This leads to some uncertainties as to where to start and end the volume scan.

Cavity number	Position (mm)	Local polymer thickness (μm)
1	0.48	139
2	0.19	106
3	0.52	145

TABLE 5.4: Local polymer thickness at the snapping position of the cavities

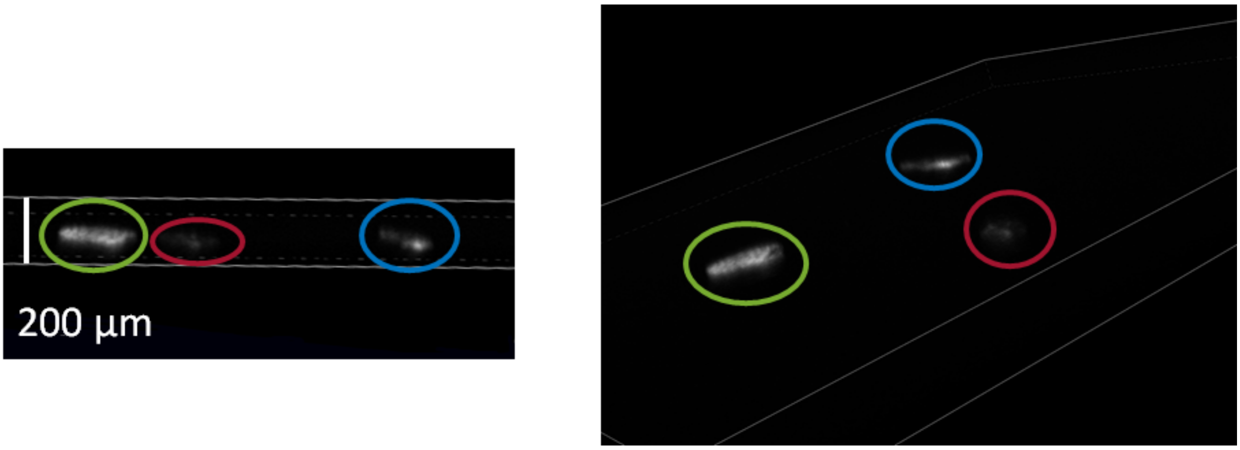

FIGURE 5.18: Volume scan of the cavities in the sample. The total scan thickness is 200 μm while the sample's confined thickness is 100 μm.

Based on the side views of the 3D scan, it is possible to see that the cavities/cracks did not appear in the exact same plane. However, it is not trivial to understand whether the damage around each cavity originated from a ductile like behaviour of damage around the whole cavity's surface or just originated from localized damage around multiple crack tips. In the absence of a time-resolved confocal measurement, the exact chronology of when the damage occurred around these pseudo stabilized cavities is therefore still ambiguous and the exact determination would require an in-situ observation of the damage during the loading, on the inflated sample. However, the damage seems to be localized in a plane.

Note on the position of the cavities in the thickness

Even if the use of mecanophores is an elegant way to observe the position of the damage in the network, the fact that the cavities did not appear on the same plane is already observable in the standard cavitation experiment with the vision through the glass slide. As already described in the analysis of the cavitation with the thickness, when several cavities appear, they interact with each other. The way the inflated cavities deform in reaction to the snapping open of other cavities informs also on their respective position in the thickness. One example is shown on Figure 5.19. In a 100 μm sample with multiple cavitation events, the fracture of 2 critical cavities merge below a non-critical cavity that finally shrinks. The position of the cavities in the thickness is an interesting parameter, as the shear varies in the thickness. Therefore, the investigation position in thickness of the nucleation events could help shed some light on the shear influence on this process.

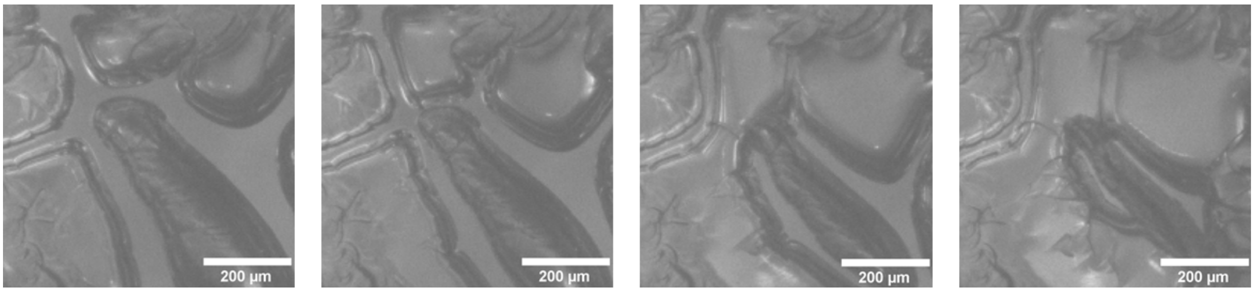

FIGURE 5.19: Two fractures (top and bottom left) merging below an existing cavity (bottom right).

5.1.4 Conclusion on the thickness effect on the cavitation behaviour

5.1.4.1 Summary of the experimental observations

First of all, all samples, regardless of the thickness, show cavitation events that **snap open**. This shows that the sudden growth of cavities is governed by an instability that allows, depending on the load, to suddenly propagate a fracture from a small nucleus to a penny shaped crack in a random plane. This crack looks like an inflated pancake as the sample is loaded. The size of the snapped cavity depends on the polymer thickness, as presented on Figure 5.20.

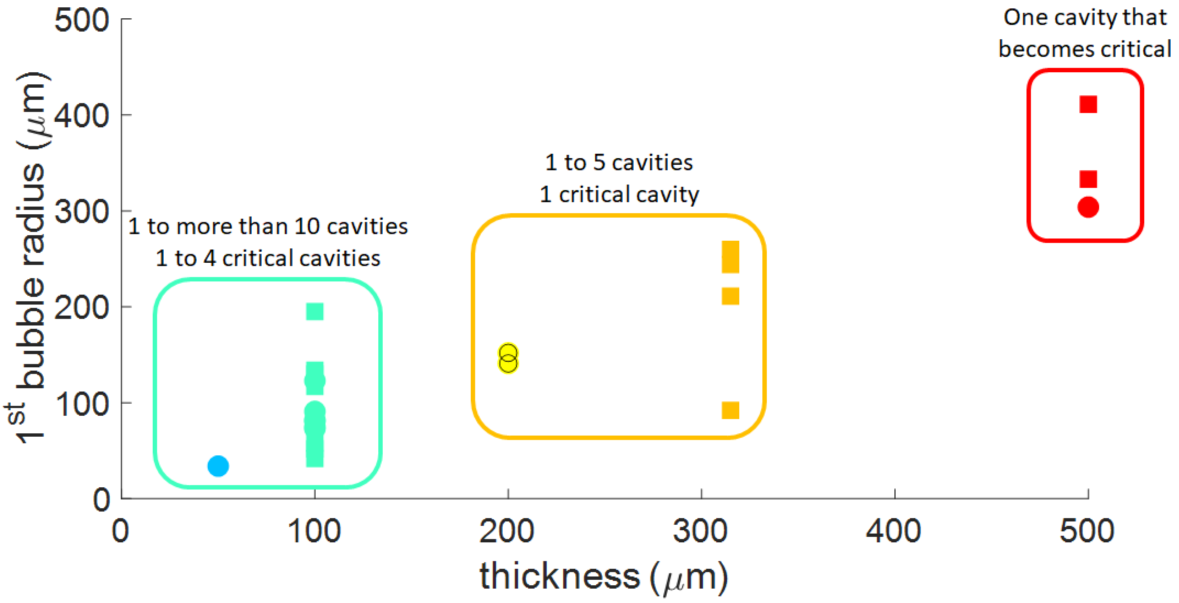

FIGURE 5.20: Thickness effect on the 1^{st} cavity's radius in the projected view through the glass slide.

Then, the following behaviour of these cavities also strongly depends on the thickness. In a reproducible manner, we observed that thick to intermediate samples show only a **few cavitation events** and **only one cavity transitions into critical fracture**. Thin samples however show a **multitude of cavitation events**, and **several of them transition into critical fracture**. Figure 5.21 shows the area evolution of the critical cavities that opened with a snapping effect. The log/log plot allows to see the different behaviours in an easier manner, the different configurations of the cavity are noted on the 100 μm sample.

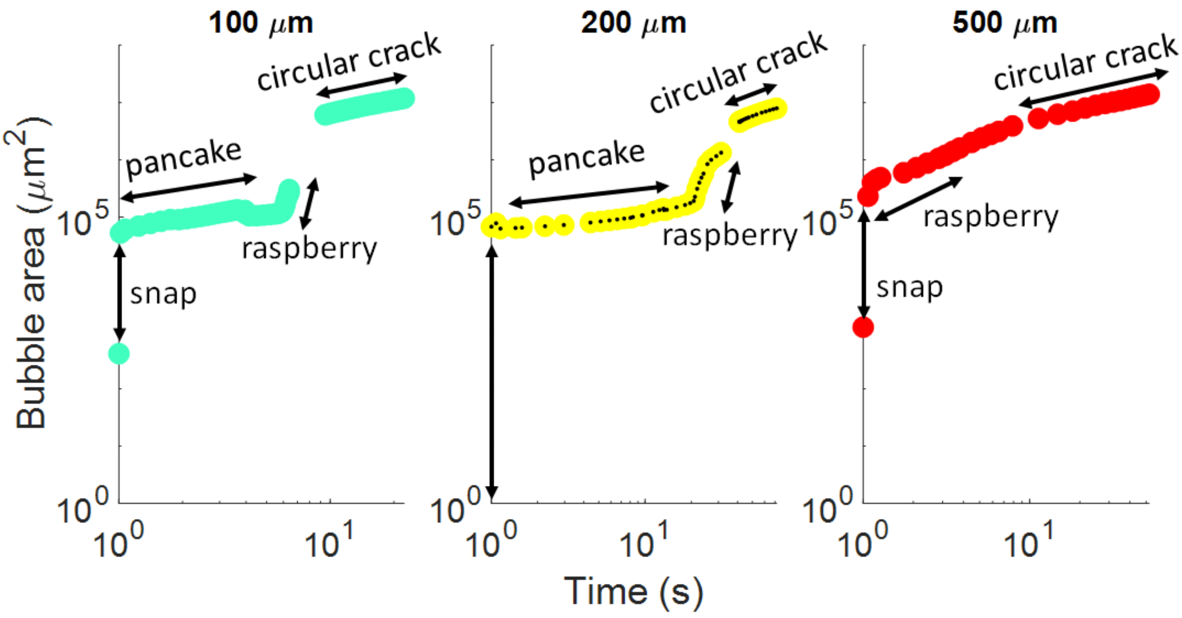

(A) Testing velocity: 5 μm/s

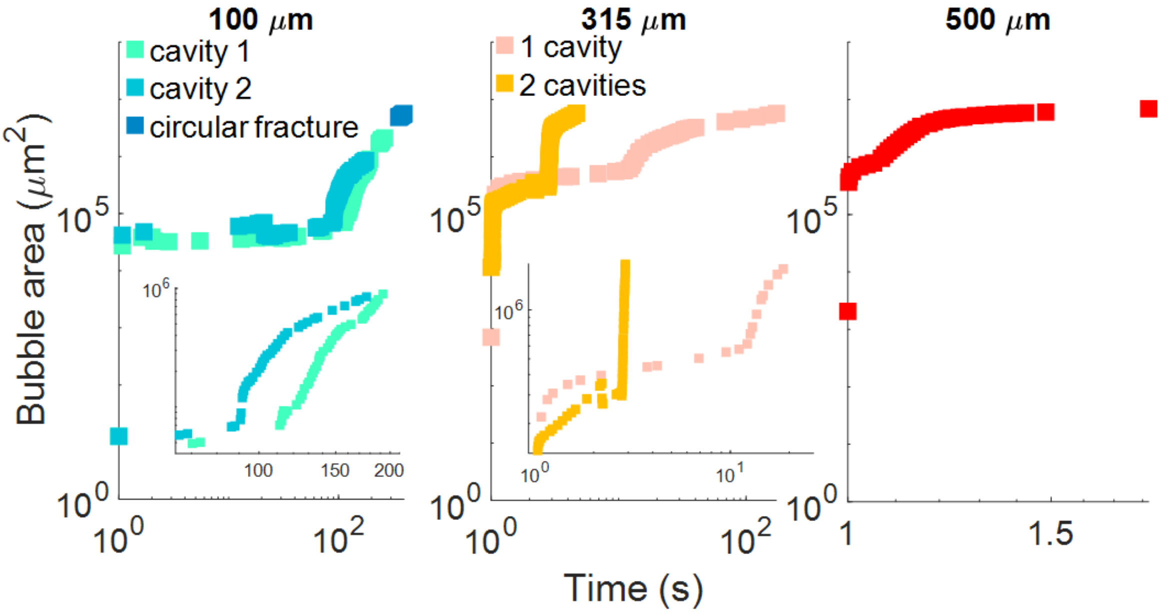

(B) Testing velocity: 0.5 μm/s

FIGURE 5.21: Thickness and testing velocity effect on the behaviour of critical cavities: Log-log plots of the area's evolution of one critical cavity with time. The moment of the snapping is put at t = 1s. (A) Testing velocity of 5 μm/s. (B) Testing velocity of 0.5 μm/s. Left insert: zoom on the transition to multiple fractures of the 2 critical cavities of OLHEA1515_100um_0.5ums. Middle insert: transition difference in OLHEA1515_315um_0.5ums_1 (pink squares - 1 cavitation event) and OLHEA1515_315um_0.5ums_2 (orange squares - 2 cavitation events). OLHEA1515_315um_0.5ums_1 transitions to the raspberry like fracture later than OLHEA1515_315um_0.5ums_2 but at a higher cavity area.

The cavities growth (after the snapping) in thin layers can be summarized, in the spirit of Morelle et al. description [13] as:

- Slow 2D isotropic growth of the inflated crack in a random plane: pancake shape.
- Destabilization of the cavity's wall: nucleation of several penny shaped extensions locally along the initial crack edge and anisotropic growth: raspberry shape.

- Merging of the different penny shaped partial cracks into one circular global fracture front.

The thick layers do not show the slow isotropic growth and directly nucleate several penny shapes that transition into global fracture. Table 5.5 summarises the area at which the critical cavities transition from the apparent stable crack growth to the destabilisation by nucleation of several penny shaped cracks and the final velocity (in $\mu m^2/s$) of the global circular crack. Only the cavities that appeared through a snapping event and transitioned into critical fracture where considered, as we suspect the defects growing into a fracture in a more linear way to not follow the same fracture mechanisms.

Thickness (μm)	Cavity area @ transition (μm^2)		Final crack velocity ($\mu m^2/s$)	
100	$1,3.10^5$	7.10^4	$1,30.10^5$	$2.76.10^4$
200	2.10^5	X	$1,35.10^5$	X
315	X	$3 - 6.10^5$	X	$2,38.10^4$
500	$4,85.10^5$	$7,5.10^5$	$2,48.10^5$	$8,15.10^4$

TABLE 5.5: Summary of the thickness effect on the cavity area at destabilization from pancake towards raspberry fracture growth and final velocity for experiments done at 5 $\mu m/s$ (black) and 0.5 $\mu m/s$ (blue).

The fact that thick layers produce big first cavities that transition into critical fracture while it takes several cavities to transit to fracture in thin samples could suggest a threshold size below which the critical fracture can not propagate. However, based on the experiments we studied, there is no clear observation of the existence of such a threshold. In the case of multiple cavitation events, it is not clear if only the area of the critical cavity is to be considered, or if the total area of cavities play a role. Furthermore, the critical cavities in the thin layers are usually further away from the center, where there is more elastic energy stored, as the confined polymer next to the apex is full of pseudo-stable cavities. Considering the thick layers, we can not conclude that they describe the threshold area either, as the critical cavities directly transition to the unstable growth. Therefore, we could only conclude that if a threshold value exists for the transition between the self-similar cavity (pancake shape) to the unstable growth via multiple penny shaped cracks (raspberry shape), it is below 5.10^5 μm^2, the smallest size observed for the thick samples.

Finally, the study of the final circular crack velocity shows little surprises. In this case, the crack propagation is almost purely a mode I, where the big hole in the middle of the sample propagates toward the sides. The faster the testing velocity, the faster the crack propagation. Also, the 500 μm shows the fastest propagation as there is more volume of polymer on the sides, therefore more elastic energy stored.

5.1.4.2 Proposed interpretation of the thickness effect

One important thing to keep in mind is that, when changing the thickness of the samples, we changed two parameters: the stored elastic energy and the value of the hydrostatic pressure field in the confined region. As was presented on Figure 4.26, for a given displacement of the half lens, the hydrostatic stress is the highest in the thinnest confined layer. However, since there is less polymer volume, the stored elastic energy is smaller than in a thicker layer.

Now, the snapping instability we observed corresponds to some extend to the work of Dollhofer et al [4]. Considering the size of the expanded cavity compared to the initial confined thickness, we can consider that the thick shell description applies, and the deadload hypothesis on the loading is not too far from our experimental loading. In this way, if we consider an initial penny-shaped crack in our sample, we can explain this snapping instability by the presence, at a certain load applied on the polymer, of a stable expanded configuration of the cavity compared to the closed penny shape. However, as the polymer network is crosslinked, the transition to the expanded configuration also requires fracture of polymer chains. This is not the exact same description as Dollhofer et al, who considered only fully reversible surface tension effects and a minimization of potential energy. We can therefore assume that the snapping instability we observe is an unstable fracture event from a small crack to a bigger inflated penny shape. In our case, the surface tension may have an effect on the nucleation of defects that grow to a size at which they can snap open, but this is far below the optical resolution.

Then, once the cavity has snapped, the thickness effect on its growth is more subtle. How can we explain that multiple cavities can snap open in a thin layer compared to a thick one? And how can we explain this apparent change of fracture behaviour from one penny-shaped crack growth to multiple nucleation of secondary cracks on the edge of the main crack leading to an anisotropic growth? One must look at the driving force for cavity growth and to the energy barriers hindering it.

First, in Dollhofer et al. theory [4], there is both a stress criterion and an energy criterion to overcome for the snapping of a cavity from the metastable closed configuration to the stable expanded one. This argument is used to explain why thin layers have a higher cavitation pressure than thick layers in probe tack experiments, as thick layer reach the energy requirement before the pressure one, and the inverse is true for thin layers [96]. In our experiments, we do observe that the cavities in thick layers appear at larger deformations (and longer times) than in 100 μm. While the experimental uncertainties do not allow us to precisely determine the displacement applied to the polymer layer, it does suggest that a higher loading is needed for the thick layers as they need to reach this pressure criteria. As soon as the cavity snaps open, the global elastic energy accumulated in the thick layer allows for the direct transition into multiple fractures. It would then mean that, in the case of thin layers, the pressure criterion may be reached but the cavity snaps open only when the energy criterion is also reached. The snap releases the stored elastic energy, resulting in a stable cavity as there is not enough elastic energy to transition into multiple penny shapes.

However, this explanation is not entirely satisfying, since other cavities subsequently snap open in thin layers! So it means that while there was not enough energy to propagate the crack from an already extended and large cavity, another small defect in the vicinity had sufficient energy to snap open? The mechanism appears to be more subtle. If we consider the simulation work on the Gent and Lindley poker-chip experiment carried out by Lopez-Pamies and coworkers ([94], [101]), it appears clearly that the cavitation is governed by the degree of triaxiality of the applied stress field. Their model requires also to define a stress criterion for the onset of cavitation in order to reproduce the multiple cavity opening that was observed in the thin samples in Gent and Lindley's experiments [1]. So, if we consider only a stress criterion for the nucleation, we could accept the idea that while there is not enough energy stored in the sample to propagate penny shaped cracks, the stress can still increase enough at another point of the sample to snap open another cavity.

Moreover, the successive cavities open in close vicinity of each other, and the opening of one cavity releases the energy over a volume around it. Gent and Tompkins had already suggested, based on cavitation experiments on pre-stretched samples, that the stress required to open a cavity was decreasing in a pre-stretched network, compared to the initially unloaded one [6]. Around an expanded cavity, the polymer is highly stretched. If this does lower the stress criterion for cavitation, it could then also explain the additional cavitation events. Furthermore, the distance we observe is only in the projected view. With the help of the mecanophores experiment, we can argue that the cavities do not open exactly in the same plane, and also do not have the same orientation compared to the glass slide. Therefore, it is possible that the stress relaxed from the opening of one cavity in one orientation does not impact too greatly another crack oriented in a different direction.

To conclude, the multiple cavitation event and its thickness dependence is really interesting, and the transition in fracture mode from one stable crack growth to the multiple penny-shaped cracks is a non trivial problem to tackle. We have some elements of explanation, but none of them seems to fully describe in a satisfying way the mechanism. Some simulations on the pressure field around the expanded cavity and its influence on other cracks would be interesting to shed some light on the interaction between cracks in thin layers.

Finally, the post-mortem observations of the fracture surfaces, even if they are pretty, do not exactly help to understand the transition of fracture process. Indeed, we can see on Figure 5.22 the different surfaces depending on the thickness. For each samples, the sites where the cavities snapped is visible as a region of high roughness. Lindsey observed the same floral pattern with a rough nucleus in triaxial loading of polyurethane elastomers [109]. He attributed the roughness of the nucleus to a very slow growing crack, while the mirror-like surfaces were assimilated to fast crack propagation zones. However, in our case, the zone of high roughness corresponds to the position of the expanded cavity, and the snap appears at high velocities. Therefore, we can not attribute this roughness to a slow propagation, and we can only conclude that the snap does produce a lot of damage in the network.

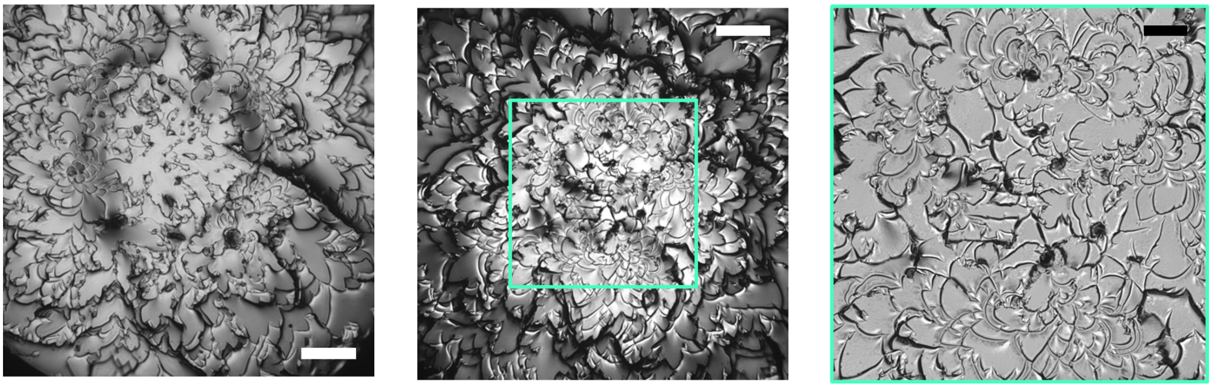

(A) 100 μm - 5 μm/s (B) 100 μm - 0.5 μm/s

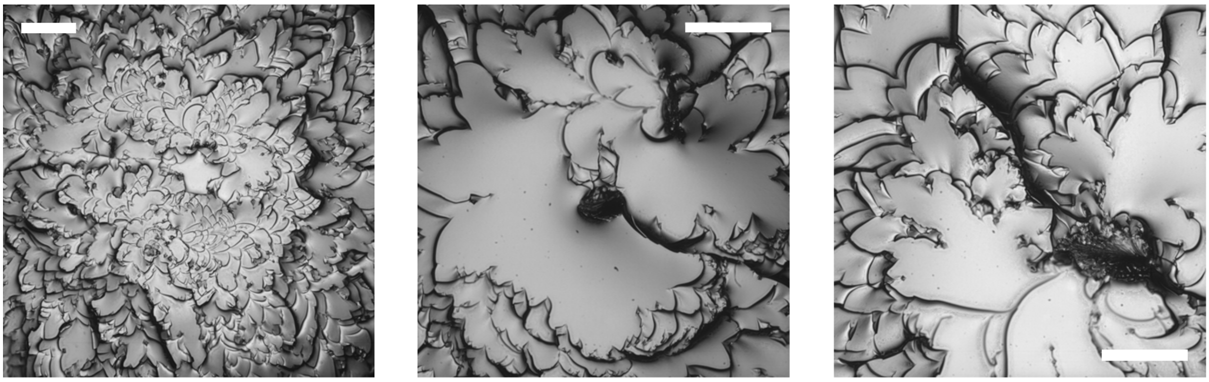

(C) 200 μm - 5 μm/s (D) 315 μm - 0.5 μm/s

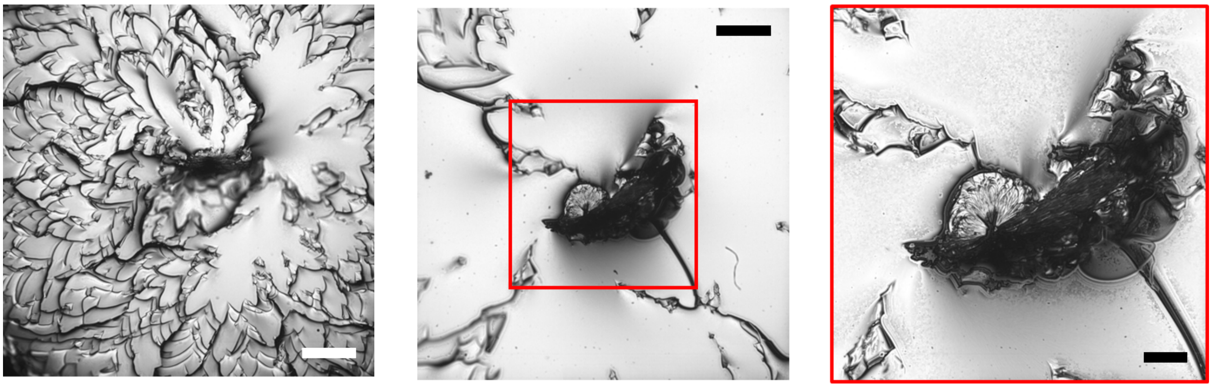

(E) 500 μm - 5 μm/s (F) 500 μm - 0.5 μm/s

FIGURE 5.22: Focus on the fracture surface depending on the thickness. (A) Scale bar: 500 μm (B) Left: Scale bar: 500 μm. Right: Zoom on the apex zone, Scale bar: 200 μm (C) Scale bar: 500 μm (D) Left: sample with 2 cavitation events, Right: sample with only one cavity. Scale bar: 500 μm. (E) Scale bar: 500 μm (F) Left: Scale bar: 500 μm, Right: Zoom on the critical cavity nucleation site. Scale bar: 200 μm

5.2 Network's formulation effect

Now that the thickness effect has been investigated, let's address how different material properties influence the cavitation, on samples of 100 μm thickness. In chapter 3, we described how changing the ratios between the two monomers and changing the oligomer's functionalization from acrylate to methacrylate could influence the Young's modulus, the fracture energy and its dependence on the testing velocity, and the strain hardening. As discussed in the state of the art on cavitation (section 4.1), all these properties should influence the cavitation resistance, either on the nucleation or the growth of the cavities.

All formulations were tested in the same conditions: samples of 100 μm thickness and a testing velocity of 5 μm/s. As we described in section 5.1, the thinner layers lead to more dispersion of the measured hydrostatic pressure for the first cavitation event, as the opening of cavities seems to be a stochastic event based on the defect distribution. Due to time restrictions, we could only test a small number of samples for each formulation. In this section, we will analyse the results we obtained on different network compositions. However it is important to keep in mind that we can only propose hypotheses since the number of tested samples is too small to ensure a statistical difference between the behaviours.

5.2.1 Increasing the strain hardening by introducing bimodality

In all the formulations we already presented, the strain hardening was not visible in uniaxial traction and could only be analysed with the biaxial inflation. In the hope of producing samples with an even more pronounced strain hardening, and therefore possibly a more visible influence on the cavitation behaviour, two new formulations were produced with the introduction of a smaller di-acrylate: IPDI(HEA)$_2$. This small molecule (M = 440 g/mol) acts as a crosslinker like the PPG8000 oligomer. The two formulations consist of:

- 1%bi: 69%w OL HEA, 1%w IPDI(HEA)$_2$, 15%w EHA, 15%w PEA, 1%w BAPO
- 5%bi: 65%w OL HEA, 5%w IPDI(HEA)$_2$, 15%w EHA, 15%w PEA, 1%w BAPO

so that the monomer ratio and the total diacrylate ratio stay the same as the usual OL HEA 15% EHA 15% PEA formulation. The effect of this increase in bimodality on the strain hardening can be seen on the normalized Mooney plot on Figure 5.23. These new network compositions were only tested in uniaxial traction. The determination of the finite extensibility (and their J_m) can therefore not be assessed as precisely as for the other formulations which were tested in bulge inflation.

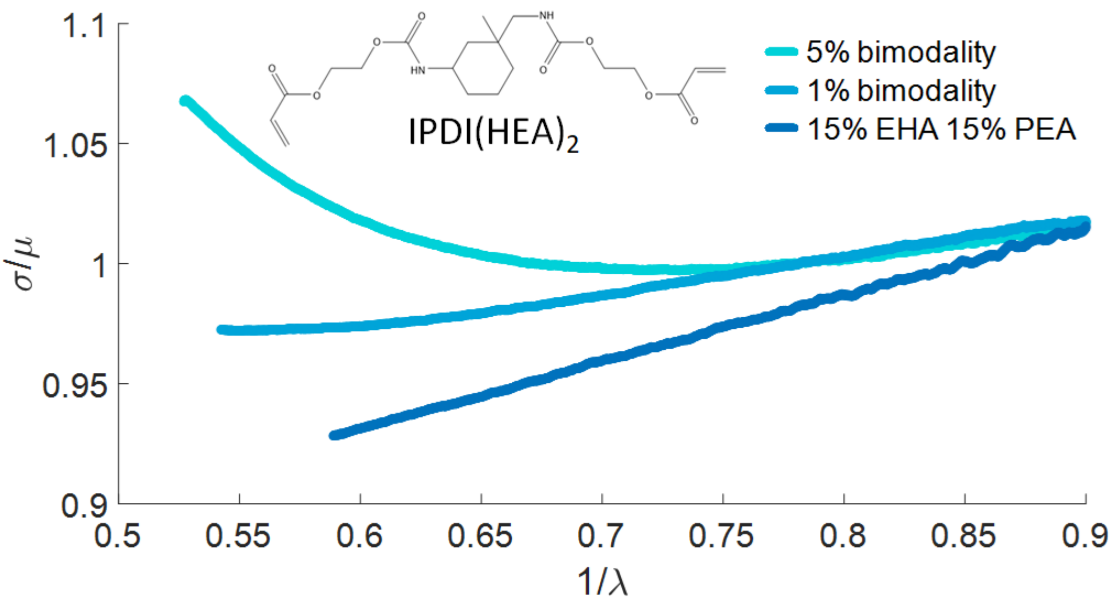

FIGURE 5.23: Increased strain hardening with an increased bimodality of the network. Mooney plot of the uniaxial data of the three formulations. Insert: molecule drawing of IPDI(HEA)$_2$.

Of course, changing the formulation and producing this network with an increasing amount of short chains did impact the elasticity and the fracture properties. They are summarized and compared to the mix with no bimodality in Table 5.6.

% bimodality	E (MPa)	Γ_c (J/m^2)			
		3.33%/s	0.67%/s	0.067%/s	0.0067%/s
0%	1.156 ± 0.025	145.32 ± 27.52	98.03 ± 11.74	58.17± 2.98	40.07 ± 5.74
1%	1.210 ± 0.16	220.48 ± 57.54	139.28 ± 27.68	65.91 ± 14.94	49.96
5%	1.488 ± 0.119	432.70 ± 171.80	175.99 ± 43.49	90.36 ± 28.39	55.92

TABLE 5.6: Influence of an increase of bimodality on E and Γ_c - Formulation OL HEA 15% EHA 15% PEA

5.2.2 Material properties effect on σ_{loc}

Let's discuss the effect of material properties on the hydrostatic pressure for the first cavitation event σ_{loc}: the Young's modulus and the fracture energy. As presented in Section 3.3, the fracture energy measured with single edge notched samples depends strongly on the stretch rate. The cavitation snapping events occur at very high uncontrolled and heterogeneous strain rates, typically faster than the stretch rates tested experimentally in uniaxial tension. Therefore, we decided to represent the evolution of the cavitation pressure as a function of the fracture energy measured in uniaxial tension at the highest stretch rate that we tested: 3.33%/s (= 0.5 mm/s). Nevertheless, we cannot be sure that it is the best descriptor for the local fracture energy in the confined sample at high stretch rates. Another point of view would be to consider the fracture energy at the slowest stretch rate possible, since it would be the closest to G$_0$, the threshold value of the fracture energy in the sense of the Lake and Thomas description [80]. The dependence of σ_{loc} to G$_c$ at the slowest stretch rate (0.0067 %/s) can be seen in Appendix D.4.

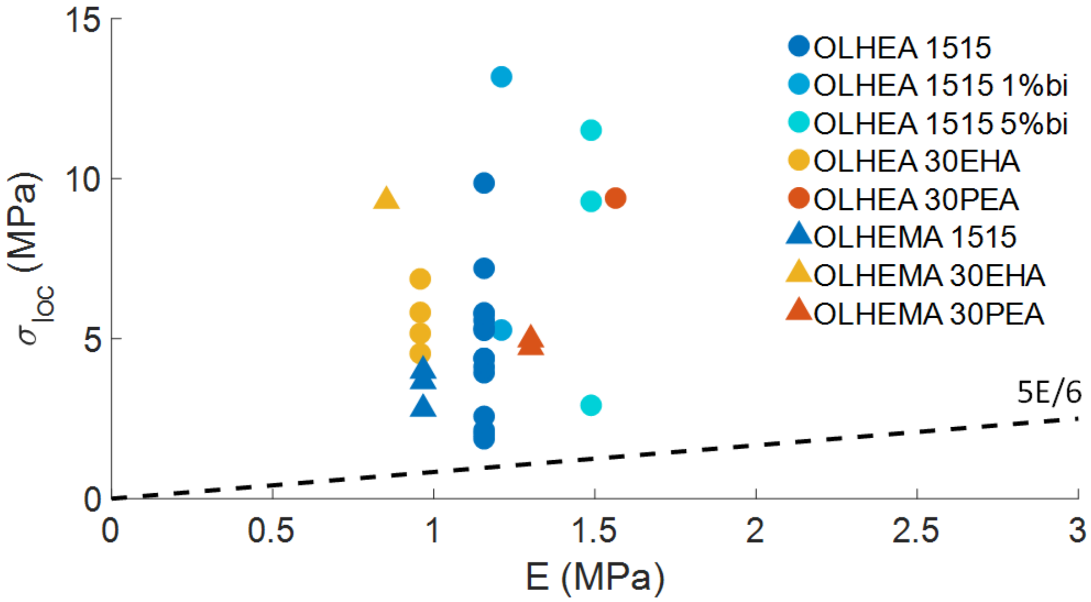

(A) Variation of the hydrostatic pressure with E

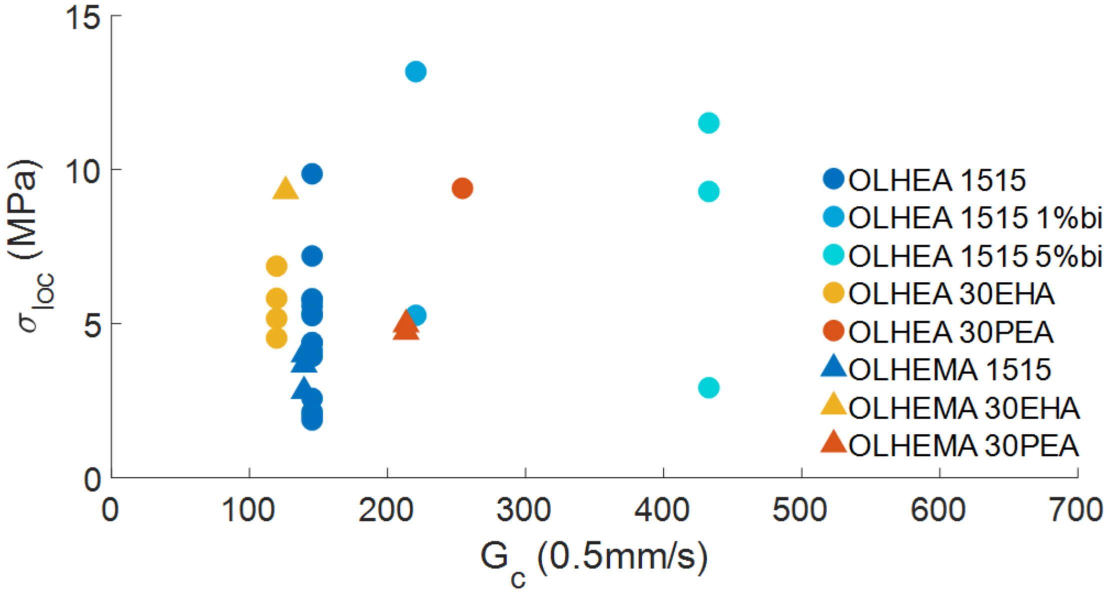

(B) Variation of the hydrostatic pressure with G_c at 3.33%/s initial stretch rate

FIGURE 5.24: Variation of the cavitation pressure with the material properties: Young's modulus (A) and fracture energy (J/m^2) (B). The initial stretch rate in the single notched samples leading to the computation of G_c is 3.33%/s, the initial stretch rate for the hydrostatic traction experiments at 5 μm/s is 5%/s for a 100 μm sample.

As can be seen on Figure 5.24 (A) and (B), the same dispersion of σ_{loc} can be seen for all formulations. However, we always detect cavitation events at pressures higher than the 5E/6 threshold, and some can occur at more than 10E!

Our hypothesis is that the dispersion of the measured hydrostatic pressure for cavitation is inherent to the small size of the samples and is linked to the defect population in the sample. When considering a small sized sample, the probability of the presence of a big defect is lower. The hydrostatic pressure to open a small defect is higher, leading to a higher cavitation resistance of the sample. However, this is a stochastic measurement, as even if the probability of having a big defect is small, it is not 0. Therefore, testing several small volume samples leads to a dispersion of the cavitation resistance, since the result depends on if a big (low σ_{loc}) or a small (high σ_{loc}) defect is present in the sample. This result has been widely observed in the testing of ductile materials in nanoindentation [110] and would be a good explanation of the apparent dispersion we see of the hydrostatic pressure with thickness (see Figure 5.1).

This suggests that the best way to describe the material properties under cavitation in thin layers would be to consider the highest pressure that was measured, as it would be representative of testing the samples containing the smallest defect. If we extrapolate, by testing a very large number of samples, we could observe a maximum value of the hydrostatic pressure, that would be representative of the opening of the nucleation of a cavity around the smallest defect present. Figure 5.25 displays the highest cavitation pressure measured for all our formulations in a 2D plot, depending on both E and G_c at the highest and slowest stretch rates.

Figure 5.25 suggests that the highest cavitation resistance possible is achieved with formulations that have both a high Young's modulus and a high fracture energy. However, more tests would be needed on the different formulations to make this conclusion more robust. Furthermore, it would be interesting to separate the effect of the Young's modulus and of the fracture energy (i.e two formulations with the same E but with statistically different G_c) to test which parameter, between the elasticity and the fracture energy, would show the greatest effect on the cavitation resistance.

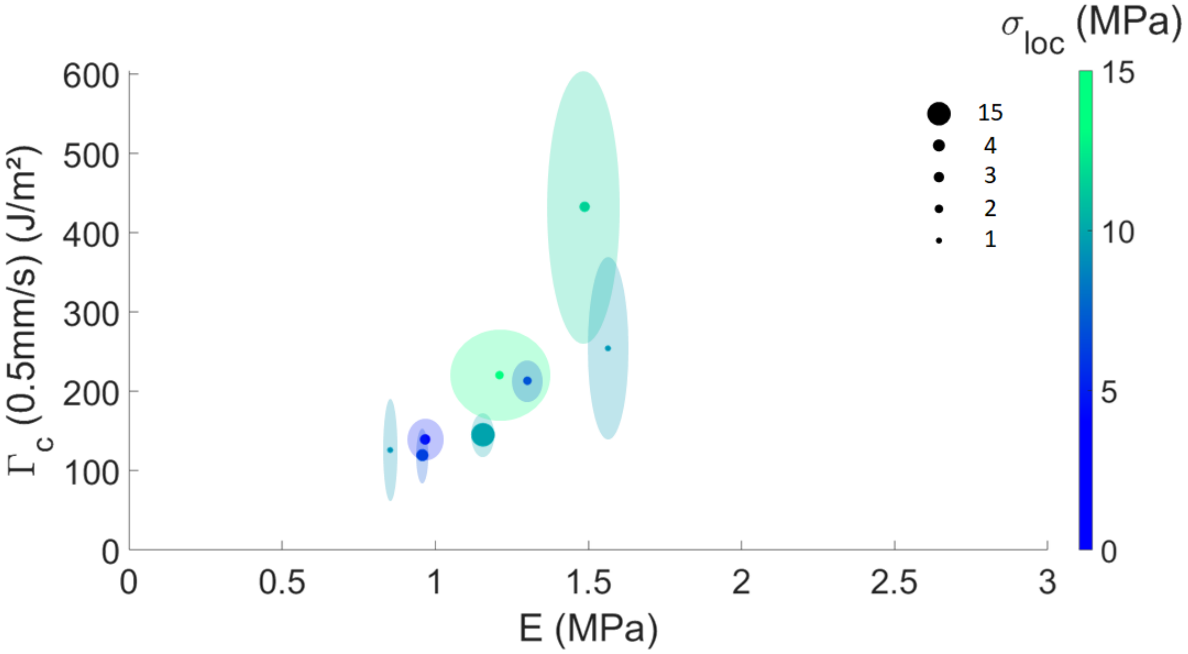

(A) G_c measured at the highest stretch rate

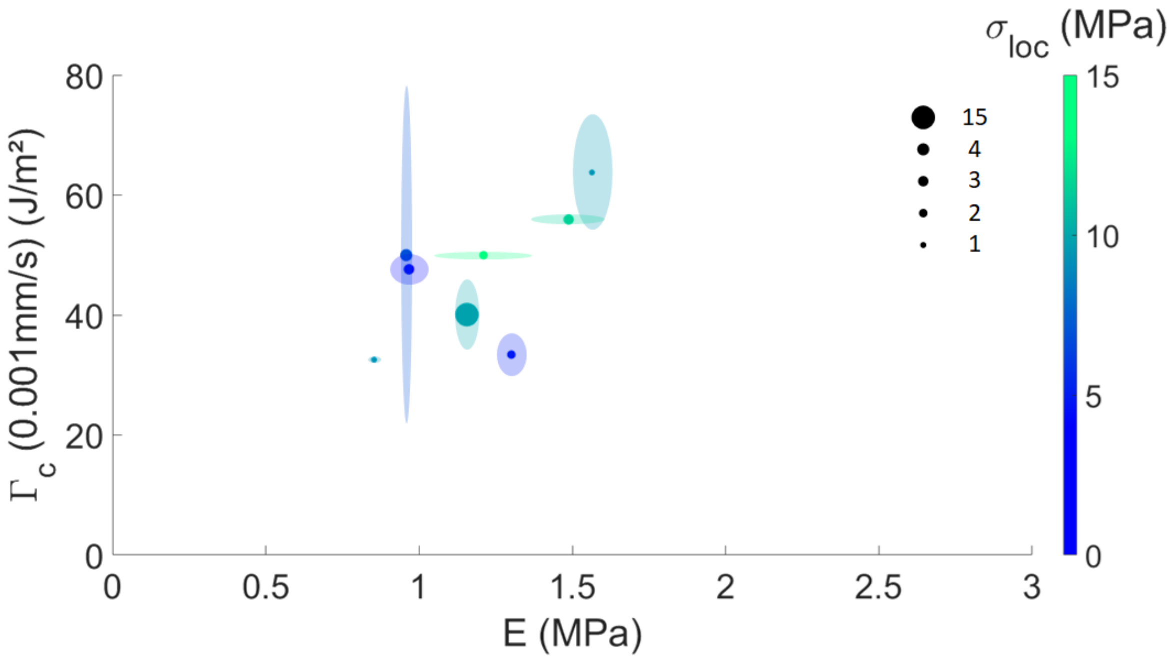

(B) G_c measured at the slowest stretch rate

FIGURE 5.25: Effect of the material's properties on the highest achievable cavitation pressure - 2D plot with E and G_c at the highest (A) and the slowest (B) stretch rate. The point size depends on the number of experiments made on each formulation, as described by the legend of black points. The color of each point describes its highest cavitation pressure, as described by the color bar. The ellipses of faded color show the experimental dispersion on the measurement of the fracture energy and the modulus.

Finally, it is striking to see that, even if they were tested only on a small number of samples, the formulations with a bimodal distribution of chain lengths (1%bi and 5%bi) show the highest cavitation pressures. Now, this could only be chance (those samples could happen to also present the smallest defects). But, it could also be an indication that that the strain hardening plays a significant role in the cavitation behaviour.

5.2.3 Material properties effect on the cavitation behaviour

Following the analysis made in the last section, let's consider now the morphology of the cavities depending on the formulation. First, Table 5.7 gives a summary of the cavitation experiments in terms of number of cavitation events and number of cavities that transition from the pancake shape (one crack) to the raspberry shape (nucleation of multiple penny shaped cracks).

The number of cavitation events does not seem to be a good descriptor of the formulation effect, as, in the same formulation, this number can change a lot from one sample to the next. However, the ratio of opened cavities to cavities that transition to critical fracture seems much more interesting. When having a closer look at the formulations showing the highest level of strain hardening, a large number of the cavities (if not all, in the case of 5%bi) transition to the multiple penny shaped crack fracture. This is not the case for the formulations with the lowest strain hardening, such as OL HEA 30% EHA. Let's investigate the cavitation behaviour and morphology during loading and the effect of strain hardening.

Formulation	J_m	# cavitation events	# critical cavities
OL HEMA 30% EHA	76.00	6	3
OL HEA 30% EHA	69.30	2 to >10	2 to 4
OL HEMA 15% 15%	*38.01*	3 to >10	2 to 3
OL HEA 15% 15%	54.88	1 to >10	1 to 5
OL HEMA 30% PEA	46.26	>10	7
OL HEA 30% PEA	34.12	>10	X
OL HEA 1%bi	X	5 to 9	5 to 9
OL HEA 5%bi	*20.24*	3 - 7	3 - 7

TABLE 5.7: Influence of the formulation on the number of cavitation events and their transition to multiple fractures. The formulations are ranked in order of increasing strain hardening (hence decreasing J_m) from top to bottom, J_m comes from the Gent fitting of the biaxial data (except for the bimodal formulations). Note on the values in italic: OL HEA 30% PEA: all samples failed by delamination of the polymer from the sphere after a few cavitation events, so no cavity transitioned per se to multiple fractures. OL HEMA 15% EHA 15% PEA: its value of J_m is unexpectedly low, see Section 3.2.3. Bimodal formulations: as they were tested only in uniaxial traction, their value of J_m may be imprecise. This is especially true for the 1% formulation, in which the Gent fitting on the uniaxial data does not show any presence of strain hardening.

5.2.3.1 High level of strain hardening - Bimodal formulations

Let's first analyse two samples made from the bimodal formulations. As presented on Figure 5.26, several cavities snap open in the OLHEA1515_1pcbi_100um_5ums sample. Each non-critical cavity (Figure 5.26 (A)) shows a rapid growth, which then gets disturbed by the fracture of the critical cavities. Figure 5.26 (C) suggests that even the non-critical cavities show a beginning of nucleation of penny-shaped cracks on their walls, as their shape in projection starts to shift. This is all the more true for cavity 4 (in black) and 6 (in dark red) that starts to fracture but finally shrinks due to the faster propagation of the crack front of critical cavities 2 and 3. The critical cavities show the evolution that was already described in the last section.

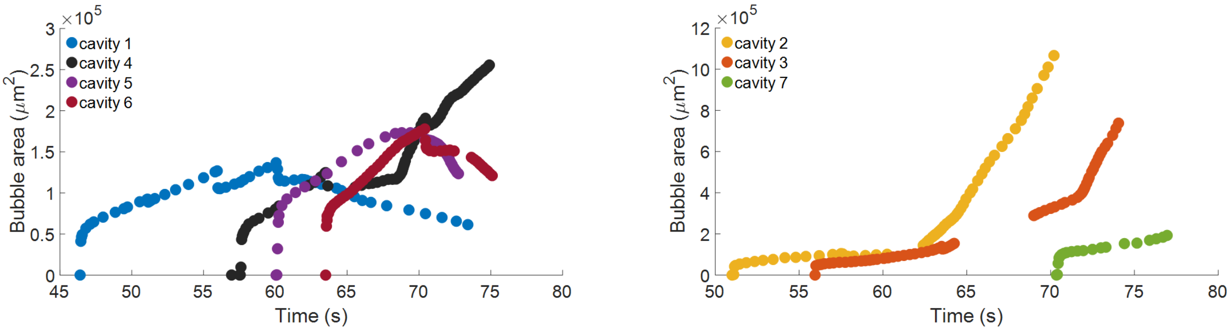

(A) Non critical cavities (B) Critical cavities

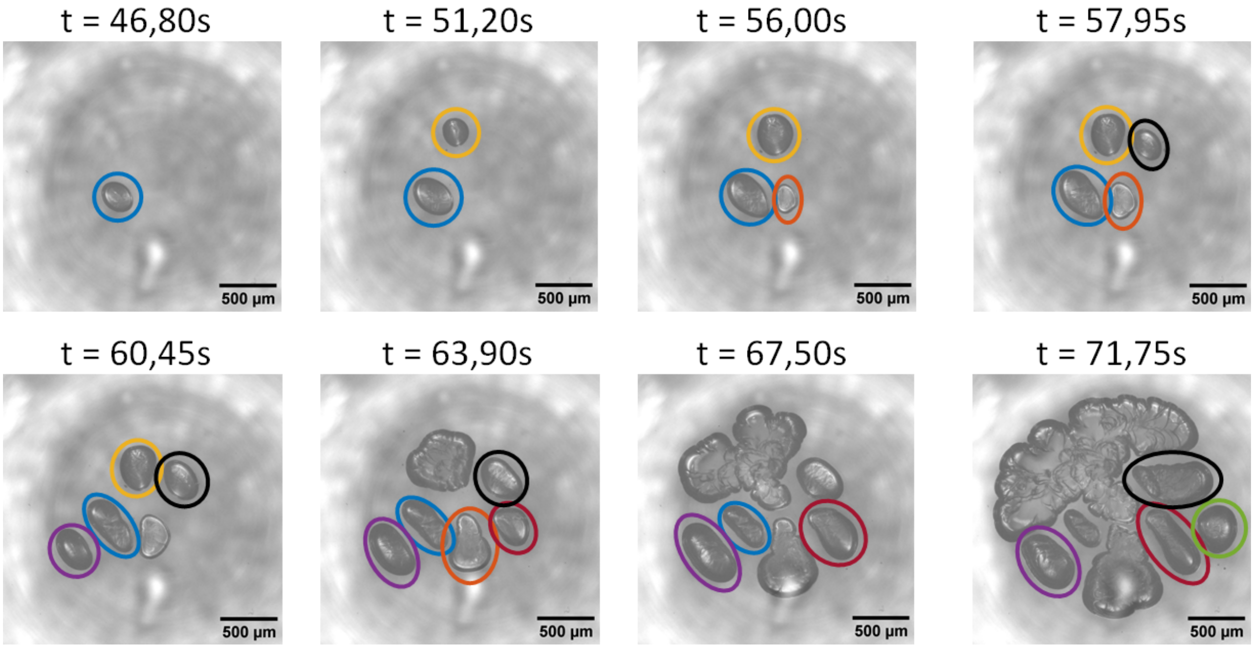

(C) Cavities evolution

FIGURE 5.26: Cavitation evolution in OLHEA1515_1pcbi_100um_5ums. (A) Evolution of the projected area with time. All cavities seem to transition to fracture, this is especially visible for cavity 4 (black). (B) Evolution of the critical cavities. (C) Corresponding cavitation events

Then, increasing the level of bimodality (and hence the strain hardening) leads to samples where all cavitation events become clearly critical fractures, as described on Figure 5.27 in sample OLHEA1515_5pcbi_100um_5ums. Besides the striking difference in the number of critical cavities, it also seems that the fracture propagates in a small number of lobes that erupts from the cavities' walls. As can be seen on Figure 5.27 (B), between the images at (t = 70.40s) and (t = 74.20s), a new penny shaped crack erupts from the side of the already growing cavity, perpendicularly to its initial spreading direction.

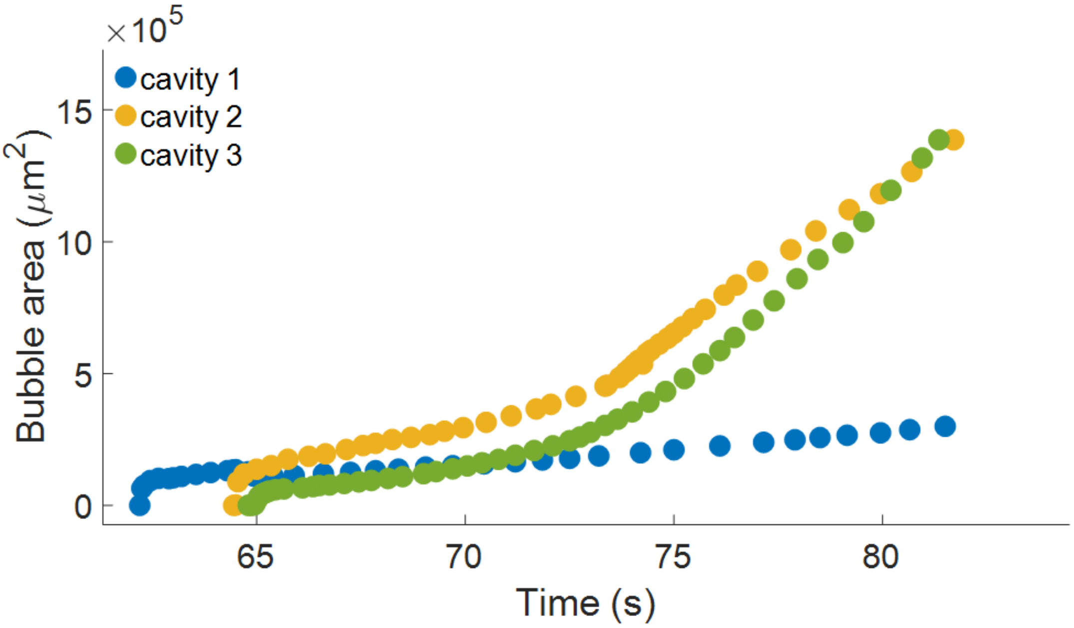

(A) Critical cavities

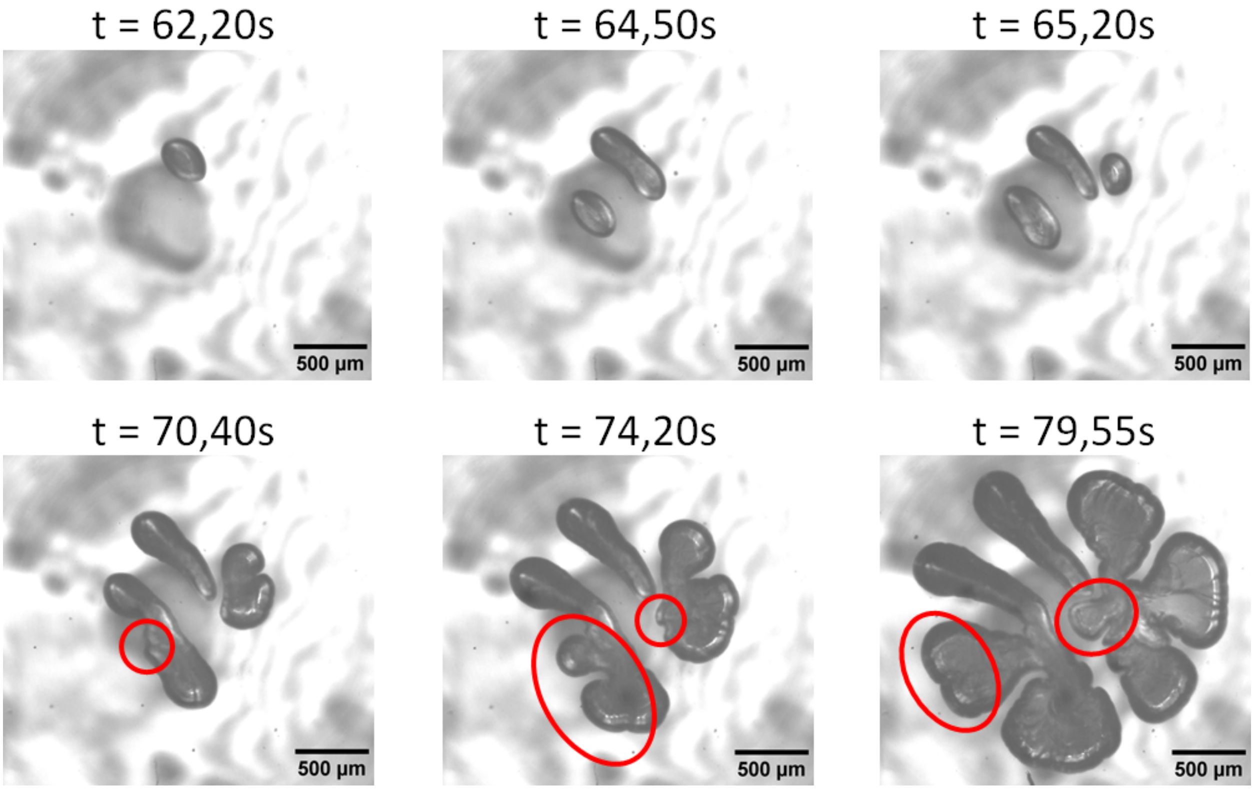

(B) Cavities evolution

FIGURE 5.27: Cavitation evolution in OLHEA1515_5pcbi_100um_5ums. (A) Evolution of the only three cavitation events which all transit into the global fracture. (B) Corresponding images, the fracture propagates quickly from the initial cavities, and it seem in a smaller number of directions. Red circles: eruption of a new penny shape, forming a new lobe in the cavitation growth. The lobe can also split in two (t = 79.55s).

This fracture behaviour is much more sudden than what was observed in the OLHEA1515_100um_5ums sample. It seems that the network with significant strain hardening shows a destabilisation of the crack front into a new defined lobe, while the OLHEA1515_100um_5ums sample transitioned in a multi penny shaped crack fracture in a smooth shape transition. This type of instability could be due to a sudden release of the stored elastic energy by a change in morphology, an unstable behaviour that has been observed by Biggins et al. on stressed on elastic meniscus beween two rigid surfaces [111]. While the mechanisms at stakes are not exactly the same (they don't observe a fracture mechanism), the destabilisation of a straight front into a wavy front can relax elastic energy which can be used for fracture propagation.

5.2.3.2 Weak strain hardening - OL HEA 30% EHA

Then, testing a formulation that has a weaker strain hardening than the OL HEA 15% EHA 15% PEA and bimodal formulations leads to the observations displayed on Figure 5.28. The OL HEA 30% EHA samples showed also a multitude of cavitation events, most of them not leading to critical fracture. However, as displayed on Figure 5.28 (B), the transition between the different modes of propagation is not as clear as what was observed in the "reference samples" of the thickness study. The transition to fracture by multiple penny shaped cracks seems to be smoother. This could be due to the fact that the fracture energy of the OL HEA 30% EHA formulation is also the lowest, leading to a less costly fracture propagation in the network.

Again, we observe that new cavitation events happen in the network even if a huge part of the network is starting to be broken down by the fracture of the critical cavities. A perfect example is the non critical cavity 2 that snaps open in one half of the sample while critical cavity 1 is tearing the other half (Figure 5.28 (C) image (t = 89.45s)). This also suggests that the pressure field inside the network after several cavitation events and after a transition to multiple fracture is not trivial.

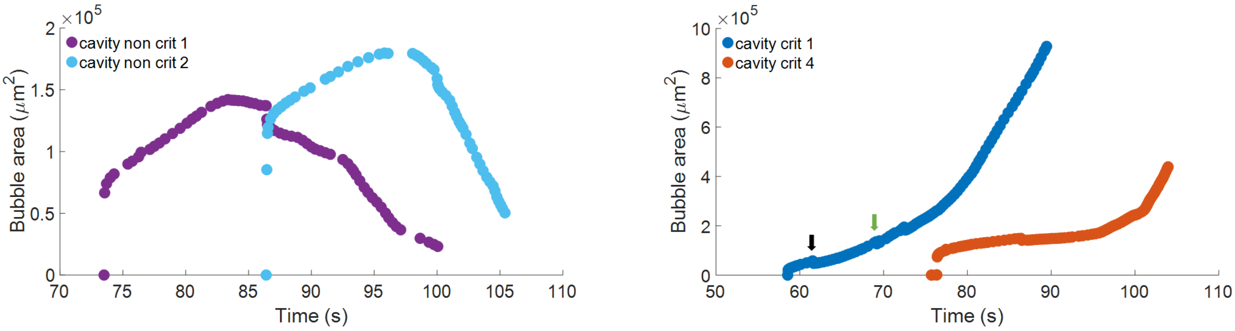

(A) Non critical cavities (B) Critical cavities

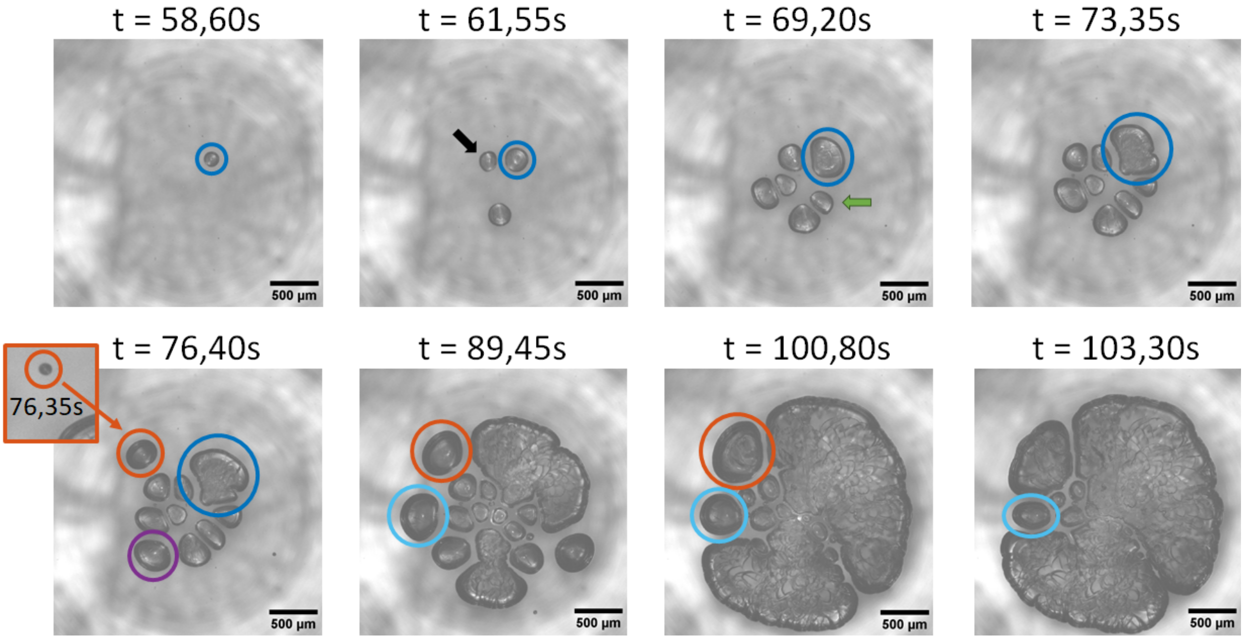

(C) Cavities evolution

FIGURE 5.28: Evolution of the cavities in OLHEA30EHA_100um_5ums. (A) Evolution of two non critical cavities. (B) Snapping and transition to global fracture of two of the critical cavities. The coloured arrows correspond to cavitation events that influence the growth of critical cavity 1. (C) Corresponding cavitation images. The cavities that influence critical cavity 1 are marked by the arrows.

5.2.3.3 Conclusion on the formulation effect

We can not conclude on a definite effect of the Young's modulus and fracture energy on the value of the critical cavitation pressure, since the testing of thin layers leads to a dispersion of the cavitation resistance measurement, and we have too few samples to make a statistical analysis. However, the most interesting feature, in our eyes, is the impact of the material properties on the morphology of the cavities and their growth dynamics.

Figure 5.29 displays the comparison of one of the critical cavities for each type of network, in a Log-Lin plot. The snapping event is put at t = 0s, which allows for the comparison of the time it takes for one cavity to transition into the multiple penny shaped cracks fracture type. As described in their respective section, the networks with high strain hardening (especially 5%bi) transition the fastest to the multi penny shaped fracture, while the network with the lowest strain hardening (OL HEA 30% EHA) presents a smooth transition from the pancake shape to the raspberry morphology.

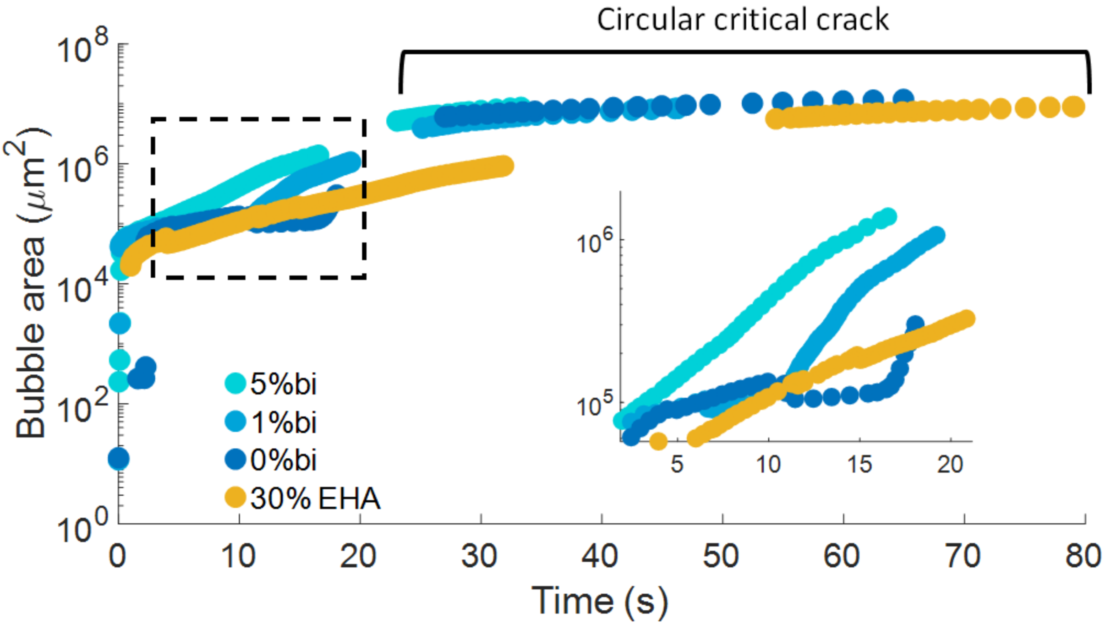

FIGURE 5.29: Strain hardening effect on the destabilisation of the cavities. Log-Lin plot of the evolution of one critical cavity with time. Insert: zoom on the destabilisation zone. The snapping event for each cavitation event is put at t = 0s.

Furthermore, the comparison of the cavities' shape with strain hardening (comparing Figure 5.27 (B) and 5.28 (C)) shows that a change in the material properties (elasticity, fracture energy and strain hardening) leads to a drastic change in the fracture pattern. The network with the most marked strain hardening leads to cavities that propagate in a small number of fracture lobes that propagate from the initial snapped cavity, while the network with less strain hardening seems to propagate a large number of penny shaped cracks on its surface. It would be interesting to find another criteria than the projected bubble area to describe this apparent difference in morphology. Studies of needle induced cavitation have proposed a study of the number of fracture lobes emerging from the initial cavity, which could be an interesting way to analyse our data ([14], [15]).

Adding this observation to the difference in the dynamics of the crack growth, and thinking back at the possibility of a threshold in cavity size between the stable pancake and the unstable raspberry, we can infer that this threshold size for stable growth changes with the degree of strain hardening and with the fracture energy. It would seem that, the higher G_c and the higher the strain hardening, the lower the number of penny shaped cracks that are nucleated in the raspberry morphology. In our study, a high strain hardening is characterized by $J_m \sim 20$ and a low strain hardening with $J_m \sim 70$ (see Table 5.7). This change of fracture behaviour can already be seen, to some extent, on the loading curves, as shown on Figure 5.30. Here, the displacement is shifted to only see the direct loading of the sample (without the accommodation steps). The complete curves and the force evolution with time can be seen in Appendix D.5.

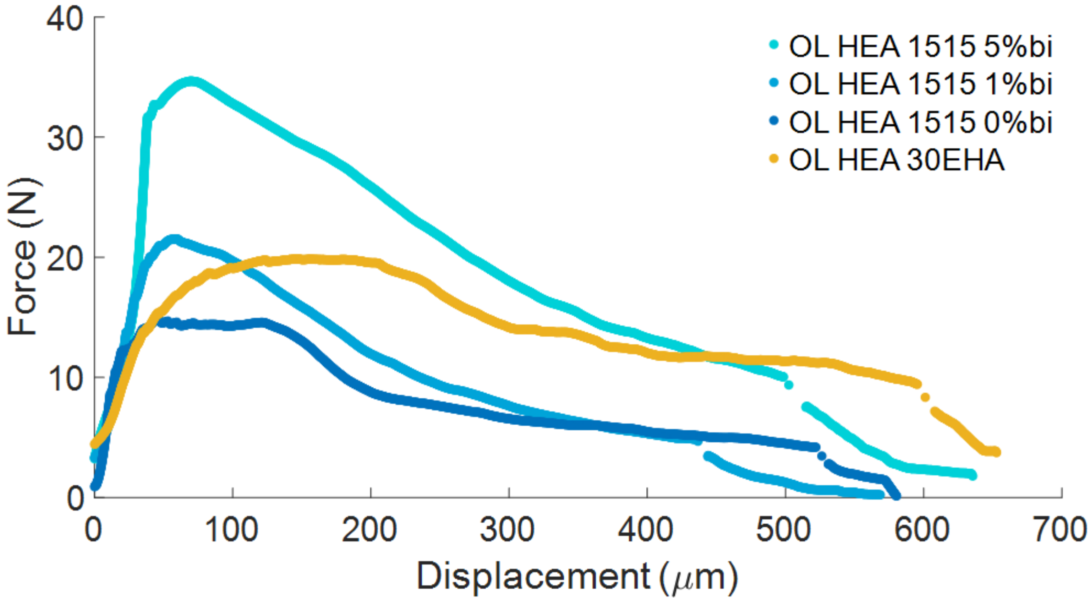

FIGURE 5.30: Loading curves and influence of the strain hardening. The network with the highest degree of strain hardening (as well as the highest E and G_c) shows a quick decrease of the force after the cavitation snapping, while the elastomer with the lowest degree strain hardening shows a much longer force plateau during which the cavities start to fracture the sample. During this force plateau, several force drops corresponding to the additional cavities opening can be observed.

As displayed on Figure 5.30, it seems that a higher strain hardening and a larger fracture energy leads to a quicker transition to the global fracture of a sample. So while a higher G_c and E also leads to a higher cavitation resistance (i.e a higher hydrostatic stress needed for the first cavitation event), it also seems that as soon as a cavity is opened and the sample is still under load, the transition to fracture is quicker. However, it is important to keep in mind that if the cavity opens at a higher stress, it also mean that the sample has more strain energy available at the moment of the nucleation, which could also explain the faster fracture propagation. It would be particularly interesting to see the effect of a constant non critical load of these samples with a high strain hardening, to see if and how the cavities would snap and propagate.

Now, in principle the differences in the cavitation process, especially the changes in the dynamics of crack propagation should leave traces the final fracture surface. Figure 5.31 presents the different fracture surfaces on the glass slide, depending on their Young's modulus and fracture energy.

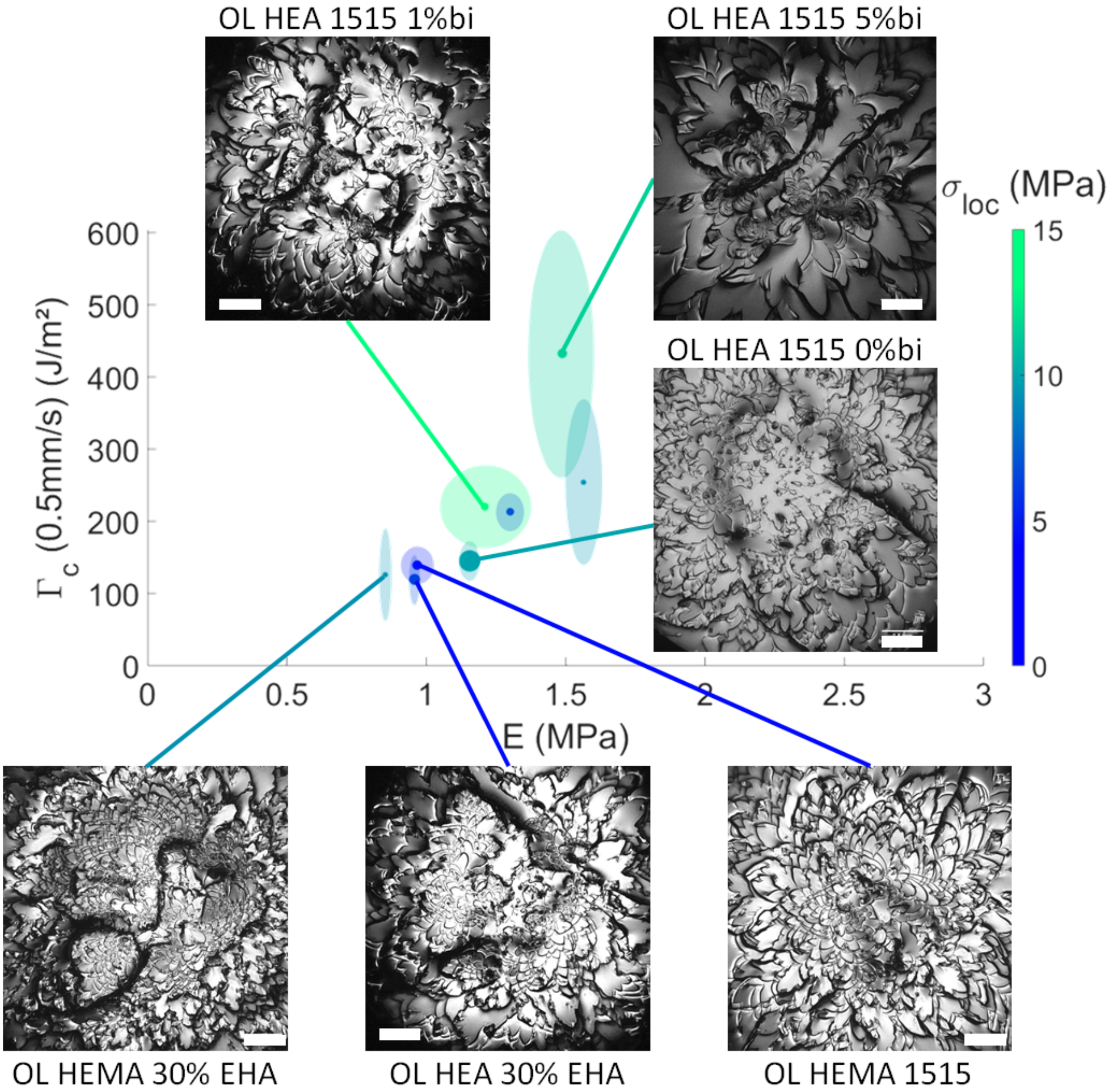

FIGURE 5.31: Fracture surfaces evolution with the material properties. The plot presents the evolution of the maximum hydrostatic pressure attainable for the first cavity as a function of the Young's modulus and the fracture energy at high initial stretch rate. Scale bar: 500 μm.

All formulations present a petal-like fracture pattern. This is representative of a fracture propagation with several crack arrests, which was observed in many fracture experiments on elastomers ([13], [109]). The petal shapes are actually step heights that come from the different penny shaped cracks that nucleate on the cavity's wall and join during their propagation [112]. The angle of the pattern can be linked to the elasticity, the fracture properties and the strain hardening of the network [107]. The roughness of the surface is supposed to also be a marker of the fracture speed. While we can not really conclude on the roughness of the nucleation zones (as discussed in Section 5.1.4.2), it is obvious that a lower fracture energy leads to a much larger roughness of the final circular crack. This seems to be coherent with the observed average velocities of the final circular crack, as presented in Table 5.8.

As all the samples have the same confined thickness and are tested at the same pulling speed (5 μm/s), the final crack velocities should be comparable. It would seem that an increase of strain

Formulation	Final crack velocity (μm^2/s)
OL HEMA 30% EHA	$1{,}13.10^5$
OL HEA 30% EHA	$1{,}15.10^5$
OL HEMA 15% EHA 15% PEA	$1{,}61.10^5$
OL HEA 15% EHA 15% PEA	$1{,}15.10^5$
OL HEA 1% bi	$1{,}57.10^5$
OL HEA 5% bi	$7{,}51.10^5$

TABLE 5.8: Formulation effect on the final circular crack velocity, testing speed 5 μm/s. The networks are ranked in increasing order of strain hardening, Young's modulus and fracture energy.

hardening (but also of E and G_c) leads to an higher final crack velocity. However, this observation should be validated by other measurements on several samples, as the exact polymer volume around the confined area varies a bit from sample to sample and could influence this circular crack velocity as a larger surrounding strained volume would represent more elastic energy in the sample as it is being torn open.

As a last remark, it is important to keep in mind that in our study, the bimodal networks that showed the higher level of strain hardening also present the higher Young's modulus and fracture energy. In this sense, it is not possible for us to truly separate the effect of the strain hardening from the other material properties. This is mostly due to experimental problems that occurred on the testing of the OL HEA 30% PEA formulation. However, additional testing and analysis of this formulation could help in order to truly understand the effect of the strain hardening, since the OL HEA 30% PEA presents a modulus and a fracture energy of the same order as the bimodal networks, but a lower level of strain hardening. Our preliminary results (see Appendix D.6) show that the direct destabilisation in a small number of penny shaped cracks after the nucleation does not occur on the OL HEA 30% PEA network, suggesting that this is a feature of the strain hardening of the material more than a feature of the fracture energy.

Chapter 6

Conclusion and Perspectives

Reaching the end of this manuscript, let's look back at our initial goals.

First, we wished to synthesise polymer networks that could act as models for the industrial resins. Based on formulations of acrylate monomers and di-(meth)acrylate functionalysed oligomers provided by DSM (then Covestro), we could produce polymer films via a free radical polymerisation driven by an intense UV flash. The thickness range achieved while assuring a homogeneous conversion in the thickness is 50 μm to 800 μm. The total polymerisation energy was kept at 1 J/cm^2, which was achieved with an illumination of 1s for the reference protocol. The T_gs of all formulations were around -60°C, leading to an elastomeric behaviour at ambient temperature. We could also investigate how this particularly quick polymerisation protocol influences the network formation in small chemistry changes, namely by changing the monomer's reactivity.

The mechanical properties of the different formulations were then investigated. The uniaxial traction test was not enough to determine the complete non-linear behaviour, so the samples were also tested in a bulge inflation test. These two tests allowed to determine the Young's modulus precisely with the small deformation test, and observe a variation of the strain hardening in the large stretches. The networks' behaviour is hyperelastic and we proposed to fit their behaviour with two constitutive equations: Gent, which leads to a direct quantification of the strain hardening (J_m) and Yeoh. The toughness of the materials was characterised by uniaxial traction of single notched samples. As often observed in elastomers, the fracture energy is dependant on the initial stretch rate, suggesting the presence of viscous dissipation and additional bond fracture around the crack tip at high testing velocities. It is important to note that, as it is often the case, we do not have a separation of the material properties. With little surprise, the materials with the highest Young's modulus also show the highest fracture energy and the highest strain hardening. To achieve a separation of the strain hardening and the fracture energy, the addition of bimodality was needed. It was achieved by replacing a portion (1 or 5%w) of the long oligomer with a small diacrylate.

As a side note, our analysis of the bulge inflation experiment was only approximate, and we detailed in which ways our assumption of complete biaxial stretch over the whole bulge was incorrect, especially at large stretches. However, we also propose an interesting way, in our opinion, to combine the contour of the inflated membrane extracted from the bulge inflation experiment with FEM analysis. Simulating the bulge inflation experiment and comparing the calculated contour to the experimental one could help determine the best constitutive equation and material parameters, leading to a fitting of the material's behaviour over a wide range of stretch states. This could prove to be an improvement over the fitting of the constitutive equation with "only" pure biaxial data.

Most importantly, we did achieve to build a set-up that can confine a thin layer of these networks in a sphere against flat geometry and load it under hydrostatic traction to produce cavitation. The range of thicknesses tested is 50 to 500 μm, the confining geometry is a 3 mm radius glass sphere against a glass slide. We had to overcome some (unexpected) experimental difficulties. First, the adhesion between the polymer and the glass surfaces was ensured by the use of a methacrylate silane. Even after an optimisation of the silanisation protocol to our use, there are still some experiments that fail due to the polymer/glass poor adhesion. Then, the sample is assembled during the polymerisation step, so the punch holding the sphere and the glass slide are fixed in their position with no degree of freedom afterwards. We do see some accommodation of the alignment during the first stages of the traction test, showing that our polymerisation protocol does not lead to a perfect alignment.

However, those experimental challenges were mostly overcome and we can present here a protocol that leads to samples of controlled thickness in the range of one to a few hundreds of μm that can be polymerised in a flash and be tested under hydrostatic traction. The force at which each cavity opens can be precisely determined and the cavitation behaviour observed during the experiment through the glass slide. Through a FEM analysis of our system, we proposed a method to determine the local hydrostatic stress for the first cavity opening from the macroscopic force measured. We only considered a linear computation since the cavitation happens at small deformations. This is the first original result of this work, on the mechanical characterization of thin layers (hundreds of micrometers) of elastomer in such a geometry.

Now, we can see how of our results on the cavitation behaviour compare with the experimental studies we presented in the state of the art. First, let's focus on the values of the cavitation pressure at which the first cavity opens. Figure 6.1 compares the critical cavitation pressure (normalized by the Young's modulus) of our formulations with the result presented By Gent and Lindley on rubber in flat/flat geometry [1] and Cristiano et al. on polyurethanes in a sphere against flat geometry [9].

The size effect on this comparison is quite obvious. In a big sample, there is always a big defect, leading to a relatively low hydrostatic pressure of cavitation. In thinner samples, the low values measured correspond also to big defects. But there are also cases where the tested volume only has small defects, leading to a higher dispersion of the measured cavitation pressures, but also to higher pressures. This would describe Cristiano et al. results as mainly a test of the defect population in the network while our high cavitation results would be closer to an intrinsic material property. The very low dispersion of the cavitation pressures in Cristiano et al. study would only be a sign that their polymerisation process was repeatable and always leading to the same range of big defect size.

However, we need to be cautious with this description, as Cristiano et al. found cavitation pressures that were not only reproducible, but also material dependent. So, if we assume that they were mainly testing one big defect in their layers, this reproducible dependence to the elasticity and the fracture energy can be explained by the fact that all their cavities transition into the critical fracture. In that sense, and if we maintain the assumption of the cavitation driven by big defects, it would mean Cristiano et al. were not so much testing the cavitation behaviour but truly the transition to critical fracture. It is also important to underline that Cristiano et al. studied PU networks that were polymerised by a slow thermal polymerisation, which is very different from our high UV free radical polymerisation. Therefore, it would have been interesting to try more reproducible polymerisations and materials in our confined geometry. However, due to the low viscosity of monomers, this represents significant changes in the experimental protocol, which we

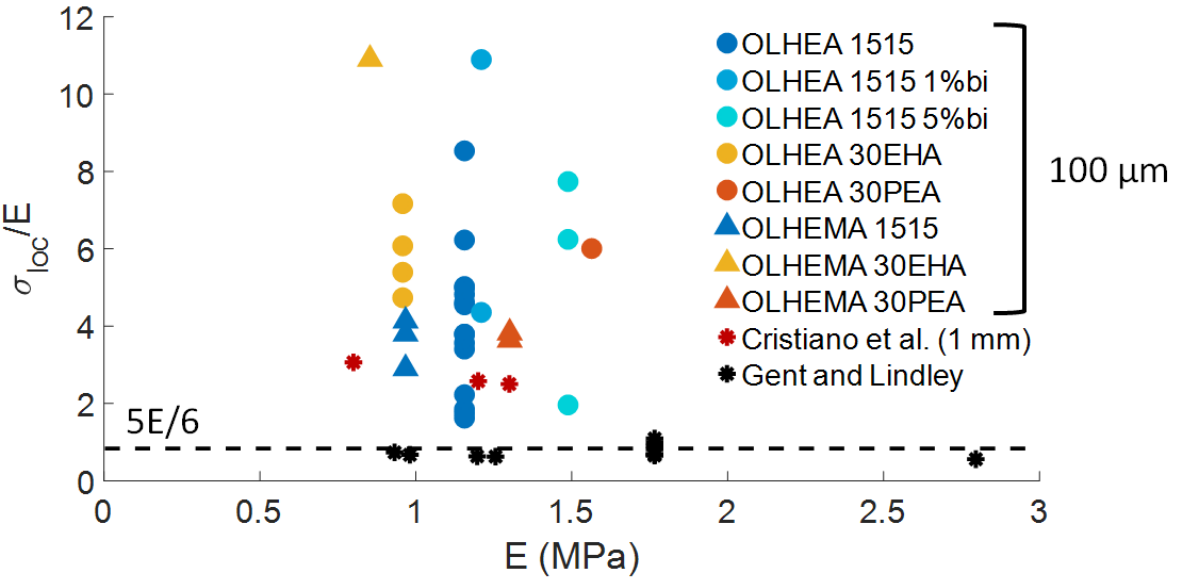

FIGURE 6.1: Comparison of the critical cavitation pressures with the literature. Gent and Lindley [1] : Different vulcanized rubbers in flat/flat geometry of 3 mm thickness. For E = 1.766 MPa, thickness variation from 560 μm to 0.365 mm. Cristiano et al. [9]: Polyurethane elastic networks in sphere/flat geometry, 1 mm of confined thickness, cavitation pressures measured at room T and at 1%/s initial stretch rate. Our experimental data points are taken at room T and at an initial stretch rate of 5%/s. The dotted black line correspond to the theoretical limit of 5E/6.

did not have time to make.

Moving on to the most interesting result of our study, we observe a cavitation behaviour and morphologies that depend on both the thickness of the sample and the material properties. All cavitation events come from a snapping event, which is an unstable crack growth in the system. Although this statement seems to contradict some recent results [5], it is directly borne out by the mecanophore experiments. This snapping instability is linked to the material properties, the stability of the cavities in the thin layers can be explained by the finite size of the sample. We observed that cavities in thick samples (500 μm) nucleate directly several penny shaped cracks and transition from the inflated pancake shape to a raspberry shape, while in thinner samples a nucleated cavity seems to grow slowly in the pancake shape, which allows for the nucleation of other small cavities. Similar morphologies of cavities have been observed by Morelle et al [13] (who proposed the raspberry description) and Kim et al [5].

Our explanation for the pseudo stabilisation of the cavities in thin layers is based on a balance between a stress criteria that allows the defects to nucleate, and an energy criteria that allows the penny shaped cracks to nucleate and propagate. The mechanism, as we picture it, is described on Figure 6.2. In smaller layers, the elastic energy build up is smaller than in thick layers, leading to the stabilisation of the inflated pancake, while thick layers store enough elastic energy to allow for the nucleation and propagation of several penny shaped cracks.

To confirm this interpretation, both an experimental way and a simulation way would be needed. On the simulation part, it would be very enlightening to conduct a simulation of our system in the same way Lopez-Pamies et al. described Gent's poker-chip experiment [101]. By using a phase field method, they could reproduce the experimental loading curves and the morphology of the cavities. Lopez-Pamies et al. interpretation of the many cavities that appear in

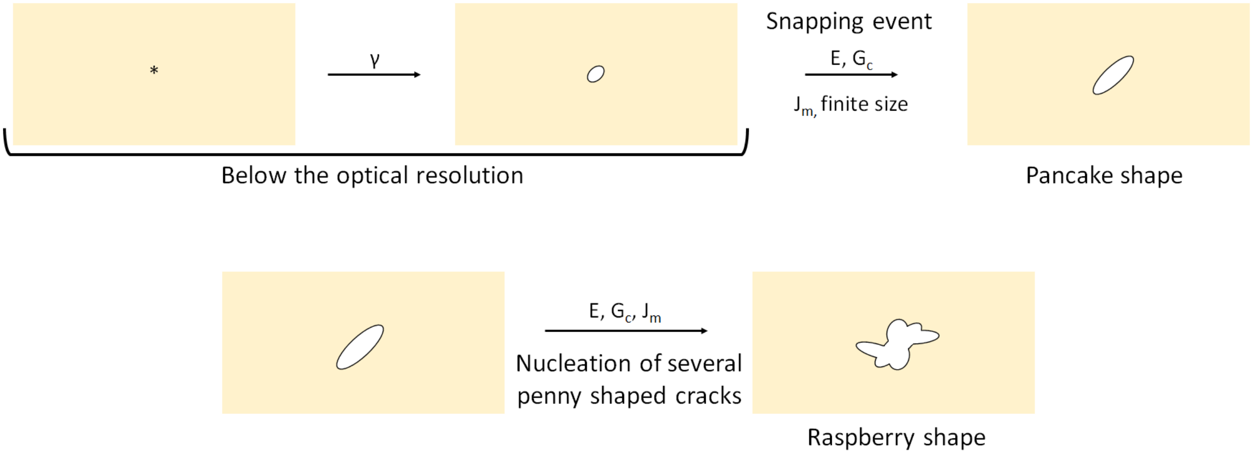

FIGURE 6.2: Proposed mechanism for the snapping and growth of a cavity during constant loading. At first, a defect nucleates and its growth is hindered by the surface tension. At that step, the defect is small enough to consider the polymer medium to be infinite. Reaching a critical size and a critical pressure, the stable position is no longer the small crack, but the expanded one. The cavity snaps: the crack propagates suddenly. This depends on the elasticity, the confinement of the material and the fracture energy. Once the cavity is expanded, several penny shaped cracks can nucleate on its walls and propagate by creating different fracture fronts.

the thin samples lies in the strain crystallisation that can happen in natural rubber, which would stabilise the cavities as the fracture energy of the highly stretched polymer on their border would increase dramatically. However, our polymer networks do not show show such strain induced crystallisation, it would therefore be interesting to see if the phase field method could also reproduce the change in cavitation behaviour in our range of thickness.
On the experimental part, one perspective would be to further the analysis of damage in the networks with the help of mecanophores. One idea would be to load a sample under constant displacement and see if cavities appear over a certain period of time. Looking at the molecular damage would help understand how the cracks propagate, at which orientation, and could even give some more insight on the nucleation phenomena. Looking at the sample while under load under the confocal could also allow for a better understanding of the position of the crack tips of the different penny shaped cracks during their propagation.

Finally, we suspect an effect of the strain hardening on the cavity's transition from the pancake shape to the raspberry shape, as described in several observations in Section 5.2. It seems that the strain hardening leads to a faster destabilisation into several penny shaped cracks and a change in the morphology of the fracture. This change in morphology depending on both the fracture energy and the strain hardening represents an elegant result that is summarized in Figure 6.3. The influence of the elastic modulus and the fracture energy on the morphology of cavities has already been reported in needle inflation experiments ([14], [15]). However, the direct comparison with their results is not trivial, as their networks are extremely soft (E = 10 kPa) and swollen in oil, but it shows that the cavity morphology is an interesting field of study. We could further our observations by testing networks with more difference between the fracture energy and the strain hardening to separate the two effects.

As final words, let's summarize:

- Free radical UV polymerisation works, but it leads to dispersion on the measurement of the mechanical properties.
- Testing thin layers of elastomers in hydrostatic traction is not easy, but we proposed a new and original method to do it.
- Based on our results, we can suggest that a higher cavitation resistance is associated with a high E, G_c and low J_m. However, when the cavity is opened, a low J_m leads to a quick transition from cavitation to fracture.
- Mostly, we can say that mechanically testing thin confined layers of polymers in tension leads to a dispersion of the measured cavitation resistance, as the cavitation behaviour is a multi-stage fracture mechanism dominated by the defect distribution for the nucleation part and by the material properties and degree of confinement for the evolution of the cavity size and shape under stress.

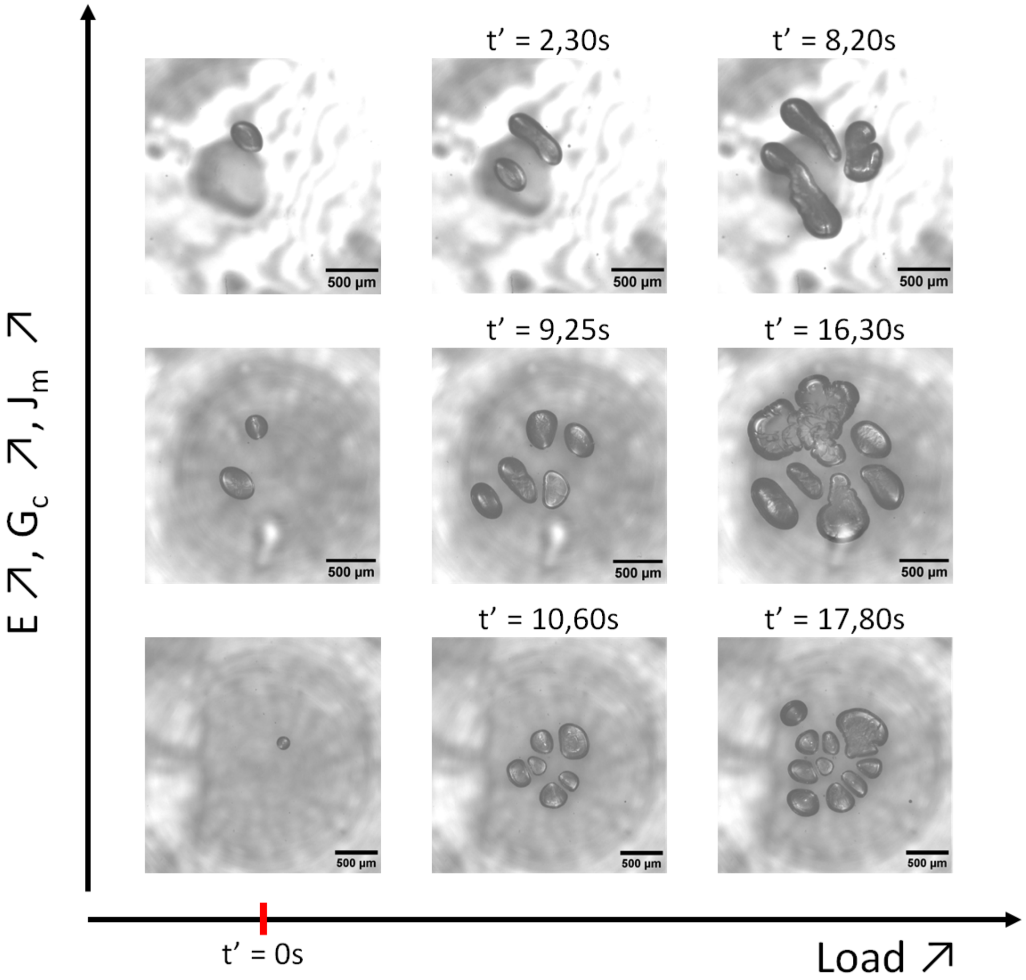

FIGURE 6.3: Strain hardening effect on the cavity's morphology. The time of the first picture is put at 0 to see the formulation effect on the dynamics of the cavity's transition to fracture. From top to bottom, by decreasing order of strain hardening: OL HEA 15% EHA 15% PEA 5%bi, OL HEA 15% EHA 15% PEA 1%bi and OL HEA 30% EHA (100 μm samples, 5 μm/s testing speed). The cavities in the highest strain hardening material (top line) seem to transition to fracture quicker and in bigger lobes than the formulation with the lowest strain hardening.

Bibliography

1. Gent, A. N. & Lindley, P. B. Internal rupture of bonded rubber cylinders in tension. en, 13 (May 1958).
2. Gent, A. N. & Wang, C. Fracture mechanics and cavitation in rubber-like solids. en. *Journal of Materials Science* **26,** 3392–3395. ISSN: 0022-2461, 1573-4803. (2022) (June 1991).
3. Kang, J., Wang, C. & Cai, S. Cavitation to fracture transition in a soft solid. en. *Soft Matter* **13,** 6372–6376. ISSN: 1744-683X, 1744-6848 (2017).
4. Dollhofer, J., Chiche, A., Muralidharan, V., Creton, C. & Hui, C. Surface energy effects for cavity growth and nucleation in an incompressible neo-Hookean material—modeling and experiment. en. *International Journal of Solids and Structures* **41,** 6111–6127. ISSN: 00207683 (Nov. 2004).
5. Kim, J. Y. *et al.* Extreme cavity expansion in soft solids: Damage without fracture. en. *Science Advances* **6,** eaaz0418. ISSN: 2375-2548 (Mar. 2020).
6. Gent, A. N. & Tompkins, D. A. Nucleation and Growth of Gas Bubbles in Elastomers. en. *Journal of Applied Physics* **40,** 2520–2525. ISSN: 0021-8979, 1089-7550 (May 1969).
7. Cho, K. & Gent, A. N. Cavitation in model elastomeric composites. en. *Journal of Materials Science* **23,** 141–144. ISSN: 0022-2461, 1573-4803 (Jan. 1988).
8. Poulain, X., Lefèvre, V., Lopez-Pamies, O. & Ravi-Chandar, K. Damage in elastomers: nucleation and growth of cavities, micro-cracks, and macro-cracks. en. *International Journal of Fracture* **205,** 1–21. ISSN: 0376-9429, 1573-2673. `http://link.springer.com/10.1007/s10704-016-0176-9` (2021) (May 2017).
9. Cristiano, A. *et al.* An experimental investigation of fracture by cavitation of model elastomeric networks. en. *Journal of Polymer Science Part B: Polymer Physics* **48,** 1409–1422. ISSN: 08876266, 10990488 (May 2010).
10. Hutchens, S. B., Fakhouri, S. & Crosby, A. J. Elastic cavitation and fracture via injection. en. *Soft Matter* **12,** 2557–2566. ISSN: 1744-683X, 1744-6848 (2016).
11. Slootman, J. *et al.* Quantifying Rate- and Temperature-Dependent Molecular Damage in Elastomer Fracture. en. *Physical Review X* **10,** 041045. ISSN: 2160-3308 (Dec. 2020).
12. Creton, C. & Ciccotti, M. Fracture and adhesion of soft materials: a review. en. *Reports on Progress in Physics* **79,** 046601. ISSN: 0034-4885, 1361-6633 (Apr. 2016).
13. Morelle, X. P., Sanoja, G. E., Castagnet, S. & Creton, C. 3D fluorescent mapping of invisible molecular damage after cavitation in hydrogen exposed elastomers. en. *Soft Matter* **17,** 4266–4274. ISSN: 1744-683X, 1744-6848 (2021).
14. Yang, S. *et al.* Hydraulic fracture geometry in ultrasoft polymer networks. en. *International Journal of Fracture* **219,** 89–99. ISSN: 0376-9429, 1573-2673. `http://link.springer.com/10.1007/s10704-019-00380-y` (2022) (Sept. 2019).
15. Milner, M. P. & Hutchens, S. B. Multi-crack formation in soft solids during high rate cavity expansion. en. *Mechanics of Materials* **154** (2021).

16. Rayleigh, L. On the pressure developed in a liquid during the collapse of a spherical cavity. en. *The London, Edinburgh, and Dublin Philosophical Magazine and Journal of Science* **34,** 94–98. ISSN: 1941-5982, 1941-5990 (Aug. 1917).
17. Patek, S. N. & Caldwell, R. L. Extreme impact and cavitation forces of a biological hammer: strike forces of the peacock mantis shrimp Odontodactylus scyllarus. *Journal of Experimental Biology* **208,** 3655–3664. ISSN: 0022-0949 (Oct. 2005).
18. Versluis, M., Schmitz, B., von der Heydt, A. & Lohse, D. How Snapping Shrimp Snap: Through Cavitating Bubbles. en. *Science* **289,** 2114–2117. ISSN: 0036-8075, 1095-9203 (Sept. 2000).
19. Amini, S., Tadayon, M., Isaiah Chua, J. & Miserez, A. Multi-scale structural design and biomechanics of the pistol shrimp snapper claw. en. *Acta Biomaterialia* **73,** 449–457 (2018).
20. Gardner, W. B. Microbending loss in optical fibers. *The Bell System Technical Journal* **54,** 457–465. ISSN: 0005-8580 (Feb. 1975).
21. Kim, H. D., Kang, S. G. & Ha, C. S. Properties of UV-curable polyurethane acrylates for primary optical fiber coating. en. *Journal of Applied Polymer Science* **46,** 1339–1351. ISSN: 1097-4628 (1992).
22. Lai, H., Peng, X., Li, L., Zhu, D. & Xiao, P. Novel monomers for photopolymer networks. en. *Progress in Polymer Science* (2022).
23. Endruweit, A., Johnson, M. S. & Long, A. C. Curing of composite components by ultraviolet radiation: A review. en. *Polymer Composites* **27,** 119–128. ISSN: 1548-0569 (2006).
24. Moad, G. A Critical Assessment of the Kinetics and Mechanism of Initiation of Radical Polymerization with Commercially Available Dialkyldiazene Initiators. en. *Progress in Polymer Science* **88,** 130–188 (2019).
25. Decker, C. & Jenkins, A. D. Kinetic approach of oxygen inhibition in ultraviolet- and laser-induced polymerizations. en. *Macromolecules* **18,** 1241–1244. ISSN: 0024-9297, 1520-5835 (June 1985).
26. Iedema, P., Schamböck, V., Koskamp, J., Schellekens, S. & Willemse, R. Photocuring of diacrylate. en. *Chemical Engineering Science* **176,** 491–502 (2018).
27. Ballard, N. & Asua, J. M. Radical polymerization of acrylic monomers: An overview. en. *Progress in Polymer Science,* 40–60 (2018).
28. Pirman, T., Ocepek, M. & Likozar, B. Radical Polymerization of Acrylates, Methacrylates, and Styrene: Biobased Approaches, Mechanism, Kinetics, Secondary Reactions, and Modeling. en. *Industrial & Engineering Chemistry Research* **60,** 9347–9367. ISSN: 0888-5885, 1520-5045 (July 2021).
29. Olaj, O. F., Bitai, I. & Hinkelmann, F. The laser-flash-initiated polymerization as a tool of evaluating (individual) kinetic constants of free-radical polymerization, 2. The direct determination of the rate of constant of chain propagation. en. *Die Makromolekulare Chemie* **188,** 1689–1702. ISSN: 0025-116X (1987).
30. Lyons, R. A. *et al.* Pulsed-Laser Polymerization Measurements of the Propagation Rate Coefficient for Butyl Acrylate. en. *Macromolecules* **29,** 1918–1927. ISSN: 0024-9297, 1520-5835 (Jan. 1996).
31. Plessis, C. *et al.* Evidence of Branching in Poly(butyl acrylate) Produced in Pulsed-Laser Polymerization Experiments. en. *Macromolecular Rapid Communications* **24,** 173–177. ISSN: 1521-3927 (2003).
32. Haehnel, A. P. *et al.* Global Trends for k_{p} ? The Influence of Ester Side Chain Topography in Alkyl (Meth)Acrylates - Completing the Data Base. en. *Macromolecules* **47,** 3483–3496. ISSN: 0024-9297, 1520-5835 (May 2014).

33. Britton, D., Heatley, F. & Lovell, P. A. Chain Transfer to Polymer in Free-Radical Bulk and Emulsion Polymerization of Vinyl Acetate Studied by NMR Spectroscopy. en. *Macromolecules* **31,** 2828–2837. ISSN: 0024-9297, 1520-5835 (May 1998).

34. Steeman, P. A. M., Dias, A. A., Wienke, D. & Zwartkruis, T. Polymerization and Network Formation of UV-Curable Systems Monitored by Hyphenated Real-Time Dynamic Mechanical Analysis and Near-Infrared Spectroscopy. *Macromolecules* **37.** Publisher: American Chemical Society, 7001–7007. ISSN: 0024-9297 (Sept. 2004).

35. Chiou, B.-S., English, R. J. & Khan, S. A. Rheology and Photo-Cross-Linking of Thiol-Ene Polymers. en. *Macromolecules* **29,** 5368–5374. ISSN: 0024-9297, 1520-5835 (Jan. 1996).

36. Chiou, B.-S. & Khan, S. A. Real-Time FTIR and *in Situ* Rheological Studies on the UV Curing Kinetics of Thiol-ene Polymers. en. *Macromolecules* **30,** 7322–7328. ISSN: 0024-9297, 1520-5835 (Nov. 1997).

37. Decker, C. UV-radiation curing chemistry. *Pigment & Resin Technology* **30,** 278–286. ISSN: 0369-9420 (Jan. 2001).

38. Dušek, K. Are cured thermoset resins inhomogeneous? en. *Die Angewandte Makromolekulare Chemie* **240,** 1–15. ISSN: 1522-9505 (1996).

39. Krzeminski, M., Molinari, M., Troyon, M. & Coqueret, X. Characterization by Atomic Force Microscopy of the Nanoheterogeneities Produced by the Radiation-Induced Cross-Linking Polymerization of Aromatic Diacrylates. en. *Macromolecules* **43,** 8121–8127. ISSN: 0024-9297, 1520-5835 (Oct. 2010).

40. Anseth, K. S., Anderson, K. J. & Bowman, C. N. Radical concentrations, environments, and reactivities during crosslinking polymerizations. en. *Macromolecular Chemistry and Physics* **197,** 833–848. ISSN: 1521-3935 (1996).

41. Decker, C. Photoinitiated crosslinking polymerisation. *Progress in Polymer Science* **21,** 593–650. ISSN: 0079-6700 (Jan. 1996).

42. Kannurpatti, A. R., Anseth, J. & Bowman, C. A study of the evolution of mechanical properties and structural heterogeneity of polymer networks formed by photopolymerizations of multifunctional (meth)acrylates. en. *Polymer* **31,** 2507–2513 (1998).

43. Brett, C. J. *et al.* Revealing structural evolution occurring from photo-initiated polymer network formation. en. *Communications Chemistry* **3,** 88. ISSN: 2399-3669 (Dec. 2020).

44. Bevington, J. C. & Harris, D. O. Reactivities of acrylates and methacrylates. en. *Journal of Polymer Science Part B: Polymer Letters* **5,** 799–802. ISSN: 1542-6254 (1967).

45. Bevington, J. C. & Malpass, B. W. Reactivities of esters of Methacylic acid - III. Studies of copolymerizations initiated by metallic sodium. en. ISSN: 0014-3057 (1964).

46. Baines, F. C. & Bevington, J. C. A tracer study of the hydrolysis of methyl methacrylate and methyl acrylate units in homopolymers and copolymers. en. *Journal of Polymer Science Part A-1: Polymer Chemistry* **6,** 2433–2440. ISSN: 0449296X, 15429350 (Sept. 1968).

47. Wen, M., Scriven, L. E. & McCormick, A. V. Differential Scanning Calorimetry and Cantilever Deflection Studies of Polymerization Kinetics and Stress in Ultraviolet Curing of Multifunctional (Meth)acrylate Coatings. en. *Macromolecules* **35,** 112–120. ISSN: 0024-9297, 1520-5835 (Jan. 2002).

48. Stansbury, J. W. Dimethacrylate network formation and polymer property evolution as determined by the selection of monomers and curing conditions. eng. *Dental Materials: Official Publication of the Academy of Dental Materials* **28,** 13–22. ISSN: 1879-0097 (Jan. 2012).

49. Verstegen, E. J. K., Faasen, J. H. P., Stapert, H. R., Duineveld, P. C. & Kloosterboer, J. G. Influence of the reaction mechanism on the shape accuracy of optical components obtained by photoreplication. en. *Journal of Applied Polymer Science* **90,** 2364–2376. ISSN: 1097-4628 (2003).

50. Anseth, K. S., Bowman, C. N. & Peppas, N. A. Polymerization kinetics and volume relaxation behavior of photopolymerized multifunctional monomers producing highly crosslinked networks. en. *Journal of Polymer Science Part A: Polymer Chemistry* **32,** 139–147. ISSN: 1099-0518 (1994).

51. Payne, J. A., Francis, L. F. & McCormick, A. V. The effects of processing variables on stress development in ultraviolet-cured coatings. en. *Journal of Applied Polymer Science* **66,** 1267–1277. ISSN: 1097-4628 (1997).

52. Wight, F. R. Oxygen inhibition of acrylic photopolymerization. en. *Journal of Polymer Science: Polymer Letters Edition* **16,** 121–127. ISSN: 1543-0472 (1978).

53. Sodré, C. S., Albuquerque, P. P. A., Isolan, C. P., Moraes, R. R. & Schneider, L. F. Relative photon absorption determination and the influence of photoinitiator system and water content on C=C conversion, water sorption/solubility of experimental self-etch adhesives. en. *International Journal of Adhesion and Adhesives* **63,** 152–157. ISSN: 01437496 (Dec. 2015).

54. Flory, P. J. & Rehner, J. Statistical Mechanics of Cross-Linked Polymer Networks I. Rubberlike Elasticity. en. *The Journal of Chemical Physics* **11,** 512–520. ISSN: 0021-9606, 1089-7690 (Nov. 1943).

55. Rubinstein, M. & Colby, R. H. *Polymer Physics* (New York: Oxford University Press, 2003).

56. Bentz, K. C., Walley, S. E. & Savin, D. A. Solvent effects on modulus of poly(propylene oxide)-based organogels as measured by cavitation rheology. en. *Soft Matter* **12,** 4991–5001. ISSN: 1744-683X, 1744-6848 (2016).

57. *Physical properties of polymers handbook* 2nd ed. en (ed Mark, J. E.) ISBN: 978-0-387-31235-4 (Springer, New York, 2006).

58. Krzeminski, M., Molinari, M., Troyon, M. & Coqueret, X. Calorimetric Characterization of the Heterogeneities Produced by the Radiation-Induced Cross-Linking Polymerization of Aromatic Diacrylates. en. *Macromolecules* **43,** 3757–3763. ISSN: 0024-9297, 1520-5835 (Apr. 2010).

59. Derjaguin, B., Muller, V. M. & Toporov, Y. P. Effect of Contact Deformations on the Adhesion of Particles. en. *Journal of Colloid and Interface Science* **53.** ISSN: 0021-9797 (1975).

60. Feige, L. & Creton, C. *Introduction of anisotropy in double network elastomers by orientation and two-step curing* PhD thesis (2020).

61. Waltz, V., Creton, C. & Rieger, J. *Design of novel soft materials and understanding how soft networks break using mechano-fluorescence* PhD thesis (2022).

62. Edwards, S. F. The statistical mechanics of polymerized material. en. *Proceedings of the Physical Society* **92,** 9–16. ISSN: 0370-1328 (Sept. 1967).

63. Treloar, L. R. G. The elasticity and related properties of rubbers. en. *Rep. Prog. Phys,* 755–826 (1973).

64. Yeoh, O. H. & Fleming, P. D. A new attempt to reconcile the statistical and phenomenological theories of rubber elasticity. en. *Journal of Polymer Science Part B: Polymer Physics* **35,** 1919–1931. ISSN: 1099-0488 (1997).

65. Gent, A. N. A new constitutive relation for rubber. *Rubber Chemistry and Technology* **1969** (1995).

66. Yeoh, O. H. Characterization of Elastic Properties of Carbon-Black-Filled Rubber Vulcanizates. *Rubber Chemistry and Technology* **63,** 792–805 (1990).
67. Rubinstein, M. & Panyukov, S. Elasticity of Polymer Networks. en. *Macromolecules* **35,** 6670–6686. ISSN: 0024-9297, 1520-5835 (Aug. 2002).
68. Kuhn, W. Dependence of the average transversal on the longitudinal dimensions of statistical coils formed by chain molecules. en. *Journal of Polymer Science* **1,** 380–388. ISSN: 1542-6238 (1946).
69. James, H. M. & Guth, E. Theory of the Elastic Properties of Rubber. en. *The Journal of Chemical Physics* **11,** 455–481. ISSN: 0021-9606, 1089-7690 (Oct. 1943).
70. Rivlin, R. S. & Saunders, D. W. Large elastic deformations of isotropic materials VII. Experiments on the deformation of rubber. en. *Philosophical Transactions of the Royal Society of London. Series A, Mathematical and Physical Sciences* **243,** 251–288. ISSN: 0080-4614 (Apr. 1951).
71. Treloar, L. R. G. Strains in an Inflated Rubber Sheet, and the Mechanism of Bursting. *Rubber Chemistry and Technology* **17,** 957–967 (1944).
72. Mott, P. H., Roland, C. M. & Hassan, S. E. Strains in an Inflated Rubber Sheet. en. *Rubber Chemistry and Technology* **76,** 326–333. ISSN: 1943-4804, 0035-9475 (May 2003).
73. Reuge, N., Schmidt, F. M., Le Maoult, Y., Rachik, M. & Abbé, F. Elastomer biaxial characterization using bubble inflation technique. I: Experimental investigations. en. *Polymer Engineering & Science* **41,** 522–531. ISSN: 1548-2634 (2001).
74. Johannknecht, R., Clauss, G. & Jerrams, S. Determination of non-linear, large, equal biaxial stresses and strains in thin elastomeric sheets by bubble inflation. *Proceedings of the Institution of Mechanical Engineers, Part L: Journal of Materials: Design and Applications* **216,** 233–243. ISSN: 1464-4207 (Oct. 2002).
75. Zhou, L., Wang, S., Li, L. & Fu, Y. An evaluation of the Gent and Gent-Gent material models using inflation of a plane membrane. en. *International Journal of Mechanical Sciences* (2018).
76. O'connell, P. A. & McKenna, G. B. A novel nano-bubble inflation method for determining the viscoelastic properties of ultrathin polymer films. en. *Scanning* **30,** 184–196. ISSN: 1932-8745 (2008).
77. Denson, C. D. & Gallo, R. J. Measurements on the biaxial extension viscosity of bulk polymers: The inflation of a thin polymer sheet. en. *Polymer Engineering & Science* **11,** 174–176. ISSN: 1548-2634 (1971).
78. Griffith, A. A. The Phenomena of Rupture and Flow in Solid. *Philos Trans R Soc Lond Ser Contain Pap Math Phys Character* (1921).
79. Ahagon, A. & Gent, A. N. Threshold fracture energies for elastomers. en. *Journal of Polymer Science: Polymer Physics Edition* **13,** 1903–1911. ISSN: 1542-9385 (1975).
80. Lake, G. J. & Thomas, A. G. The strength of highly elastic materials. en. *Proceedings of the Royal Society of London. Series A. Mathematical and Physical Sciences* **300** (Aug. 1967).
81. Gent, A. N. & Schultz, J. Effect of Wetting Liquids on the Strength of Adhesion of Viscoelastic Material. *The Journal of Adhesion* **3,** 281–294. ISSN: 0021-8464 (Mar. 1972).
82. Andrews, E. H., Kinloch, A. J. & Melville, H. W. Mechanics of adhesive failure. II. *Proceedings of the Royal Society of London. A. Mathematical and Physical Sciences* **332.** Publisher: Royal Society, 401–414 (Mar. 1973).
83. Greensmith, H. W. Rupture of rubber. X. The change in stored energy on making a small cut in a test piece held in simple extension. en. *Journal of Applied Polymer Science* **7,** 993–1002. ISSN: 1097-4628 (1963).

84. Chen, Y.-J., Mays, J. W. & Hadjichristidis, N. The influence of alkylene spacers on conformational and thermal properties of poly (aryl methacrylates). en. *Journal of Polymer Science Part B: Polymer Physics* **32,** 715–719. ISSN: 1099-0488 (1994).
85. Zosel, A. The effect of fibrilation on the tack of pressure sensitive adhesives. en. *International Journal of Adhesion & Adhesives* **18,** 265–271 (1998).
86. Gent, A. N. Elastic Instabilities of Inflated Rubber Shells. en. *Rubber Chemistry and Technology* **72,** 263–268. ISSN: 1943-4804, 0035-9475 (May 1999).
87. Mangan, R. & Destrade. Gent models for the inflation of spherical balloons. en. *International Journal of Non-Linear Mechanics* **68,** 52–58 (2015).
88. Kokubo, S. & Vana, P. Easy Access to the Characteristic Ratio of Polymers Using Ion-Mobility Mass Spectrometry. en. *Macromolecular Chemistry and Physics* **218,** 1600373. ISSN: 1521-3935 (2017).
89. Boudraa, K. E., Bouchaour, T., Beyens, C. & Maschke, U. Novel interpenetrating polymer network composed of poly(butyl acrylates) and poly(ethyl-hexyl acrylate). *International Journal of Polymer Analysis and Characterization* **25,** 18–33. ISSN: 1023-666X (Jan. 2020).
90. Gent, A. N. Cavitation in Rubber: A Cautionary Tale. *Rubber Chemistry and Technology* **63,** 49–53. ISSN: 0035-9475 (July 1990).
91. Gent, A. N. & Park, B. Failure processes in elastomers at or near a rigid spherical inclusion. en. *Journal of Materials Science* **19,** 1947–1956. ISSN: 1573-4803 (June 1984).
92. Williams, M. L. & Schapery, R. A. Spherical flaw instability in hydrostatic tension. en. *International Journal of Fracture Mechanics* **1,** 64–72. ISSN: 0020-7268, 1573-2673. (2020) (Mar. 1965).
93. Lin, Y. & Hui, C. Cavity growth from crack-like defects in soft materials. en. *International Journal of Fracture* **126,** 205–221. ISSN: 1573-2673. (2019) (Apr. 2004).
94. Lefèvre, V., Ravi-Chandar, K. & Lopez-Pamies, O. Cavitation in rubber: an elastic instability or a fracture phenomenon? en. *International Journal of Fracture* **192,** 1–23. ISSN: 1573-2673 (Mar. 2015).
95. Gent, A. N. & Tompkins, D. A. Surface energy effects for small holes or particles in elastomers. en. *Journal of Polymer Science Part A-2: Polymer Physics* **7,** 1483–1487. ISSN: 1542-9377 (1969).
96. Chiche, A., Dollhofer, J. & Creton, C. Cavity growth in soft adhesives. en. *The European Physical Journal E* **17,** 389–401. ISSN: 1292-895X (Aug. 2005).
97. Lopez-Pamies, O., Idiart, M. I. & Nakamura, T. Cavitation in elastomeric solids: I—A defect-growth theory. en. *Journal of the Mechanics and Physics of Solids* **59,** 1464–1487. ISSN: 00225096 (Aug. 2011).
98. Hou, H.-S. & Abeyaratne, R. Cavitation in elastic and elastic-plastic solids. en. *Journal of the Mechanics and Physics of Solids* **40,** 571–592. ISSN: 0022-5096 (Jan. 1992).
99. Long, R. & Hui, C.-Y. Effects of triaxiality on the growth of crack-like cavities in soft incompressible elastic solids. en. *Soft Matter* **6,** 1238. ISSN: 1744-683X, 1744-6848 (2010).
100. Denecour, R. L. & Gent, A. N. Bubble formation in vulcanized rubbers. en. *Journal of Polymer Science Part A-2: Polymer Physics* **6,** 1853–1861. ISSN: 1542-9377 (1968).
101. Kumar, A. & Lopez-Pamies, O. The poker-chip experiments of Gent and Lindley (1959) explained. en. *J. Mech. Phys. Solids* **150** (2021).
102. Creton, C. & Lakrout, H. Micromechanics of flat-probe adhesion tests of soft viscoelastic polymer films. fr. *Journal of Polymer Science Part B: Polymer Physics* **38,** 965–979. ISSN: 1099-0488 (2000).

103. Yamaguchi, T., Morita, H. & Doi, M. Modeling on debonding dynamics of pressure-sensitive adhesives. en. *The European Physical Journal E* **20,** 7–17. ISSN: 1292-8941, 1292-895X (May 2006).

104. Kundu, S. & Crosby, A. J. Cavitation and fracture behavior of polyacrylamide hydrogels. en. *Soft Matter* **5,** 3963. ISSN: 1744-683X, 1744-6848. `http://xlink.rsc.org/?DOI=b909237d` (2019) (2009).

105. Zimberlin, J. A., Sanabria-DeLong, N., Tew, G. N. & Crosby, A. J. Cavitation rheology for soft materials. en. *Soft Matter* **3,** 763–767. ISSN: 1744-6848 (May 2007).

106. Lindsey, G. H. *Hydrostatic tensile fracture of a polyurethane elastomer* en. Tech. rep. (Defense Technical Information Center, Fort Belvoir, VA, Feb. 1966).

107. Baumberger, T., Caroli, C., Martina, D. & Ronsin, O. Magic Angles and Cross-Hatching Instability in Hydrogel Fracture. en. *Physical Review Letters* **100,** 178303. ISSN: 0031-9007, 1079-7114 (May 2008).

108. Smith, M. *ABAQUS/Standard User's Manual, Version 6.9* English (Dassault Systèmes Simulia Corp, United States, 2009).

109. Lindsey, G. H. Triaxial Fracture Studies. en. *Journal of Applied Physics* **38,** 4843–4852. ISSN: 0021-8979, 1089-7550 (Nov. 1967).

110. Morris, J. R., Bei, H., Pharr, G. M. & George, E. P. Size Effects and Stochastic Behavior of Nanoindentation Pop In. en. *Physical Review Letters* **106,** 165502. ISSN: 0031-9007, 1079-7114 (Apr. 2011).

111. Biggins, J. S., Saintyves, B., Wei, Z., Bouchaud, E. & Mahadevan, L. Digital instability of a confined elastic meniscus. en. *PNAS* **110,** 12545–12548 (July 2013).

112. Gent, A. N. & Pulford, C. T. R. Micromechanics of fracture in elastomers. en. *Journal of Materials Science* **19,** 3612–3619. ISSN: 1573-4803 (Nov. 1984).

Appendix A

Appendix on the formulation

A.1 Components informations

Abbr.	Chemical name	Molecular mass (g/mol)	CAS
OL HEA	PPG(8000)(IPDIHEA)$_2$	8635	X
OL HEMA	PPG(8000)(IPDIHEMA)$_2$	8665	X
EHA	2 ethylhexyl acrylate	184.28	103-11-7
EHMA	2 ethylhexyl methacrylate	198.30	688-84-6
PEA	2 phenoxyethyl acrylate	192.21	48145-04-6
PEMA	2 phenoxyethyl acrylate	206.24	10595-06-9
BAPO	Phenylbis(2,4,6-trimethylbenzoyl)phosphine oxide	418.46	162881-26-7

TABLE A.1: Molecular mass of the components

A.2 UV Lamp calibration

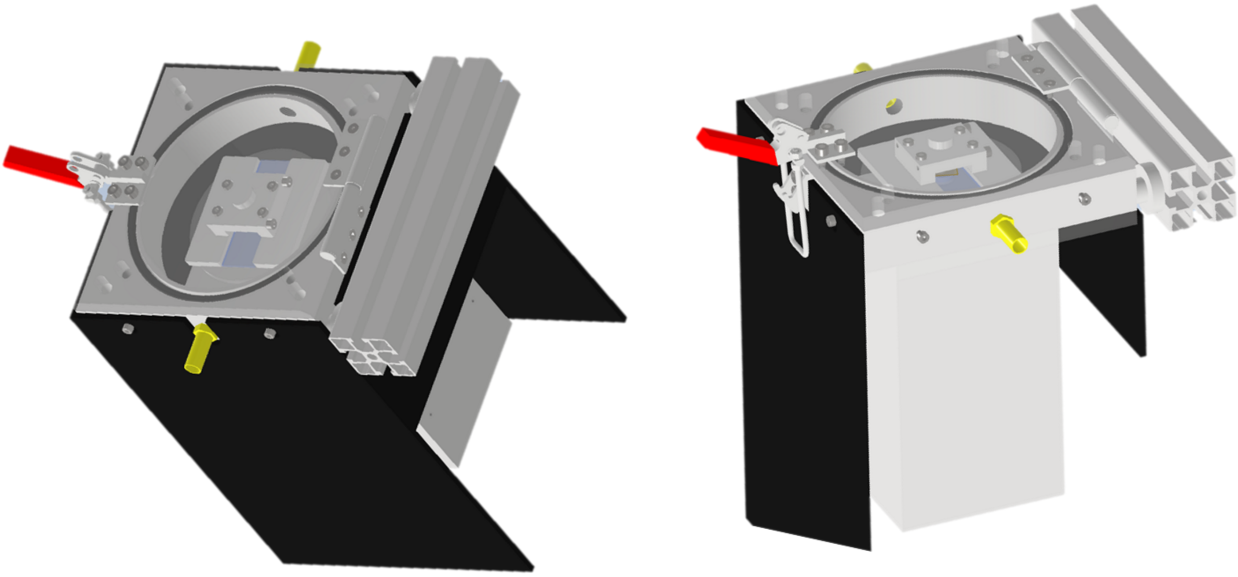

(A) Polymerisation chamber designed by the workshop

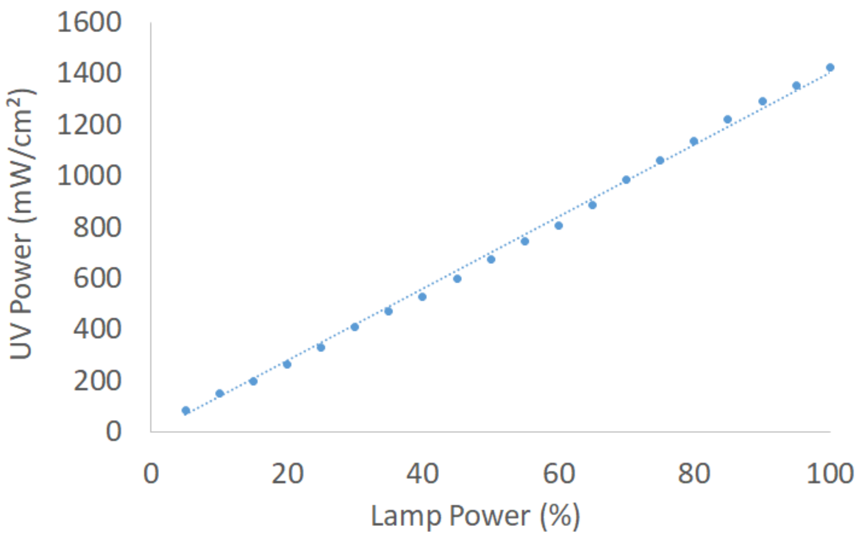

(B) Calibration of the Phoseon Firejet FJ801 395 nm

FIGURE A.1: Polymerisation chamber and Lamp calibration. (A) Polymerisation set-up: the black cardboard is used to protect the user from the emitted UV light. (B) Calibration of the Phoseon Firejet FJ801 395 nm - 10 mm between the lamp and the polymerisation chamber. The power is measured with a EIT UV Power Puck® II through a 2 mm thick borosilicate glass slide. The value of the UVV (between 395 and 445 nm) is reported here. This corresponds to the experimental conditions of the cavitation samples.

Lamp power (%)	UVV (mW/cm^2)	Time for 1 J/cm^2 (s)
5	86.755	11.5
15	202.306	4.9
30	410.887	2.4
70	986.425	1
100	1428.323	0.7

TABLE A.2: Corresponding times for the polymerisation of polymer films

A.3 Characterization of the extractibles

Network: OL HEA 15% EHA 15% PEA - swelling in ethyl acetate for 1 week. The solvent is then dried under vacuum and the extractibles are analyzed by SEC (in THF) or by NMR (in $CDCl_3$).

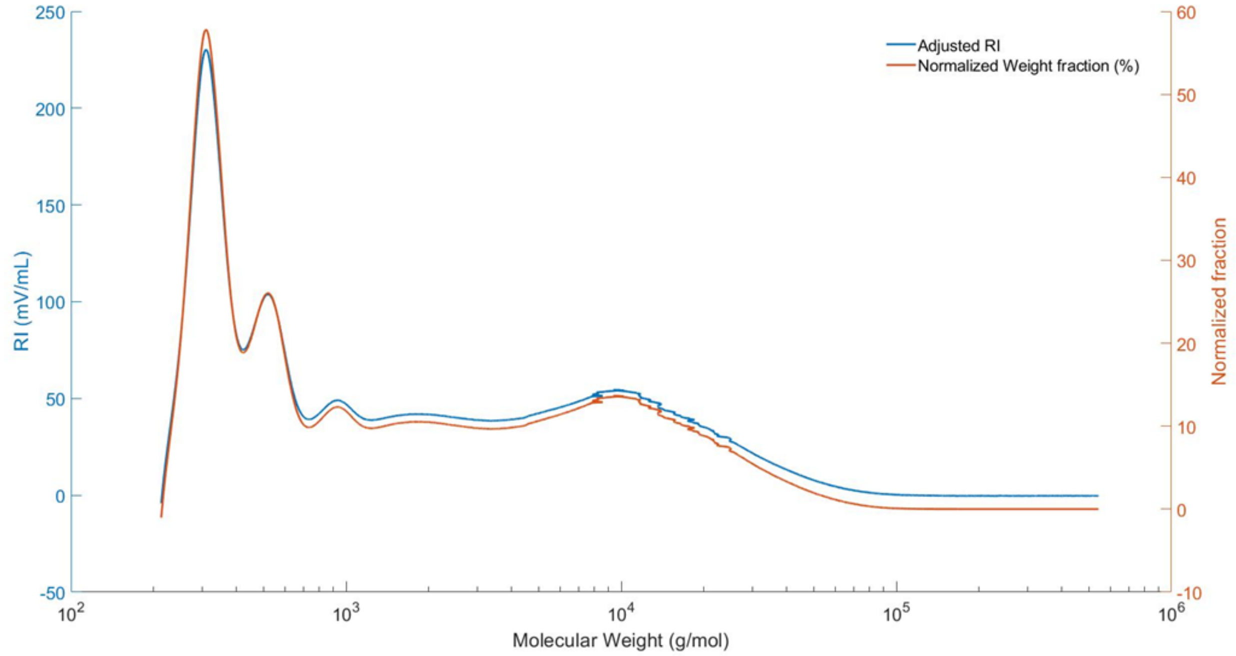

FIGURE A.2: SEC measurement of the extractibles - (70% 1s)

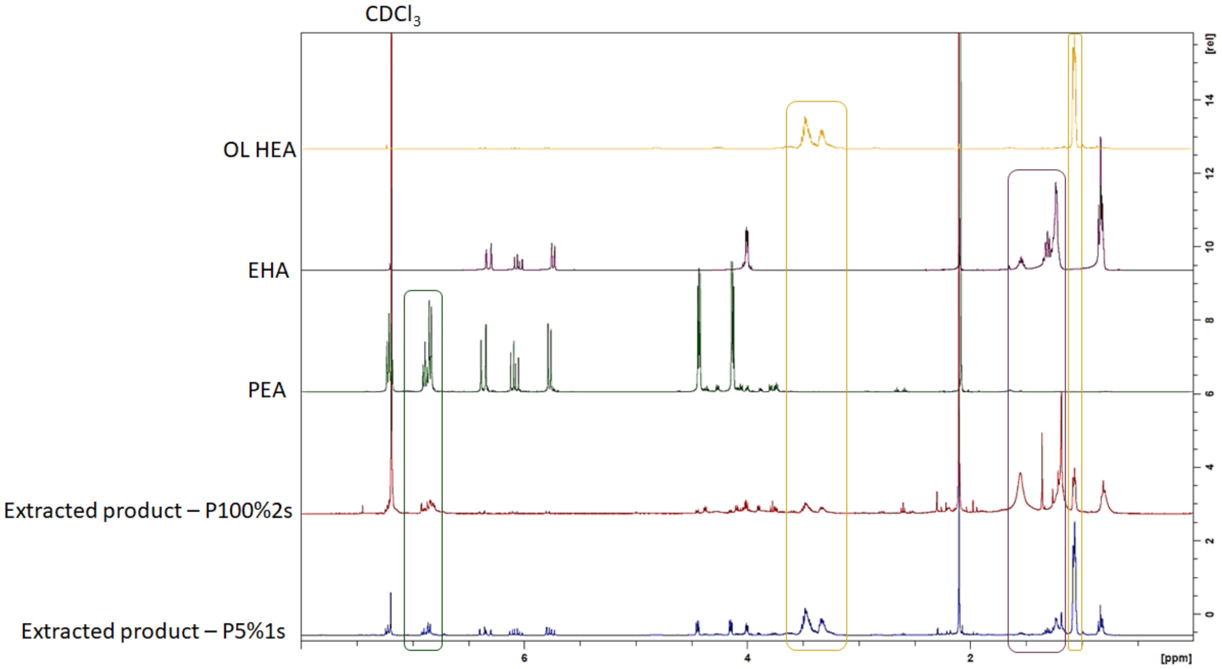

FIGURE A.3: NMR ^{1}H measurement of extractibles for polymerisation protocols of (5% 1s) and (100% 1s), comparison with the signal of the components

A.4 Polymerisation of pure monomer formulations

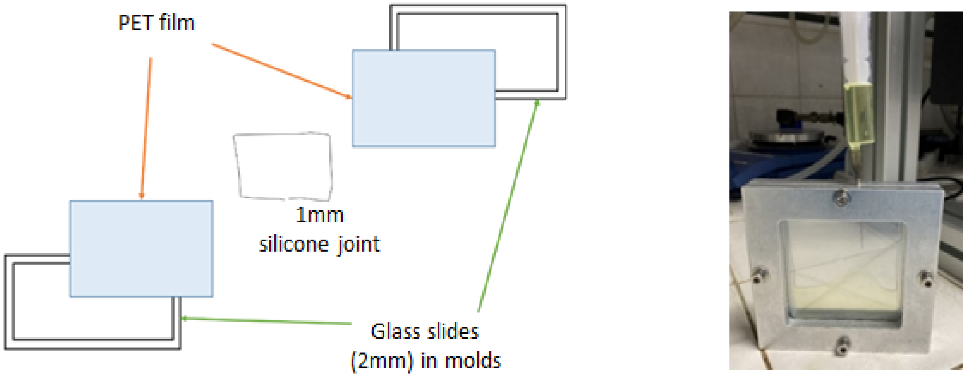

FIGURE A.4: Mold for the polymerisation of pure monomer formulations

A.5 AFM protocols

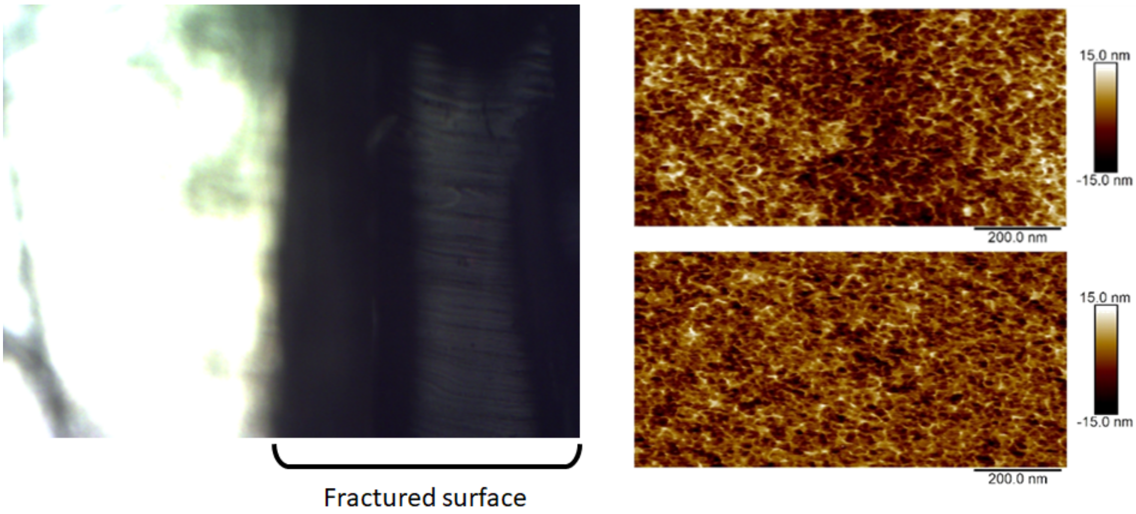

FIGURE A.5: AFM measurement on the fracture surface of OL HEA 30% PEA. The sample is fractured after immersion in liquid N_2, the resulting surface is observed with the same AFM protocol as the surfaces. The height scans are displayed on the left and compared to the surface scan and no difference can be spotted.

The AFM observation made on the thickness showed no significant difference to the surface scan. This validates the fact that the surface scan are representative to the bulk properties, inferring that the formulation inside the film is homogeneous. The heterogeneities are also not surface dependant.

One last question was whether the heterogeneities are also formed with pure PEA formulations. The surfaces of pure PEA networks (0% BDA - polymerisation protocol (70% 5s)) were scanned with the same AFM protocol as usual, the DMT fit of the modulus and the sample's height are displayed on Figure A.6. It appears that the PEA networks are completely homogeneous, meaning that the heterogeneities formation in the resin formulations are only due to the

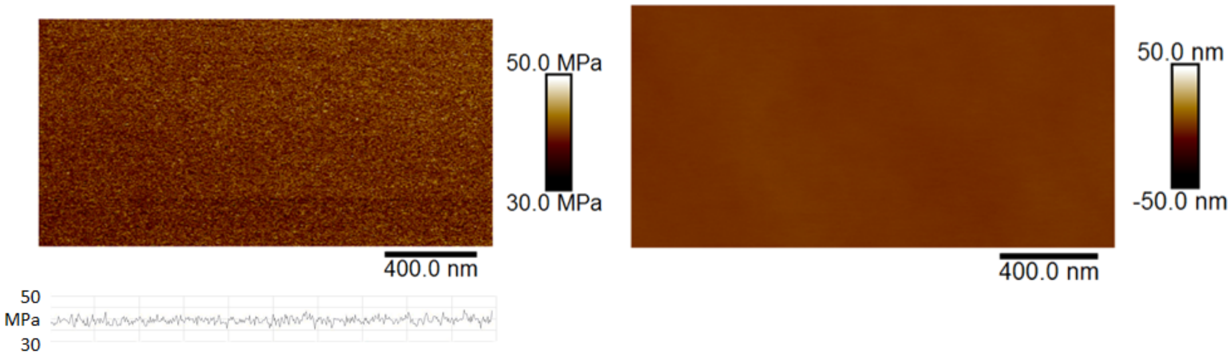

(A) DMT modulus fit and modulus variation

(B) Height measurement

FIGURE A.6: AFM measurement of a pure PEA (0% BDA - 70% 5s) network surface. (A) The modulus variation is measured over the length of the scanned area.

PEA miscibility with the oligomer and the reactivity. The AFM tip is calibrated with PDMS samples with known modulus, and this leads to surprisingly high modulus for the PEA formulation. It can be due to the viscoelasticity of the network, as the surface is tested at 1 kHz.

Appendix B

Appendix on the mechanical properties

B.1 Strain energy models - Small strain behaviour

Three models are considered in our study: Neo-Hookean, Gent and Yeoh. While the NH model only correctly describes the uniaxial data, Gent and Yeoh describe the complete non linear elasticity behaviour, especially the strain hardening of our materials. Let's derive their expressions in small deformations to link their coefficients to the simple linear elasticity description.

NH model

$$\begin{aligned}\sigma_{NH,t,uni} &= \frac{E}{3}.\left(\lambda^2 - \frac{1}{\lambda}\right) = \frac{E}{3}.\left((1+\epsilon)^2 - \frac{1}{1+\epsilon}\right)\\ (\epsilon \to 0) &\simeq \frac{E}{3}.(1+2\epsilon-(1-\epsilon))\\ \sigma_{NH,t,uni} &\simeq E\epsilon\end{aligned} \tag{B.1}$$

$$\begin{aligned}\sigma_{NH,t,bi} &= \frac{E}{3}.\left(2\lambda^2 - \frac{1}{\lambda^4}\right) = \frac{E}{3}.\left(2(1+\epsilon)^2 - \frac{1}{(1+\epsilon)^4}\right)\\ (\epsilon \to 0) &\simeq \frac{E}{3}.(2(1+2\epsilon)-(1-4\epsilon))\\ \sigma_{NH,t,bi} &\simeq 2.E\epsilon\end{aligned} \tag{B.2}$$

There is a slope difference of 2 between the uniaxial and the biaxial theoretically, which can also be seen in our experimental tests.

Models considering the strain hardening

For these computations, it is interesting to first compute the small strain behaviour of $J_{1,uni}$ and $J_{1,bi}$.

$$\begin{aligned}J_{1,uni} &= \lambda^2 + \frac{2}{\lambda} - 3 = (1+\epsilon)^2 + \frac{2}{1+\epsilon} - 3 \simeq 1+2\epsilon+2(1-\epsilon)-3 = 0\ (\epsilon \to 0)\\ J_{1,bi} &= 2\lambda^2 + \frac{1}{\lambda^4} - 3 = 2(1+\epsilon)^2 + \frac{1}{(1+\epsilon)^4} - 3 \simeq 2(1+2\epsilon)+(1-4\epsilon)-3 = 0\ (\epsilon \to 0)\end{aligned} \tag{B.3}$$

Gent model

$$\begin{aligned}
\sigma_{G,t,uni} &= \frac{E}{3}.\frac{\lambda^2 - \dfrac{1}{\lambda}}{1 - \dfrac{J_{1,uni}}{J_m}} = \frac{E}{3}.\frac{(1+\epsilon)^2 - \dfrac{1}{1+\epsilon}}{1 - \dfrac{J_{1,uni}}{J_m}} \\
(\epsilon \to 0) &\simeq \frac{E}{3}.(1 + 2\epsilon - (1-\epsilon)) \\
\sigma_{G,t,uni} &\simeq E\epsilon
\end{aligned} \tag{B.4}$$

$$\begin{aligned}
\sigma_{G,t,bi} &= \frac{E}{3}.\frac{\lambda^2 - \dfrac{1}{\lambda^4}}{J_{1,bi}} J_m = \frac{E}{3}.\frac{(1+\epsilon)^2 - \dfrac{1}{(1+\epsilon)^4}}{1 - \dfrac{J_{1,bi}}{J_m}} \\
(\epsilon \to 0) &\simeq \frac{E}{3}.(1 + 2\epsilon - (1-4\epsilon)) \\
\sigma_{G,t,bi} &\simeq 2E\epsilon
\end{aligned} \tag{B.5}$$

We verify here that there is the same slope dependence between the stress and the stretch at small strains, and that E defined in the Gent model is truly the material's Young modulus.

Yeoh

$$\begin{aligned}
\sigma_{Y,t,uni} &= 2(C_1 + 2C_2 J_{1,uni} + 3C_3 J_{1,uni}^2)\left(\lambda^2 - \frac{1}{\lambda}\right) = 2(C_1 + 2C_2 J_{1,uni} + 3C_3 J_{1,uni}^2)\left((1+\epsilon)^2 - \frac{1}{1+\epsilon}\right) \\
(\epsilon \to 0) &\simeq 2C_1(1 + 2\epsilon - (1-\epsilon)) \\
\sigma_{Y,t,uni} &\simeq 6C_1\epsilon
\end{aligned} \tag{B.6}$$

$$\begin{aligned}
\sigma_{Y,t,bi} &= 2(C_1 + 2C_2 J_{1,bi} + 3C_3 J_{1,bi}^2)\left(\lambda^2 - \frac{1}{\lambda^4}\right) = 2(C_1 + 2C_2 J_{1,bi} + 3C_3 J_{1,bi}^2)\left((1+\epsilon)^2 - \frac{1}{(1+\epsilon)^4}\right) \\
(\epsilon \to 0) &\simeq 2C_1(1 + 2\epsilon - (1-4\epsilon)) \\
\sigma_{Y,t,uni} &\simeq 12C_1\epsilon
\end{aligned} \tag{B.7}$$

We see here that the material's modulus is defined by $6C_1$.

B.2 Bulge inflation analysis

Correction of the stretch and the stress

Figure B.1 describes the correction applied on the stretch in the bulge inflation. The beginning of the curve is linearly fitted and the intercept at $\sigma = 0$ is computed. If the intercept is above 1, the whole stretch is shifted by this intercept value, this leads to **the corrected stretch**. The stress computation depends on the stretch, therefore the **corrected stress** is computed with the corrected stretch. All the experimental curves displayed in this study are the true corrected stress versus the corrected stretch.

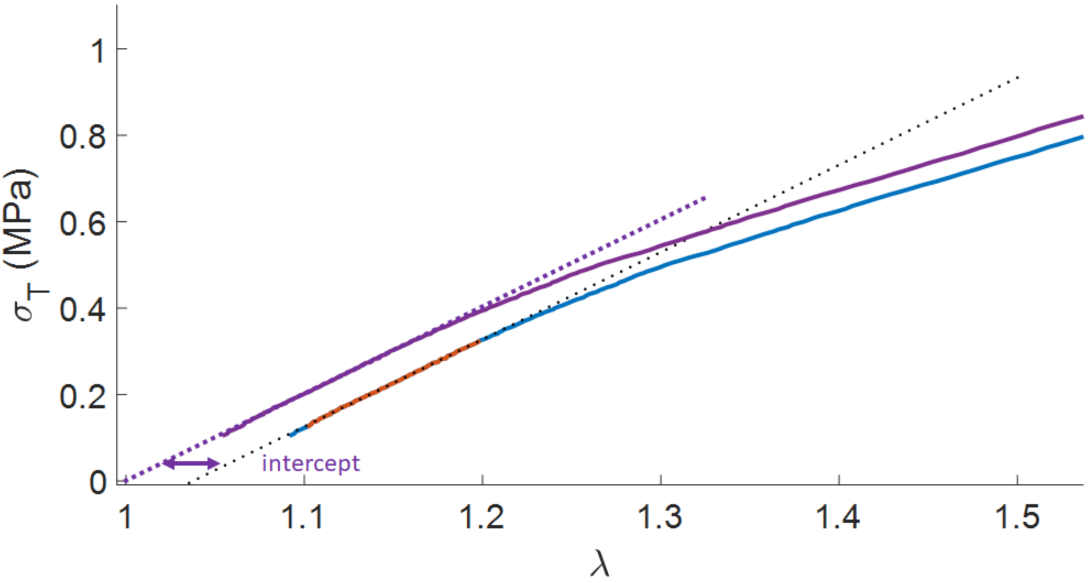

FIGURE B.1: Correction of the stretch in biaxial inflation. Blue curve: initial computed stress and stretch. Orange portion: zone where the linear stretch is computed. Purple curve: shifted stretch to go to ($\lambda = 1 \Rightarrow \sigma = 0$)

Complete cycles in bulge inflation

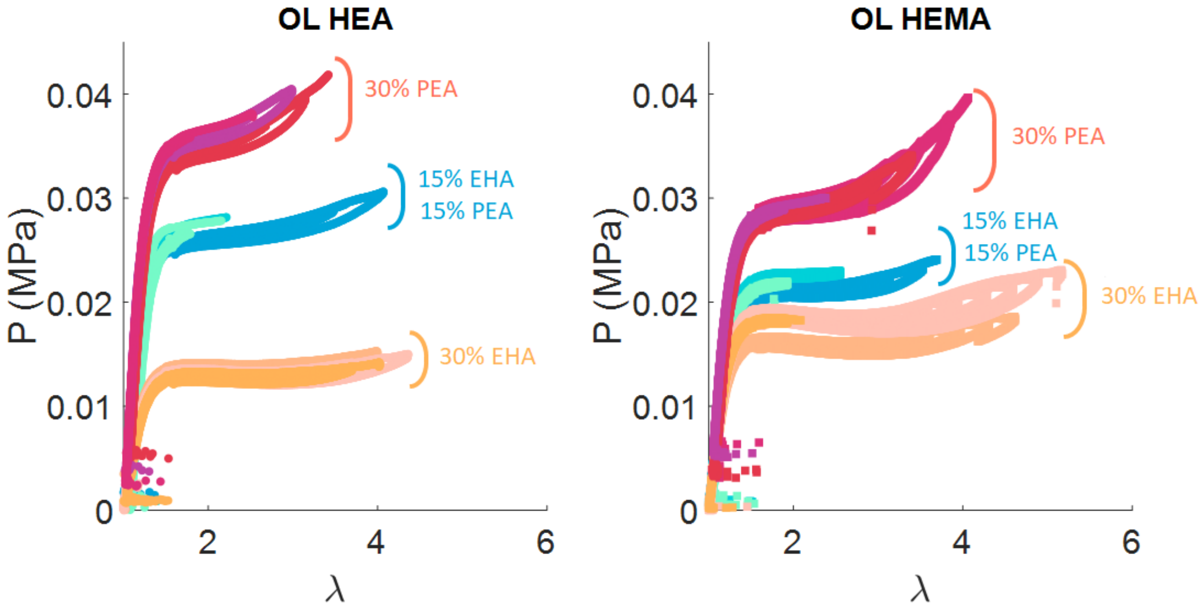

(A) All pressure cycles

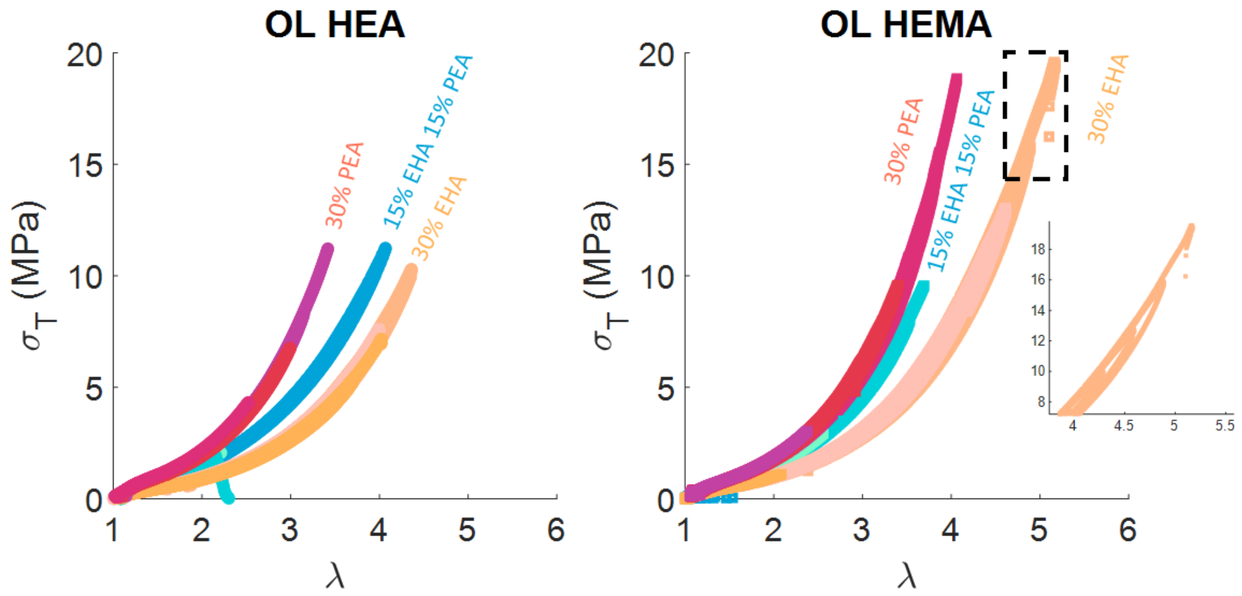

(B) Computed stress with the Hoop equation and the elliptic curvature

FIGURE B.2: Pressure and True Hoop stress versus mean stretch for all formulations - volume controlled experiment until rupture. (B) Insert: zoom on the hysteresis for the OL HEMA 30% EHA 3 sample

Discussion on the assumptions

The bulge analysis is based on three strong assumptions:

- The sample thickness does not change during the clamping in the sample holder.
- The stretch over the whole bulge can be computed via a circular assumption of the bulge's contour.
- The stretch is uniformly biaxial on the whole bulge during the whole experiment.

We will discuss these assumptions here and try to determine their respective error on the computation.

First, let's discuss the initial sample thickness. The thickness was measured at different spots on the polymer sheet via a touch probe before sending the samples to the FIBEr laboratory and showed a variability of at most 3%. This can be considered as negligible. However, when clamping the polymer sheet, it can be slightly pre-stretched, leading to a thinning of the sample. This uncertainty on the initial thickness impacts the stress computation. However there is no way to exactly determine its impact. It must not be too important, as polymer sample that have the same initial thickness (OL HEA 30% EHA 2 and 4 and all OL HEMA 30% PEA samples) have a very similar behaviour. This shows that either there is no pre-stretching, or it is really reproducible between the samples. We can therefore conclude this is not an important error on the measurements.

Then, the stretch measurement via the circular assumption of the contour can be put into question, especially when higher inflation volumes are reached. We can compute the exact length of deformed polymer at each inflation and compare this stretch measurement with the one made with the circular assumption. Now, the computation of the exact polymer length is not straightforward, as a portion of the bulge is invisible and there are some detection issues due to the tank's wall reflection. However, we can use the elliptic fit to extract a good approximation of the contour. The sample holder is 3 mm thick, so we know the coordinates of the two contour points where the polymer is clamped: on the x-axis, they are located at -3 mm, 0 being the x-coordinate of the first experimental points accessible, and they are apart from $L_0/2$, symmetrically opposed from the axis of the polymer bulge. The fits are computed with the experimental data and those two fixed points. As seen on Figure B.3, the circular fit always goes through the two fixed points while the ellipse fit doesn't always include the clamped positions. The stretch is measured by:

$$\lambda = \frac{perimeter}{L_0} \tag{B.8}$$

and the relative error between the two stretches is computed as:

$$Relative\ error = \frac{\mid \lambda_{spherical\ assumption} - \lambda_{perimeter} \mid}{\lambda_{perimeter}} * 100 \tag{B.9}$$

The ellipse fit doesn't follow the exact shape of the clamped polymer membrane, so we don't know exactly how the polymer length variates. However, we can estimate 2 extreme cases: either compute the polymer length from the ellipse fit as is, meaning that we overestimate the polymer length by not respecting the clamped conditions, or force the shape of the ellipse to include a gap of L_0, meaning that we truncate ellipse perimeter. The two computations and the respective errors are displayed on Figure B.3 (B) and (C).

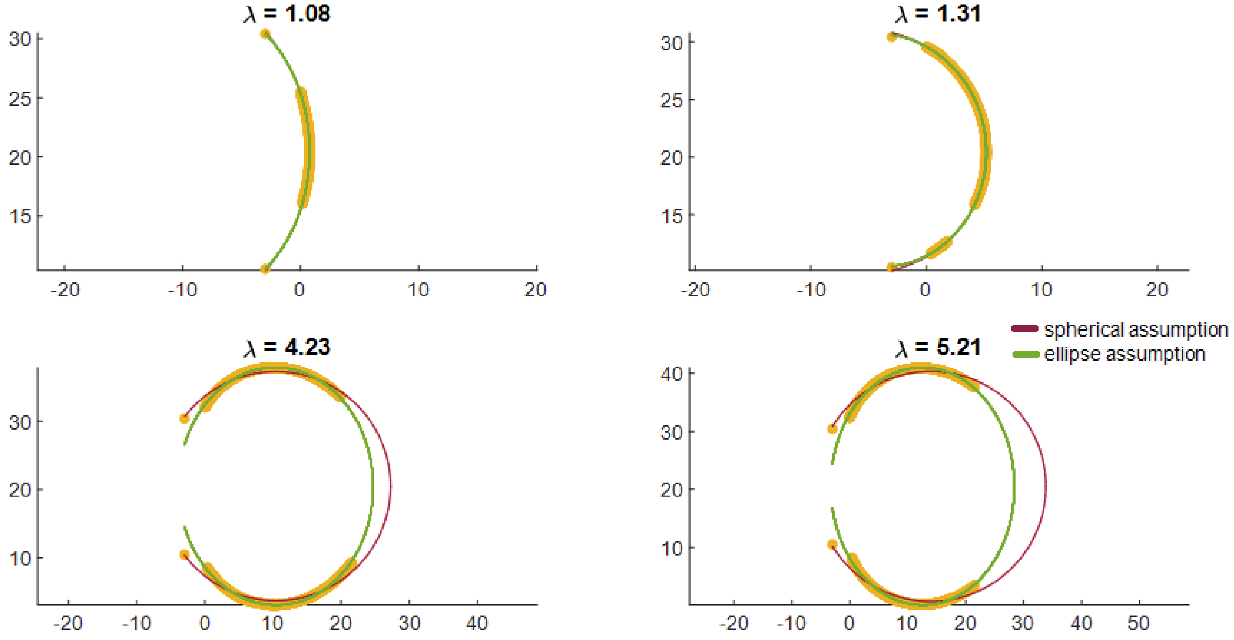

(A) Circular and ellipse fitting for different stretches

For both cases, the relative error reaches a high value for small deformations, for $\lambda < \pi/2$, meaning before the bulge increases over the half sphere. This is surprising, as for small deformations, the spherical assumption is still valid [74]. One possibility for this discrepancy is the interpolation over the polymer part that is not seen. For small deformations, this represents a large fraction of the total perimeter, and the behaviour of the bulge near the holding points is not known. Therefore, computations of the exact polymer length may not be the most trustworthy for the small deformations. For large strains, the error depends on the computation. For the ellipse fit without consideration of the clamped distance, meaning the overestimation of the stretch, the error is below 5%. For the other extreme, the error increases for very high stretches. However, it

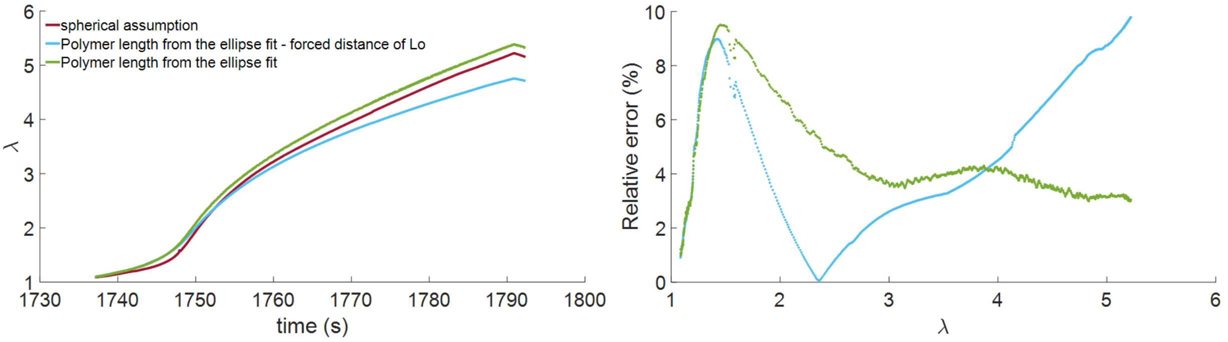

(B) Stretch computation from the spherical assumption and the polymer length

(C) Relative error between the 2 computations

FIGURE B.3: Error estimation between the spherical assumption and the polymer length measurement for the mean stretch computation - OL HEMA 30% EHA.

remains below 10%. We can conclude that while the spherical approximation is not the best for high stretches, it is an assumption that takes into account the clamped distance better than the ellipse one, and it proves good enough for the mean stretch computation. Furthermore, it may lead to less numerical errors than the perimeter computation of a contour from the ellipse fit, which is not trivial.

Finally, the main error is our computation is to assume that the stretch is truly biaxial over the whole bulge. Based on the Abaqus model of OL HEMA 30%PEA 3, the mean stretch based on the circular assumption of the modelled contour can be computed and compared with the true biaxial stretch at the contour's apex. The biaxial stress can also be compared to our computation based on the mean stretch and the ellipse curvature assumption. As can be seen on Figure B.4 (A), the error made when computing the whole stretch and deducing the stress is quite high compared to the true biaxial values. This leads to an overall shift of the stress/stretch curve to smaller values. This error computation will be dependant on the studied material, but it still gives us an idea of how off we are in our experimental analysis.

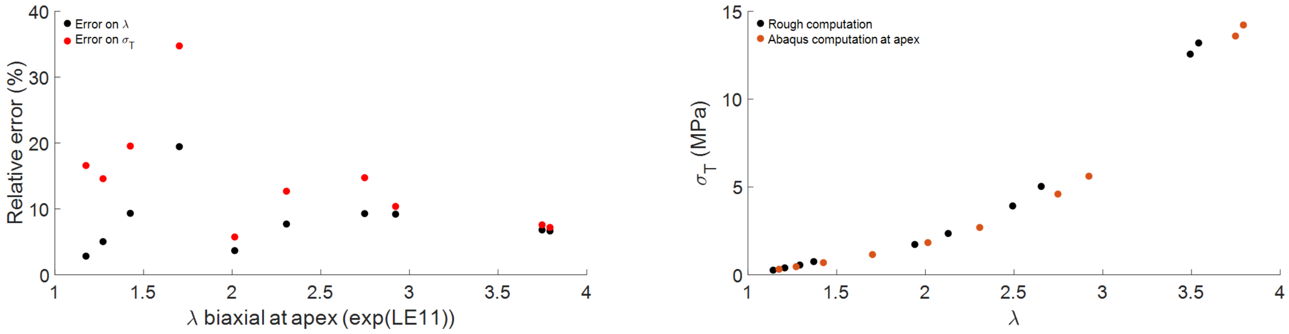

(A) Relative error between the true biaxial stress and stretch and the approximative computation

(B) Difference in the true biaxial stress/stretch behaviour and the rough computation

FIGURE B.4: Error estimation for the rough computation of the stretch and stress over the whole bulge

B.3 Non-linear elasticity analysis

Comparison between the biaxial and the uniaxial testing

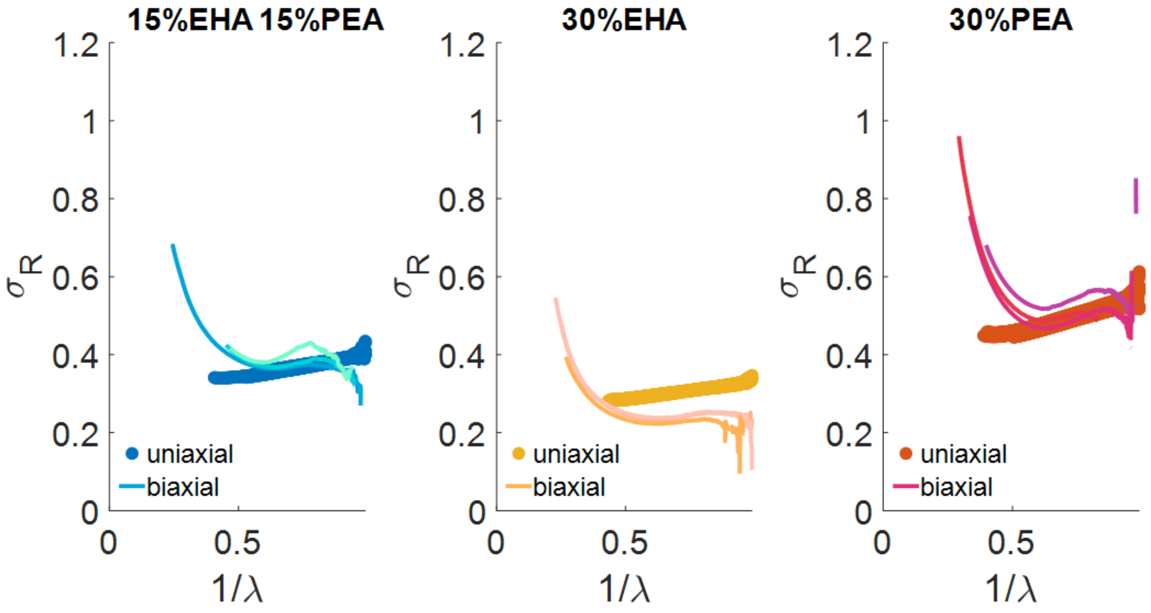

(A) OL HEA

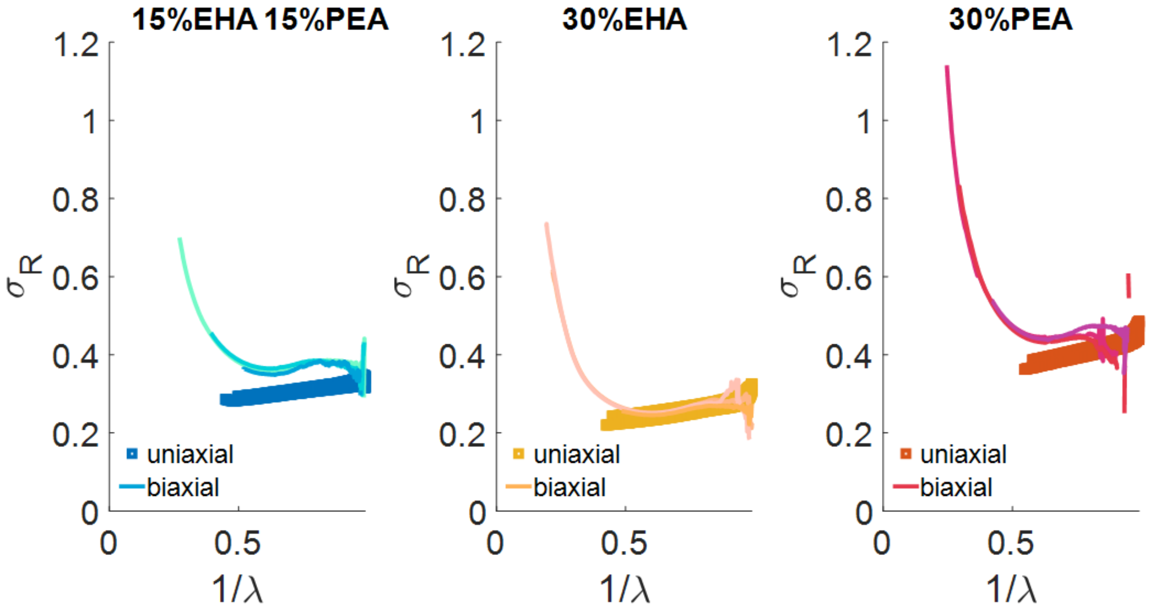

(B) OL HEMA

FIGURE B.5: Mooney plots - comparison of the uniaxial and the biaxial testing.

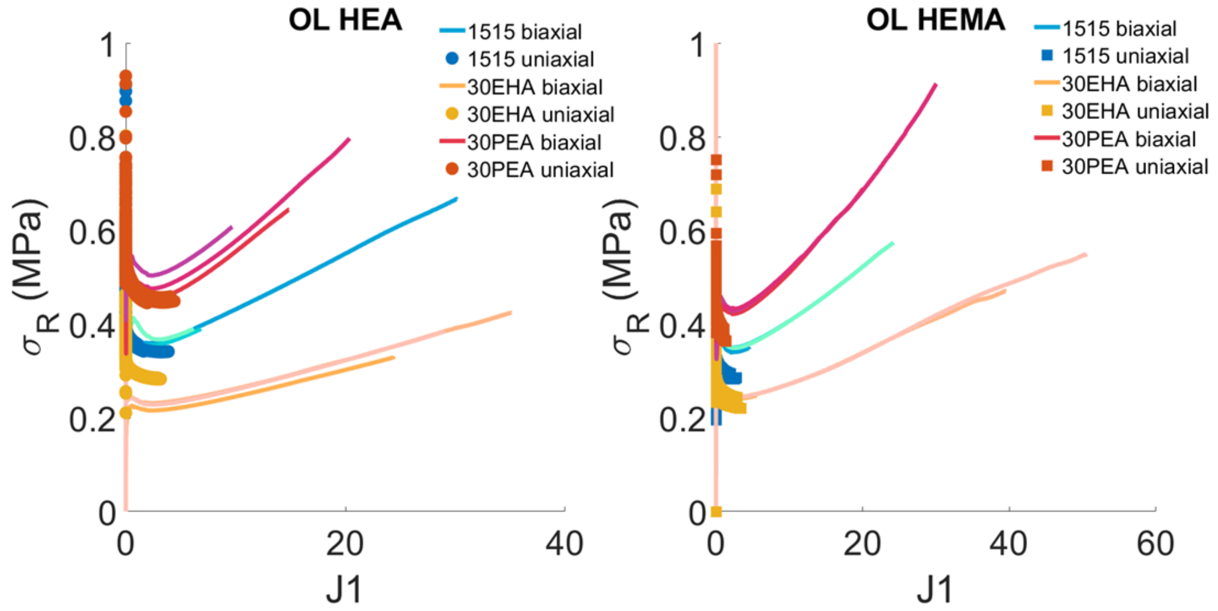

FIGURE B.6: Biaxial and uniaxial test plotted versus J1. Reduced Mooney stress

Gent and Yeoh fits

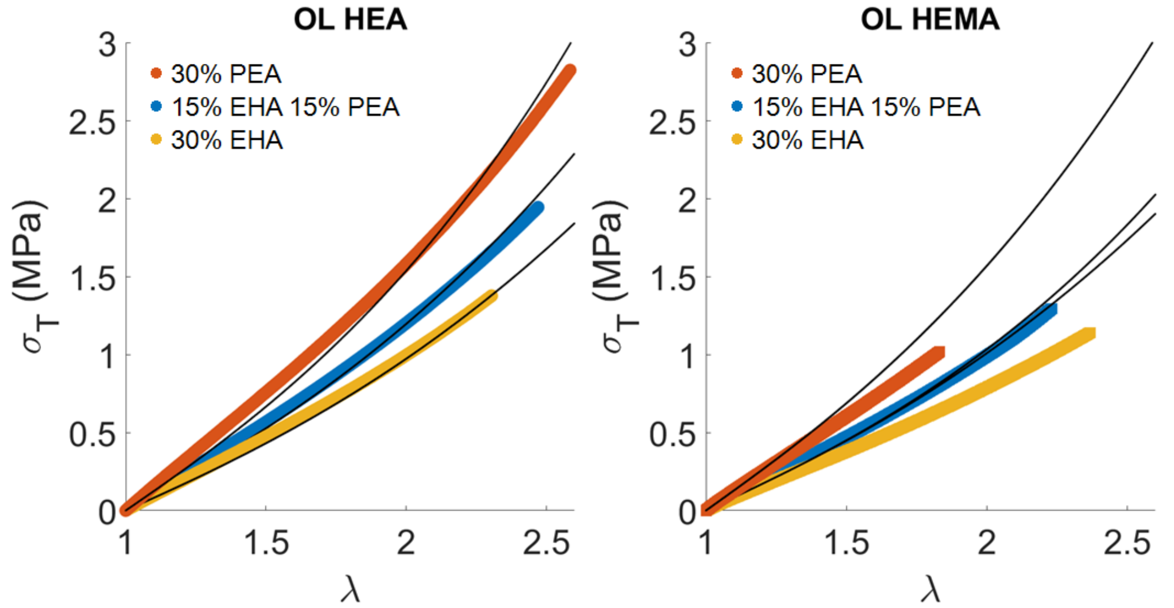

(A) Gent modelling of uniaxial tests

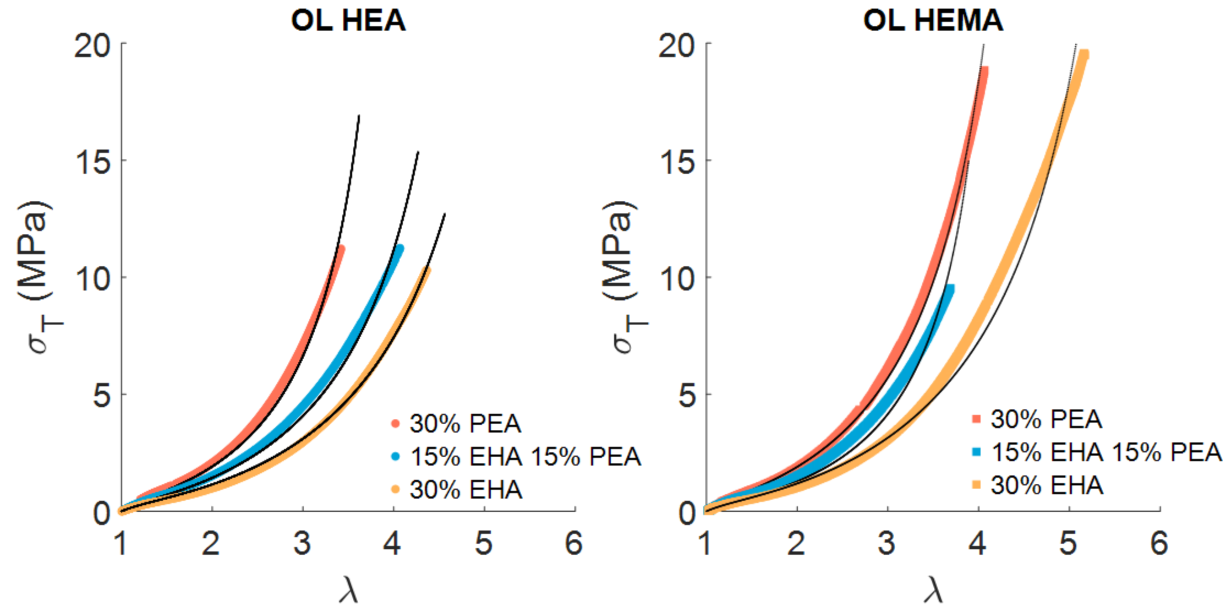

(B) Gent modelling of biaxial tests

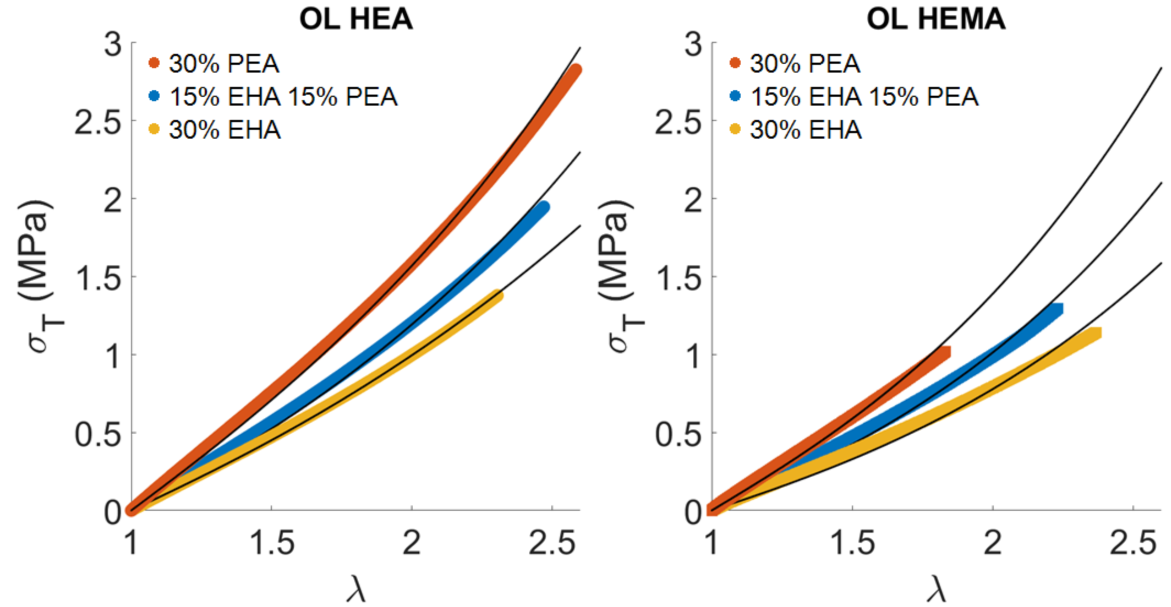

(C) Yeoh modelling of uniaxial tests

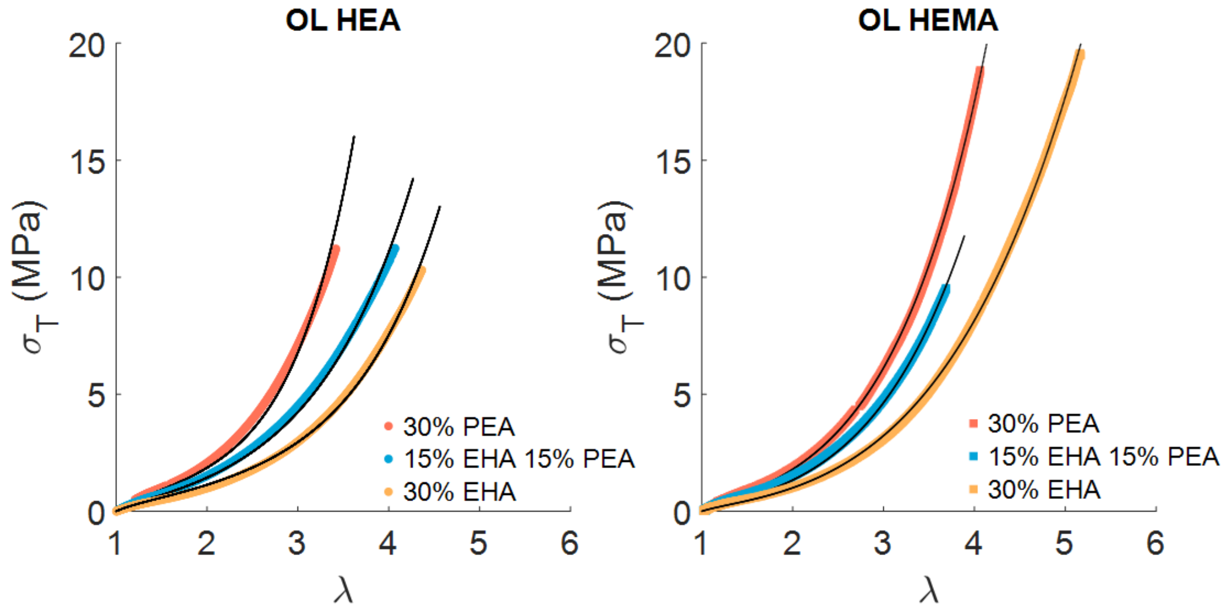

(D) Yeoh modelling of biaxial tests

FIGURE B.7: Gent and Yeoh fits of the networks behaviour. The fits are done with one uniaxial test leading to the longest deformation and all biaxial tests leading to a stretch longer than 2.5. The fits are shown in thin lines. (B) and (D): The insert show the fit on small deformations in biaxial testing

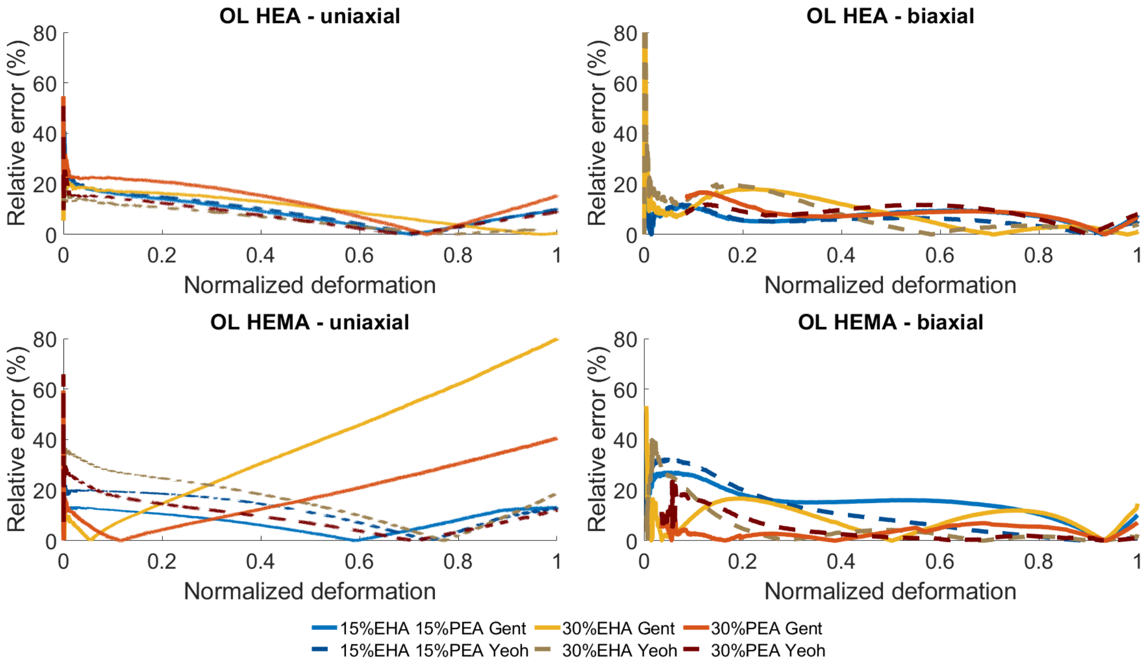

FIGURE B.8: Relative error of the Gent and Yeoh fit versus the experimental data in uniaxial and biaxial test

B.4 Influence of the formulation on the fracture curves

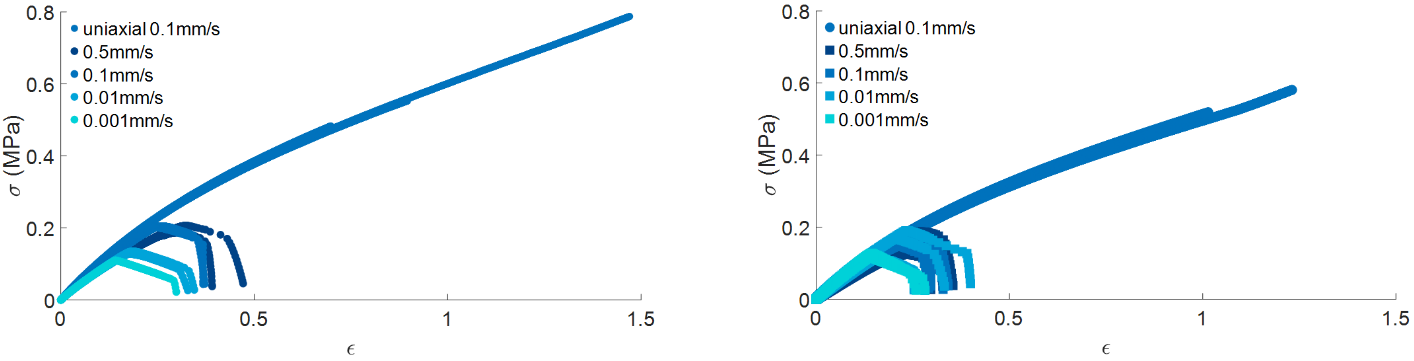

(A) OL HEA 15% EHA 15% PEA

(B) OL HEMA 15% EHA 15% PEA

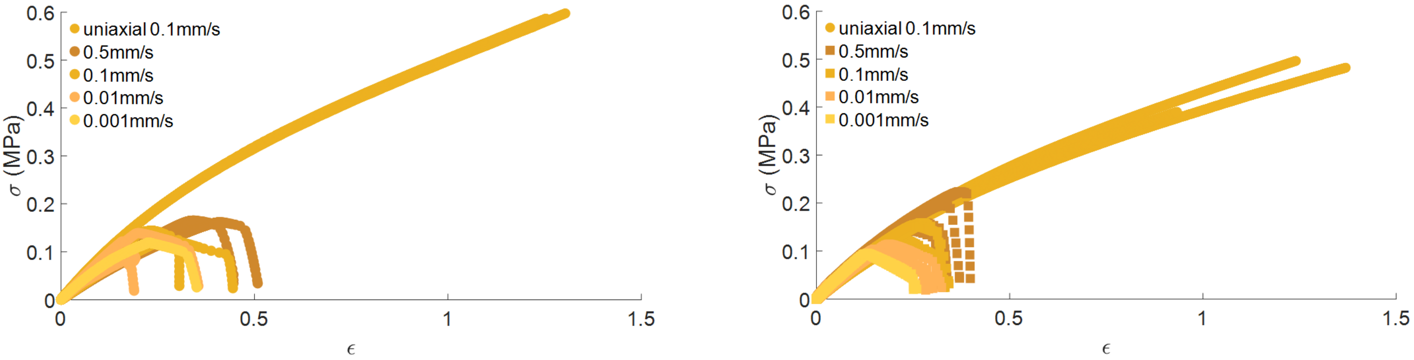

(C) OL HEA 30% EHA

(D) OL HEMA 30% EHA

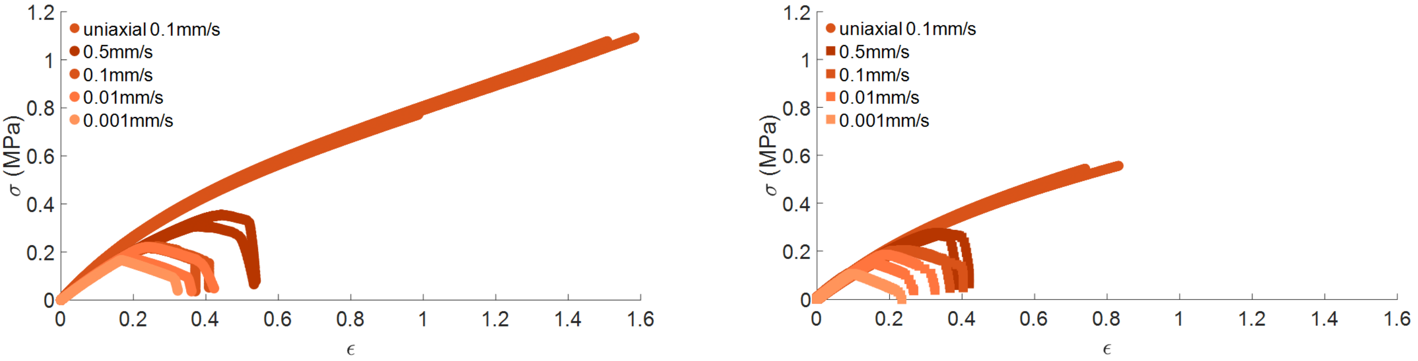

(E) OL HEA 30% PEA

(F) OL HEMA 30% PEA

The variability between samples leads to a variability of the behaviour in small strains. The maximum stress and deformation at break of the fracture sample depends on the velocity but also may vary with the initial crack length.

Appendix C

Appendix on the cavitation set-up production

C.1 Silanisation solution

The silane solution is prepared following these steps:

- 115 mL ethanol 96% - 76.5%v
- 25.5 mL acetic acid – 17%v
- 6 mL H2O MilliQ – 4%v
- 3.75 mL silane added when stirring – 2.5%v

The hydrolysis is done at ambient temperature for 20 min, while stirring.

C.2 Materials

Glass surfaces:
Borosilicate glass slides bought from Ediver: 75 mm x 25 mm, 2 mm thickness, tolerance of 0.5 mm
Borosilicate half sphere glass lenses (N-BK7) bought from Edmund Optics, diameter 6 mm

Displacement:
Motor displacement: Newport
Displacement stage: M-UMR8.25
Motor: TRA25PPD + ADAPT-TRA25
Controller: SMS100PP + SMC-PS80 + SMS-USB
Displacement stages for the sensors: Opto Sigma TASB-1

Displacement sensors: $\mu\epsilon$
Controller:
DT6220 capacitive multi channel controller
DL6220 Demodulator with integrated preamplifier
Sensors:
CCm1,4C Sensor cable capaNCDT 1.4 m long
CS005 Capacitive Displacement Sensor (50 μm for the force measurement)
CCm1,4B Sensor cable capaNCDT 1.4 m long
CS1 Capacitive Displacement Sensor (1 mm for the displacement measurement)

C.3 Cavitation set-up: Double cantilever for the force measurement

Theoretical model and stiffness prediction

The stiffness for one blade of thickness h, length L_0 and width b is:

$$S_{1blade} = \frac{Eb}{2}\left(\frac{h}{L_0}\right)^3 \tag{C.1}$$

with E = 75.10^9 Pa the Young's modulus of the aluminium used for the blade. When using a double cantilever, the 4 blades are in parallel, so the total stiffness is:

$$S_{tot} = 4.S_{1\ blade} = 2Eb\left(\frac{h}{L_0}\right)^3 \tag{C.2}$$

In practice, the theoretical stiffness is decided for the experimental needs. Based on preliminary tests, a force of around 20 N is expected, and the double cantilever is required to be quite stiff. A deflection of only 1 μm for 20 N seems appropriate, that means a theoretical stiffness of $S_{tot} = 2.10^7$ N/m. This means:

$$h = L_0.\left(\frac{2Eb}{S_{tot}}\right)^{1/3} = 1.66\ mm \tag{C.3}$$

Calibration and force resolution

The double cantilever is calibrated by hanging different weights and linking the applied force to the measured displacement. This leads to the following calibration curve, the slope linking F and δ is the stiffness.

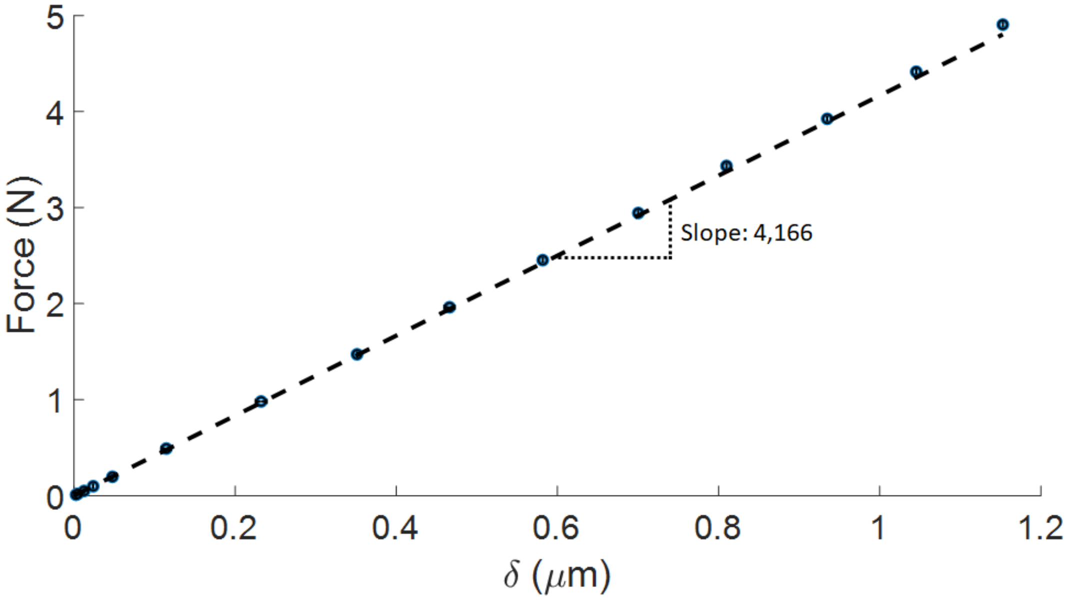

FIGURE C.1: Double cantilever stiffness calibration. Different masses are put on the double cantilever and the displacement measured. The blue points are the experimental measurements (with the standard deviation), the broken line is the theoretical stiffness.

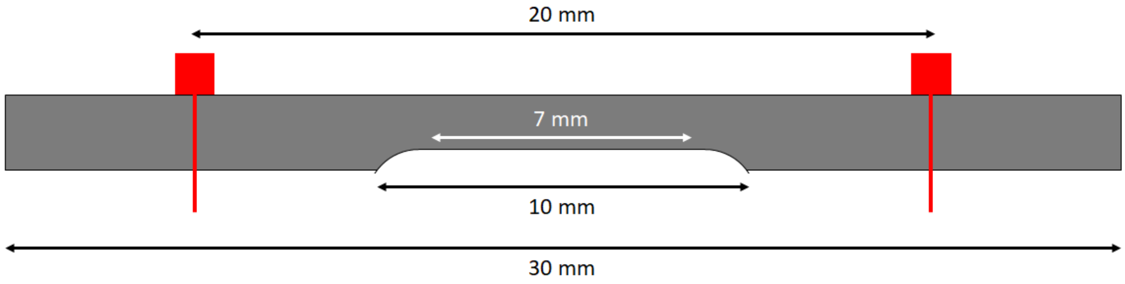

FIGURE C.2: Schematic of the blade for the double cantilever. The theoretical length that gets deformed is L_0 = 7 mm and the width of the blade is b = 10 mm. The blade is screwed tight to the set-up.

The measured stiffness is below the theoretical value. This is due to the fact that the metal blades are originally 2 mm thick. The thickness difference between the "thin" part of the blade that deforms and the "thick" that is screwed to the set-up is not that big, leading to a global deformation of the whole blade. Therefore, the length of the blade L_{exp} is longer than the predicted L_0:

$$L_{exp} = h.\left(\frac{2Eb}{S_{tot}}\right)^{2/3} = 11.81\ mm$$

while L_0 = 7 mm in the theoretical computation.

The force resolution can then be computed. The resolution of the capacitive sensor for the force measurement is $\delta l = 1\ nm$, while the measured distance is in μm, which means this error is negligible. The error on the stiffness is $\delta k = 0,107.10^6$ N/m and is the main error source:

$$\frac{\delta F}{F} = \sqrt{\left(\frac{\delta k}{k}\right)^2 + \left(\frac{\delta l}{l}\right)^2} \sim \frac{\delta k}{k} = 2.57\% \qquad \text{(C.4)}$$

The error on the force is therefore 2.57% of the measured value.

C.4 Experimental problems and high cavitation pressures

In the experiments we conducted on the 100 μm layers, we also observed samples that presented a very high cavitation resistance, with a hydrostatic pressure for the opening of the 1^{st} cavity to the order of 30E. However, when looking at the Force versus displacement curves, we observed a strange behaviour, as presented on Figure C.3.

When comparing these experimental curves to the ones we presented as OK in Chapters 4 and 5, the curves presented on Figure C.3 seem very dodgy. Indeed, when looking back at the experimental set-up, the punch, which is pulled on, slides in the fixed part. Now, if the punch is not exactly perpendicular to the glass slide, it is possible that it frictions with the mobile part. As the force is measured by the deflection of the fixed part, if it is blocked with the punch, the force measured is just the friction with the punch. In some cases, the punch slips suddenly during the loading, as can be seem on the yellow curve of Figure C.3.

Experimentally, this friction and slippage were also detected as small metallic sounds were heard as the punch was slipping. Also, this sudden load on the polymer as the punch slips lead to multiple cavitation events (2 to 3), something we did not observe in the experiments without punch friction. Therefore, we decided to put those experiments aside, as the measured force for

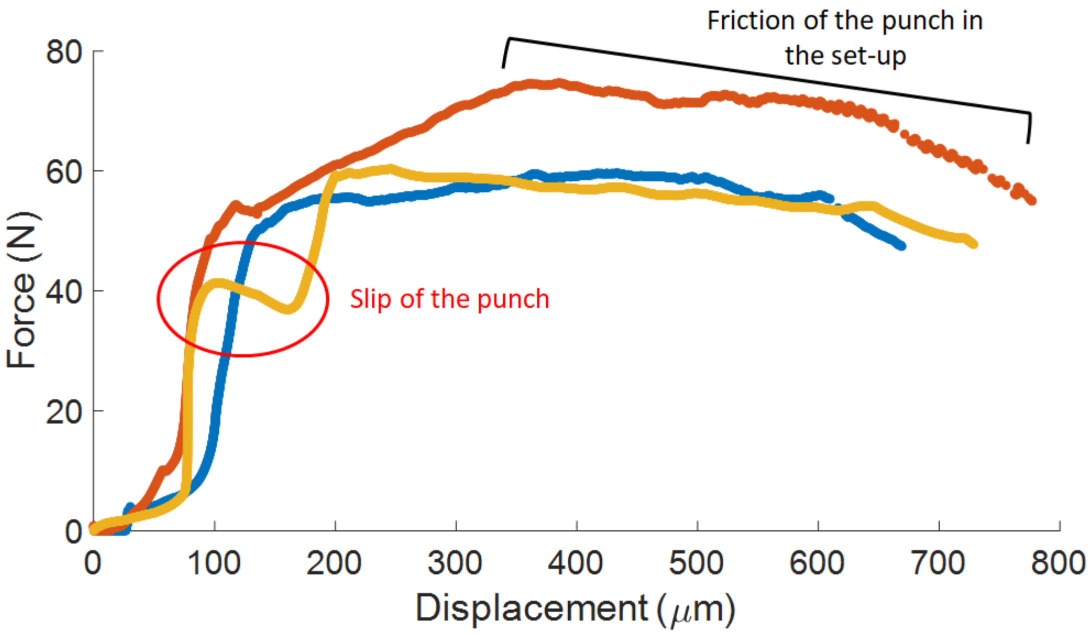

FIGURE C.3: Force versus displacement curves that present a suspect behaviour. When the force changes drastically before the cavitation events, or doesn't decrease after the breakage of the polymer, the experiment is considered NOT OK.

the first cavitation event could be artificially higher (since one part of the force could just be applied to the punch rather than the confined polymer layer).

However, in the case case of these forces were indeed applied on the polymer layer, Figure C.4 shows the new type of hydrostatic forces that would be observed for the different formulations. Interestingly, the bimodal formulations show again very high hydrostatic pressures.

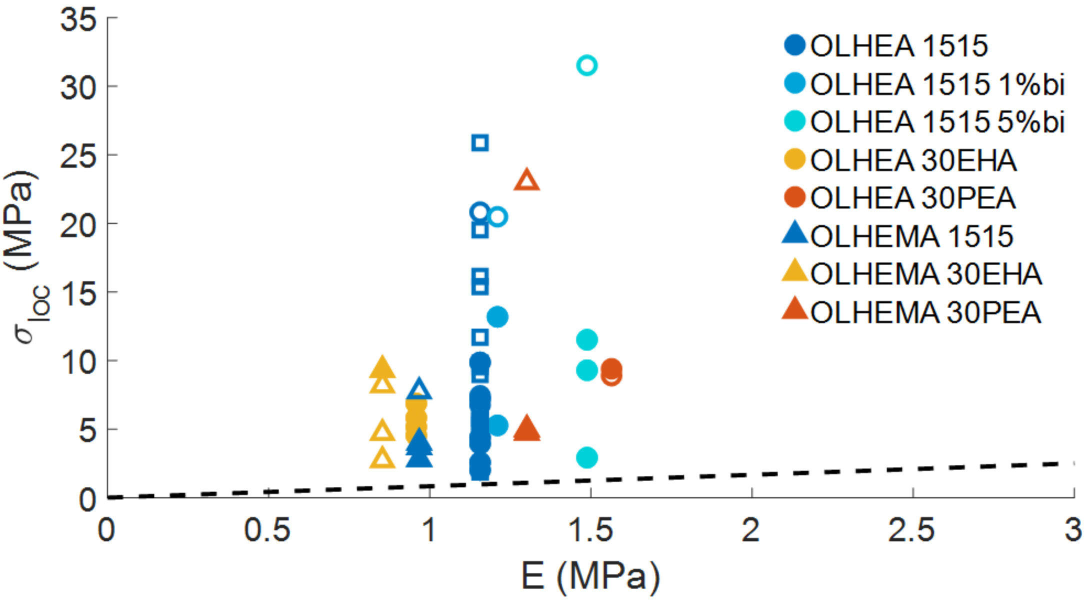

FIGURE C.4: Variation of the cavitation pressure with the Young modulus - including the suspicious samples displayed in open symbols.

The thickness effect on the hydrostatic pressure would also be more obvious, as described on

Figure C.5. In that case, the observation of the thin layer containing a distribution of defect sizes smaller than the thick layer seems very attractive. However, we need to stress again that the results plotted with the open symbols are suspicious and this high hydrostatic pressure could very well only be an effect of the punch friction to the fixed part of the set-up.

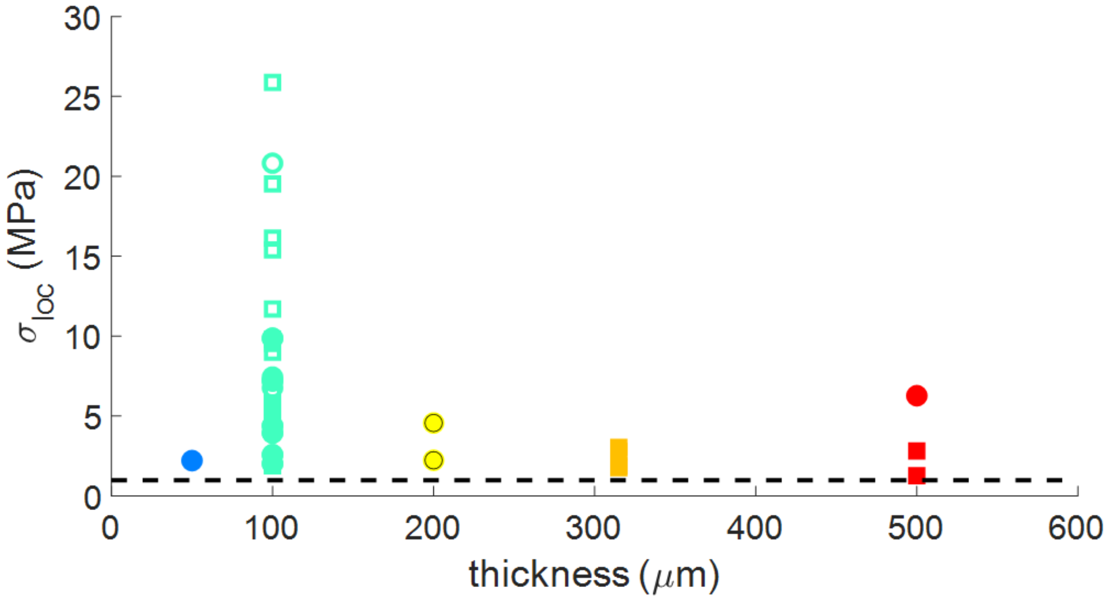

FIGURE C.5: Variation of the cavitation pressure with the thickness - including the suspicious samples displayed in open symbols. Formulation: OL HEA 15% EHA 15% PEA - circles: testing velocity 5 μm/s, squares: testing velocity 0.5 μm/s

This section should act as a small reminder that when building a set-up, some unexpected behaviours may happen, that seem obvious when observed, but are not that trivial to foresee. Therefore, when building a set-up, it is crucial to have a close and doubtfull look at the raw data of the experiments to see if the measured values are indeed what we think (and hope) they are. This problem has been now fixed, the place where the punch slides in the fixed part has been widen to avoid friction.

Appendix D

Appendix on the cavitation behaviour

D.1 Thick layers - 500 μm

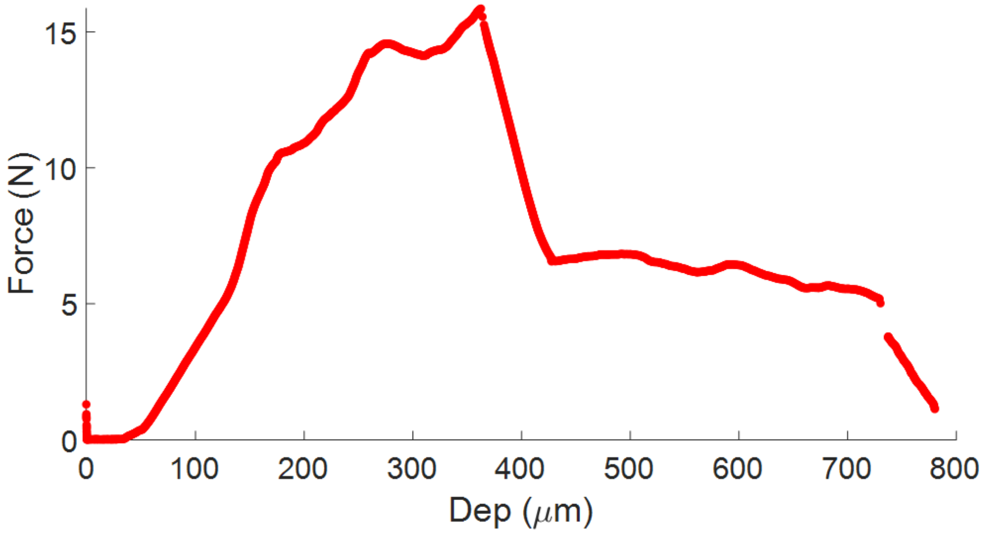

FIGURE D.1: Loading curve of the 500 μm sample at 0.5 μm/s. The somewhat weird behaviour before the snap is attributed to movements of the glue between the lens and the punch during the loading, which causes background changes.

D.2 Very thin layers

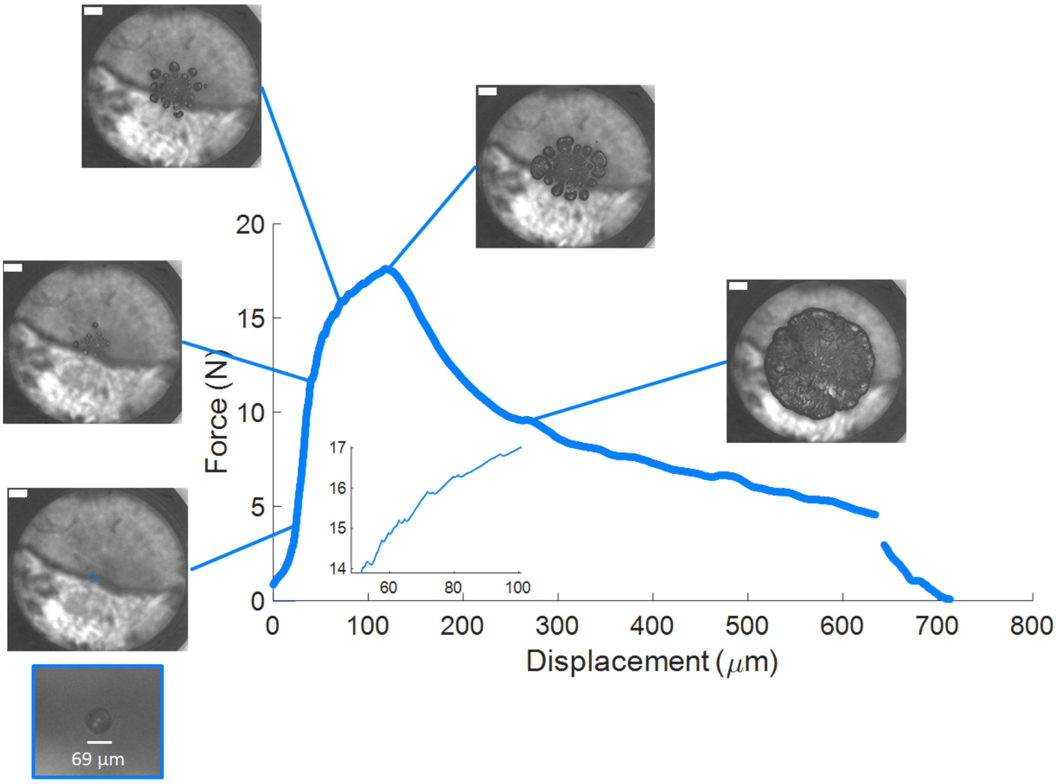

FIGURE D.2: Loading curve of a 50 μm sample at 5 μm/s and corresponding cavitation events. Scale bar: 500 μm. The dirty background did not allow for a precise analysis of the cavities' growth.

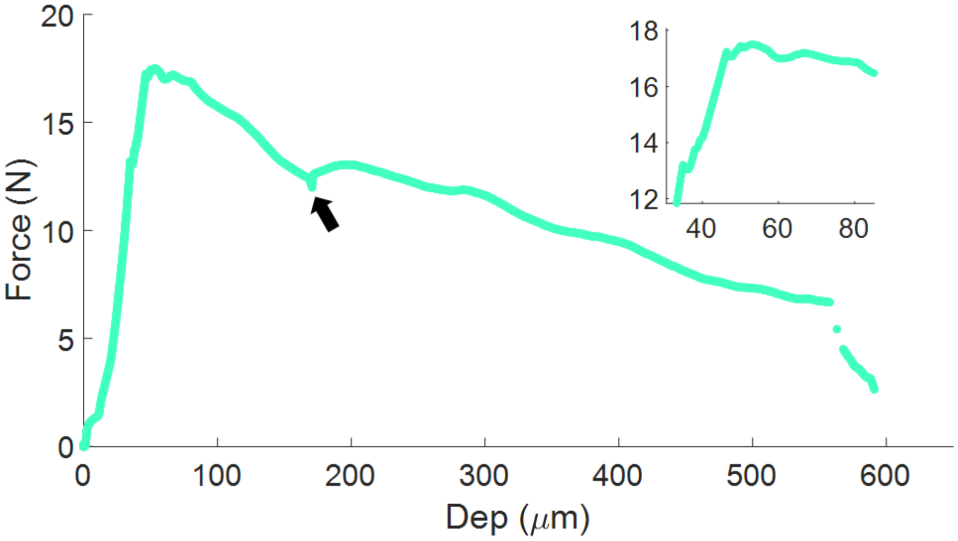

FIGURE D.3: Loading curve of a 100 μm sample at 0.5 μm/s. The black arrows shows the moment of the switch to 5 μm/s for the final circular crack propagation. Insert: zoom on the cavitation events.

D.3 Mixing DACL into the polymer mix

In order to maximise the dispersion of the DACL mecanophore in the viscous polymer mix of (70% OL HEA + 15% EHA + 15% PEA), the following procedure was followed:

- Mixing the OL HEA to the EHA and PEA monomer with magnetic stirrer
- Dissolving the BAPO and the DACL powders in dry acetone (5 mL were used for 66 mg of powder)
- Mixing the polymer mix with the acetone until complete incorporation
- Filtrating with a 0.45 μm filter to remove all possible remaining aggregates
- Letting the whole mixture dry under the hood overnight, under constant agitation

D.4 Hydrostatic pressure as a function of G_c(0.0067%/s)

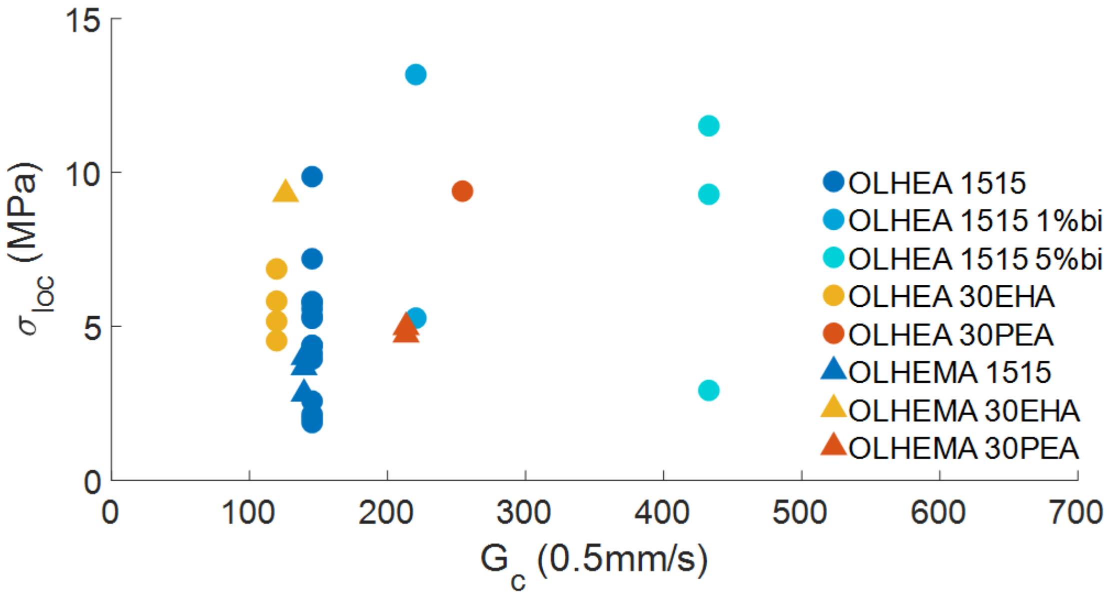

FIGURE D.4: Variation of the cavitation pressure with fracture energy - slow testing rate: 0.0067%/s, the initial stretch rate for the hydrostatic traction experiments at 5 μm/s is 5%/s for a 100 μm sample.

D.5 Formulation effect on the loading curve - v = 5 μm/s

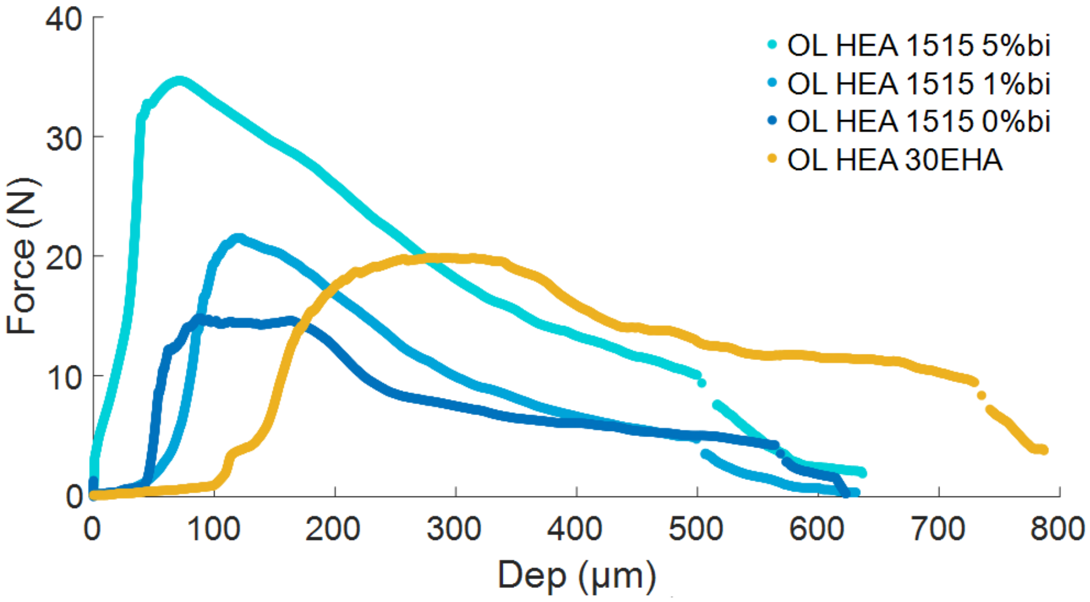

(A) Complete Force versus displacement curve and effect of the formulation

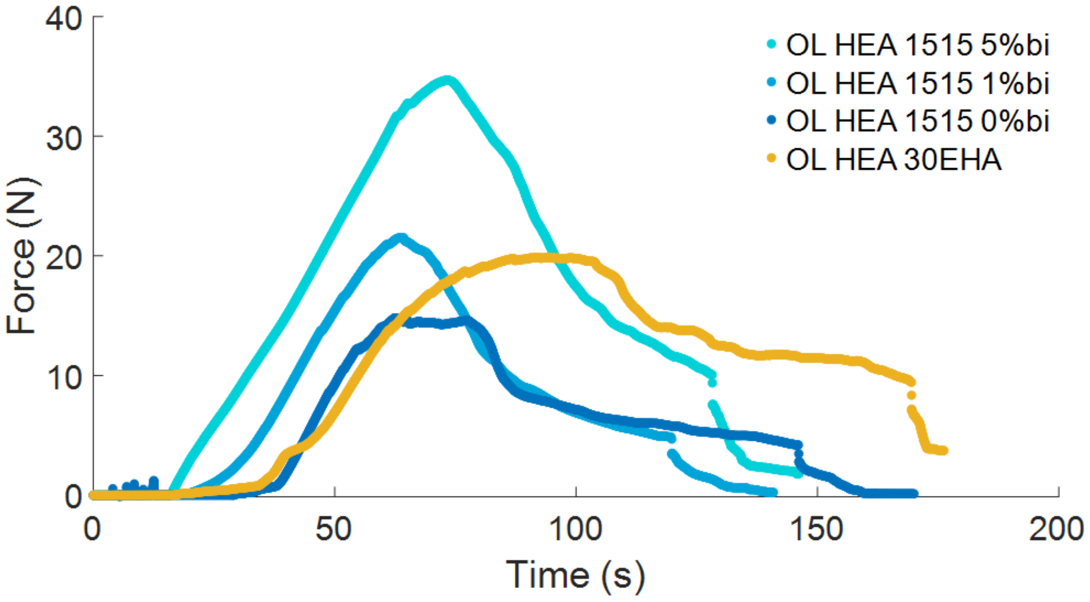

(B) Complete Force versus time curve and effect of the formulation

FIGURE D.5: Loading curves depending on the formulation - testing velocity: 5 μm/s, corresponding to the experiments described in Section 5.2.

D.6 Insight on the cavitation behaviour of OL HEA 30% PEA and OL HEMA 30% PEA

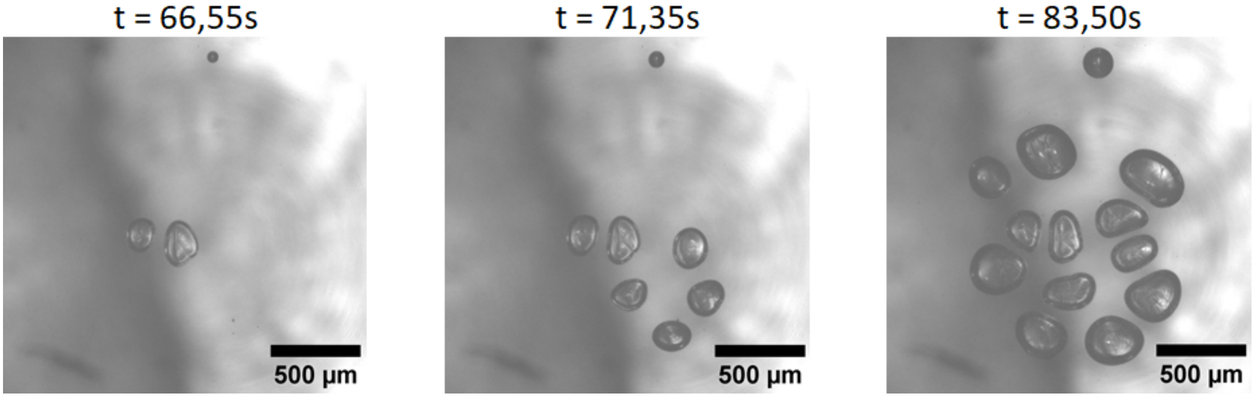

(A) OL HEA 30% PEA - E = 1.564 MPa, $G_c = 63.76 \pm 9.56$ J/m^2

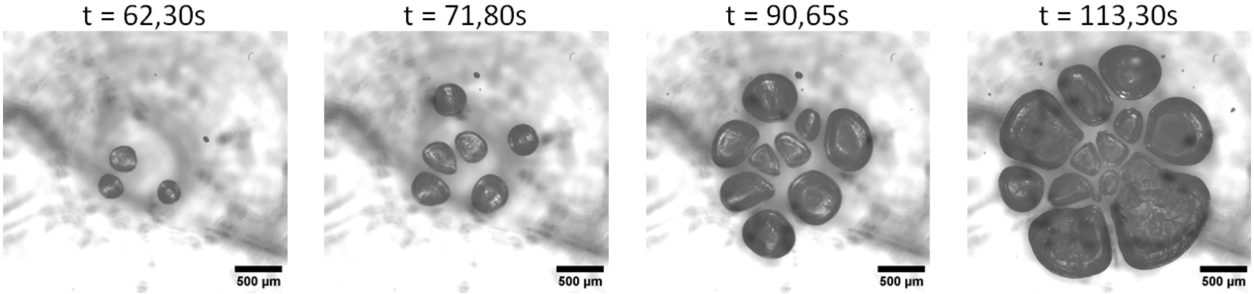

(B) OL HEMA 30% PEA - E = 1.301 MPa, $G_c = 33.40 \pm 3.39$ J/m^2

FIGURE D.6: Preliminary observations of the 30% PEA networks. It seems that even with a high fracture energy and a high Young's modulus, the cavities stay stable in a pancake shape, compared to the formulations with the higher strain hardening. The fracture energy displayed was measured in the single notched sample at 0.0067%/s initial stretch rate.

RÉSUMÉ

Chaque seconde, 29 To de données sont échangées sur Internet et plus de 90% d'entre elles transitent par fibre optique. Les fibres de verre sont protégées par plusieurs couches de résines polymères de propriétés mécaniques différentes, la vitesse de production des câbles conduit à une accumulation de contraintes internes, pouvant mener à un phénomène de cavitation dans la première couche de protection de la fibre de verre. Afin d'étudier ce phénomène, nous avons synthétisé des réseaux élastomères à base d'oligomères fonctionnalisés di-(méth)acrylates (PPG8000) et de monomères acrylates (EHA et PEA) en polymérisation radicalaire par illumination UV flash (1s) de haute intensité. Par leur formulation et leur procédé de polymérisation, nos réseaux sont des systèmes modèles représentatifs des revêtements industriels. Après avoir étudié l'influence du processus de polymérisation sur la structure du réseau, nous avons caractérisé les propriétés mécaniques du matériau (élasticité, énergie de fracture, raidissement) au travers de tests de traction uniaxiale et de gonflement de membrane.

Enfin, nous proposons un montage innovant et original pour tester des couches minces confinées de une à plusieurs centaines de micromètres d'épaisseur sous traction principalement hydrostatique dans une géométrie sphère/plan. Le montage, conçu en interne, permet d'observer en temps réel la nucléation et la croissance de cavités pendant le test. Une analyse par éléments finis a permis de relier la force macroscopique mesurée à la pression hydrostatique locale où le premier événement de cavitation se produit. Toutes les formulations et les épaisseurs testées ont montré une résistance à la cavitation bien supérieure à la limite théorique de 5E/6, la diminution de l'épaisseur conduit à une dispersion accrue vers des pressions élevées pour le premier événement de cavitation. La différence de confinement produit un effet reproductible sur le comportement de la cavitation. Les échantillons épais (500 μm) présentent un unique événement de cavitation critique qui transite vers une fracture de mode I sur l'ensemble de l'échantillon, la diminution de l'épaisseur conduit à des événements de cavitation multiples qui semblent être stabilisés sur une plus grande gamme de pressions appliquées. L'impact de la formulation du réseau sur la transition de ces cavités multiples en fracture de mode I est analysée. Nous suggérons un effet de l'énergie de fracture et du raidissement des différents matériaux sur la morphologie des cavités pendant leur croissance.

MOTS CLÉS

Micromécanique, Cavitation, Elastomères

ABSTRACT

Every second, 29 Tb of data are exchanged on the internet and more than 90% of it travels through optic-fibre cables. The glass fibres are protected by several layers of polymer resins of different mechanical properties. The rapidity of the coating process leads to a build-up of internal stresses that can eventually provoke cavitation in the first coating, decreasing the fibre protection. To shed some light on this cavitation behaviour, we investigated elastomer networks based on di-(meth)acrylate functionalized oligomers (PPG8000) and acrylate monomers (EHA and PEA) polymerised in a flash (less than 1 second at high UV intensities). Both the formulation and the polymerisation protocol are comparable to the industrial coatings, making it a representative model system. After an investigation of the influence of the polymerisation process on the network structure, we characterized the material properties (elasticity, strain hardening, toughness) in uniaxial traction tests and bulge inflations.

Finally, we designed and built an original set-up to test thin confined layers of one to several hundreds of micrometers under mainly hydrostatic traction in a sphere against flat geometry. With this set-up we could observe the nucleation and growth of the cavities as a function of load in real time. From finite element simulations we also determined the local hydrostatic pressure at the location of the first cavitation event. For all formulations and tested thicknesses, the cavitation resistance was well above the theoretical limit of 5E/6. However, reduced thicknesses also led to an increased dispersion to high values of measured pressures for the first cavitation event. The difference in confinement showed a reproducible effect on the cavitation behaviour. Thick samples (500 μm) presented one single cavitation event that transitioned to a mode I fracture over the whole sample while decreasing the confined thickness led to multiple cavitation events that appeared to be stabilized over a longer range of applied load. The transition of these multiple cavitation events into mode I fracture processes was observed and analysed. We saw marked differences between the different model formulations and suggest that both toughness and a high level of strain hardening of the elastomer have an effect on the cavities morphology during their growth.

KEYWORDS

Micromechanics, Cavitation, Elastomers